

New Synthetic Analogues for Biological Fe/S Clusters



Dissertation
For the Award of the Degree
“Ph.D. Division of Mathematics and Natural Sciences”
of the Georg-August-Universität Göttingen
Within the Doctoral Program Chemistry of the Georg-August University School
of Science (GAUSS)

Submitted by

Lanxia Hu

From Shandong, P. R. China

Göttingen 2022

Thesis Committee

Prof. Dr. Franc Meyer

Institute of Inorganic Chemistry, Georg-August University Göttingen

Prof. Dr. Inke Siewert

Institute of Inorganic Chemistry, Georg-August University Göttingen

Members of the Examination Board

Reviewer: Prof. Dr. Franc Meyer

Institute of Inorganic Chemistry, Georg-August University Göttingen

Second Reviewer: Prof. Dr. Inke Siewert

Institute of Inorganic Chemistry, Georg-August University Göttingen

Further members of the Examination Board

Jun.-Prof. Dr. Lisa Vondung

Institute of Inorganic Chemistry, Georg-August University Göttingen

Jun.-Prof. Dr. Anna Krawczuk

Institute of Inorganic Chemistry, Georg-August University Göttingen

Dr. Holm Frauendorf

Institute of Organic and Biomolecular Chemistry, Georg-August University Göttingen

Dr. Michael John

Institute of Organic and Biomolecular Chemistry, Georg-August University Göttingen

Date of the oral examination: 21.02.2023

Table of Contents

Chapter 1. Introduction	1
1.1 Iron-Sulfur Clusters in Nature	1
1.2 Synthetic [2Fe-2S] Clusters	3
1.3 Synthetic [4Fe-4S] Clusters	8
1.4 Mössbauer Spectroscopy.....	12
1.5 Outline and Focus of This Thesis.....	17
Chapter 2. Homoleptically Bis(benzimidazolate)-Coordinated Diferric Cluster as Modified Model for Rieske Cluster	19
2.1 Introduction	19
2.2 Synthesis and Structural Characterization.....	20
2.3 Characterization in Solution.....	22
2.4 Redox Properties	24
2.5 Characterization in the Solid State	26
2.6 Attempts to Synthesize the Mixed-Valent Cluster.....	28
2.7 Conclusions	29
Chapter 3. The Quest for Rieske-Type [2Fe-2S] Clusters	30
3.1 Introduction.....	30
3.2 Attempts to Synthesize a Novel Rieske-Type [2Fe-2S] Cluster.....	31
3.3 Conclusions	37
Chapter 4. Synthesis of Bidentate Imidazolin-2-Imines Ligands and Their Mononuclear Iron/Nickel Complexes.....	38
4.1 Introduction.....	38
4.2 Ligand Synthesis	41
4.3 Complex Synthesis and Structural Characterization.....	44
4.4 Characterization in Solution.....	47
4.5 Characterization in the Solid State	51
4.6 Conclusions	54
Chapter 5. Well-Defined [2:2] Site-Differentiated $[\text{Fe}_4\text{S}_4\text{L}^5_2\text{Cl}_2]^{0/1+}$ Complexes Ligated by a Bidentated Imidazolin-2-imine	55
5.1 Introduction.....	55
5.2 Synthesis and Structural Characterization.....	56
5.3 Characterization in Solution.....	59
5.4 Redox Properties	61
5.5 Characterization in the Solid State	62
Chapter 6. Well-Defined [2:2] Site-Differentiated $[\text{Fe}_4\text{S}_4\text{L}^5_2(\text{SR})_2]^{0/1+}$ Complexes: Syntheses and Characterization	67
6.1. Introduction.....	67
6.2. Synthesis and Structural Characterization.....	68
6.3 Characterization in Solution.....	71
6.4 Redox Properties	75
6.5. Characterization in the Solid State	78
6.6 Conclusions	84
Chapter 7. Summary	86
Chapter 8. Experimental Section	90
8.1 General Considerations	90
8.2 Ligand Synthesis	91

8.3 Complex Synthesis	92
8.4 Electrochemical Measurements.....	97
8.5 Mössbauer Measurements.....	98
8.6 Magnetic Susceptibility.....	99
Chapter 9. Appendix.....	100
9.1 Crystallographic Details.....	100
9.2. Supplementary Spectra and Information	106
9.3 Calculation	122
Formula Overview.....	142
References.....	145
List of Abbreviations	150
Curriculum Vitae.....	152
Acknowledgement.....	154

Chapter 1. Introduction

1.1 Iron-Sulfur Clusters in Nature

Iron-sulfur (Fe/S) clusters are ubiquitous and among the oldest metallocofactors that can be found on earth. In 1960, Fe/S proteins were first detected via EPR spectroscopy by Beinert and coworkers in a mitochondrial ferredoxin.^[1] Since then, a great variety of iron-sulfur clusters have been reported both in biological systems and in the scientific community.^[2] Their most common task is electron transfer. In addition, they are instrumental in crucial cellular processes, ranging from respiration, gene expression, metabolism and enzyme catalysis, and more.^{[3], [4]}

Iron-sulfur clusters are more than multifunctional, and they are structurally quite versatile. In nature, their main forms are [2Fe-2S] clusters, cuboidal [3Fe-4S] clusters, as well as [4Fe-4S] clusters. But other Fe/S shapes like mononuclear species, linear [3Fe-4S] clusters, and the [8Fe-7S] P-cluster exist as well (Figure 1.1). In biological Fe/S clusters, the iron atoms are commonly tetrahedrally coordinated with four sulfurs (FeS₄). These Fe or Fe/S cores are secured in proteins by covalently binding to the side chains of amino acids which are proximate to them, most commonly by cysteine (Cys) residues.

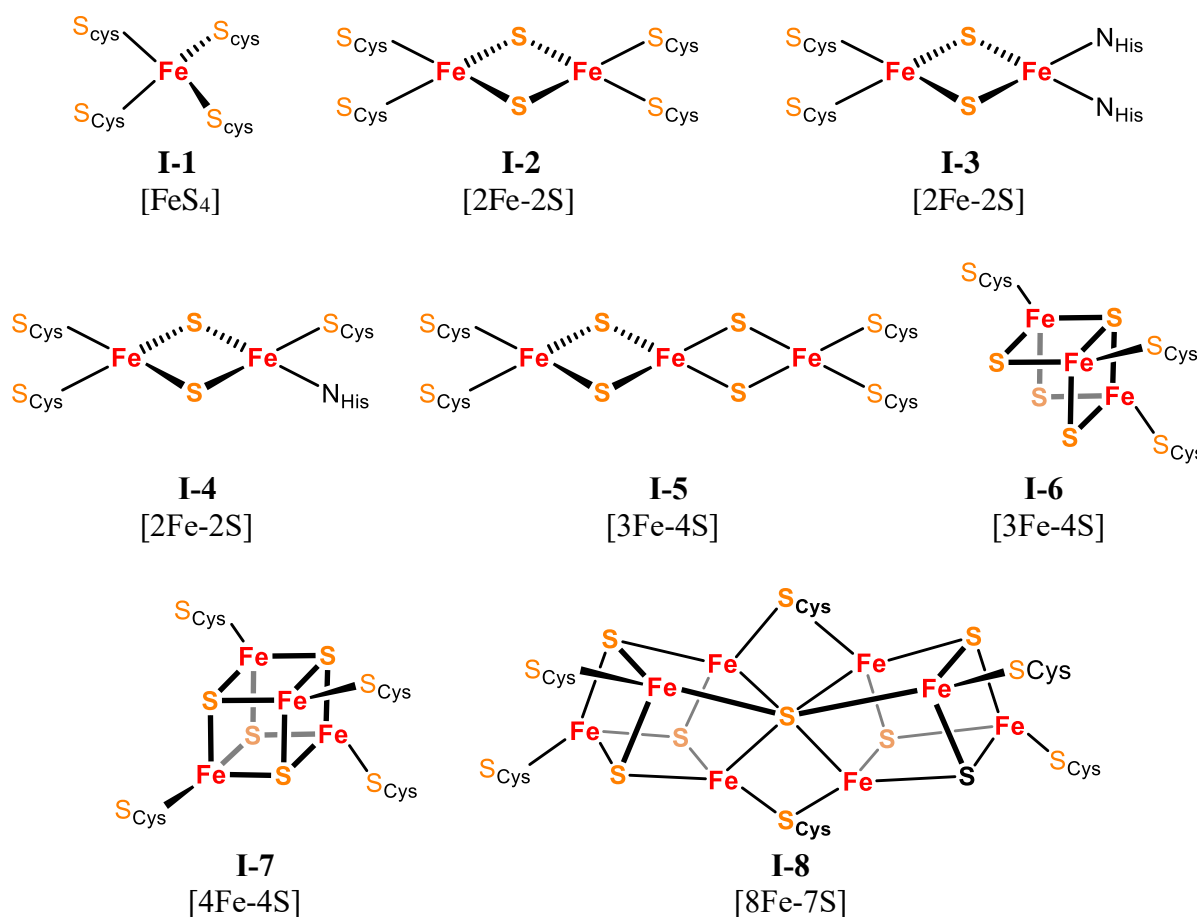


Figure 1.1. Examples of structural motifs in natural iron-sulfur clusters.

Fe(Cys)₄, the simplest Fe/S center, comprises one mononuclear iron ion and four cysteine residues. Several proteins involve this kind of Fe(Cys)₄ center in nature, like Rubredoxin,

Superoxide reductase, Desulfiredoxin, and so on.^[5] Among them, Rubredoxins are the most common and well-studied member of the mononuclear Fe/S family.^[6] Rubredoxin proteins mainly exist in anaerobes, archaea, and bacteria.^{[5], [7], [8]} They are small proteins but can be assembled into larger structures by adding elemental sulfur. Rubredoxins do not belong to iron-sulfur proteins in the strict sense since they do not have inorganic sulfide. Rubredoxins, like Rieske proteins and Ferredoxins, are involved in the electron transfer process in the biological system. In addition, they also participate in a variety of biological processes like the reduction of O₂, alkane oxidation, and hydrocarbon oxidation.^{[5], [7]}

[2Fe-2S] clusters are one of the most widespread Fe/S cluster forms found in nature. Each iron of the [2Fe-2S] core is tetrahedrally coordinated by two inorganic bridging S atoms and two protein residues.^[5] Most of the protein residues bound to Fe atoms of [2Fe-2S] cores are cysteine, but beyond that, histidine is another common protein residue connected with [2Fe-2S] cores. There are several primary coordination environments of biological [2Fe-2S] cores, such as four cysteine residues (ferredoxin)^[5], two cysteine and two histidine residues (Rieske center)^[5], three cysteine and one histidine residue (mitoNEET protein)^{[9], [10]}, etc.^{[11], [12]} The common oxidation states for the biological [2Fe-2S] clusters involve diferric ([2Fe-2S]²⁺) as well as mixed valent Fe³⁺Fe²⁺ ([2Fe-2S]¹⁺) forms. The diferrous form ([2Fe-2S]⁰) has already been generated artificially in spinach and parsley by chemical reduction with chromium(II) reductants. But this form ([2Fe-2S]⁰) has so far not been found in any biological function, which may be because the reduction potential of [2Fe-2S]⁰ is out of the physiological range. [2Fe-2S] clusters are quite multifunctional. Apart from their main task, electron transfer,^[5] they are able to donate sulfur and sense small molecules like NO, and O₂.^{[13], [14]}

[3Fe-4S] clusters are less common and less well-studied compared to [2Fe-2S] clusters or [4Fe-4S] clusters. The cuboidal-type [3Fe-4S] clusters have a similar structure to [4Fe-4S] clusters, but the iron atom from one corner of the [4Fe-4S] cluster is missing. Most of the biologically relevant cuboidal [3Fe-4S] clusters were formed by the degradation of [4Fe-4S] clusters. And the interconversions between cuboidal [3Fe-4S] and [4Fe-4S] clusters have been found in *Desulfovibrio Africanus*.^[15] There are two [4Fe-4S]^{2+/1+} clusters in the ferredoxin III of the *Desulfovibrio Africanus*. One is unstable and can reversibly and easily lose an iron atom to form a cuboidal [3Fe-4S] cluster under oxidative conditions.^{[15], [16]} The cuboidal-type [3Fe-4S] clusters are mainly found in ferredoxins of anaerobic bacteria.^[5] The roles of these ferredoxins in a biological system are still not very clear, yet they have been thought their main task is electron transfer. Besides, they have also been found involved in sensing.^[17] In mitochondrial aconitase, a linear-type [3Fe-4S] cluster was found when exposed to a high pH (pH > 9) or urea conditions.

[4Fe-4S] clusters, the same as [2Fe-2S] clusters, are one of the most abundant Fe/S cluster forms found in nature. They are usually thought to be the first cluster type in the early biological environment and act as ubiquitous electron transfer sites in most anaerobic bacteria. Structurally, these [4Fe-4S] clusters form a distorted cubane, with four Fe atoms and four S atoms alternately positioned in the eight vertexes of the cube. Each iron of the cubane is coordinated by three inorganic sulfur atoms and one other group, usually a cysteine in the proteins. These [4Fe-4S] clusters are comparably stable to most other Fe/S forms, and they are found cycling between four redox states, [4Fe-4S]⁰⁻³⁺. Among these redox states, the cycle between [4Fe-4S]⁺ and [4Fe-4S]²⁺ couple is the most commonly found in the electron transfer process. One major family of electron transfer proteins containing the [4Fe-4S]^{2+/1+} couple that has been discovered is ferredoxin. An all-ferrous [4Fe-4S]⁰ cluster was found in the *Azotobacter Vinelandii* nitrogenase at biochemically relevant potentials in biological active iron protein (NifH) by Watt and coworkers in 1994.^[18] It was supposed that the [4Fe-4S]⁰ clusters probably function during the N₂ reduction process involved in nitrogenase catalysis.^{[18], [19]} The [4Fe-4S]⁰ clusters can be obtained by further reducing [4Fe-4S]⁺ with titanium (III) citrate, and a crystal structure was

reported in 2001 by Rees and coworkers.^[19] The $[4\text{Fe-4S}]^{3+/2+}$ couple is found in the high-potential Fe/S proteins (HiPIPs)^[20] which is a particular kind of high redox potential $[4\text{Fe-4S}]$ ferredoxin. HiPIPs play a role in anaerobic electron transfer in photosynthetic bacteria.^[21] All-ferric $[4\text{Fe-4S}]^{4+}$ has not been found in the biological system, although $[4\text{Fe-4S}]^{4+}$ clusters have been synthesized already.^{[22], [23]} The $[4\text{Fe-4S}]$ family is the most well-studied and the cluster form with the most functions among the Fe/S clusters, such as electron transfer, sensing, sulfur donation, and catalysis.^{[2], [5]}

$[8\text{Fe-7S}]$ cluster, named P^{N} cluster, from nitrogenase, is composed of two $[4\text{Fe-4S}]$ cubanes, which share a $\mu_6\text{-S}$ apex.^[24] The P^{N} cluster is bound to the protein with two bridging cysteine residues and four terminal cysteine residues. This cluster can transfer the electrons from the $[4\text{Fe-4S}]$ cluster of the iron protein to the iron-molybdenum cofactor, the other cluster of the MoFe protein, which is the active site of the catalysis. Both the P^{N} -cluster and the iron-molybdenum cofactor are the largest Fe/S clusters found in nature and are necessarily complex to transport electrons and catalyze N_2 fixation.

1.2 Synthetic $[2\text{Fe-2S}]$ Clusters

Since the initial discovery of biological Fe/S clusters in the 1960s, the synthetic inorganic, active-site analogues have supplied tunable, well-defined models of biological cofactors and provided valuable insight into the structures, spectroscopic properties, and functions of Fe/S clusters. These clusters are anchored to the protein backbone mainly by cysteinyl residues in the living organism.^{[25], [26]} Compared to biological blueprints, synthetic Fe/S clusters have quite high reactivity towards H_2O and O_2 because of the lability of bridging sulfides. In addition, most of the synthetic Fe/S clusters show far more negative reduction potentials in comparison with biological clusters, probably because the excess of negative charge could not be spread out through hydrogen bonds or other similar interactions with the surrounding ligand scaffold. Nakamura and coworkers have verified this assumption by investigating Fe/S clusters like $[\text{Fe}_2\text{S}_2(\text{SC}_6\text{H}_3\text{-2,6-(NHCOR)}_2)_4]^{2-}$ (Figure 1.2, bottom) containing hydrogen bonds, which show that the intramolecular hydrogen bonds ($\text{NH}\dots\text{S}$) between the $[2\text{Fe-2S}]$ core and surrounding ligands clearly contribute to the anodic shift of the redox potential in $[2\text{Fe-2S}]$ and $[4\text{Fe-4S}]$ ferredoxin model clusters.^[27]

In 1973, the first synthetic $[2\text{Fe-2S}]$ analogue $[\text{Fe}_2\text{S}_2(o\text{-(CH}_2\text{S)}_2\text{Ph)}_2]^{2-}$ (Figure 1.2, top left) was reported by Holm and coworkers, which was synthesized in a self-assembly reaction from deprotonated *o*-xylyldithiolato ligands, FeCl_3 and NaSH .^[28] After that, a great variety of synthetic Fe/S clusters were reported.^{[2], [29], [30]} The reduced species $[\text{Fe}_2\text{S}_2(o\text{-(CH}_2\text{S)}_2\text{Ph)}_2]^{3-}$ was detected electrochemically by Holm and coworkers in 1975. Furthermore, they made the chemical reduction of $[\text{Fe}_2\text{S}_2(o\text{-(CH}_2\text{S)}_2\text{Ph)}_2]^{2-}$ and investigated its spectroscopy properties in situ, which evidenced the localized Fe^{3+} , Fe^{2+} oxidation state configuration.^[31] Gibson and Beardwood isolated and characterized the first reduced $[2\text{Fe-2S}]$ cluster bearing a bidentate bis(benzimidazolato) ligand in 1992. They proposed that the ground state of this reduced species was $S = 1/2$ with partially delocalized mixed valence.^[32]

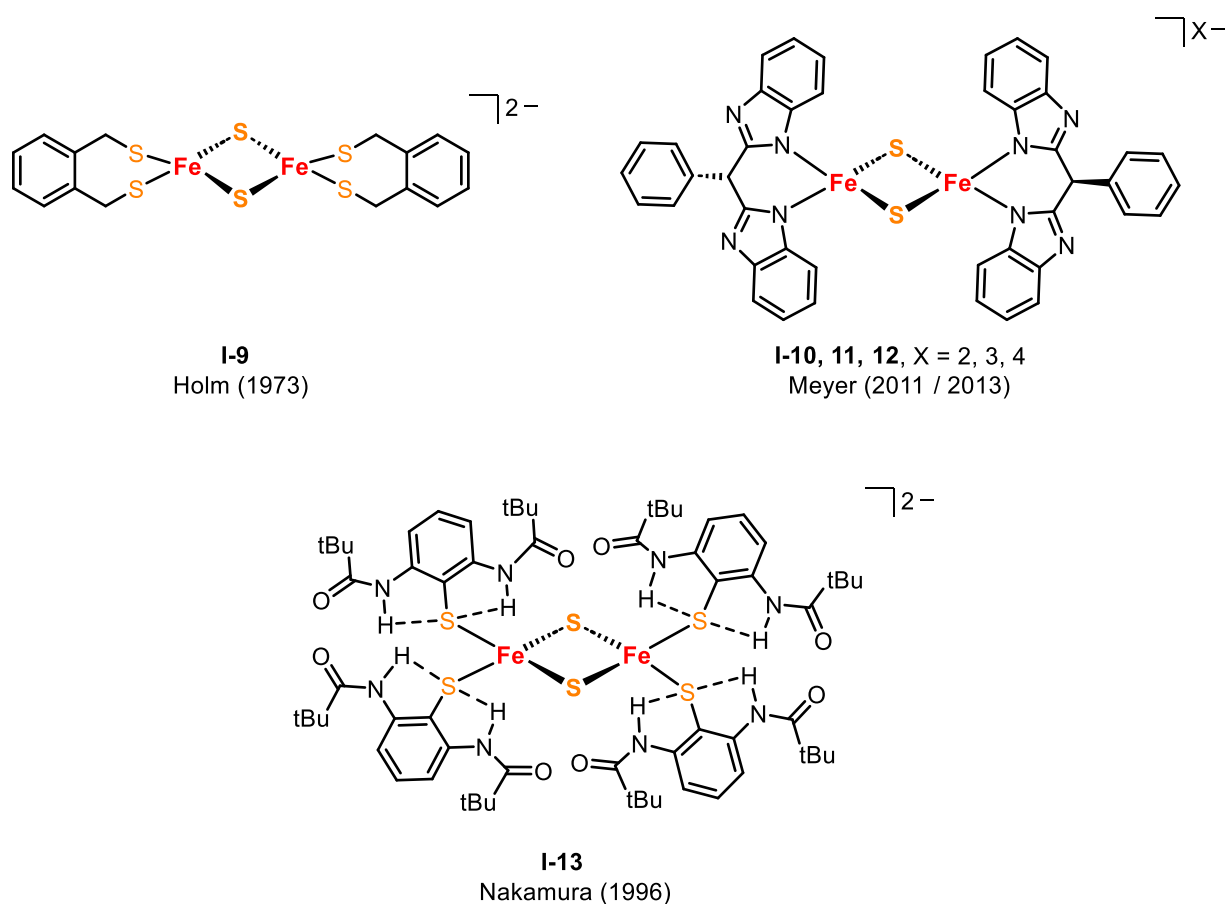


Figure 1.2. The first synthetic [2Fe-2S] cluster (top left), the first synthetic mixed-valent and the first synthetic super-reduced diferrous [2Fe-2S] clusters (top right), the [2Fe-2S] cluster $[\text{Fe}_2\text{S}_2(\text{SC}_6\text{H}_3\text{-}2,6\text{-(NHCOR)}_2)_4]^{2-}$ containing intramolecular hydrogen bonds (bottom).

In 2011, the Meyer group reported the first crystal structure, magnetic measurements, and full spectroscopic characterization of a mixed-valent $[2\text{Fe-}2\text{S}]^{1+}$ cluster (Figure 1.2, top right).^[33] The direct current temperature-dependent magnetic susceptibility measurements of this reduced species confirmed the antiferromagnetic coupling of the two iron ions resulting in the ground state $S = 1/2$ with the unpaired electron partially delocalized over the $[2\text{Fe-}2\text{S}]$ core. And the core structure of this $[2\text{Fe-}2\text{S}]^{1+}$ cluster undergoes minor changes compared to its oxidized form, which reflects the low reorganization energy that may make $[2\text{Fe-}2\text{S}]$ complexes ideal electron transfer sites in the biological system. Two years later, in 2013, the first diferrous $[2\text{Fe-}2\text{S}]^0$ cluster (Figure 1.2, top right) bearing the same bis(benzimidazolato) ligand was isolated and characterized by X-ray diffraction by the Meyer group.^[34] ^{57}Fe Mössbauer parameters of this diferrous $[2\text{Fe-}2\text{S}]^0$ cluster are in good agreement with those of the few reports available for artificially prepared all-ferrous $[2\text{Fe-}2\text{S}]$ ferredoxins and Rieske clusters. The ground state ($S_T = 0$) of this diferrous cluster was confirmed, and it provided a lower limit for magnetic exchange coupling ($-J \geq 30 \text{ cm}^{-1}$).

The very useful $[2\text{Fe-}2\text{S}]$ precursor $(\text{NET}_4)_2[\text{Fe}_2\text{S}_2\text{Cl}_4]$ (Figure 1.3, left) was reported in 1977 by Holm and coworkers from the reaction of $(\text{NET}_4)_2[\text{Fe}_2\text{S}_2(\text{SR})_4]$ with $\text{R}'\text{COCl}$ in MeCN in 45–65 % yield.^[35] And the synthesis of this precursor was improved six years later via a straightforward self-assembly reaction using $(\text{SiMe}_3)_2\text{S}$ and $(\text{NET}_4)_2[\text{FeCl}_4]$, and the yield can reach 96 %.^[36] This precursor $[\text{Fe}_2\text{S}_2\text{Cl}_4]^{2-}$ has been used to synthesize most of the diferric clusters by ligand exchange reactions with deprotonated nitrogen, oxygen, and sulfur donor

ligands affording homoleptic or heteroleptic [2Fe-2S] clusters. But $[\text{Fe}_2\text{S}_2\text{Cl}_4]^{2-}$ is not the only one used as precursor in exchange reactions of the Fe/S syntheses, since sulfur- or nitrogen-coordinated [2Fe-2S] clusters (Figure 1.3, right) can also act as precursors.^[37]

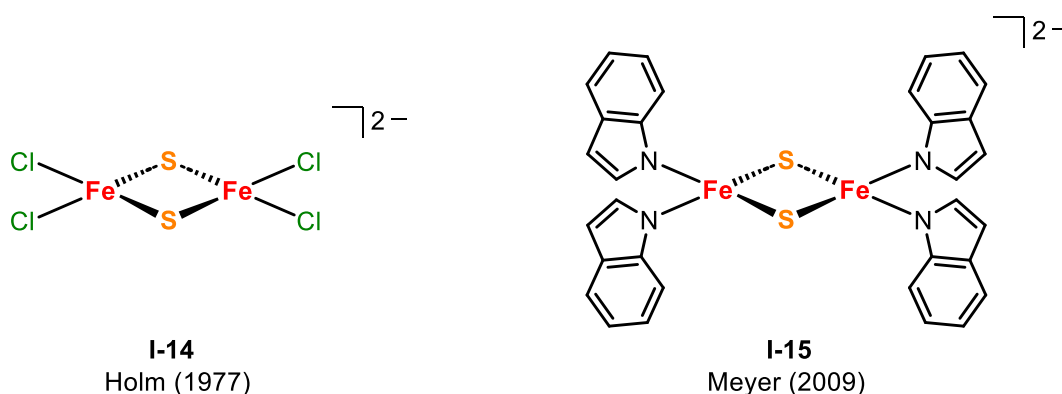


Figure 1.3. [2Fe-2S] precursors $[\text{Fe}_2\text{S}_2\text{Cl}_4]^{2-}$ (left) and $[\text{Fe}_2\text{S}_2(\text{indolate})_4]^{2-}$ (right).

Most of the iron ions in the [2Fe-2S] clusters show tetrahedral coordination. However, in 2008 the Meyer group reported the first synthetic [2Fe-2S] cluster (Figure 1.4, up left) bearing five-coordinate ferric ions through secondary bonding interactions between the metal ions and additional thioether-S. This study shows that secondary interactions may play a role in modulating electronic properties of biological [2Fe-2S] clusters. Furthermore, the Meyer group reported the first genuinely five-coordinate [2Fe-2S] cluster (Figure 1.4, up right) with tridentate 2,6-di(imidazole-2-yl)pyridine ligands in 2010.^[38] The $\text{Fe}\cdots\text{Fe}$ distance and Fe-S-Fe angles of this five-coordinate cluster slightly increase compared to typical four-coordinated [2Fe-2S] clusters. This unique cluster has been isolated and studied structurally and spectroscopically. However, it has limited stability in solution, which hindered its further investigation.

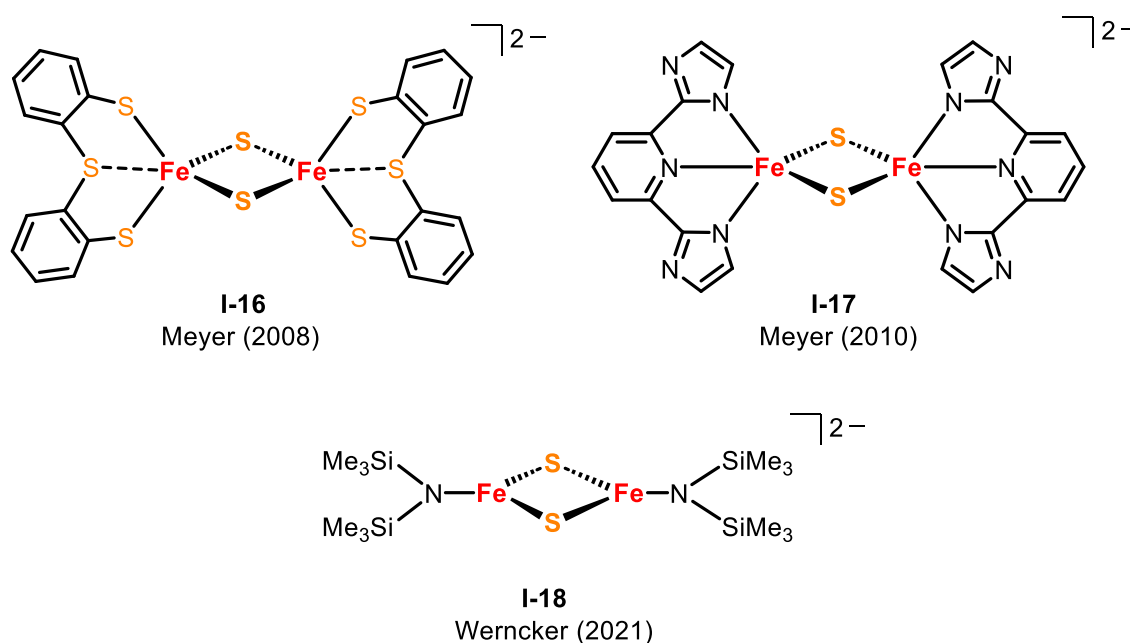


Figure 1.4. Synthetic [2Fe-2S] clusters featuring five-coordinate iron centers (top) and three-coordinate iron centers (bottom).

In 2021 Werncke and coworkers reported a rare diferrous $[2\text{Fe}-2\text{S}]^0$ cluster with three-coordinate metal ions (Figure 1.4, bottom), which was synthesized by reducing a four-coordinate $[2\text{Fe}-2\text{S}]^{2+}$ cluster with concomitant amide ligands loss; its structure has been confirmed by X-ray diffraction.^[39] Magnetic susceptibility measurements of this unique diferrous $[2\text{Fe}-2\text{S}]^0$ cluster show it has extraordinarily strong antiferromagnetic coupling, $J = -348 \text{ cm}^{-1}$. Further investigation of the physical as well as chemical properties of this unique $[2\text{Fe}-2\text{S}]^0$ cluster is still ongoing.

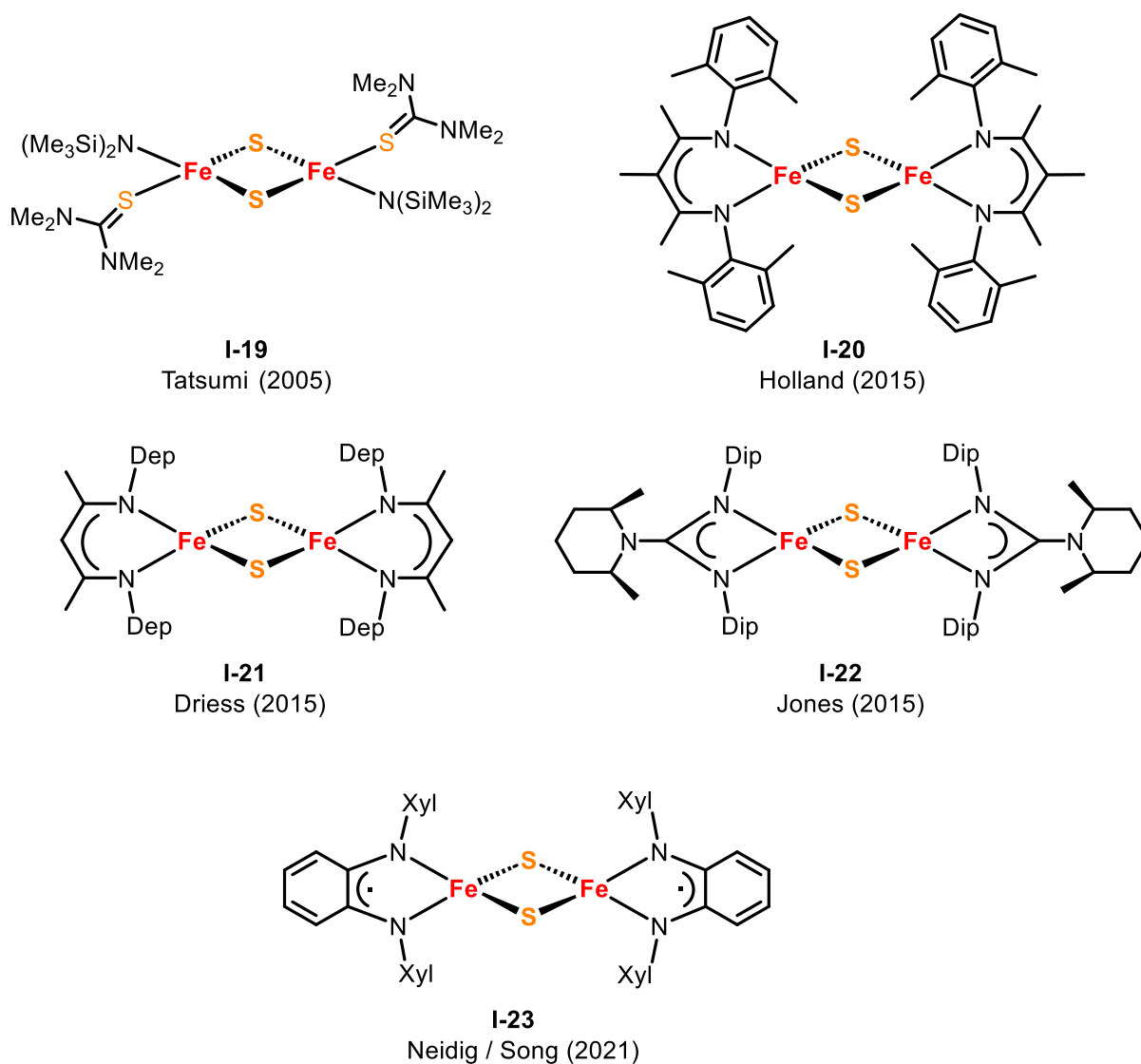


Figure 1.5. Synthetic neutral $[2\text{Fe}-2\text{S}]$ clusters.

In 2005, a neutral $[2\text{Fe}-2\text{S}]$ complex (Figure 1.5, up left) symmetrically coordinated by two tetramethylthiourea and two hexamethyldisilamides molecules was firstly synthesized by Tatsumi and coworkers.^[22] The solubility of this neutral $[2\text{Fe}-2\text{S}]$ cluster is improved compared to the ionic $[2\text{Fe}-2\text{S}]$ clusters. It is also soluble in less polar solvents such as toluene and hexane, which makes new reactivity studies possible. Later on, three neutral $[2\text{Fe}-2\text{S}]$ clusters bearing N-donating ligands were reported in 2015 by Holland^[40], Driess^[41], and Jones^[42], respectively (Figure 1.5). The last synthetic step for these three neutral complexes relied on elemental sulfur insertion. All three clusters were isolated and structurally spectroscopically characterized. The

neutral [2Fe-2S] cluster reported by Holland's group (Figure 1.5, up right) was also characterized in its reduced form, showing an extensive delocalization. Recently, the Neidig and Song groups reported another neutral [2Fe-2S] cluster (Figure 1.5) bearing *o*-phenylenediamide ligands.^[43] This novel neutral [2Fe-2S] cluster is able to store four electrons reversibly and shows catalytic activity towards the silylation of dinitrogen. Crystallographic and spectroscopic studies of this neutral [2Fe-2S] cluster showed that the first two reduction processes were ligand-base, and the last two reduction processes were metal-based. All these five clusters were isolated and structurally and spectroscopically characterized. The third reduction gave a mixed-valence species, where the single electron was localized and the fourth reduction afforded a super-reduced diferrous [2Fe-2S] cluster, which exhibited limited stability.

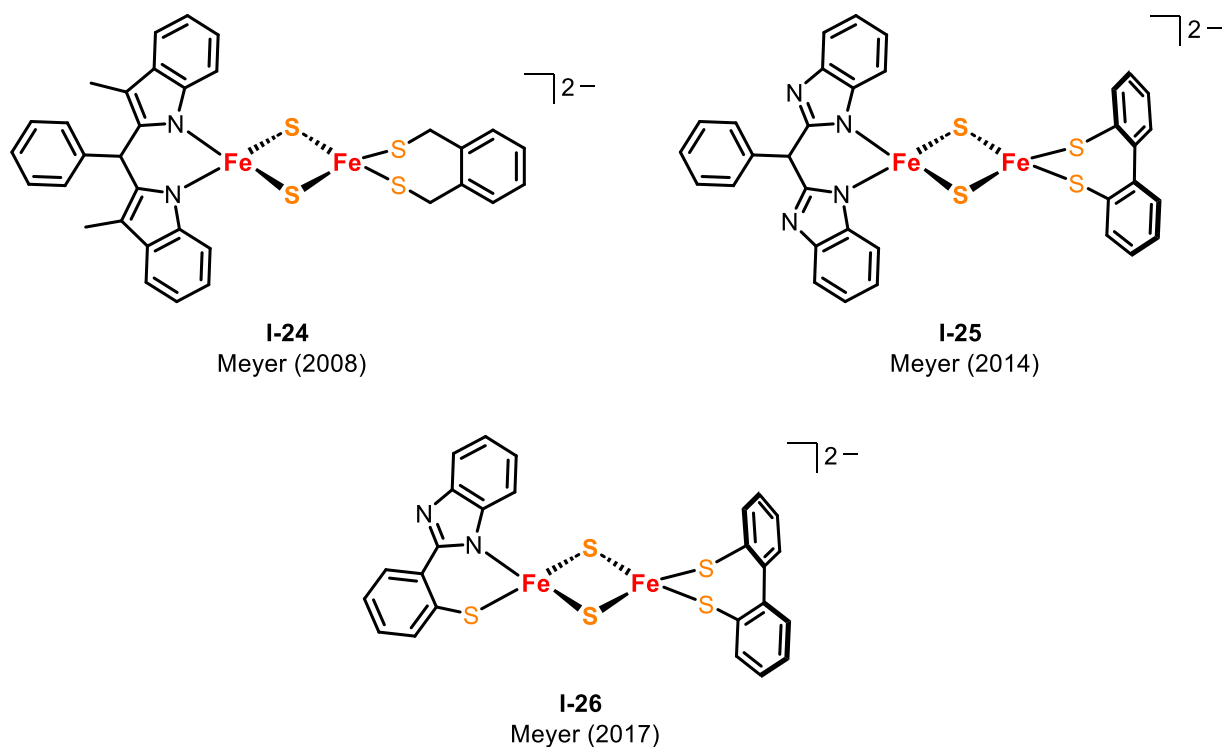


Figure 1.6. Synthetic asymmetrical [2Fe-2S] clusters.

Whereas all above-mentioned [2Fe-2S] clusters are symmetrical, synthesizing asymmetrically ligated clusters is much more challenging. Ligand scrambling and many accompanying side reactions, especially the formation of symmetrical [2Fe-2S] by-products, must be effectively suppressed. Therefore, only three synthetic heteroleptic [2Fe-2S] clusters have been published. The first heteroleptic [2Fe-2S] cluster, reported in 2008, (Figure 1.6, up left) was a structural model of the Rieske cluster which was found in the bovine heart and showed asymmetrical [N₂] [S₂] coordination. This heteroleptic cluster was obtained by a sequential ligand exchange strategy starting from the chloride cluster (NEt₄)₂[Fe₂S₂Cl₄].^[44] The low average *g* value (*g*_{av} = 1.92) of its reduced species is consistent with the finding for Rieske proteins (*g*_{av} ≈ 1.90–1.91).^{[45], [46]} While this heteroleptic cluster can act as a structural and spectroscopic model of the Rieske cluster in both the diferric and one-electron reduced state, functional studies like fast concerted proton and electron transfer is not possible because of the lack of peripheral N atoms. In 2014, the Meyer group reported the second generation Rieske model (Figure 1.6, up right), which has a similar ligand set to the first Rieske cluster mode but with the peripheral N atoms.^[47] This heteroleptic cluster is a high-fidelity Rieske model, as it serves as a structural and spectroscopic

model and a functional model for proton-coupled electron transfer. This study also showed that this diferric cluster underwent a tautomerization process upon protonation at the terminal benzimidazolate N atoms and formed a conjugated ligand system, which evoked the evolution of an intense absorption band in the visible absorption spectra. Three years later, the Meyer group reported the third asymmetrical [2Fe-2S] cluster (Figure 1.6, bottom) which was the first structural model of MittoNEET [2Fe-2S] clusters featuring unique Cys₃His coordination. This cluster was shown to be a high fidelity MittoNEET model, which mimics well the structural and spectroscopic properties and can undergo proton-coupled electron transfer at the [NS] ligated site. These investigation for asymmetrical [2Fe-2S] clusters provide valuable information and a multitude of new perspectives for the understanding of biological cofactors.

1.3 Synthetic [4Fe-4S] Clusters

The Iron-sulfur clusters with distorted cubic [4Fe-4S] core structures are the most versatile and well-investigated member of the Fe/S family. These cubic clusters can have many different supporting ligands as well as oxidation states ([4Fe-4S]⁰⁻⁴⁺) wherein [4Fe-4S]¹⁻³⁺ are the most common oxidation states.^{[2], [48]} They are found in a multitude of crucial biological processes such as electron transfer, respiration, enzymatic catalysis, photosynthesis, and gene regulation.^{[2], [49], [50]}

The first synthetic [4Fe-4S] cluster [Fe₄S₄(SCH₂Ph)₄]²⁻ bearing thiobenzyl ligands emulating cysteine was reported in 1972 by Holm and coworkers, which was also the first synthetic Fe/S cluster (Figure 1.7, left). These studies revealed that the solid structure of this [4Fe-4S] cluster was quite similar to the Fe/S active site of the *Chromatium* protein. In addition, this cubic cluster showed equal oxidation levels as the active sites of high-potential iron protein(red) and ferredoxin_(ox). A great variety of synthetic [4Fe-4S] clusters have been reported after the first [4Fe-4S] cluster was reported. A unique example is a water-soluble [4Fe-4S] cluster bearing carboxylates in the ligands (Figure 1.7, right), which is stable enough to determined its pK_a in water. The redox study of this prominent cluster shows one thermodynamically reversible reduction process, and the one-electron reduction potential (-0.58 V vs. hydrogen electrode) is in accordance with that of the ferredoxins (-0.53V to -0.58 V).^{[51], [52]}

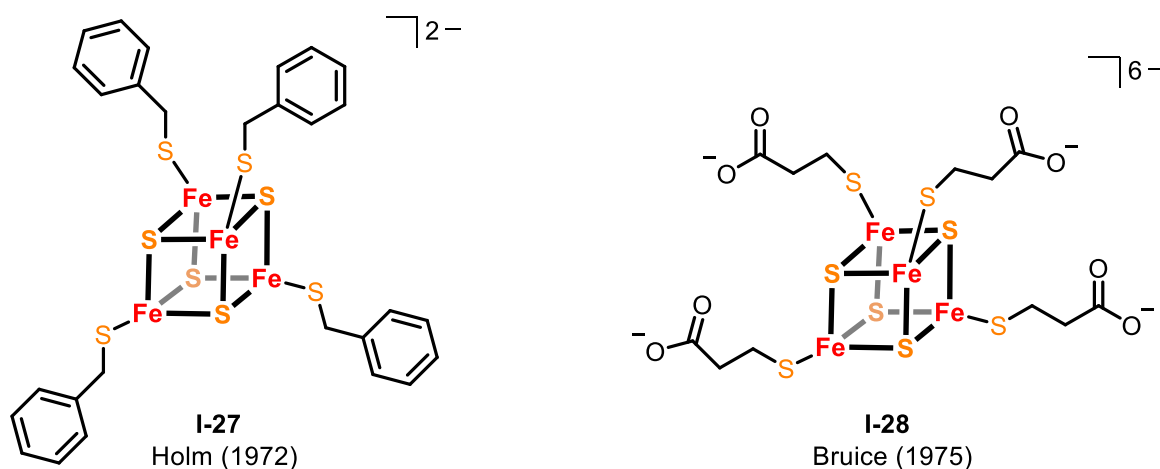


Figure 1.7. The first synthetic [4Fe-4S] cluster (left), first water-soluble [4Fe-4S] cluster (right).

Notably, [4Fe-4S] clusters with different oxidation states have been isolated and characterized, especially all ferric [4Fe-4S]⁴⁺ and all ferrous [4Fe-4S]⁰ clusters. The fully-oxidized [4Fe-4S]⁴⁺ cluster has not been discovered in a biological system to date. However, Tatsumi and coworkers already synthesized this kind of all-ferric cluster (Figure 1.8, left) bearing silylamide ligands in 2005 for the first time.^[22] This unique cluster was made from Fe[N(SiMe₃)₂]₂ and elemental sulfur, isolated and crystallographically characterized. And oxidation studies revealed that this [4Fe-4S]⁴⁺ cluster exhibits two reduction events, one is reversible, and another one is quasi-reversible. The ready availability of this all-ferric cluster from sulfur and an iron-amide precursor provides a new reaction system for synthesizing larger Fe/S clusters. All ferrous cluster [4Fe-4S]⁰ has already been demonstrated in *Azotobacter vinelandii* nitrogenase iron protein in highly reduced condition. However, it has not been proven to be necessarily physiologically relevant yet. The first all-ferrous cluster [Fe₄S₄(CN)₄]⁴⁻ (Figure 1.8, middle) was reported by Holm and Zhou in 2005, which was synthesized by complexes [Fe₄S₄(CN)₄]³⁻ and K[Ph₂CO].^[53] The structure of [Fe₄S₄(CN)₄]⁴⁻ was confirmed by single-crystal X-ray diffraction (XRD), and the [4Fe-4S]⁰ oxidation state was demonstrated by Mössbauer studies. The isomer shift of the Mössbauer spectrum, the core volume, bond distances as well as visible absorption spectrum of [Fe₄S₄(CN)₄]⁴⁻ are in good agreement with the fully reduced iron protein. However, this [4Fe-4S]⁰ cluster is highly unstable, which hinders its further reactivity investigation. In 2008 Holm and coworkers reported another stable all ferrous [4Fe-4S]⁰ cluster [Fe₄S₄(Prⁱ₂NHCMe₂)₄] (Figure 1.8, right), which is stable under aprotic anaerobic conditions and can be synthesized by phosphine substitution of Fe₈S₈ or Fe₁₆S₁₆ clusters, or by cluster self-assembly.^[54] [Fe₄S₄(Prⁱ₂NHCMe₂)₄] was the first all-ferrous [4Fe-4S] cluster with Fe-C σ bonds, and its formulation has been confirmed by single-crystal XRD as well as the isomer shifts of the Mössbauer spectrum. In 2022, the Mougel group reported the whole series of [4Fe-4S]⁰⁻⁴⁺ complexes for the first time by use of bulky arylthiolate ligands.^[55] Five complexes were all fully characterized and their structures were confirmed by single-crystal XRD. Furthermore, the electronic ground state ($S = 4$) of the superreduced member [4Fe-4S]⁰ was confirmed, which provided a key argument in the debates of the geometric and electronic structure of [4Fe-4S]⁰ oxidation state in Fe/S cubane cofactors.

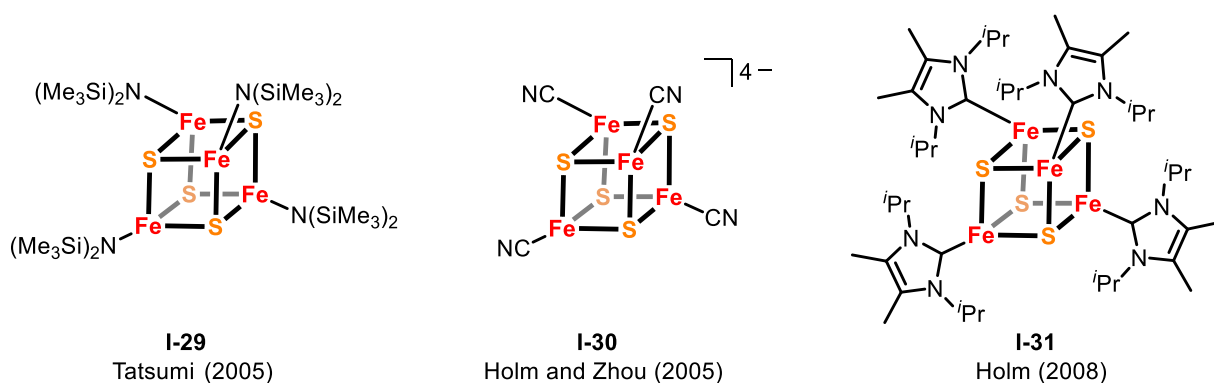


Figure 1.8. The first all-ferric [4Fe-4S]⁴⁺ cluster (left), the first all-ferrous [4Fe-4S]⁰ cluster (which is highly unstable) (middle), the stable all-ferrous [4Fe-4S]⁰ cluster (right).

All above-mentioned [4Fe-4S] clusters are symmetrical, while the synthetic asymmetrical [4Fe-4S] clusters, including [3:1] and [2:2] site-differentiated [4Fe-4S] clusters, also have been studied a lot, especially the [3:1] site-differentiated [4Fe-4S] clusters.^{[2], [30]} The syntheses of the asymmetrical [4Fe-4S] clusters are usually very challenging since it is usually quite hard in restricting the reactivity to some instead of all iron sites of the [4Fe-4S] core, such as ligand substitution reactions. Holm and Stack published a facile strategy to solve this unselective

substitution in 1987, which is the landmark of the asymmetrical [4Fe-4S] cluster syntheses.^[56] A tridentate thiolate ligand was used to coordinate to three iron sites of the [4Fe-4S] core leaving the fourth iron center available to coordinate a unique group (Figure 1.9, top). This strategy has laid the groundwork for the syntheses of several asymmetrical [4Fe-4S] clusters. Also, it has a longstanding influence on the design of this kind of tridentate chelating ligands for the cubic [4Fe-4S] clusters. For example, Pohl and Tatsumi and their coworkers reported similar trithiolate ligands in 1997^{[57], [58]}, and 2012^[59], respectively. The Suess group reported a couple of tridentate neutral scorpionate ligands (LN₃) in 2018^[60], 2019^[61], and 2020^[62], which are in contrast to earlier tridentate thiol-coordinating moieties (LS₃). In one example, two cubic clusters were stabilized by a triiminophosphorane scorpionate ligand, with Cl or Et at the fourth metal site (Figure 1.9, bottom left).^[61] Characterization of this alkyl-ligated cluster indicates that the alkyl group can partially or completely localize the charge distribution at alkylated iron in enzymatic reactions, which is first observed in a tetrahedrally coordinated cubic Fe/S cluster. Another example in 2020,^[62] Suess reported the first [4Fe-4S]³⁺-alkyl cluster stabilized by a tridentate scorpionate ligand (Figure 1.9, bottom right), which acts as a synthetic model for short-lived intermediates in a variety of reactions such as dipthamide biosynthesis and terpene biosynthesis. Characterization of this [4Fe-4S]³⁺-alkyl cluster reflected the valence localization of Fe(III) at the alkylated Fe site, which also persists in solution at room-temperature. This effect is first observed for [4Fe-4S]³⁺ complexes outside of the protein. Other [3:1] site-differentiated [4Fe-4S] clusters ligated by tridentate ligands also have been reported, although they were rarely investigated by X-ray crystallographic studies.^{[63], [64], [65]}

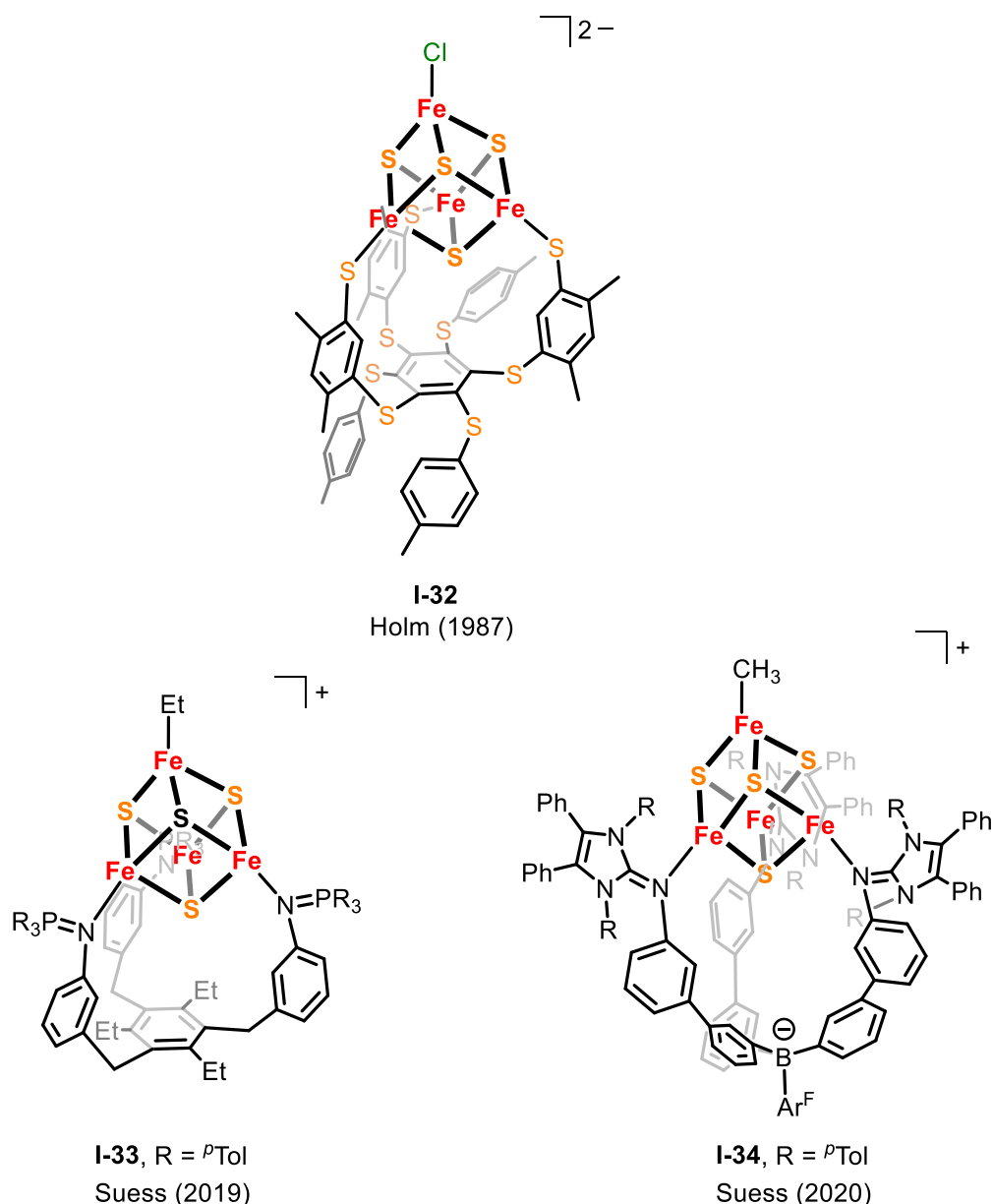


Figure 1.9. The first synthetic [3:1] site-differentiated [4Fe-4S] cluster (top), a synthetic analogue of enzymatic [4Fe-4S]-alkyl intermediates (bottom left), a [4Fe-4S]³⁺-alkyl cluster stabilized by a tridentate scorpionate ligand (bottom right).

With respect to asymmetrical cubanes, the current understanding of this kind of [4Fe-4S] clusters in the scientific community is mainly focused on [3:1] site-differentiated [4Fe-4S] clusters. In contrast, examples of the synthesis and characterization of [2:2] site-differentiated [4Fe-4S] clusters are extremely limited.^[2] The first [2:2] site-differentiated [4Fe-4S] cluster [Fe₄S₄Cl₂(SC₆H₅)₂]²⁻ (Figure 1.10, top left) was isolated and confirmed via X-ray crystallographic and electrochemical studies by Coucouvanis and coworkers in 1982.^[66] This unique [4Fe-4S] cluster was made from dibenzyl trisulfide and [(C₆H₅)₄P]₂[Fe₄(SC₆H₅)₆Cl₄] in a 2:1 ratio. A new cluster [Fe₄S₄Cl₄]²⁻ forms when the ratio exceeds 4:1. And this new cluster [Fe₄S₄Cl₄]²⁻ can be isolated in the maximum yield when the ratio is 8:1. Other two unique [2:2] site-differentiated cubic type clusters [Fe₄S₄R₂(Et₂dtc)₂]²⁻ (R = Cl, SPh) containing a pair of bidentate ligands (Figure 1.10, top right) were reported by Coucouvanis and coworker in 1983

and 1985, respectively.^{[67], [68]} Their studies showed that introducing the bidentate ligand, Et_2NCSS^- , on the cubic cores leads to substantial core structural changes. The significant increase of the isomer shift ($\delta = 0.16$ mm/s) in the five-coordinated iron site compared to the previous four-coordinated iron site must be ascribed to the change in geometry (coordination number) for these sites. In 1992, Pohl and coworkers reported a [2:2] site-differentiated [4Fe-4S] cluster with a bidentate ligand coordinating with two iron sites of the [4Fe-4S] core (Figure 1.10, bottom left).^[69] And two neutral [2:2] site-differentiated [4Fe-4S] clusters bearing bidentate phosphine ligands $[\text{Fe}_4\text{S}_4(\text{depe})_2\text{R}_2]$ ($\text{R} = \text{Cl}, \text{SPh}$) (Figure 1.10, bottom right) were published by Coucouvanis and coworkers in 2002;^[70] the crystal structure of $[\text{Fe}_4\text{S}_4(\text{depe})_2\text{Cl}_2]$ was determined by X-ray crystallography. The spectroscopic and electrochemical properties of both clusters have been determined and analyzed. ^{57}Fe Mössbauer spectroscopic studies showed that the five-coordinated irons are assigned as Fe^{2+} and four-coordinated irons are attributed to Fe^{3+} .

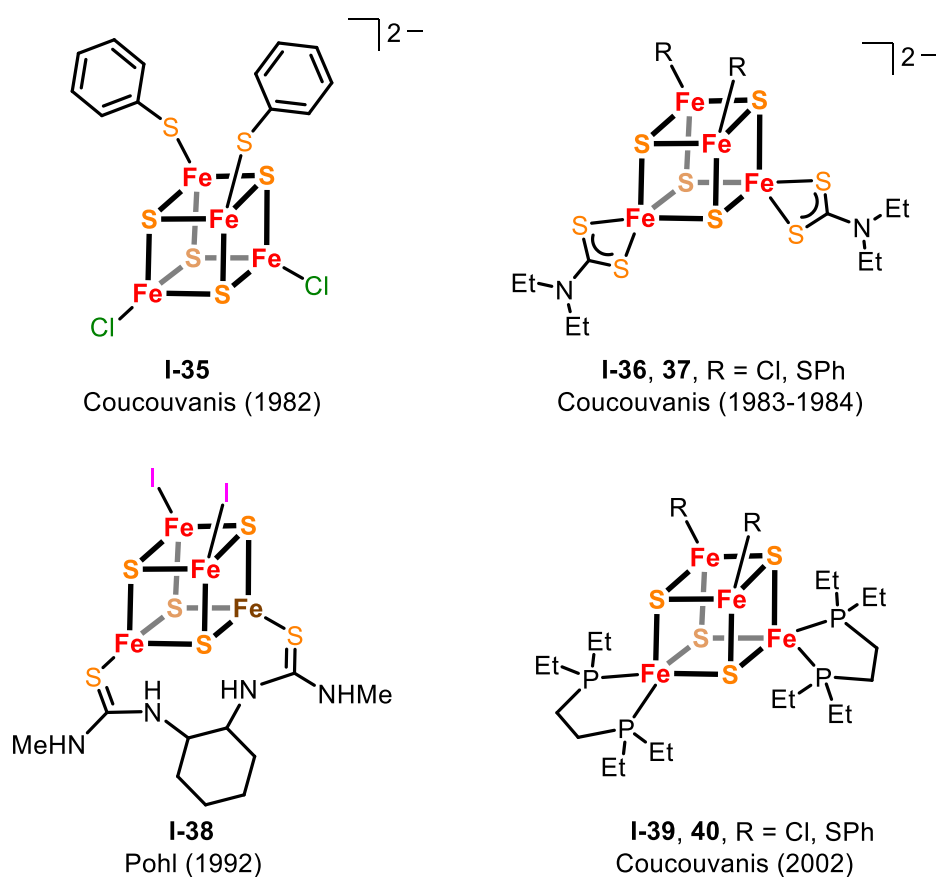


Figure 1.10. The first synthetic [2:2] site-differentiated [4Fe-4S] cluster (top left), [2:2] site-differentiated [4Fe-4S] clusters ligated by bidentate ligands (top right and bottom).

1.4 Mössbauer Spectroscopy

Mössbauer spectroscopy was discovered by the German physicist Rudolf L. Mössbauer^[71] in 1958 based on his outstanding discovery, the recoilless emission and resonance absorption of gamma radiation.^[72] This discovery evoked the evolvement of a new technique for measuring the hyperfine interactions between the nuclear core and surrounding electrons. And this new technique allows probing especially small energy changes of nuclear levels with high accuracy

for certain atoms, specifically iron atoms. It is a very powerful tool to measure key properties such as symmetry, spin states, and formal oxidation states.^{[73], [74]}

When an atom decays from the excited nuclear state (E_e) to the ground state (E_g), a γ -quantum is emitted. The γ radiation could result in the excitation of another nucleus if this energy can match the required resonance energy (Scheme 1.1). But according to the conservation of momentum, the nucleus exhibits a recoil momentum which is in the opposite direction of the spread of the photon. During this transition, the energy gap between the excited state and ground state is ΔE ,

$$\Delta E = E_e - E_g \quad (1.1)$$

the emitted γ radiation has the energy E_γ ,

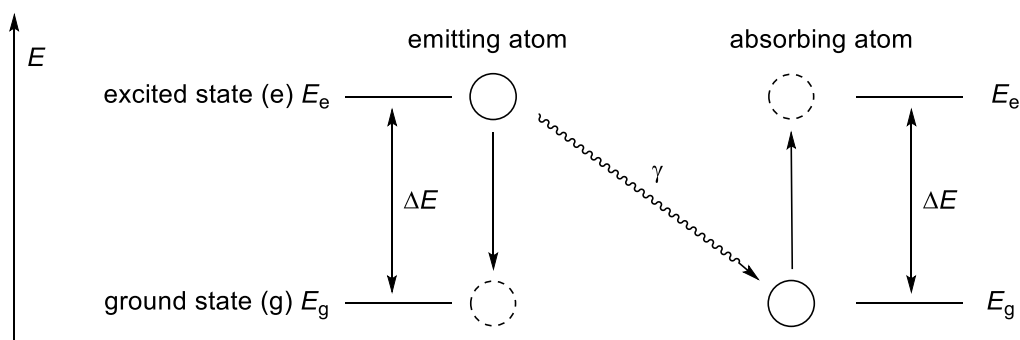
$$E_\gamma = \Delta E - E_R \quad (1.2)$$

where E_R is the recoil energy which has relation to the energy of emitted photon E_γ , the mass of the nucleus, as well as the velocity of light,

$$E_R = \frac{E_\gamma^2}{2mc^2} \quad (1.3)$$

The absorbing nucleus of the γ -quantum has the same recoil energy. But, with the contrary direction, the absorption line is shifted by $2E_R$ in total compared to the emission line, which means the emission and absorption lines do not overlap. For Fe^{57} , the recoil energy is around six orders of magnitude larger than the natural line width. Thus, it is impossible to observe nuclear resonance absorption of γ radiation under this condition.

Scheme 1.1. Schematic overview of emission and absorption of γ radiation.

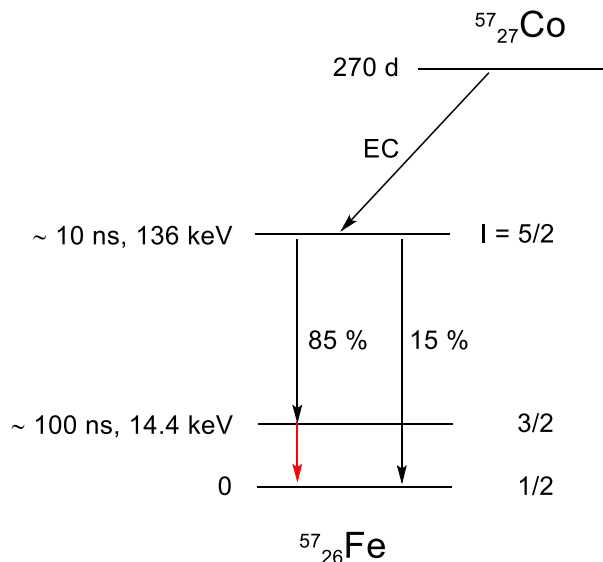


In order to avoid the recoil effect during the emission and absorption of radiation, Mössbauer cooled the absorber, carrying out this experiment at low temperatures. In this way, the absorbing atoms are incorporated in the lattice, so the binding effect of the nuclei in the solid state can make m (in equation 1.3) drastically increase, which makes the recoilless emission and absorbing of γ -rays possible.

The most widely investigated isotope for Mössbauer spectroscopy is ^{57}Fe . The appropriate source of γ radiation is ^{57}Co , which is generated in the cyclotron and then diffused into a rhodium matrix, and its half-life is 270 days. ^{57}Co decays through electron capture from K-shell, reducing proton number by one and therefore turning to ^{57}Fe with the spin state $I = 5/2$ (136 keV). After about 10 ns, this excited state decays directly to ground state $I = 1/2$ with 15% probability or to

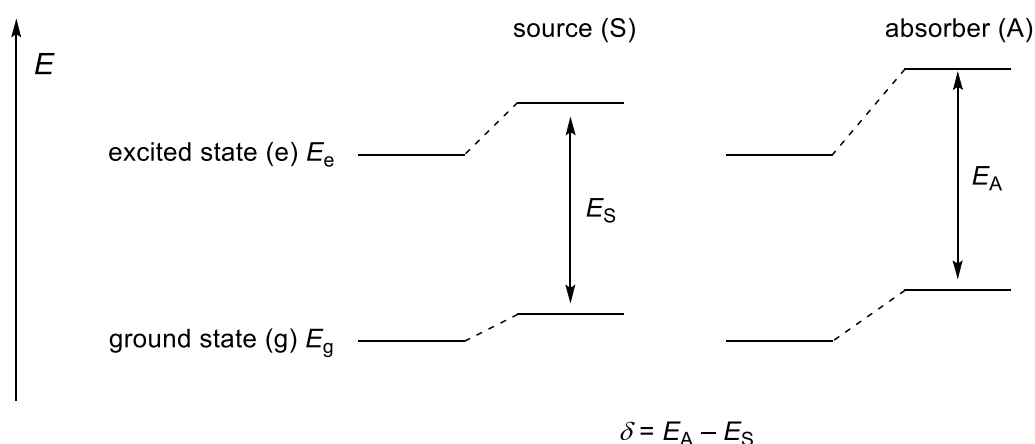
$I = 3/2$ state with 85% probability (Scheme 1.2). For the latter, both the emitted γ -quanta (14.4 keV energy) and the half-life (ca. 100 ns) are adequately suited for ^{57}Fe Mössbauer spectroscopy. Other common isotopes for Mössbauer spectroscopy include ^{119}Sn , as well as ^{121}Sb .^[73]

Scheme 1.2. Simplified nuclear decay of ^{57}Co for ^{57}Fe Mössbauer spectroscopy.



Because the sample and the source nuclei are not in exactly the same chemical or physical environment, their nuclear energies are at different levels. To achieve correspondingly different resonance frequencies for the excitation of nuclei, the emitted frequency of the photon must be modulated by moving the source at different velocities (Doppler effect). Two main parameters can be obtained from the Mössbauer spectroscopy in the case of no additional external or internal magnetic field: isomer shift δ and quadrupole splitting ΔE_Q .

Scheme 1.3. Coulomb interaction of protons with surrounding electrons perturbs the energy levels between the nuclear excited and ground states.



The isomer shift δ is based upon the Coulomb interaction of protons with electrons (mostly s-electrons) and gives valuable information on oxidation state, spin state, as well as bonding properties (e.g., electronegativity and covalency). In the Mössbauer experiment, the source material (e.g., ^{57}Co) is usually different from the absorber material, so the electronic densities

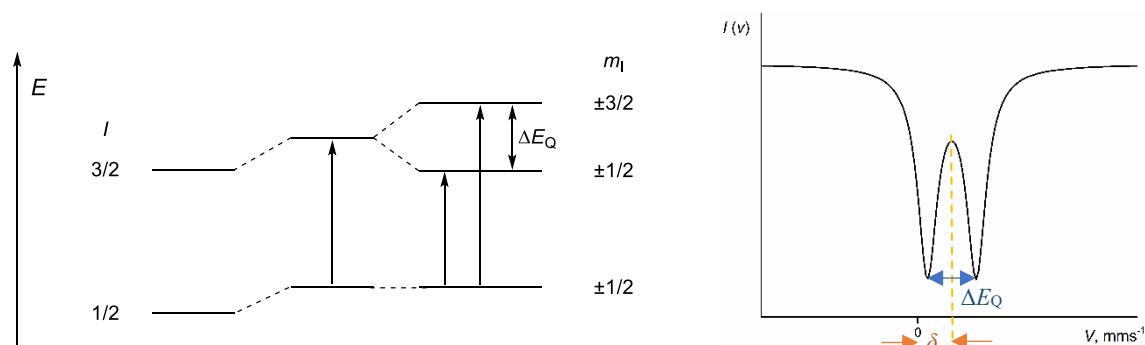
setup of electronic shells (e.g., 1s, 2s, etc.) at the nuclei are not identical for source and absorber. Thus, the source and the absorber have different Coulomb interactions, which can affect nuclear excited and ground states levels to varying degrees. This result in measured isomer shift (Scheme 1.3).

Many factors can affect the isomer shift. Among them, *s*-electrons densities (from all *s*-electron shells) are directly relevant to the isomer shift because of the position of the *s*-electrons at the nucleus. Although *p*-, *d*-, and *f*-electrons don't have a direct contribution to the isomer shift, they can indirectly influence the isomer shift, since these *p*-, *d*-, and *f*-electrons can help to shield the *s* electrons. The chemical bonds, *i.e.*, σ -donation and d_{π} - p_{π} back-donation, between metal ions and ligands can influence the isomer shift to different extents, depending on the ligands' nature. That is why the values of the isomer shift δ can cover a broad range for iron in different complexes with the same oxidation state.

Electric quadrupole interaction happens when the nuclear states exhibit an electric quadrupole moment (*i.e.*, spin $I > 1/2$ state) and the electric field distribution of a nucleus is non-spherical. For ^{57}Fe , the $I = 1/2$ ground state does not possess an electric quadrupole moment. In comparison, the $I = 3/2$ excited state can cause an electric quadrupole moment, which could interact with the inhomogeneous electrical field. This electric quadrupole interaction in a non-cubic environment can split the degenerated $I = 3/2$ state into two doubly degenerate sub-states with nuclear spin states $m_I = \pm 1/2$ and $\pm 3/2$ (Scheme 1.4, left). The quadrupole splitting ΔE_Q (Scheme 1.4, right) is the energy difference between these two degenerate sub-states, which can be observed in the Mössbauer spectrum as the distance between two resonance lines. The two resonance lines mean two transitions from the unsplit ground state to two energetically distinct sub-states, *i.e.*, two split excited states (Scheme 1.4, left). Quadrupole splitting (ΔE_Q) can give information on the spin state, oxidation state, and electronic environment of the Mössbauer atom.

Two general factors can affect the quadrupole splitting. One is the lattice contribution, including information on coordination geometry, particularly the symmetry of the coordination of the ligands. The other one is the valence electron contribution, *i.e.*, the anisotropic distribution of *d* electrons in the valence shell at the nucleus. These two factors can generally affect the total electric field gradient.

Scheme 1.4. Mössbauer transitions with a quadrupole splitting (left). Schematic Mössbauer spectrum (right).



Mössbauer spectroscopy has played an indispensable role in the investigation of biological as well as synthetic iron-sulfur complexes. This technique is useful in discovering new iron-sulfur clusters, describing formal oxidation states and electronic properties, determining sample composition, etc. For example, Mössbauer spectroscopy is helpful in determining the composition of a mixture because the integral of every doublet of the Mössbauer spectrum

corresponds to the ratio of this species in the sample. Another example where Mössbauer spectroscopy is useful in analyzing histidine coordination in Rieske clusters. Since only one doublet exists in the diferric all-cysteine coordinated [2Fe-2S] complexes. Diferric Rieske-type [2Fe-2S] complexes display two distinct doublets with a ratio of 1:1. The iron ion of the Rieske-type [2Fe-2S] core ligated by histidine ligands shows a slight larger isomer shift and larger quadrupole splitting than the cysteine coordinated iron site.

1.5 Outline and Focus of This Thesis

Iron-sulfur (Fe/S) clusters are omnipresent and are essential components in virtually all life forms due to their versatile structures and functions. Biological systems extensively employ iron-sulfur clusters, especially with rhombic [2Fe-2S] and cubane-type [4Fe-4S] cores for electron transfer, catalysis, or other functions such as oxygen sensing and DNA regulation. Studies on synthetic iron-sulfur complexes, such as [2Fe-2S] and [4Fe-4S] clusters, have provided deeper insight into their structures and functions.

The reduction potentials of synthetic Fe/S clusters are usually much more negative than their natural counterparts, which may be because they have quite different coordination environments, including hydrogen bonds. Some studies showed that as the intramolecular NH...S bonds increase, the redox potentials of Fe/S clusters shift positively, and these kind of clusters are more stable.^[27] However, it has been challenging to get synthetic Fe/S clusters with positive potentials like their natural counterparts. A good attempt might be the use of neutral ligands instead of anionic ligands to synthesize Fe/S clusters.

Furthermore, new types of Fe/S clusters are still being found in nature and synthesized in the laboratory today, such as novel Fe/S clusters with unique geometries and nuclearities, in high oxidation states, or with a unique mode of site-differentiation. These developments are stimulating continuous efforts to imitate biological Fe/S clusters or investigate their novel functions beyond electron transfer, like catalysis, coupled proton and electron transfer, and sensing.

The work in my PhD mainly focuses on establishing novel synthetic analogues for biological [2Fe-2S] and [4Fe-4S] clusters. Rieske-type Fe/S clusters in which one iron is coordinated by two histidine imidazoles and the other iron is ligated by two cysteine residues, acting as variants of [2Fe-2S] ferredoxin, are unique biological electron transfer cofactors. In biological Rieske-type [2Fe-2S] clusters, the relative orientation of two imidazole rings coordinated with the same iron ion of the [2Fe-2S] core is near perpendicularity. However, in reported synthetic [2Fe-2S] clusters, the dihedral angles between imidazole rings (3° - 48°) are much smaller than 90° . One goal of the present work was to synthesize a [2Fe-2S] cluster with Rieske-type heteroleptic ligation in which the dihedral angles are close to 90° in order to investigate the effect of this perpendicular arrangement on the cluster's properties. To mimic this kind of natural coordination model, the ligand H_2L^1 with a large and rigid bridge linking two (benz-)imidazoles was used to synthesize [2Fe-2S] clusters.

As mentioned above, most synthetic Fe/S clusters are coordinated by anionic ligands, and have much more negative reduction potentials than their natural counterparts. To obtain Fe/S clusters with a higher reduction potential, in chapter 4, two neutral imidazoline-2-imines ligands (L^5 and L^6) with strong nucleophilicity were synthesized and their metalation has been investigated. With these new imidazoline-2-imine ligands in hand, the synthesis of [2Fe-2S] clusters by reacting $[\text{H}_2\text{L}^5](\text{PF}_6)_2$ with [2Fe-2S] precursor $(\text{NEt}_4)_2[\text{Fe}_2\text{S}_2\text{Cl}_4]$ in the presence of base was tried. Unexpectedly, instead of a [2Fe-2S] complex, a rare 2:2 site-differentiated [4Fe-4S]³⁺ cluster $[\text{Fe}_4\text{S}_4\text{L}^5_2\text{Cl}_2](\text{PF}_6)$ ($\mathbf{6}(\text{PF}_6)$) was obtained. Complex $\mathbf{6}(\text{PF}_6)$ was fully characterized and the redox properties were investigated, which lead to the one-electron reduced species $[\text{Fe}_4\text{S}_4\text{L}^5_2\text{Cl}_2]$ ($\mathbf{6}$). The electronic properties of $\mathbf{6}(\text{PF}_6)$ and $\mathbf{6}$ have been investigated by various spectroscopic methods, through which the effects of site differentiation on both clusters were unfolded. (chapter 5).

Most of the [4Fe-4S] clusters are ligated by cysteine residues in biological systems, which have various functional roles. $\mathbf{6}(\text{PF}_6)$ can act as precursor for [4Fe-4S] clusters with different substitutions via salt metathesis reactions. To gain an insight into the electronic effect of cysteine

residues coordinated to such [4Fe-4S] clusters, in chapter 6, the chlorides of **6**(PF₆) were substituted by various thiolates, and a series of 2:2 site-differentiated [4Fe-4S] clusters, [Fe₄S₄L⁵₂(4-Br-C₆H₄S)₂] **7**, [Fe₄S₄L⁵₂(4-Br-C₆H₄S)₂](PF₆) **7**(PF₆), [Fe₄S₄L⁵₂(4-NO₂-C₆H₄S)₂] **3**, [Fe₄S₄L⁵₂(4-Br-C₆H₄S)₂](PF₆) **3**(PF₆), [Fe₄S₄L⁵₂(4-OMe-C₆H₄S)₂] **4**), were synthesized and fully characterized, and their redox properties were investigated. The detailed research of these complexes deepened our understanding of site-differentiated [4Fe-4S] clusters.

Chapter 2. Homoleptically Bis(benzimidazolate)-Coordinated Diferric Cluster as Modified Model for Rieske Cluster

2.1 Introduction

In biological systems, the [2Fe-2S] moiety in proteins with terminal [N]-ligation (histidine) have garnered increasing attention because of their unique functions.^[75] One of the most prominent examples is the Rieske-type [2Fe-2S] cluster in which one iron coordinated by two histidine imidazoles and the other iron was ligated by two cysteine residues. Rieske-type clusters are unique biological electron transfer cofactors, and can act as variants of [2Fe-2S] ferredoxin. In biological Rieske-type [2Fe-2S] cluster, the two histidine rings point with the N^δ towards the iron with an angle close to the expected 109° in this tetrahedral coordination. And the relative orientation of the imidazole (Im) rings towards each other is near perpendicularity ($\angle(\text{Im}/\text{Im}) \approx 90^\circ$). However, in previously reported synthetic [2Fe-2S] clusters, the dihedral angles between imidazole rings show only between 3° - 48° .^{[44], [47]} The goal of the present work was to synthesize a Rieske-type [2Fe-2S] cluster in which the dihedral angles are close to 90° in order to investigate the effect of this perpendicular arrangement on the cluster's properties.

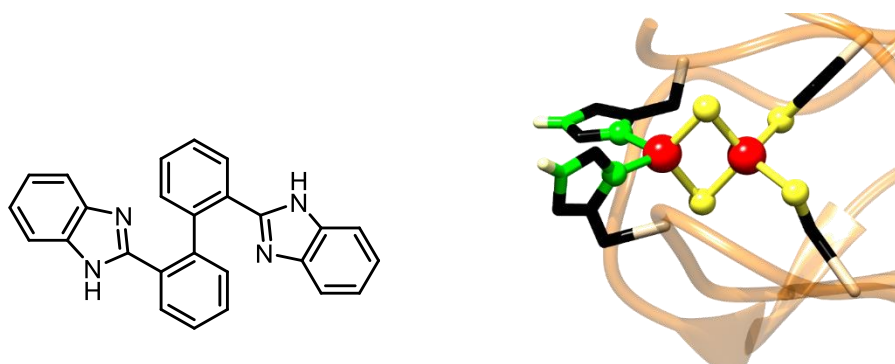


Figure 2.1. 2,2'-bis[2-(1-hydrobenzimidazol-2-yl)]biphenyl (H_2L^1)^[76] (left). 2Cys 2His coordinated [2Fe-2S] cluster of Rieske protein from cytochrome b6f (PDB: 1vf5) (right).

To mimic this kind of natural coordination model, a larger and more rigid bridge linking the (benz-)imidazole is needed. In 2004, Potenza and coworkers reported the ligand 2,2'-bis[2-(1-hydrobenzimidazol-2-yl)]biphenyl (H_2L^1) (Figure 2.1),^[76] which could be a good candidates to mimic the natural Rieske coordination model. The diphenyl backbone of this ligand should decrease the solubility of the product compared to the ligand with the alkyl backbone and facilitate crystallization of the product. Besides, the ligand with a diphenyl backbone can provide enough flexibility to “wrap” around the [2Fe-2S] core while it favors a relative orientation of the two (benz)imidazole rings close to the natural mode.

This chapter describes the synthesis and characterization of a new [2Fe-2S] cluster $(\text{NEt}_4)_2\mathbf{1}$ ligated by the bidentate dianionic capping ligand L^1 . The availability and investigations of the homoleptic [2Fe-2S] complex $(\text{NEt}_4)_2\mathbf{1}$ may lay the groundwork for the synthesis of the asymmetrically coordinated model of the Rieske cluster bearing the L^1 ligand.

2.2 Synthesis and Structural Characterization

The [2Fe-2S] cluster (NEt₄)₂**1** (Figure 2.2) was synthesized via a standard salt metathesis reaction, starting from ligand **H₂L¹** together with the precursor (NEt₄)₂[Fe₂S₂Cl₄].^[36] Ligand **H₂L¹** was deprotonated with potassium hydride in THF under an inert atmosphere and then added dropwise to a solution of (NEt₄)₂[Fe₂S₂Cl₄] in MeCN at -35°C. Crystallization from the crude reaction product and then diffusing Et₂O into the MeCN solution at rt afforded pure product of (NEt₄)₂**1** in yield of 40% as black blocks. The crystal of (NEt₄)₂**1** was further confirmed by single crystal X-ray diffraction (Figure 2.3). The molecular structure of (NEt₄)₂**1** is depicted in Figure 2.2, and corresponding bond lengths and angles are listed in Table 2.1.

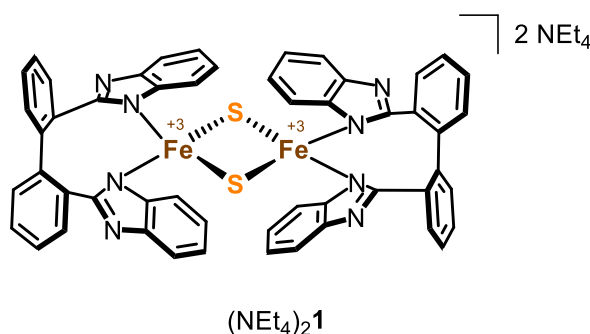


Figure 2.2. Synthetic [2Fe-2S] cluster coordinated by 2,2'-bis[2-(1-hydrobenzimidazol-2-yl)]biphenyl.

Complex (NEt₄)₂**1** crystallized in the monoclinic space group *P*2₁/*c* in combination with two MeCN molecules, with one unit cell containing four (NEt₄)₂**1** molecules. Due to an inversion center in the middle of the central Fe₂S₂ diamond, both iron centers are in geometrically equal coordination environments. The Fe⋯Fe distance in (NEt₄)₂**1** (2.784 Å) is slightly larger than in its analogue **I-41** (2.686 Å, Figure 2.4 and Table 2.1)^[77] and **I-10** (2.702 Å, Figure 2.4 and Table 2.1)^[33]. To the best of our knowledge, this Fe⋯Fe distance (2.784 Å) is also a little longer than the known synthetic four-coordinate [2Fe-2S] complexes (2.67–2.76 Å) from the literature.^[78] ^[79] The long Fe⋯Fe distance in (NEt₄)₂**1** may be because of the larger steric hindrance of **L¹** ligand. The distances Fe-S and Fe-N in (NEt₄)₂**1** (2.205 Å, 2.005 Å) are very similar to those in **I-41** (2.196 Å, 1.989 Å) and **I-10** (2.201 Å, 1.984 Å), and they are comparable to those reported for other N-ligated [2Fe-2S]²⁺ clusters.^{[79], [80]}

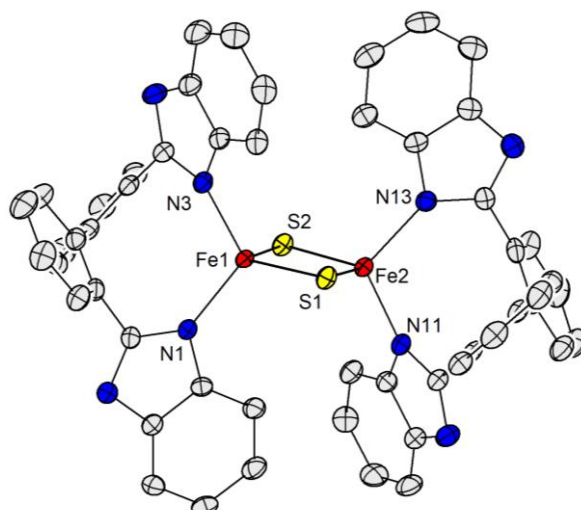


Figure 2.3. Molecular structure of the anion of the complex $(\text{NEt}_4)_2\mathbf{1}$ (thermal displacement ellipsoids shown at 50% probability). Hydrogen atoms, counterions, and solvent molecules have been omitted for clarity.

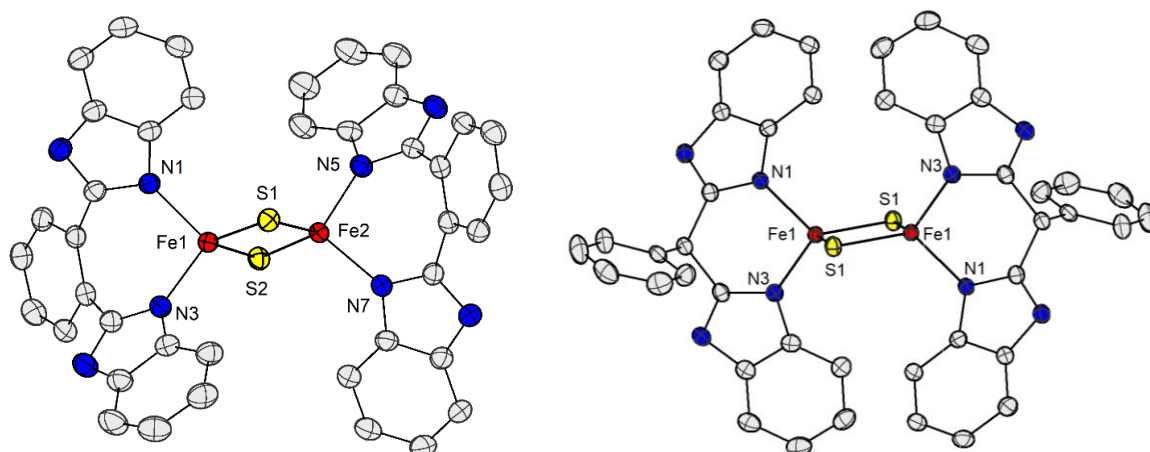


Figure 2.4. Molecular structure of the anion of the complex **I-41** (left) and **I-10** (right) (thermal displacement ellipsoids shown at 50% probability). Hydrogen atoms, counterions, and solvent molecules have been omitted for clarity.^{[77], [33]}

Table 2.1. Selected lengths (Å) and angles (deg) of diferric clusters $(\text{NEt}_4)_2\mathbf{1}$, **I-41**, and **I-10**.

	$(\text{NEt}_4)_2\mathbf{1}$	I-41	I-10
Fe \cdots Fe	2.7838(7)	2.6862(7)	2.7019(4)
Fe- μ S	2.2010(9)/2.2103(9) 2.2144(9)/2.1950(9)	2.1959(8)/2.1975(6) 2.1938(8)/2.1983(6)	2.1938(4)/2.2081(6)
Fe-N	2.0110(25)/1.9995(26) 2.0000(25)/2.0097(25)	1.9988(21)/1.9822(21) 1.9934(21)/1.9821(21)	1.990(2)/1.978(10)
N-Fe-N	111.26(31)/109.15(41)	99.57(98)/99.69(69)	92.84(60)
μ S-Fe- μ S	101.66(53)/101.68(13)	104.53(03)/104.57(03)	104.27(20)
Fe- μ S-Fe	78.19(33)/78.38(63)	75.353(21)/75.44(52)	75.73(20)

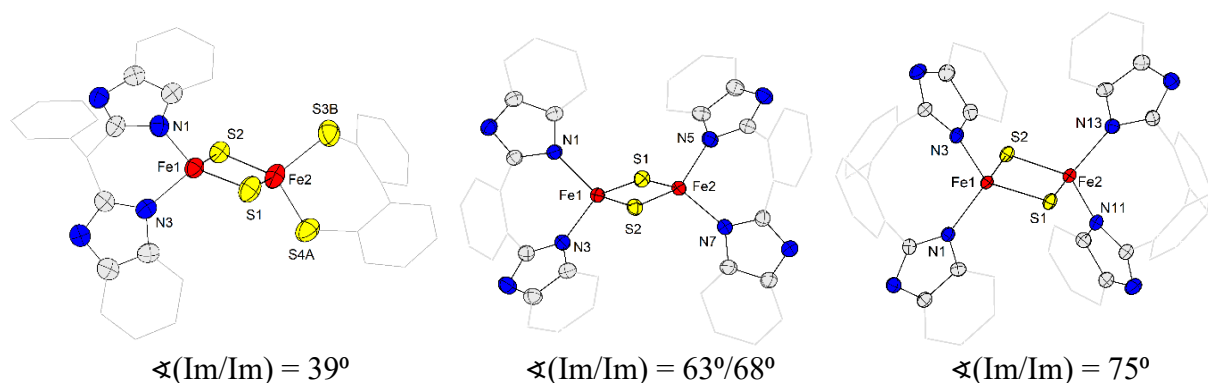


Figure 2.5. Molecular structures of the anions of the complexes Rieske-type **I-25** (left), **I-41** (middle), and $(\text{NEt}_4)_2\mathbf{1}$ (right) in the crystals (thermal displacement ellipsoids shown at 50% probability), emphasizing the orientation of the imidazole rings. Hydrogen atoms, counterions, and solvent molecules have been omitted for clarity.

The relative orientation of the imidazole rings in the complex $(\text{NEt}_4)_2\mathbf{1}$ is 75° , which is larger than in clusters **I-41** ($\angle(\text{Im}/\text{Im}) = 63^\circ/68^\circ$). Both angles are much larger than that in the reported for other $[2\text{Fe}-2\text{S}]$ complexes ($3^\circ\text{--}48^\circ$), like the complex **I-25** ($\angle(\text{Im}/\text{Im}) = 39^\circ$)^[47] (Figure 2.5) and **I-10** ($\angle(\text{Im}/\text{Im}) = 41^\circ$). As shown in Figure 9.2.9, the energy-minimized DFT calculated structure of cluster $\mathbf{1}^{2-}$ is in good agreement with that obtained by X-ray diffraction.

2.3 Characterization in Solution

In order to gain further understanding of the solution abilities of the $(\text{NEt}_4)_2\mathbf{1}$, positive/negative-ion electrospray ionization mass spectrometry (ESI(+/-)-MS), NMR spectroscopy, UV-Vis spectroscopy, and cyclic voltammetry (CV) were performed.

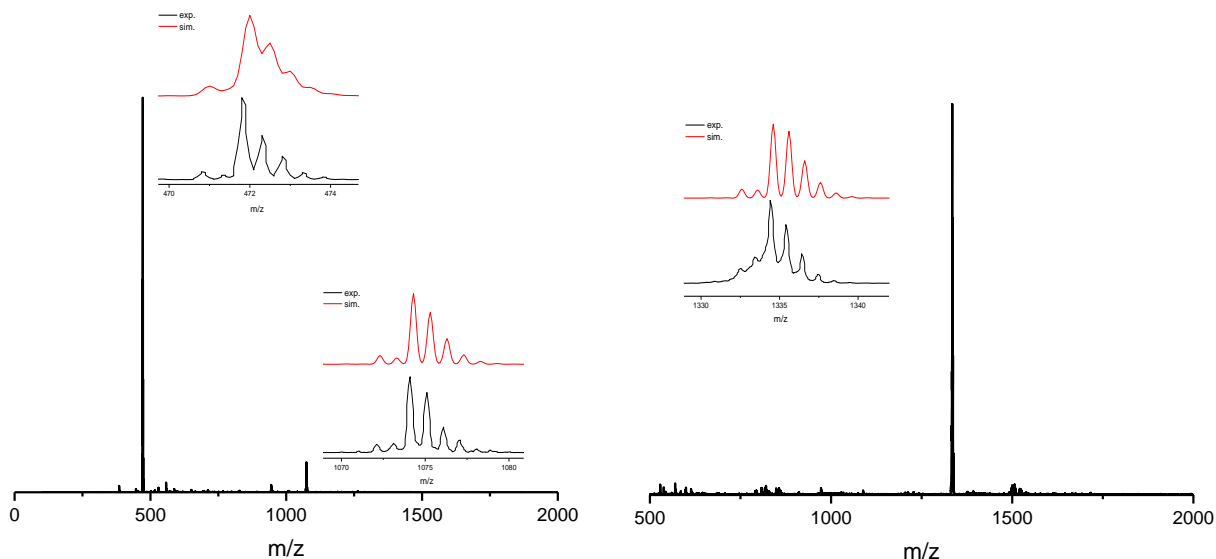


Figure 2.6. Negative ion ESI-MS spectrum of $(\text{NEt}_4)_2\mathbf{1}$ in MeCN solution (right). The insets show the experimental and expected isotopic distribution pattern for $[\text{M}-\text{NEt}_4]^-$ and $[\text{M}-2\text{NEt}_4]^{2-}$. Positive ion ESI-MS spectrum of $(\text{NEt}_4)_2\mathbf{1}$ in MeCN solution (left). The insets show the experimental and simulated isotopic distribution pattern for $[\text{M}+\text{NEt}_4]^+$.

The positive and negative ion ESI mass spectra showed that $(\text{NEt}_4)_2\mathbf{1}$ is stable in solution; dominant peaks with characteristic isotopic distribution patterns were observed at $m/z = 472.04$ for $\mathbf{1}^{2-}$, $m/z = 1074.25$ for $[(\text{NEt}_4)\mathbf{1}]^-$ and 1334.57 for $[(\text{NEt}_4)_3\mathbf{1}]^+$ (Figure 2.6). The identity of the complex is substantiated by an excellent agreement between the experimental and the simulated isotopic distribution patterns.

The ^1H NMR spectrum of complex $(\text{NEt}_4)_2\mathbf{1}$ in MeCN-d_3 at room temperature could be recorded due to the strong antiferromagnetic coupling of the iron atoms. Complex $(\text{NEt}_4)_2\mathbf{1}$ exhibits D_{2h} symmetry in CD_3CN solution with contact-shifted resonances between +11 to 0 ppm (Figure 2.7). The pronounced broadening of the ^1H resonances of complex $(\text{NEt}_4)_2\mathbf{1}$ suggests that like other $[2\text{Fe-2S}]^{2+}$ complexes^{[44], [38]}, $(\text{NEt}_4)_2\mathbf{1}$ features an $S = 0$ ground state with some thermal population of paramagnetic excited states. A detailed signal assignment was based on the comparison with literature known ligand 2,2'-bis[2-(1-hydrobenzimidazol-2-yl)]biphenyl and similar $[2\text{Fe-2S}]$ compounds, such as compound **I-41**. The signal for H7 could not be detected because of enhanced paramagnetic relaxation deriving from proximity to the Fe atoms, which is similar to previous observations.^[47]

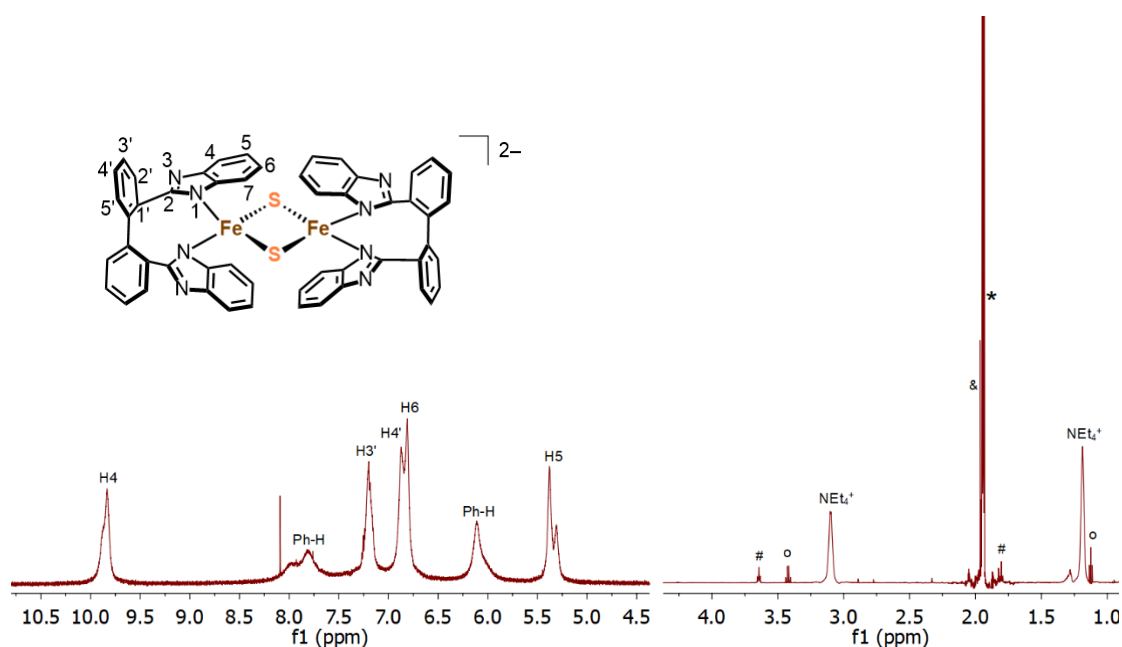


Figure 2.7. ^1H NMR spectrum of $(\text{NEt}_4)_2\mathbf{1}$ recorded in MeCN-d_3 (600.3 MHz, 298 K). Signals of the NEt_4^+ , CD_3CN (*), residual THF (#), MeCN (&), and Et_2O (°) have been labeled.

The variable temperature electronic absorption spectrum for complex $(\text{NEt}_4)_2\mathbf{1}$ was recorded in MeCN solution from 238 K to 343 K (Figure 2.8). At 238 K, the UV-vis spectrum shows three absorption bands at $\lambda_{\text{max}} = 432, 475$ and 595 nm that can be assigned to ligand (including μS) $\rightarrow \text{Fe}^{3+}$ charge transfer (ligand-to-metal, LMCT) transitions according to TD-DFT calculations (Table 9.3.1). The intensities of all three bands decreased as the solution of $(\text{NEt}_4)_2\mathbf{1}$ was heated up. And more notably, complex $(\text{NEt}_4)_2\mathbf{1}$ is stable at elevated temperatures like 343 K.

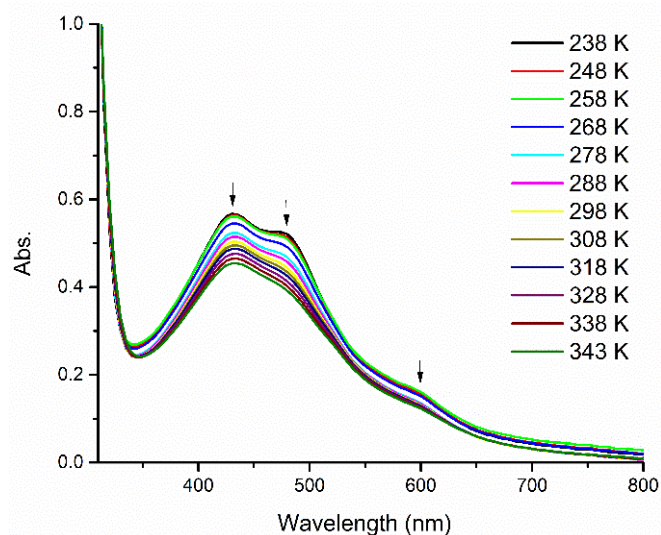


Figure 2.8. Temperature-dependent UV-vis absorption spectra of $(\text{NEt}_4)_2\mathbf{1}$ in MeCN solution under a N_2 atmosphere.

2.4 Redox Properties

Electrochemical experiments were carried out to investigate the electrochemical properties of the complex $(\text{NEt}_4)_2\mathbf{1}$. The CV of $(\text{NEt}_4)_2\mathbf{1}$ in MeCN under an N_2 atmosphere shows one reversible redox process at $E_{1/2} = -1.43$ V vs. Fc/Fc^+ (Figure 2.9). In addition, the currents for the redox process of $(\text{NEt}_4)_2\mathbf{1}$ vary linearly with the square root of the scan rate and $\Delta E_p = 73$ mV for the separation of anodic and cathodic peak potentials, indicative of diffusion-controlled processes (Figure 2.9 right). The redox wave at $E_{1/2} = -1.43$ V vs. Fc/Fc^+ can be assigned to the formation of the one-electron reduced species $\mathbf{1}^{3-}$. This reduction potential ($E_{1/2} = -1.43$ V vs. Fc/Fc^+) of $(\text{NEt}_4)_2\mathbf{1}$ is negatively shifted about 180 mV compared to $\mathbf{I-41}$ ($E_{1/2} = -1.25$ V vs. Fc/Fc^+)^[81], and 290 mV compared to $\mathbf{I-10}$ ($E_{1/2} = -1.14$ V vs. Fc/Fc^+), indicating a more electron rich $[2\text{Fe-2S}]$ core of complex $(\text{NEt}_4)_2\mathbf{1}$.

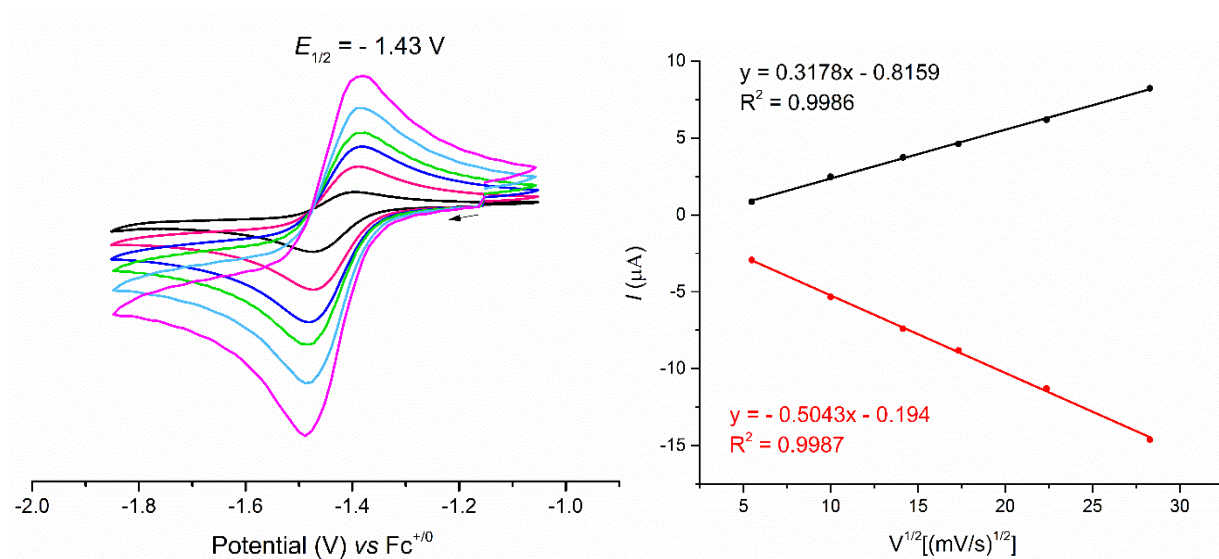


Figure 2.9. (Left) Scan rate-dependent CVs of $(\text{NEt}_4)_2\mathbf{1}$ (1.0 mM) in MeCN/0.1 M Bu_4NPF_6 under an N_2 atmosphere at rt. CVs were recorded at scan rates of 30, 100, 200, 300, 500, and 800

mV s^{-1} . (Right) Linear dependence of current on square root of scan rate of $(\text{NEt}_4)_2\mathbf{1}$. The forward peak (black) and backward peak (red) of $[\text{2Fe-2S}]^{2/3+}$ redox couple.

After the confirmation of electrochemical accessibility of mixed-valent species $\mathbf{1}^{3-}$, the chemical reduction was investigated via UV-Vis titration experiments of $(\text{NEt}_4)_2\mathbf{1}$ with CoCp^*_2 (Figure 2.10, left). The addition of 1.0 eq CoCp^*_2 to $(\text{NEt}_4)_2\mathbf{1}$ leads to the formation of $(\text{CoCp}^*_2)(\text{NEt}_4)_2\mathbf{1}$. No further changes of the absorption spectra are observed when more than 1.0 eq of CoCp^*_2 is added. Reduction led to the decreasing intensity of the bands in the region between 400 nm and 700 nm, and the increasing intensity of a shoulder at around 340 nm. The intensity of the shoulder at 595 nm decreases, and the bands at 432 nm and 475 nm appear. Furthermore, a broad band at about 525 nm develops. Two isosbestic points (at around 380 nm and 715 nm) indicate clean conversion to the mixed-valent species $(\text{CoCp}^*_2)(\text{NEt}_4)_2\mathbf{1}$. Complex $(\text{CoCp}^*_2)(\text{NEt}_4)_2\mathbf{1}$ is not stable in MeCN solution even at -35°C . The absorption spectra of $(\text{CoCp}^*_2)(\text{NEt}_4)_2\mathbf{1}$ (Figure 2.10, right) changed a lot within 2 hours in MeCN at -35°C , indicating that it will be challenging to isolate the pure complex of $(\text{CoCp}^*_2)(\text{NEt}_4)_2\mathbf{1}$ by chemical purification.

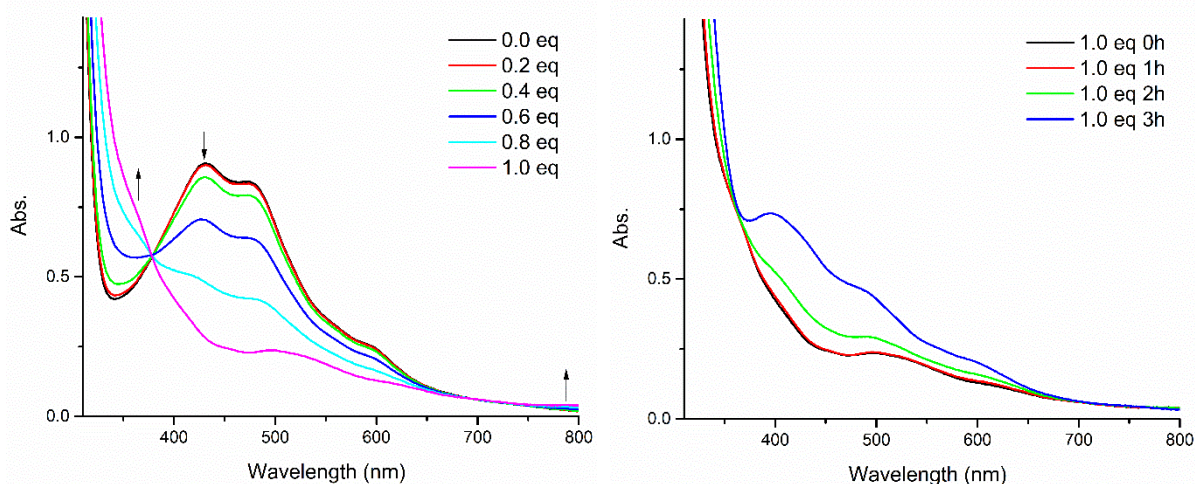


Figure 2.10. UV-vis spectra of titration of cluster $(\text{NEt}_4)_2\mathbf{1}$ with CoCp^*_2 in MeCN at -35°C (left). UV-vis spectra of $(\text{NEt}_4)_2\mathbf{1}$ in MeCN solution being kept at -35°C (right).

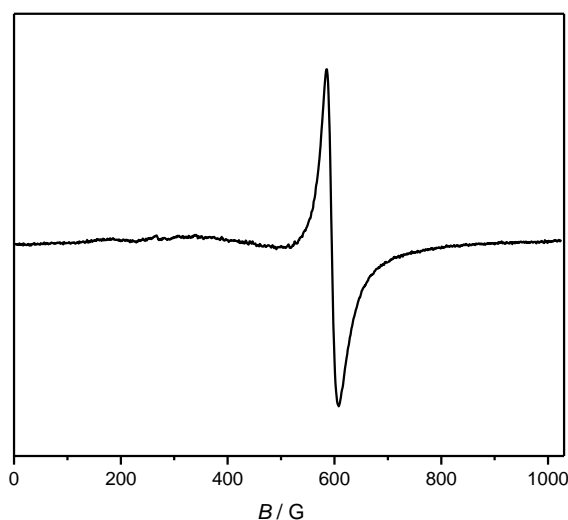


Figure 2.11. Experimental EPR spectrum of the cluster $(\text{CoCp}^*_2)(\text{NEt}_4)_2\mathbf{1}$ in MeCN at 133 K.

EPR measurement was performed to gain more insight into the electronic structure of mixed-valent $(\text{CoCp}^*_{2})(\text{NEt}_4)_2\mathbf{1}$. In order to avoid side products forming, a sample of complex $(\text{NEt}_4)_2\mathbf{1}$ mixed with 0.8 equivalent of CoCp^*_{2} in MeCN was transferred to an EPR tube in a glovebox and rapidly frozen in liquid nitrogen, and the EPR spectrum was measured at 133 K as a vitreous solvent matrix. The obtained EPR spectrum of $(\text{NEt}_4)_3\mathbf{1}$ (Figure 2.11) shows a narrow and almost isotropic spectrum ($g = 1.933$) with no discernable hyperfine interactions, indicating the formation of the mixed-valent species $(\text{CoCp}^*_{2})(\text{NEt}_4)_2\mathbf{1}$ and its $S = 1/2$ ground state. A measurement at a lower temperature may provide more information. Complex $(\text{CoCp}^*_{2})(\text{NEt}_4)_2\mathbf{1}$ shows a lower g value ($g = 1.933$) than homoleptic $[\text{N}_2/\text{N}_2]$ analogue $(\text{NEt}_4)\mathbf{I-10}$ ($g_{\text{av}} = 1.945$), but higher than $[\text{N}_2/\text{N}_2]$ analogue $(\text{NEt}_4)\mathbf{I-41}$ ($g_{\text{av}} = 1.919$), and higher than the first Rieske analogue $(\text{NEt}_4)\mathbf{I-24}$ ($g_{\text{av}} = 1.918$). While $g = 1.933$ for $(\text{CoCp}^*_{2})(\text{NEt}_4)_2\mathbf{1}$ is in good agreement with $g_{\text{av}} = 1.935$ found for the second Rieske model $(\text{CoCp}^*_{2})\mathbf{I-25}$. And it is reasonably in between the reported $g_{\text{av}} = 1.96$ for $[\text{2Fe-2S}]$ ferredoxins with four cysteine ligands and $g_{\text{av}} = 1.90\text{--}1.91$ for biological Rieske clusters. Mouesca has shown that for mixed-valent $[\text{2Fe-2S}]$ clusters, the average g value tends to increase towards the free electron value ($g = 2.0023$) with the increasing electronic delocalization.^[82] Therefore, the value $g = 1.933$ for $(\text{CoCp}^*_{2})(\text{NEt}_4)_2\mathbf{1}$ might reflect increased valence delocalization compared to $(\text{NEt}_4)\mathbf{I-24}$ ($g_{\text{av}} = 1.918$) and $(\text{NEt}_4)\mathbf{I-41}$ ($g_{\text{av}} = 1.919$), indicating increased symmetry of complex $(\text{CoCp}^*_{2})(\text{NEt}_4)_2\mathbf{1}$.

2.5 Characterization in the Solid State

The zero-field ^{57}Fe Mössbauer spectrum of complex $(\text{NEt}_4)_2\mathbf{1}$ in the solid state was recorded at 80K. It (Figure 2.12) shows a single quadrupole doublet with isomer shift $\delta = 0.31 \text{ mm s}^{-1}$, which is characteristic of the tetrahedrally coordinated high-spin ferric complex. Isomer shifts have been empirically related to the oxidation states s of the iron atoms according to $\delta = 1.43 - 0.40s$ (a correlation found for tetrahedral $[\text{S}_4]$ -ligated iron sites at 77K by linear regression analysis).^{[83],[84]} Applying the experimental δ values for the $[\text{FeN}_2\text{S}_2]$ systems $(\text{NEt}_4)_2\mathbf{1}$ to this equation reveals the expected oxidation state of $s \approx 3$. It suggests that the above correlation is not only valid for tetrahedral $[\text{S}]$ -coordinate Fe sites but also for $[\text{FeN}_2\text{S}_2]$ -coordinate complexes.

Table 2.2. Zero field ^{57}Fe Mössbauer parameters [mm s^{-1}] for solid $(\text{NEt}_4)_2\mathbf{1}$, $\mathbf{I-41}$ and $(\text{CoCp}^*_{2})(\text{NEt}_4)_2\mathbf{1}$ at 80 K.

Compound	δ	ΔE_Q
$(\text{NEt}_4)_2\mathbf{1}$	0.31	0.27
I-41	0.27	0.82
I-10	0.24	0.87
crude complex of $(\text{CoCp}^*_{2})(\text{NEt}_4)_2\mathbf{1}$	0.54/0.63	0.78/1.32

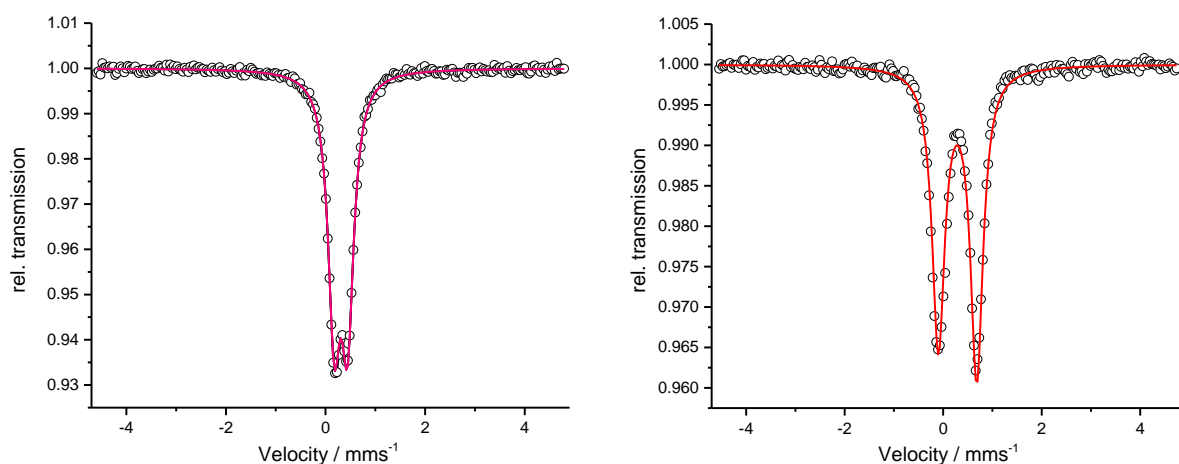


Figure 2.12. Zero field ^{57}Fe Mössbauer spectra of solid samples of $(\text{NEt}_4)_2\mathbf{1}$ (left) and $\mathbf{I-41}$ (right) at 80 K. Simulation of the data gave the following parameters: (left) $\delta = 0.31 \text{ mm s}^{-1}$, $\Delta E_Q = 0.27 \text{ mm s}^{-1}$; (right) $\delta = 0.27 \text{ mm s}^{-1}$, $\Delta E_Q = 0.82 \text{ mm s}^{-1}$.

Surprisingly, the quadrupole splitting of $(\text{NEt}_4)_2\mathbf{1}$ ($\Delta E_Q = 0.27 \text{ mm s}^{-1}$) is smaller than that of the benzimidazolate coordinated $[2\text{Fe-2S}]$ analogue $\mathbf{I-41}$ ($\Delta E_Q = 0.82 \text{ mm s}^{-1}$) and $\mathbf{I-10}$ ($\Delta E_Q = 0.87 \text{ mm s}^{-1}$). And this value ($\Delta E_Q = 0.27 \text{ mm s}^{-1}$) is even smaller than those values obtained for the monodentate homoleptic $[\text{N}]$ -ligated $[2\text{Fe-2S}]$ cluster $[\text{Fe}_2\text{S}_2(\text{C}_4\text{H}_4\text{N})_4]^{2-}$ [79],[85] ($\Delta E_Q = 0.49 - 0.61 \text{ mm s}^{-1}$) and $[\text{S}]$ -coordinated $[2\text{Fe-2S}]$ clusters ($[\text{Fe}_2\text{S}_2(\text{S}_2\text{-o-xy})_2]^{2-}$ ($\Delta E_Q = 0.36 \text{ mm s}^{-1}$); $[\text{Fe}_2\text{S}_2(\text{SPh})_4]^{2-}$ ($\Delta E_Q = 0.32 \text{ mm s}^{-1}$ [83]). The quadrupole splitting of $(\text{NEt}_4)_2\mathbf{1}$ is especially small ($\Delta E_Q = 0.27 \text{ mm s}^{-1}$) because it is d^5 high spin system without any valence contribution to the electric field gradient and quite symmetrical tetrahedral environment of the iron centers.

The direct current (dc) temperature-dependent magnetic susceptibility data for the complex $(\text{NEt}_4)_2\mathbf{1}$ were recorded on a powder polycrystalline sample on a Quantum Design MPMS3 SQUID magnetometer in the range of 2–255 K under 0.5 T applied dc field. The $\chi_{\text{M}}T$ value linearly decreases on cooling due to thermal depopulation of the excited states from $0.28 \text{ cm}^3 \text{ mol}^{-1} \text{ K}$ at 255 K to ~ 0 at 80 K (Figure 2.13) indicating a dominant strong antiferromagnetic magnetic exchange coupling between the two high-spin Fe(III) centres resulting in a diamagnetic ground state ($S_{\text{T}} = 0$). The residual moment below 80 K stems from the paramagnetic impurities. The experimental data was modelled using the *julX* program (E. Bill: Max-Planck Institute for Chemical Energy Conversion, Mülheim/Ruhr, Germany) by using a fitting procedure to the Heisenberg-Dirac-van-Vleck (HDvV) spin Hamiltonian (eq. 2.1),

$$\hat{H} = -2J\hat{S}_1\hat{S}_2 + g\mu_B\vec{B}(\vec{S}_1 + \vec{S}_2) \quad (2.1)$$

Temperature-independent paramagnetism (*TIP*) and paramagnetic impurities (*PI*) were included according to $\chi_{\text{calc}} = (1 - PI) \cdot \chi + PI \cdot \chi_{\text{mono}} + TIP$. The best fit to the experimental data provides the intramolecular magnetic exchange coupling between the high-spin Fe(III) centres as $J = -195 \text{ cm}^{-1}$ ($g_1 = g_2 = 2.0$ (fixed)). This is comparable to the Fe(III)-Fe(III) exchange coupling reported for related $[2\text{Fe-2S}]$ clusters. [86], [87]

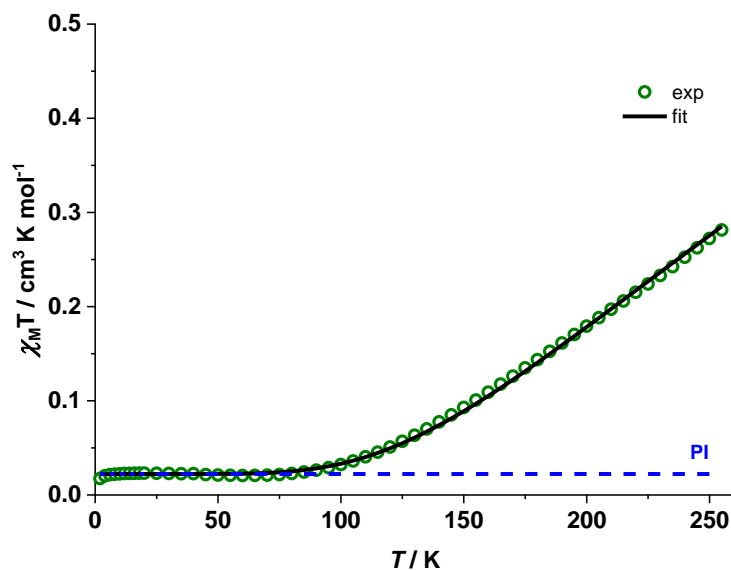


Figure 2.13. Plot of $\chi_M T$ vs. T for $(\text{NEt}_4)_2\mathbf{1}$ at an applied field of 0.5 T. The solid black line is a fit to experimental data; Best fit parameters for $(\text{NEt}_4)_2\mathbf{1}$ are: $J = -195 \text{ cm}^{-1}$, $PI = 0.5\%$, $TIP = 16 \cdot 10^{-6} \text{ cm}^3 \text{ mol}^{-1}$ (subtracted), $g_1 = g_2 = 2.00$ (fixed).

2.6 Attempts to Synthesize the Mixed-Valent Cluster

On the other hand, in order to further confirm the statement on the stability of the mixed-valent species $(\text{CoCp}^*_2)(\text{NEt}_4)_2\mathbf{1}$ as mentioned above, next, the bulk synthesis of the mixed-valent species $(\text{CoCp}^*_2)(\text{NEt}_4)_2\mathbf{1}$ was tried by addition of one equivalent CoCp^*_2 to a solution of $(\text{NEt}_4)_2\mathbf{1}$ in MeCN at $-35 \text{ }^\circ\text{C}$. After stirring for 5 minutes, the crude product was precipitated with Et_2O and then rinsed with THF and Et_2O .

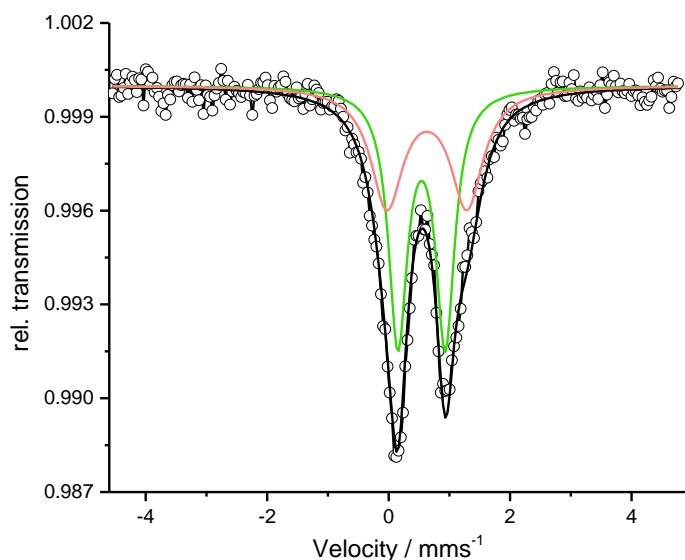
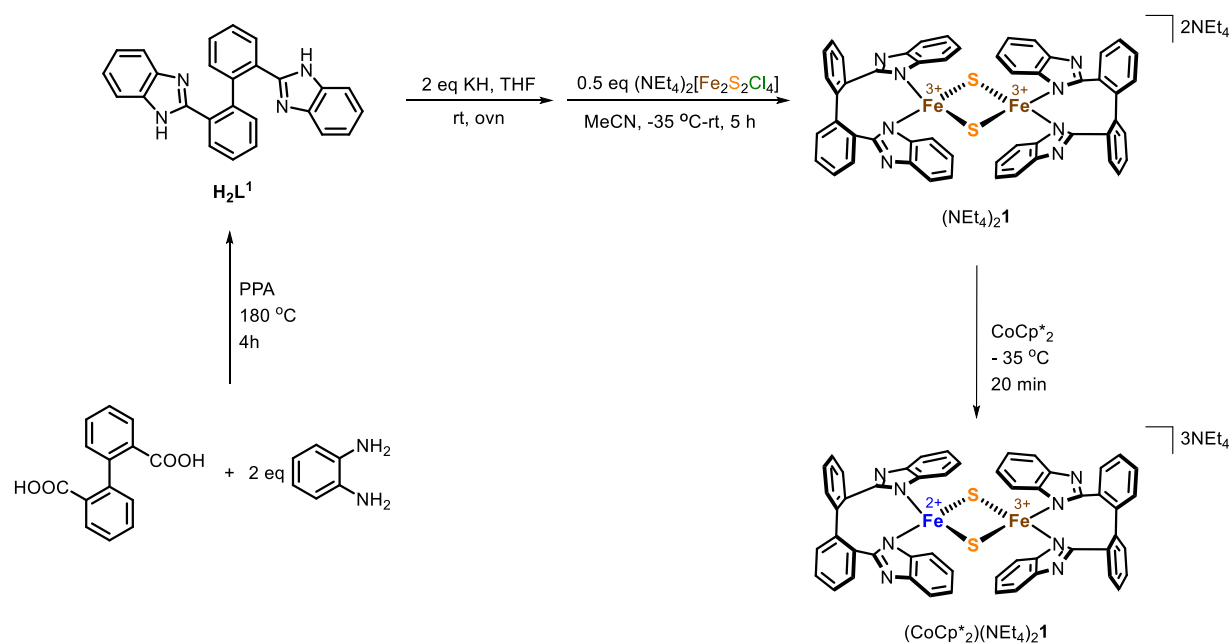


Figure 2.14. Zero field ^{57}Fe Mössbauer spectrum of the solid crude product of the reduced compound $(\text{CoCp}^*_2)(\text{NEt}_4)_2\mathbf{1}$ at 80 K.

The zero-field ^{57}Fe Mössbauer spectrum for the reduced crude product in the solid state was collected at 80 K. The Mössbauer spectrum can be fitted with two quadrupole doublets with $\delta_1 = 0.54 \text{ s}^{-1}$, $\Delta E_{\text{Q}1} = 0.78 \text{ mm s}^{-1}$ for ‘ferric’ contribution and $\delta_2 = 0.63 \text{ mm s}^{-1}$, $\Delta E_{\text{Q}2} = 1.32 \text{ mm s}^{-1}$ for the ‘ferrous’ contribution with an intensity ratio of almost 1:1 (Table 2.2) as expected for a mixed-valent $[\text{Fe}_2\text{S}_2]$ cluster (Figure 2.14). However, so far the attempts to get the pure reduced species of $(\text{CoCp}^*_2)(\text{NEt}_4)_2\mathbf{1}$ in crystalline form by diffusion of Et_2O into a MeCN/DMF solution of $(\text{CoCp}^*_2)(\text{NEt}_4)_2\mathbf{1}$ or by layering with MeCN, DMF and Et_2O at $-35 \text{ }^\circ\text{C}$ failed, which is consistent with the limited stability of the reduced cluster, as evidenced for the UV-vis titration of cluster $(\text{NEt}_4)_2\mathbf{1}$ with CoCp^*_2 .

2.7 Conclusions



In summary, a modified bis(benzimidazolato)-coordinated Rieske model $(\text{NEt}_4)_2\mathbf{1}$ was prepared and fully characterized. The small quadrupole splitting of $(\text{NEt}_4)_2\mathbf{1}$ ($\Delta E_{\text{Q}} = 0.27 \text{ mm s}^{-1}$) reflects the decreased electric field gradient resulting from the higher symmetry of electronic charge distribution. Electrochemical studies show that $(\text{NEt}_4)_2\mathbf{1}$ exhibits one reversible redox event for $1^{2-/3-}$ pair. In addition, UV-vis titration experiments show that the mixed-valent species of $(\text{CoCp}^*_2)(\text{NEt}_4)_2\mathbf{1}$ is not stable even at low temperatures, indicating that isolation of the pure mixed-valent complex is highly challenging.

Chapter 3. The Quest for Rieske-Type [2Fe-2S] Clusters

3.1 Introduction

Rieske-type [2Fe-2S] clusters, as variants of [2Fe-2S] ferredoxins, can serve as unique biological electron transfer cofactors. The coordination environment of Rieske-type [2Fe-2S] core differs from the common [2Fe-2S] core of ferredoxins, where one iron ion is coordinated by two nitrogen donors from histidine imidazoles, the other is coordinated by two sulfur donors from cysteine thiolates.^[88] This unique coordination environment leads to distinct spectroscopic signatures (e. g. two distinct quadrupole doublets in the zero-field ⁵⁷Fe Mössbauer spectrum; characteristic low g_3 value of the reduced [2Fe-2S]⁺ species) and functional characteristics (e. g. pH-dependent reduction potential).

For the past several years, the electronic structures and properties of iron-sulfur cofactors have been better known by investigating their synthetic analogues. Many examples of homoleptic-coordinated [2Fe-2S] clusters have been reported over the last decades. In contrast, the synthesis of asymmetrically heteroleptic-coordinated [2Fe-2S] clusters is still challenging because of the competing formation of the homoleptic-coordinated byproducts. Only two synthetic Rieske-type [2Fe-2S] clusters have been reported so far.^{[44], [47]} The first structural model for Rieske clusters, **I-24**, (Figure 3.1, left) was reported in 2008 by the Meyer group.^[44] The bidentate [N₂] capping ligand of **I-24**, serving as a mimic for the natural histidine residues, has no peripheral nitrogen atoms, so this Rieske-type [2Fe-2S] cluster cannot undergo protonation on PCET reactions like Rieske proteins.

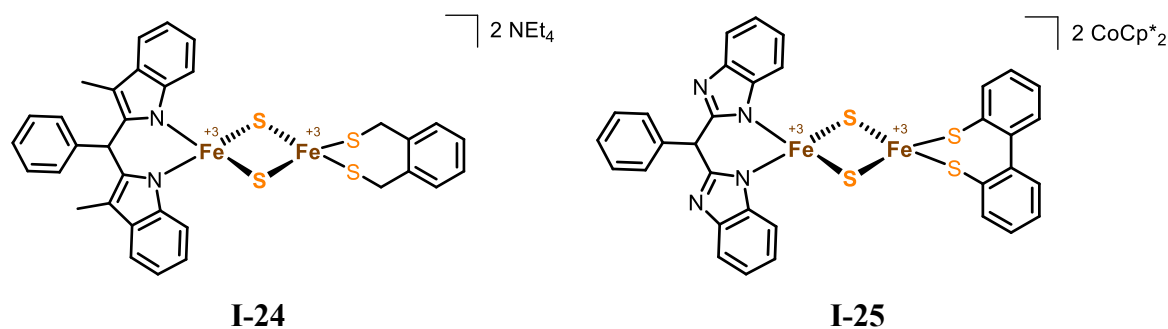


Figure 3.1. The first structural Rieske model (**I-24**) and the second Rieske model (**I-25**) have been published in the literature.^{[44], [47]}

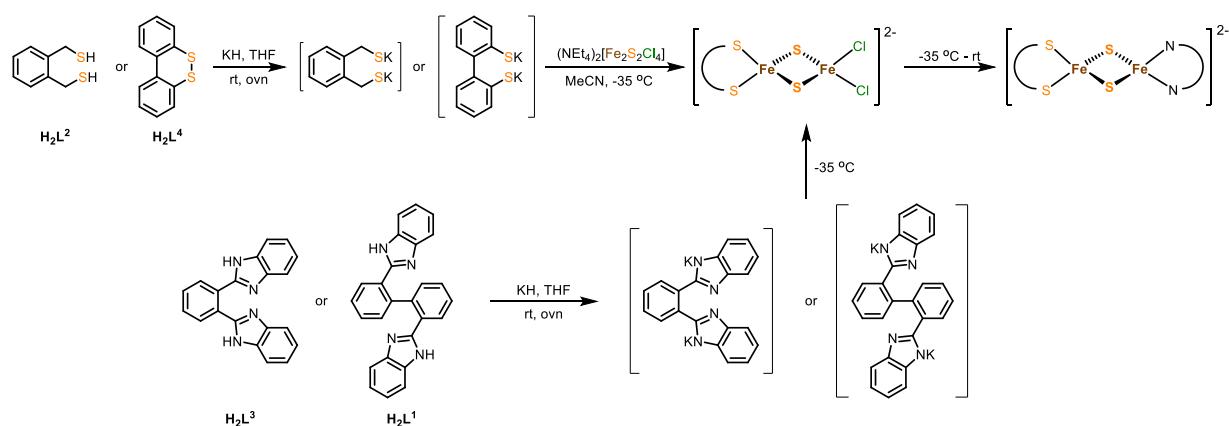
In 2014, the Meyer group reported the second Rieske-type [2Fe-2S] cluster **I-25** (Figure 3.1, right), in which the ligand set is similar to the first Rieske-type [2Fe-2S] cluster **I-24**. The major difference between the first and the second generation Rieske-type [2Fe-2S] models is that the second model, **I-25**, includes peripheral nitrogen atoms to mimic the histidine ligands of biological Rieske clusters. Besides, to better dissolve and crystallize, the sulfur ligand was substituted with a biphenyldithiolate ligand.

3.2 Attempts to Synthesize a Novel Rieske-Type [2Fe-2S] Cluster

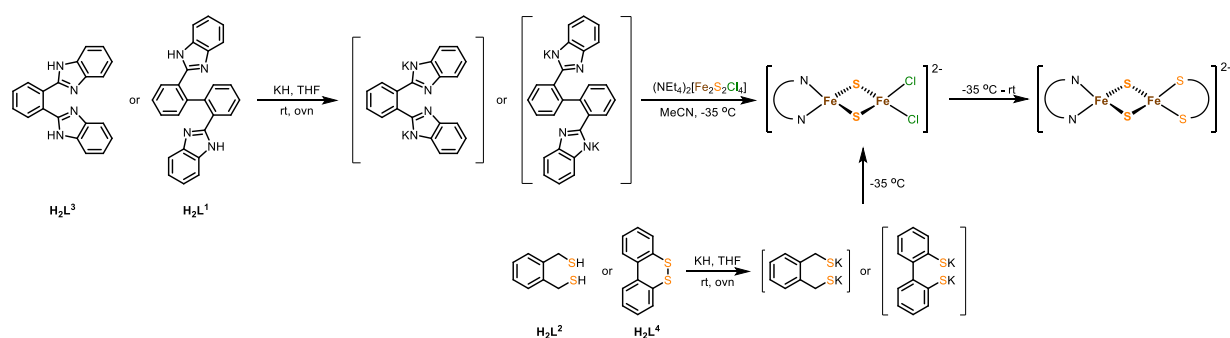
To synthesize a third Rieske-type [2Fe-2S] cluster, 1,2-phenylenedimethanethiol (H_2L^2) and dibenzo[*c,e*][1,2]dithiine (H_2L^4) were chosen to serve as the mimic for the natural cysteine residues. Besides, 1,2-bis(1*H*-benzo[*d*]imidazol-2-yl)benzene (H_2L^3) and 2,2'-bis(1*H*-benzo[*d*]imidazol-2-yl)-1,1'-biphenyl (H_2L^1) were used to model the histidine ligation. Analogous to the first and the second Rieske-type [2Fe-2S] clusters, the new Rieske cluster was synthesized in a one-pot ligand exchange reaction (Scheme 3.1). One equivalent of H_2L^2 (or H_2L^4) was deprotonated with potassium hydride and then added to a solution of $(\text{NEt}_4)_2[\text{Fe}_2\text{S}_2\text{Cl}_4]$ in acetonitrile at $-35\text{ }^\circ\text{C}$ to furnish the $[\text{S}_2]$ cap. H_2L^3 (or H_2L^1), after deprotonation with potassium hydride, was subsequently added to the former mixture at $-35\text{ }^\circ\text{C}$ and served as the $[\text{N}_2]$ capping ligand (Scheme 3.1, A). The Rieske-type cluster was also tried to synthesize by the reverse sequence, viz. by sequential addition of the deprotonated $[\text{N}_2]$ ligand and the deprotonated $[\text{S}_2]$ ligand at $-35\text{ }^\circ\text{C}$ to a cooled solution of $(\text{NEt}_4)_2[\text{Fe}_2\text{S}_2\text{Cl}_4]$ (Scheme 3.1, B). In addition to different ligands, different ratios of $[\text{N}_2]$ and $[\text{S}_2]$ ligands also have been tested.

Scheme 3.1. Synthetic approaches to the third Rieske-type [2Fe-2S] cluster.

A).



B).



The crude reaction mixtures (Scheme 3.1, A, and B) were analyzed by ESI mass spectrometry. Take the analysis of $[\text{Fe}_2\text{S}_2\text{L}^1\text{L}^2]^{2-}$ as an example (Scheme 3.2). Apart from the dominant Rieske-type [2Fe-2S] cluster peak at 363.7 for $[\text{M-2NEt}_4]^{2-}$, homoleptic species $[\text{Fe}_2\text{S}_2\text{L}^1\text{L}^2]^{2-}$ (471.8) and $[\text{Fe}_2\text{S}_2\text{L}^2\text{L}^2]^{2-}$ (255.7) could also be detected, respectively. Similar to other Rieske-type [2Fe-2S] clusters syntheses, degradation of the products to give mononuclear $[\text{N}]$ -coordinate or $[\text{S}]$ -

coordinate iron complexes could not be avoided even at $-35\text{ }^{\circ}\text{C}$. Therefore, peaks for mononuclear species (824.9 for $[\text{FeL}^1]^-$ or 391.7 for $[\text{FeL}^2]^-$) were detected by ESI mass analysis (Figure 3.2).

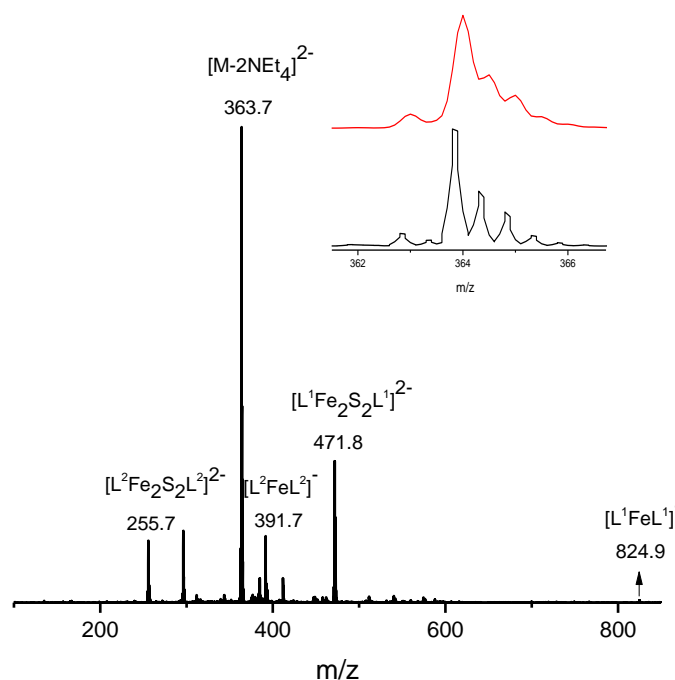
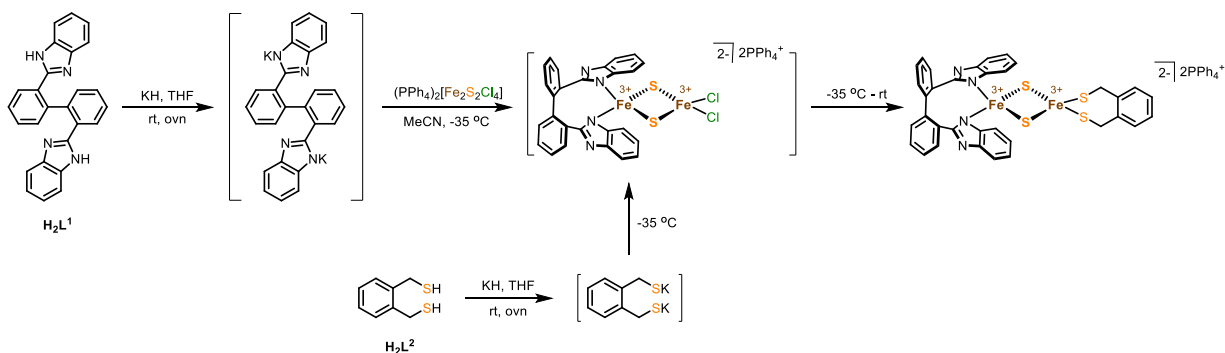


Figure 3.2. Negative ion ESI-MS of crude reaction mixtures in MeCN solution. The insets show the experimental and simulated isotopic distribution pattern for Rieske cluster $[\text{M}-2\text{NEt}_4]^{2-}$.

Despite the dominant peaks of the target Rieske-type [2Fe-2S] cluster ($[\text{M}-2\text{NEt}_4]^{2-}$) in the ESI mass spectra, several crystallization attempts from MeCN / Et₂O, DMF / Et₂O, MeCN + DMF / Et₂O, saturated MeCN solution, and saturated DMF solution have been tried, single crystals could not be obtained in good quality.

Scheme 3.2. synthetic approaches for the third Rieske-type [2Fe-2S] cluster $(\text{PPh}_4)_2\mathbf{2}$.



Then the precursor $(\text{NEt}_4)_2[\text{Fe}_2\text{S}_2\text{Cl}_4]$ was exchanged by $(\text{PPh}_4)_2[\text{Fe}_2\text{S}_2\text{Cl}_4]$ in order to increase the crystallization ability of the synthetic Rieske-type [2Fe-2S] clusters. Ligand $\mathbf{H}_2\mathbf{L}^1$ was first deprotonated with potassium hydride and then was added to a cooled solution of $(\text{PPh}_4)_2[\text{Fe}_2\text{S}_2\text{Cl}_4]$ in acetonitrile at $-35\text{ }^{\circ}\text{C}$ to furnish the $[\text{N}_2]$ cap. And then, $\mathbf{H}_2\mathbf{L}^2$, after deprotonation with potassium hydride, was added as the $[\text{S}_2]$ capping ligand at $-35\text{ }^{\circ}\text{C}$ (Scheme

3.2). Rieske-type [2Fe-2S] cluster (PPh₄)₂**2** could be crystallized from an acetonitrile solution slowly diffused of diethyl ether, affording few crystals suitable for X-ray diffraction (Figure 3.3).

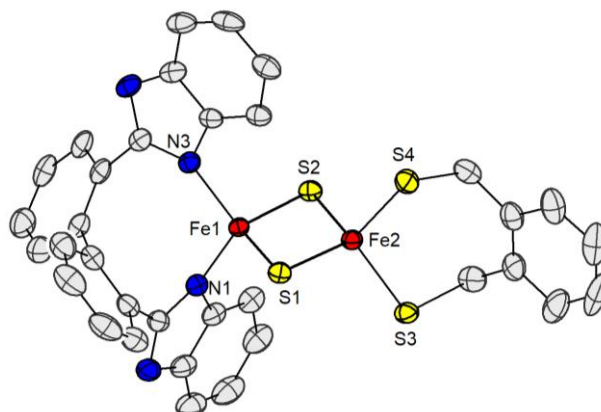


Figure 3.3. Molecular structure of the anion of the complex (PPh₄)₂**2** (thermal displacement ellipsoids shown at 50% probability). Hydrogen atoms, counterions, and solvent molecules have been omitted for clarity.

Table 3.1. Selected bond lengths (Å) and angles (deg) of diferric clusters (NEt₄)₂**1**, (PPh₄)₂**2**, **I-24**^[44], and **I-25**^[47].

	(NEt ₄) ₂ 1	(PPh ₄) ₂ 2	I-24	I-25
Fe...Fe	2.7838(7)	2.7264(6)	2.7027(8)	2.686(1)
Fe _N -μS	2.2010(9)/2.2103(9)	2.2175(9)/	2.201(1)/	2.191(2)/
	2.2144(9)/2.1950(9)	2.1909(9)	2.221(1)	2.205(2)
Fe _S -μS	-	2.2015(10)/	2.223(1)/	2.200(2)/
		2.2188(9)	2.200(1)	2.206(1)
Fe-N	2.0110(25)/1.9995(26)	2.0141(22)/	1.953(4)/	1.988(4)/
	2.0000(25)/2.0097(25)	2.0183(22)	1.976(4)	1.984(5)
Fe-S	-	2.3094(8)/	2.297(1)/	2.44(2)/
		2.2785(9)	2.291(1)	2.22(2)
N-Fe-N	111.263(103)/	113.566(100)	94.2(2)	91.6(2)
	109.154(103)			
S-Fe-S	-	110.093(35)	108.25(5)	102.8(8)
μS-Fe _N -μS	101.665(31)/	103.850(33)	104.63(5)	104.88(6)
	101.681(31)			
μS-Fe _S -μS	-	103.466(33)	104.61(5)	104.57(6)
Fe-(μS)-Fe	78.193(29)/	76.191(26)/	75.31(5)/	75.44(6)/
	78.386(29)	76.384(27)	75.39(4)	75.03(5)

Cluster (PPh₄)₂**2** crystallizes in the triclinic space group *P*-1 with one unit cell containing one MeCN molecule. A comparison of geometric parameters of (PPh₄)₂**2** with homoleptic [N₄]-ligated synthetic [2Fe-2S] cluster (NEt₄)₂**1**, the first synthetic Rieske cluster **I-24**, and the second synthetic Rieske cluster **I-25** are shown in table 3.1. The Fe...Fe distance in 2²⁻ (2.726 Å) is shorter than in the homoleptic cluster (NEt₄)₂**1** (2.784 Å). But it is slightly longer than the first synthetic Rieske cluster **I-24** (2.703 Å) and the second synthetic Rieske cluster **I-25** (2.687 Å). And this distance is in good agreement with the value in the biological system (2.71-2.72 Å).^[47] The Fe-N bond lengths and the N-Fe-N angle in (PPh₄)₂**2** (2.014 / 2.019 Å, 113.6°) are larger

than in the first synthetic Rieske cluster **I-24** (1.953 / 1.975 Å, 94.1°) and the second synthetic Rieske cluster **I-25** (1.984 / 1.988 Å, 91.7°), which most likely result from the rather rigid conjugated system of the bidentate **L¹** capping ligand. The structural parameters of the [N]-ligated iron atoms show good agreement, not only concerning heteroleptic clusters (PPh₄)₂**2**, **I-24**, and **I-25**, but also in comparison with the homoleptic cluster (NEt₄)₂**1**. The relative orientation of two imidazole rings in the cluster (PPh₄)₂**2** shows an interplanar angle of 80°, which is similar to cluster (NEt₄)₂**1** ($\angle(\text{Im}/\text{Im}) = 75^\circ$). These angles of imidazole rings in (PPh₄)₂**2**, and (NEt₄)₂**1** are close to the perpendicular orientation of the imidazole rings of histidine residues in naturally occurring Rieske clusters. Besides, these angles are much larger than what was reported in other [2Fe-2S] clusters, like in cluster **I-25** ($\angle(\text{Im}/\text{Im}) = 39^\circ$) (Figure 3.4).

Table 3.2 summarizes the geometric parameters of diferric cluster (PPh₄)₂**2** and biological Rieske clusters. It should be noticed that proteins are in their mixed-valent state, while the model compound (PPh₄)₂**2** is diferric. The geometric parameters for both metal ions Fe_S and Fe_N are comparable to the corresponding values observed for biological Rieske clusters. The Fe_{N/S}-μS distances within the [2Fe-2S] core are shorter in the case of the model compound (PPh₄)₂**2**, which could be explained as a result of different oxidation states of the metal centers and the presence of several hydrogen bonds from the bridging sulfur atoms to the surrounding amino acid residues in biological sites. And the same argumentation applies to Fe_N-N and Fe_S-S distances, which are in good agreement with the natural systems. The N-Fe-N angle in (PPh₄)₂**2** (113.57°) is much larger than the angle in the biological Rieske clusters **RFS** (90.52°), **SOXF** (92.12°), and **RIE** (90.78°), which most likely results from a more rigid chelate system of the bidentate **L¹** capping ligand. As shown in Figure 9.2.11, the energy-minimized DFT calculation structure of cluster (PPh₄)₂**2** is in good agreement with that obtained by X-ray diffraction.

Table 3.2. Selected bond lengths (Å) and angles (deg) of diferric cluster (PPh₄)₂**2** and biological Rieske clusters. It should be noted that the latter are in the mixed-valent state, whereas (PPh₄)₂**2** is in its diferric form.

	(PPh ₄) ₂ 2	RFS ^[89]	SOXF ^[88]	RIE ^[90]
Fe··Fe	2.7264(6)	2.72	2.719	2.71
Fe _N -μS	2.2175(9)/ 2.1909(9)	2.28 / 2.31	2.258 / 2.259	2.23 / 2.25
Fe _S -μS	2.2015(10)/ 2.2188(9)	2.35 / 2.34	2.267 / 2.263	2.24 / 2.25
Fe-N	2.0141(22)/ 2.0183(22)	2.19 / 2.23	2.100 / 2.083	2.13 / 2.16
Fe-S	2.3094(8)/ 2.2785(9)	2.24 / 2.31	2.348 / 2.332	2.22 / 2.29
N-Fe-N	113.566(100)	90.52	92.12	90.78
S-Fe-S	110.093(35)	110.19	109.73	105.61
μS-Fe _N -μS	103.850(33)	109.14	106.24	105.62
μS-Fe _S -μS	103.466(33)	105.70	105.81	105.64

RFS: soluble domain of Rieske protein from spinach chloroplast *b₆f* complex;

SOXF: Rieske protein II from *S. acidocaldarius*;

RIE: soluble domain of Rieske protein from bovine mitochondrial *bc₁* complex.

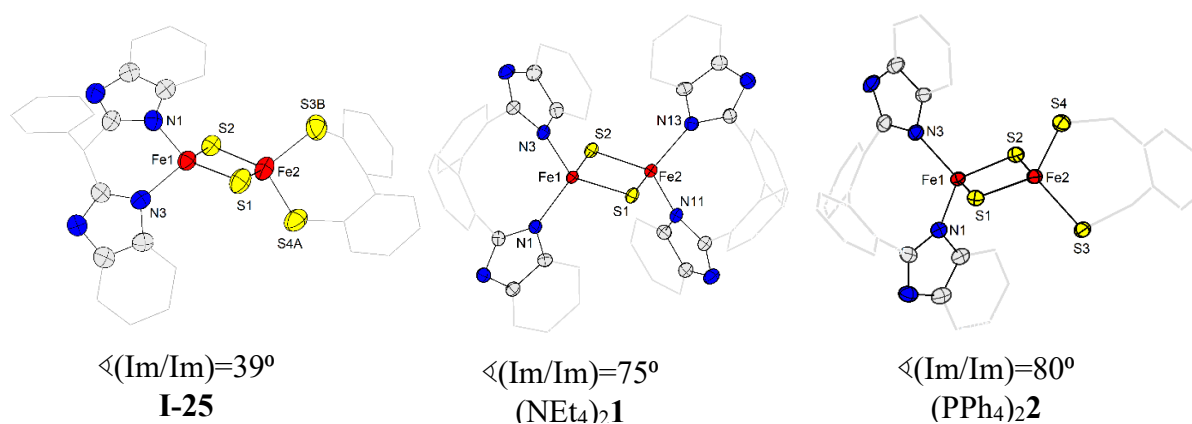


Figure 3.4. Molecular core structures of the anions of a reported Rieske-type [2Fe-2S] cluster (**I-25**), the complexes **(NEt₄)₂1**, and **(PPh₄)₂2** in the crystal (thermal displacement ellipsoids shown at 50% probability). For clarity, hydrogen atoms, counterions, and solvent molecules have been omitted.

The attempt to get the clean complex **(PPh₄)₂2** in larger quantities was not successful. After recrystallization, the dark-purple twinkling crystals (Figure 3.5) are usually a mixture of Rieske-type cluster **(PPh₄)₂2**, homoleptic [N]/[S]-coordinate [2Fe-2S] clusters or monomeric complexes (confirmed by MS measurements, Figure 3.2). Although crystallization efforts were made for different reaction stoichiometry (equivalents of added [N]-donor ligand and [S]-donor ligand were varied), different recrystallization solvents (MeCN / Et₂O, DMF / Et₂O, MeCN + DMF / Et₂O, saturated MeCN solution, and saturated DMF solution), and different reaction time (0.5 h, 1 h, 2 h, overnight), the defined and stable Rieske cluster **(PPh₄)₂2** was not obtained in satisfyingly large quantities due to the ligand scrambling. Thus, it remains unclear whether compound **(PPh₄)₂2** is accessible in reasonable yields by this synthetic route (or at least reasonable amounts). Though its existence was unambiguously demonstrated by X-ray diffraction and MS measurements.

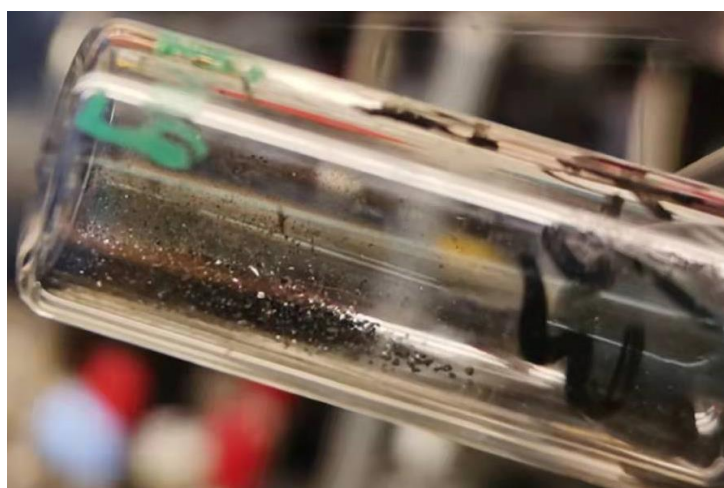


Figure 3.5. Crystal mixture after recrystallization of crude products of **(PPh₄)₂2**.

After several recrystallization steps of crude product **(PPh₄)₂2**, suitable crystals were measured again by X-ray diffraction. Two different crystals are suitable for X-ray diffraction, namely homoleptic [S]-coordinate [2Fe-2S] cluster **I-9** (Figure 3.6) and homoleptic mononuclear [N]-

coordinate $(\text{PPh}_4)_2\mathbf{10}$ (Figure 3.7). It remains unclear in this case how these two compounds form. One possibility could be that they may come from the decomposition of $(\text{PPh}_4)_2\mathbf{2}$ or, on the other hand, they may directly form as byproducts during the synthesis, since both species were already characterized by MS measurement of the crude product after synthesis of $(\text{PPh}_4)_2\mathbf{2}$.

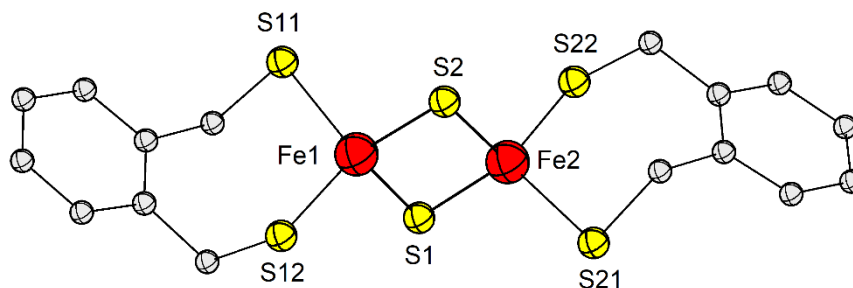


Figure 3.6. Molecular structure (50% probability thermal ellipsoids) of the homoleptic [2Fe-2S] cluster of **1-9** was determined by X-ray crystallography. All hydrogen atoms and the PPh^+ counterions have been omitted for clarity. Selected atom distances [\AA] and interatomic angles [$^\circ$]: Fe1-S11 2.290, Fe1-S12 2.292, Fe1-S1 2.226, Fe1-S2 2.186, Fe2-S22 2.297, Fe2-S21 2.291, Fe2-S1 2.194, Fe2-S2 2.228, S11-Fe1-S12 109.63, S2-Fe1-S1 105.03, S2-Fe2-S1 104.69, Fe1-S2-Fe2 75.19, Fe1-S1-Fe2 75.04, S22-Fe2-S21 107.45.

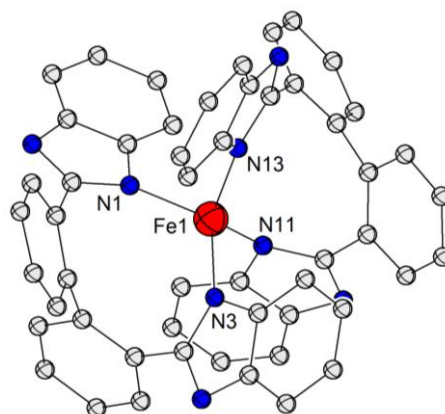
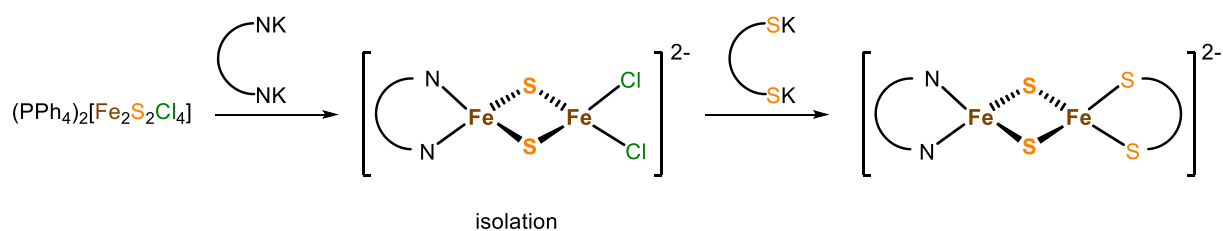
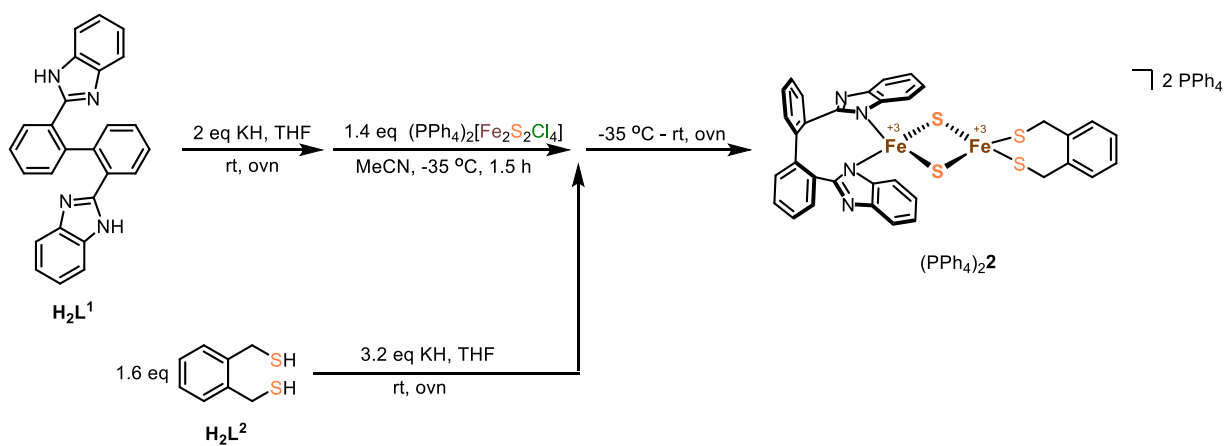


Figure 3.7. Molecular structure (50% probability thermal ellipsoids) of the complex of $\mathbf{10}^{2-}$ determined by X-ray crystallography. Hydrogen atoms, counterions, and solvent molecules have been omitted for clarity. Selected atom distances [\AA] and interatomic angles [$^\circ$]: Fe1-N1 2.058, Fe1-N3 2.066, Fe1-N11 2.059, Fe1-N13 2.046, N1-Fe1-N13 101.40, N1-Fe1-N3 122.65, N3-Fe1-N11 100.47, N11-Fe1-N13 121.04, N13-Fe1-N3 106.55, N1-Fe1-N11 106.28.

A stepwise ligand exchange strategy starting from precursor $(\text{PPh}_4)_2[\text{Fe}_2\text{S}_2\text{Cl}_4]$ with isolation of the intermediate species might be a better approach towards Rieske-type [2Fe-2S] cluster $(\text{PPh}_4)_2\mathbf{2}$, which was already used by Joachim Ballmann for the synthesis of the first Rieske [2Fe-2S] cluster **I-24**. Firstly, ligand \mathbf{L}^1 was deprotonated with KH and then added to a solution $(\text{PPh}_4)_2[\text{Fe}_2\text{S}_2\text{Cl}_4]$ in MeCN at -35°C to furnish the $[\text{N}_2]$ cap (Scheme 3.3). Then isolate and purify the first asymmetrically ligated [2Fe-2S] product $(\text{PPh}_4)_2[\text{Fe}_2\text{S}_2\mathbf{L}^1\text{Cl}_2]$ and afterward react $(\text{PPh}_4)_2[\text{Fe}_2\text{S}_2\mathbf{L}^1\text{Cl}_2]$ with the $[\text{S}_2]$ -ligand in MeCN at low temperature.

Scheme 3.3. Proposed synthetic approach for the third Rieske-type [2Fe-2S] cluster (PPh₄)₂**2**.**3.3 Conclusions**

In summary, discrete approaches toward novel Rieske-type [2Fe-2S] clusters were examined utilizing two bidentate [N]-ligands and [S]-ligands. And finally, a new Rieske-type [2Fe-2S] cluster (PPh₄)₂**2** was synthesized and characterized by X-ray crystallography. However a larger amount of pure crystals of (PPh₄)₂**2** could not be obtained yet for further characterization, though many crystallization efforts were performed, like different reaction stoichiometry, different recrystallization solvents, and different reaction times. A stepwise ligands exchange strategy with isolation of the intermediate product might be a better approach toward the Rieske-type [2Fe-2S] cluster (PPh₄)₂**2**.

Chapter 4. Synthesis of Bidentate Imidazolin-2-Imines Ligands and Their Mononuclear Iron/Nickel Complexes

4.1 Introduction

In the last two chapters, new [2Fe-2S] complexes bearing anionic ligands were synthesized. And the current understanding of [2Fe-2S] clusters in the scientific community is also focused on [2Fe-2S] complexes ligated by mostly anionic ligands because of their good donor property. However, this kind of [2Fe-2S] clusters with anionic ligands and overall 2- charge in the differic forms usually have comparatively lower reduction potentials than native [2Fe-2S] clusters (Figure 4.1).^{[11], [2]} One good attempt of getting [2Fe-2S] complexes with higher reduction potentials is to use neutral ligands with strong nucleophilicity. Imidazolin-2-imines may be the most prominent example of this kind of neutral ligands, which can both sterically and electronically provide strong electron donating ability.^[91]

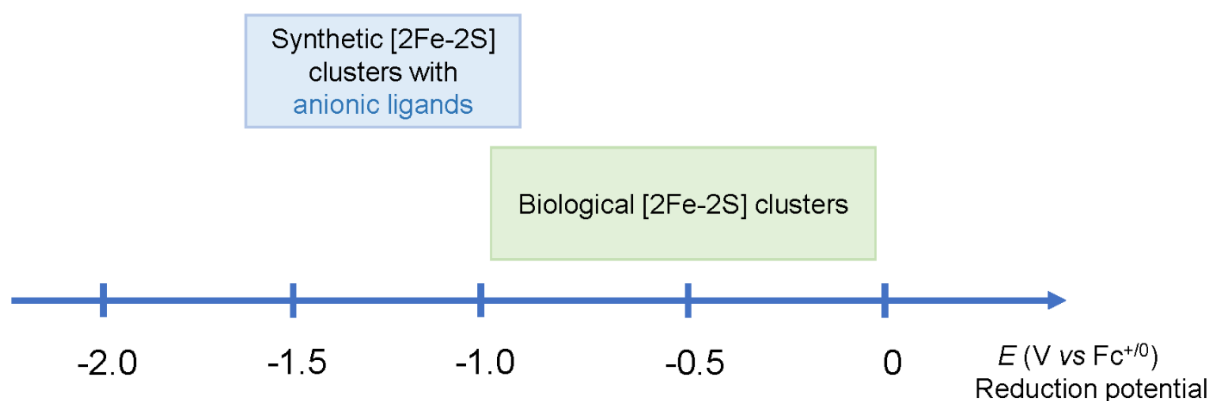
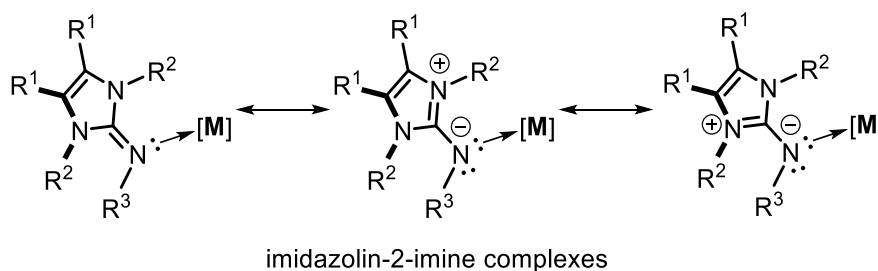


Figure 4.1. Ranges of the redox potentials of biological and synthetic [2Fe-2S] clusters.^{[11], [2]}

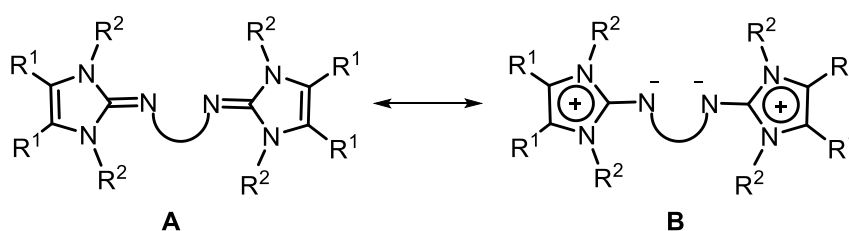
The imidazolin-2-imines can serve as precursors for the generation of anionic imidazolin-2-iminato ligands (imidazolin-2-imides). They act as imido-type ligands towards early transition metals and metals in a higher oxidation state and they were also used as ancillary ligands in a number of catalysis,^[92] especially in olefin polymerization and alkyne metathesis.^[93] Imidazolin-2-imine ligands were first developed by Kuhn et al.,^[94] and their chemistry was further extended by Tamm et al. who provided synthetic access to a great variety of such ligands through a Staudinger-type reaction between N-heterocyclic carbenes and trimethylsilyl azide.^[95] Since then, imidazolin-2-imines ligands (Scheme 4.1) have become a useful ligand class in transition metal,^{[96], [97]} main group^[98] and even Fe/S cluster chemistry^[60]. In imidazolin-2-imine ligated transition metal complexes, one lone pair of electrons on the donor N atom is used for σ bonding with the metal. The imidazolyl rings are oriented nearly perpendicularly to the remaining lone pair of electrons on N, thereby breaking down the delocalization with the imidazolyl π system and localizing the local lone pair electrons as the potential π donor for metal ligand interaction.^{[99], [100], [101]} Thus, the imidazolin-2-imine donors are best represented by their zwitterionic Lewis structure, which is expected to be a strongly binding, weak-field ligand.

Scheme 4.1. Imino and ylidic resonance structures of imidazolin-2-imines bound to transition metals.

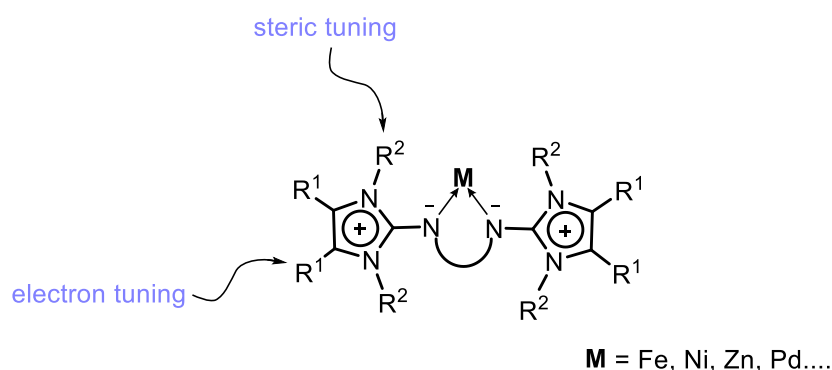


Bis(imidazolin-2-imine) ligands have been extensively applied in organometallic reactions,^[102]^[103] especially used as ancillary ligands in homogeneous catalysis.^[104] These bis(imidazolin-2-imine) ligands with a symmetric *N,N'*-substitution pattern usually form C_s - or C_{2v} -symmetric chelate complexes with four chemically equivalent nitrogen substituents (R^2 in Scheme 4.2).^[105] Because the imidazole moiety can efficiently stabilize a positive charge,^[95] these diimine species are very basic and can serve as strong N-donor ligands towards transition metals. The resulting strong polarization of the exocyclic C=N bond can be described by the two limiting resonance structures **A** and **B** for the ligands (Scheme 4.2). And the contribution of the dipolar mesomeric form increases significantly upon coordination to transition metal complex fragments.

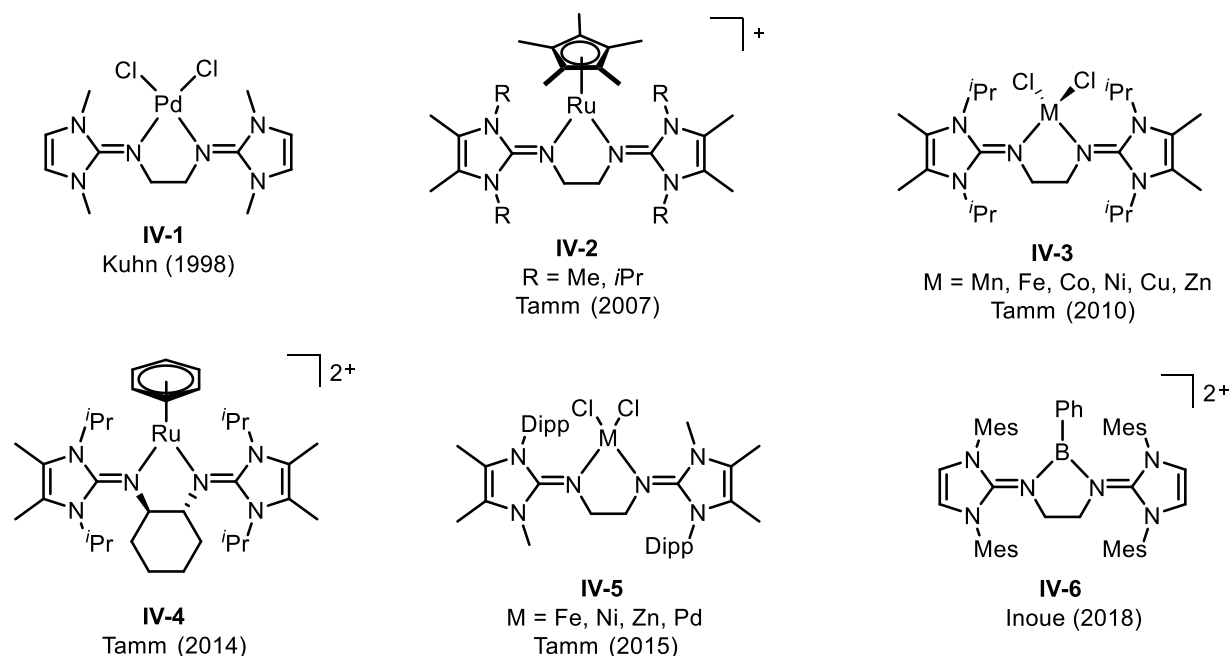
Scheme 4.2. Mesomeric structures (**A**, **B**) for bidentate bis(imidazolin-2-imine) ligands.



As a consequence of this charge separation, the imidazole rings in the resulting metal complexes usually adopt a perpendicular orientation relative to the N–M–N plane, precluding any significant π -interaction with the metal-bound nitrogen atoms. Therefore, the bis(imidazolin-2-imine) ligands are expected to be strongly binding, weak-field ligands. Moreover, the structure of bis(imidazolin-2-imine)-metal complexes reveals further ways to tune the electronic property and steric environment of the coordinated metal through simple modification of the imidazolyl ring substituents (Scheme 4.3). Thus, we anticipate that the strong σ and π donor properties of imidazolin-2-imine ligands will find further utility in Fe/S cluster chemistry that would mimic the donor properties of cysteine thiolates in proteins.

Scheme 4.3. Schematic presentation of bis(imidazolin-2-imine) metal complexes.

The first fully-characterized mononuclear transition metal complexes based on a bis(imidazolin-2-imine) ligand was reported in 1998 by Kuhn et al.,^[106] which is a diamagnetic, square-planar Pd(II) complex (Scheme 4.4). Later, Tamm showed the reactions of the bis(imidazolin-2-imine) ligands with tetrameric $[\text{Cp}^*\text{RuCl}]_4$ can afford cationic 16-electron Ru(II) complexes with a two-legged piano stool geometry.^[99] The same group also reported a series of first row transition metal (from Mn to Zn) dichloride complexes with the diimine ligand *N,N'*-bis(1,3-diisopropyl-4,5-dimethylimidazolin-2-ylidene)-1,2-ethanediamine^[107]. Except for the zinc species, all complexes are paramagnetic.

Scheme 4.4. Representative mononuclear bis(imidazolin-2-imine) transition metal and main group complexes.

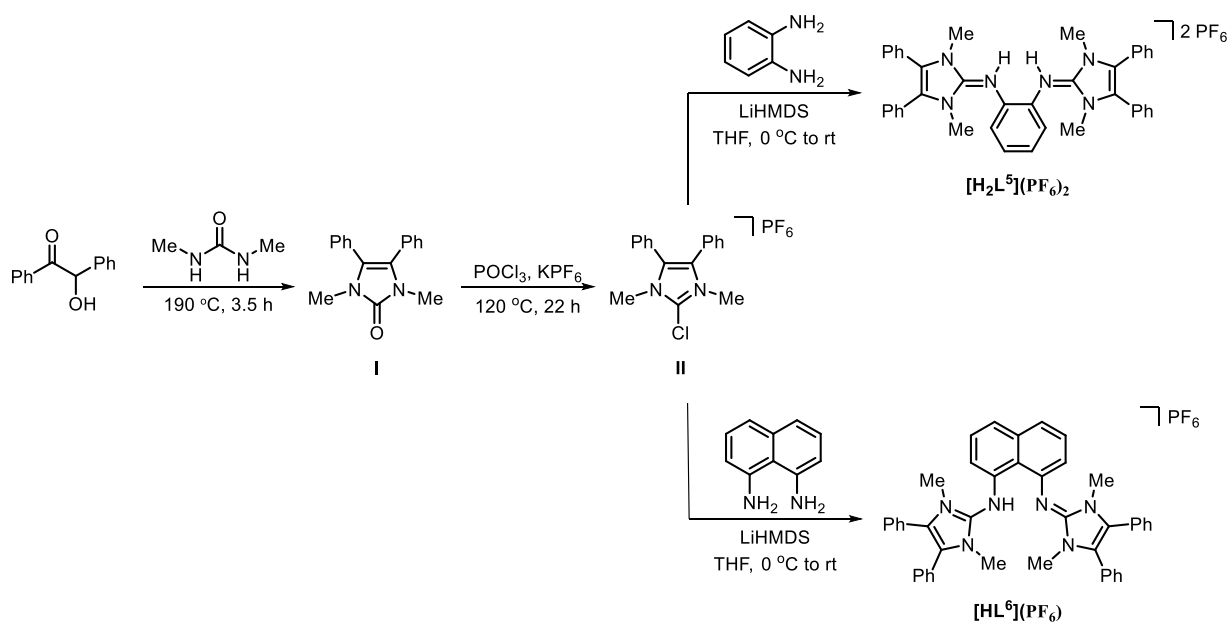
In 2015, the Tamm group introduced unsymmetrical imidazolin-2-ylidene moieties with nitrogen substituents of distinctly different size, that are able to form chiral C_2 -symmetric complexes by adopting a conformationally stable anti-orientation of the two different substituents.^[108] The tetrahedral iron, nickel, and zinc complexes exhibit, as expected, a C_2 -symmetric conformation in the solid state. In 2018, the Inoue group exploited the bulky bis(imidazolin-2-imine) ligand to stabilize the elusive electron-deficient and low-coordinate boron dication species, due to its

enhanced electron-donor properties of the bulky bis(imidazolin-2-imine) ligand.^[109] Thus, N-donor ligands derived from imidazolin-2-imines have become a widely used subclass of guanidine-type ligands. The neutral monodentate imines can be linked to each other to afford bidentate and potentially chelating ligands that display rich coordination chemistry and the ability to bind almost any transition metal in a somewhat higher oxidation state, and even main group elements.

4.2 Ligand Synthesis

With a minor modification of the established synthetic route for imidazolin-2-imines,^[60] the new bidentate imidazolin-2-imine ligand $[\mathbf{H}_2\mathbf{L}^5](\text{PF}_6)_2$ presented in this work was prepared as shown in Scheme 4.5. First, dehydrative condensation of 2-hydroxy-1,2-diphenylethan-1-one with 3 equivalents of 1,3-dimethylurea at 190 °C using ethylene glycol as the solvent afforded 1,3-dihydroimidazol-2-one. Subsequent deoxychlorination of 1,3-dihydroimidazol-2-one with excess POCl_3 at 120 °C and anion exchange with KPF_6 provided 2-chloroimidazolium hexafluorophosphate in 67% overall yield after recrystallization from acetone-isopropanol. *O*-Phenylenediamine was then condensed with 2 equivalents of 2-chloroimidazolium hexafluorophosphate in the presence of LiHMDS in THF at low temperature (0 °C). Quenching of the reaction mixture with aqueous HPF_6 furnishes bisimidazolium salt $[\mathbf{H}_2\mathbf{L}^5](\text{PF}_6)_2$ in 89% yield. Slow evaporation of a DCM solution including $[\mathbf{H}_2\mathbf{L}^5](\text{PF}_6)_2$ at room temperature led to the growing of yellowish crystals (Figure 4.2).

Scheme 4.5. Synthetic approaches to the bidentate imidazolin-2-imine ligands, $[\mathbf{H}_2\mathbf{L}^5](\text{PF}_6)_2$ and $[\mathbf{HL}^6](\text{PF}_6)$.



The second bidentate imidazolin-2-imine ligand $[\mathbf{HL}^6](\text{PF}_6)$ was synthesized by a similar method, where 1,8-naphthalenediamine was used as the condensation partner instead. Bisimidazolium salt $[\mathbf{HL}^6](\text{PF}_6)$ was obtained in 52% yield. Diffusion of *n*-pentane into a saturated THF solution of $[\mathbf{HL}^6](\text{PF}_6)$ at room temperature afforded single crystals of the neutral \mathbf{L}^6 (Figure 4.3); HPF_6 got lost during the crystallization of $[\mathbf{HL}^6](\text{PF}_6)$.

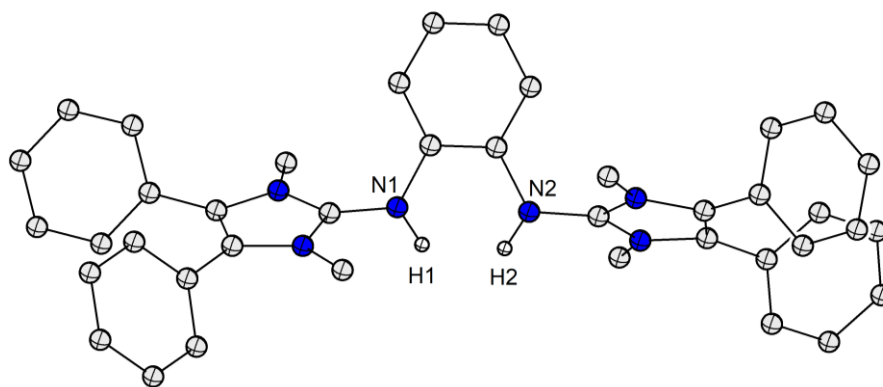


Figure 4.2. Molecular structure of the cation of the bisimidazolium salt $[\text{H}_2\text{L}^5](\text{PF}_6)_2$ in the crystal (thermal displacement ellipsoids shown at 50% probability). Hydrogen atoms, counterions and solvent molecules have been omitted for clarity. Selected atom distances [Å] and interatomic angles [°]: C7-N1 1.361, C7-N3 1.338, C7-N4 1.341, C24-N2 1.367, C24-N5 1.337, C24-N6 1.342, N1-H1 0.880, N2-H2 0.880.

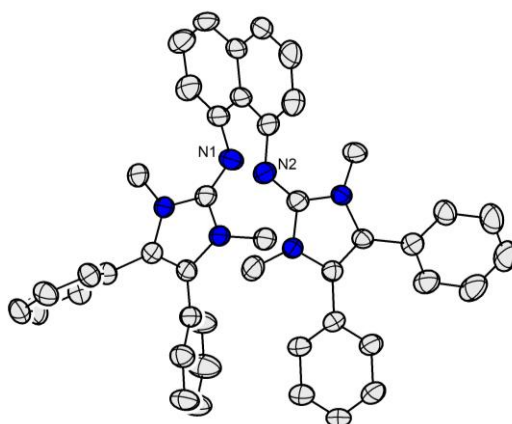


Figure 4.3. Molecular structure of the neutral L^6 in the crystal (thermal displacement ellipsoids shown at 50% probability). Hydrogen atoms, and solvent molecules have been omitted for clarity. Selected atom distances [Å] and interatomic angles [°]: C11-N1 1.283, C11-N3 1.385, C11-N4 1.375, C28-N2 1.284, C28-N5 1.379, C28-N6 1.378.

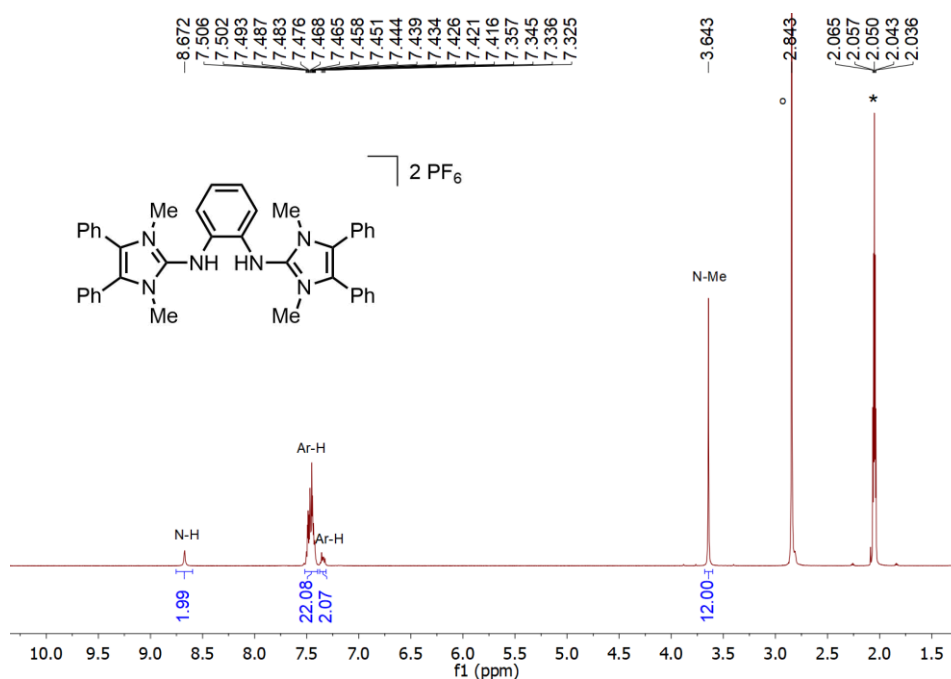


Figure 4.4. ^1H NMR spectrum of $[\text{H}_2\text{L}^5](\text{PF}_6)_2$ recorded in acetone- d_6 (300.1 MHz, 298 K). Signals of the acetone- d_6 (*) and the residual H_2O (o) have been labeled.

The ^1H -NMR spectrum of $[\text{H}_2\text{L}^5](\text{PF}_6)_2$ was measured in acetone- d_6 at room temperature (Figure 4.4). In this spectrum, based on integration, the broad singlet at $\delta = 8.67$ ppm can be attributed to the protons on the nitrogen atoms due to their relatively strong basicity driven by the aromatization of the imidazole rings. The singlet at $\delta = 3.64$ ppm can be assigned to the methyl group bound directly to the nitrogen atoms of the imidazolium rings, which each bears a pair of symmetric methyl group. The remaining multiple peaks between 7.33 ppm and 7.57 ppm should be associated with aryl groups with similar chemical shift.

The ^1H -NMR spectrum of $[\text{HL}^6](\text{PF}_6)$ was measured in CDCl_3 at room temperature (Figure 4.5). Unlike $[\text{H}_2\text{L}^5](\text{PF}_6)_2$, $[\text{HL}^6](\text{PF}_6)$ was isolated in the form of mono-salt with HPF_6 . Due to its strong intramolecular hydrogen-bonding ($\text{N}\cdots\text{H}-\text{N}$), the stable six-membered ring disfavors a second protonation by HPF_6 . The bridged-proton is observed at low field of $\delta = 15.18$ ppm as a broad singlet, which is in consistent with the common intramolecular hydrogen-bonding. The singlet at $\delta = 3.44$ ppm can be assigned to the chemically equivalent methyl group attached to the nitrogen atoms of the imidazole ring. Three resonances at $\delta = 7.28$ (t, $J_{\text{HH}} = 8.0$ Hz, 2H, naph-3,3'-H), 7.20 (d, $J_{\text{HH}} = 8.4$ Hz, 2H, naph-4,4'-H) and 6.40 (d, $J_{\text{HH}} = 7.6$ Hz, 2H, naph-2,2'-H) ppm revealing a characteristic ABC system are assigned to naphthalene protons (Figure 4.5). The remaining multiple peaks between 7.40 ppm and 7.32 ppm should be those for the ^1H nuclei on the phenyl groups directly bound to the imidazole ring.

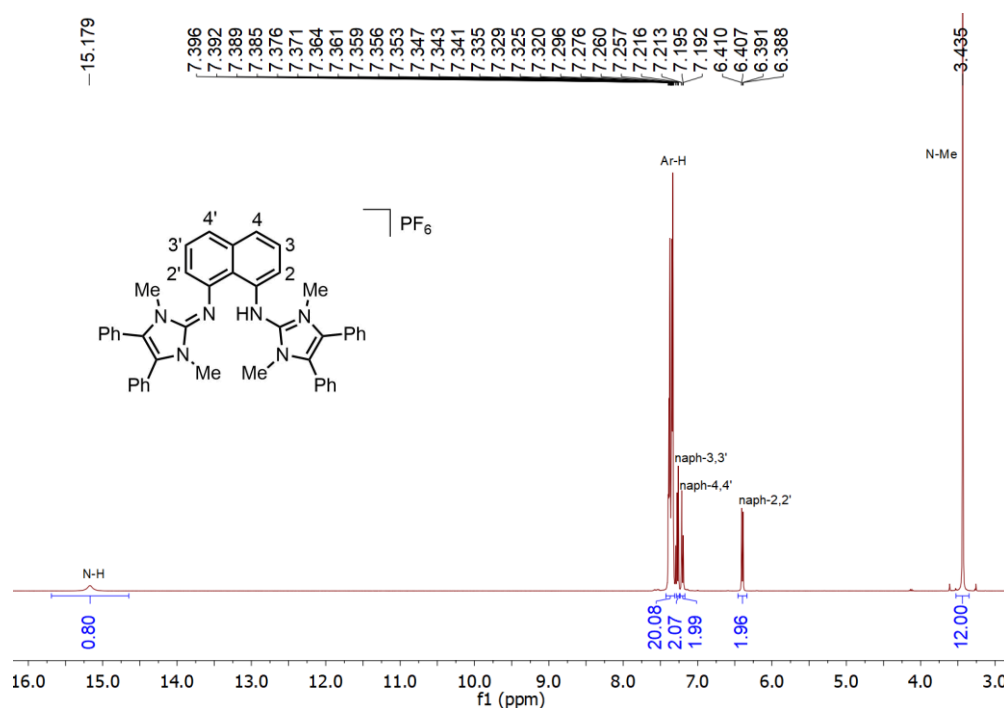


Figure 4.5. ¹H NMR spectrum of [HL⁶](PF₆) recorded in CDCl₃ (400.3 MHz, 298 K).

4.3 Complex Synthesis and Structural Characterization

Bis(imidazolin-2-imine)-ligated complexes **FeL⁵Cl₂**, **NiL⁵Br₂**, and **NiL⁶Br₂** were prepared by the reaction of the bis(imidazolin-2-imine) ligand **L⁵** and **L⁶** with Fe(II) or Ni(II) salts. First, direct deprotonation of the above bis(imidazolin-2-imine) ligand precursors [**H₂L⁵**](PF₆)₂ and [**HL⁶**](PF₆) was achieved in THF by using potassium hydride as a base at room temperature in the glovebox. The resulting free bis(imidazolin-2-imine) ligands **L⁵** and **L⁶** were in situ trapped by [FeCl₂·THF] or [NiCl₂·DME] (DME = 1,2-dimethoxyethane) to produce bis(imidazolin-2-imine)-ligated transition metal complexes **FeL⁵Cl₂** (**3**), **NiL⁵Br₂** (**4**), and **NiL⁶Br₂** (**5**). Water has to be strictly excluded to avoid protonation of the ligands (since both ligands **L⁵** and **L⁶** are structurally similar to a “proton sponge”). The composition of all three complexes was confirmed by elemental analysis and mass spectrometry. Complex **3** was purified by diffusion of *n*-pentane into its saturated THF solution, and was collected as crystalline solid in 73% yield. The structure of **3** was confirmed by single-crystal X-ray diffraction analysis (vide infra). The complexes **4** and **5** were crystallized for X-ray diffraction by diffusion of Et₂O into a THF solution of the complexes in 42% and 53% yield, respectively. All complexes incorporate solvents upon crystallization (**3**·3THF, **4**·THF, and **5**·2THF), and molecular structures of complexes [LMX₂] (L = **L⁵**, M = Fe, X = Cl for **3**; L = **L⁵**, M = Ni, X = Br for **4**; L = **L⁶**, M = Ni, X = Br for **5**) are shown in Figure 4.6, Figure 4.7, and Figure 4.8 respectively. Pertinent structural data of complexes **3** and **4** are assembled in table 4.1 and for complex **5** in table 4.2.

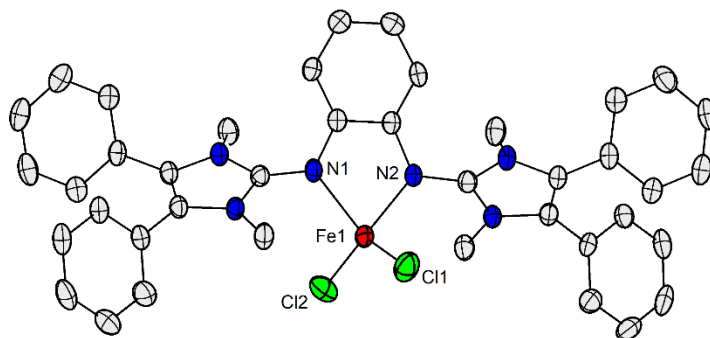


Figure 4.6. Molecular structure of complex **3** in the crystal (thermal displacement ellipsoids shown at 50% probability). Hydrogen atoms, and solvent molecules have been omitted for clarity.

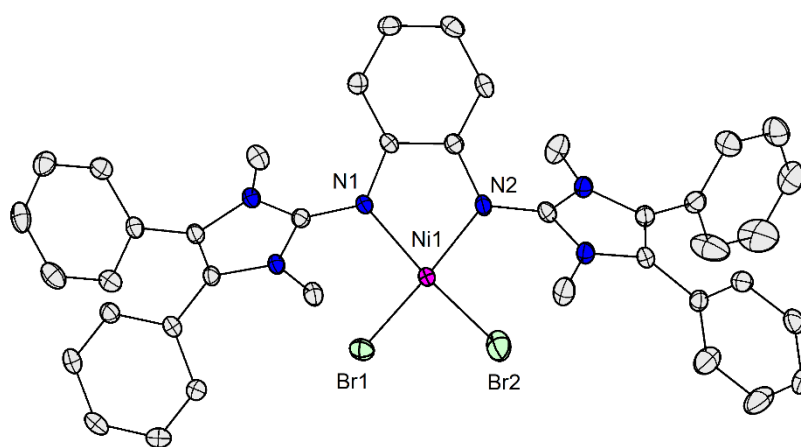


Figure 4.7. Molecular structure of complex **4** in the crystal (thermal displacement ellipsoids shown at 50% probability). Hydrogen atoms and solvent molecules have been omitted for clarity.

The lengths of metal-chlorine, metal-bromine, and metal-nitrogen bonds are similar to those established for the corresponding bis(imidazolin-2-imine)-ligated iron and nickel analogues $[\text{Fe}(\text{BL}^{i\text{Pr}})\text{Cl}_2]^{[107]}$, $[\text{Ni}(\text{btmgb})\text{Br}_2]^{[110]}$, and $[\text{Ni}(\text{btmgn})\text{Br}_2]^{[110]}$. Complexes **3** and **4** crystallize both in the monoclinic space group $P2_1$ in combination with three THF in **3**, and $P2_1/c$ with one THF in **4**. Complex **5** crystallizes in the orthorhombic space group $P2_12_12$ with two molecules in the unit cell. All three complexes display crystallographic C_2 -symmetry about an axis passing through the metal atom and the center of the carbon-carbon bond which is on the phenylene or naphthylene group bound directly to the nitrogen atoms. In complexes **3** and **4**, the metal atoms are four-coordinate and display distorted tetrahedral arrangements, constituting a five-membered chelate ring with N1-M-N2 bite angles of around $80.04\text{--}82.36^\circ$, which are in good agreement with the structural parameters found for analogues $[\text{M}(\text{BL}^{i\text{Pr}})\text{Cl}_2]$ ($\text{BL}^{i\text{Pr}} = \text{N,N}'\text{-bis}(1,3\text{-diisopropyl-4,5-dimethylimidazolin-2-ylidene)-1,2\text{-ethanediamine}$; $\text{M} = \text{Mn, Fe, Co, Ni, Cu, Zn}$), $81.29\text{--}84.40^\circ$,^[107] and are significantly smaller than expected for the ideal tetrahedral arrangement (109.5°). Accordingly, an expanded X-M-X ($\text{M} = \text{Fe}$, $\text{X} = \text{Cl}$; $\text{M} = \text{Ni}$, $\text{X} = \text{Br}$) angle of 125.94° for **3** is observed (Table 4.1); in the nickel complex **4**, however, a relatively small Br1-Ni1-Br2 angle of 104.39° is found (Table 4.1), which is in good agreement with **4** being more strongly distorted toward a square-planar coordination. In complex **5**, the N1-M1-N1' bite angle (Table 4.2) is 95.30° , and Br1-Ni1-Br1' is 116.93° , comparable to the analogue $[\text{Ni}(\text{btmgn})\text{Br}_2]$:

N1-Ni-N4 90.13° and Br1-Ni-Br2 122.85° .^[110] Since the molecular structures of the three complexes (**3**, **4**, **5**) all display C_2 -symmetry, the degree of distortion from an ideal tetrahedron toward a square can be named as a dihedral angle between the N1-M-N2 (or N1') and X-M-X planes, which can adopt angles between 0° (square) and 90° (tetrahedron). In all cases (Table 4.1 and 4.2), these angles significantly deviate from 90° and follow the order **3** (81.22°) > **5** (74.82°) > **4** (61.64°).

Table 4.1. Selected bond lengths (Å) and angles (deg) of complexes **3** and **4**.

	3	4
M-N1	2.0692(23)	1.9957(23)
M-N2	2.0496(20)	1.9710(16)
M-Cl1/Br1	2.2774(10)	2.3744(4)
M-Cl2/Br2	2.2562(11)	2.3918(4)
C7-N1	1.3311(33)	1.337(3)
C7-N3	1.3581(34)	1.3585(23)
C7-N4	1.3640(34)	1.3590(28)
C24-N2	1.3393(33)	1.3389(32)
C24-N5	1.3587(34)	1.3477(40)
C24-N6	1.3491(34)	1.3581(30)
N1-M-N2	80.043(82)	82.363(79)
N1-M-Cl1/Br1	115.077(65)	100.854(54)
N1-M-Cl2/Br2	105.607(67)	140.110(54)
N2-M-Cl1/Br1	104.590(65)	130.562(56)
N2-M-Cl2/Br2	116.563(67)	103.178(57)
Cl1/Br1-Fe1-Cl2/Br2	125.937(39)	104.387(15)
Angle between MN_2 and MX_2 planes	81.22	61.64

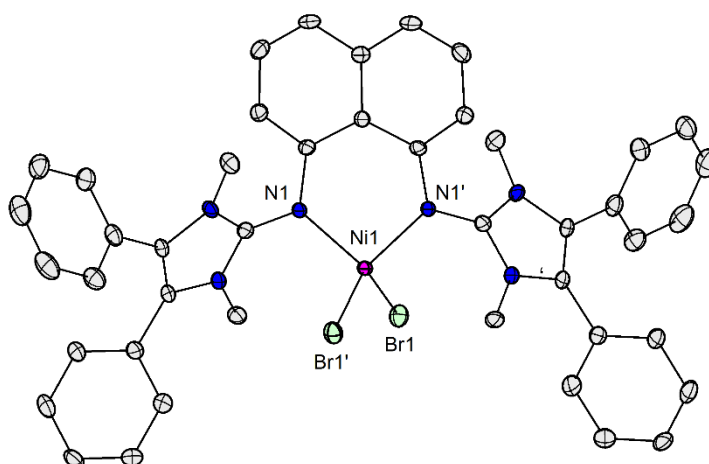


Figure 4.8. Molecular structure of complex **5** in the crystal (thermal displacement ellipsoids shown at 50% probability). Hydrogen atoms, and solvent molecules have been omitted for clarity.

Table 4.2. Selected bond lengths (Å) and angles (deg) of complex **5**.

	5
Ni-N1	1.9557(29)
Ni-Br1	2.4031(4)
C7-N1	1.3467(39)
C7-N2	1.3493(43)
C7-N3	1.3626(39)
N1-Ni-N1'	95.297(117)
N1-Ni-Br1	100.802(83)
N1-Ni-Br1'	121.148(82)
Br1-Ni1-Br2	116.933(9)
Angle between MN ₂ and MX ₂ planes	74.82

4.4 Characterization in Solution

The three complexes, namely **3**, **4**, **5**, were characterized by ¹H NMR spectroscopy in solution. The ¹H NMR spectrum of complex **3** (Figure 4.9) in THF-d₈ shows paramagnetically shifted resonances, the most dramatically affected being those for the ¹H nuclei on the phenylene group directly bound to the N donor (shifted from $\delta = 7.33$ – 7.51 to $\delta = 17.53$ and 8.66) and N-Me (shifted from $\delta = 3.64$ to $\delta = 16.19$), which were identified by two-dimensional NMR spectra (see Chapter 9).

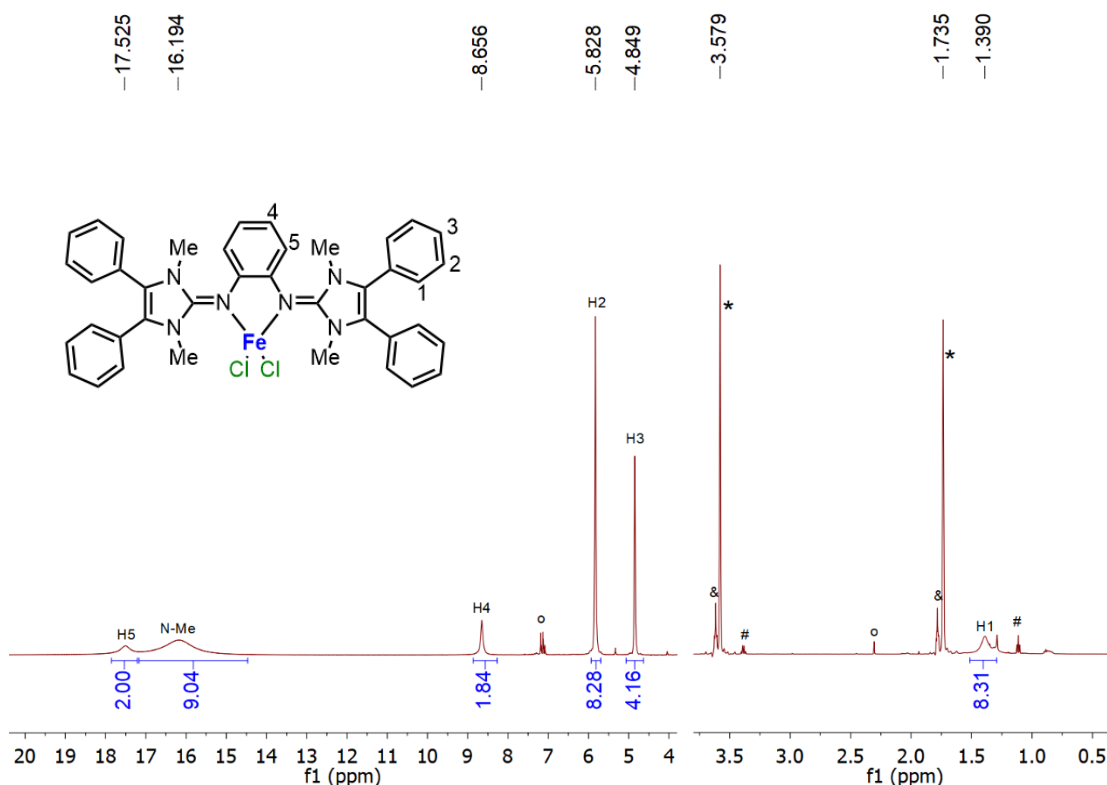


Figure 4.9. ¹H NMR spectrum of complex **3** recorded in THF-d₈ (600.3 MHz, 298 K). Signals of the THF-d₈ (*) and residual toluene (°), THF (&), Et₂O (#) have been marked.

Three broad singlets at $\delta = 5.83$, 4.85 and 1.39 ppm are assigned to the ^1H nuclei on the phenyl group directly bound to the imidazole ring. At room temperature, **3** displays C_{2v} symmetry on the NMR time scale (400 MHz).

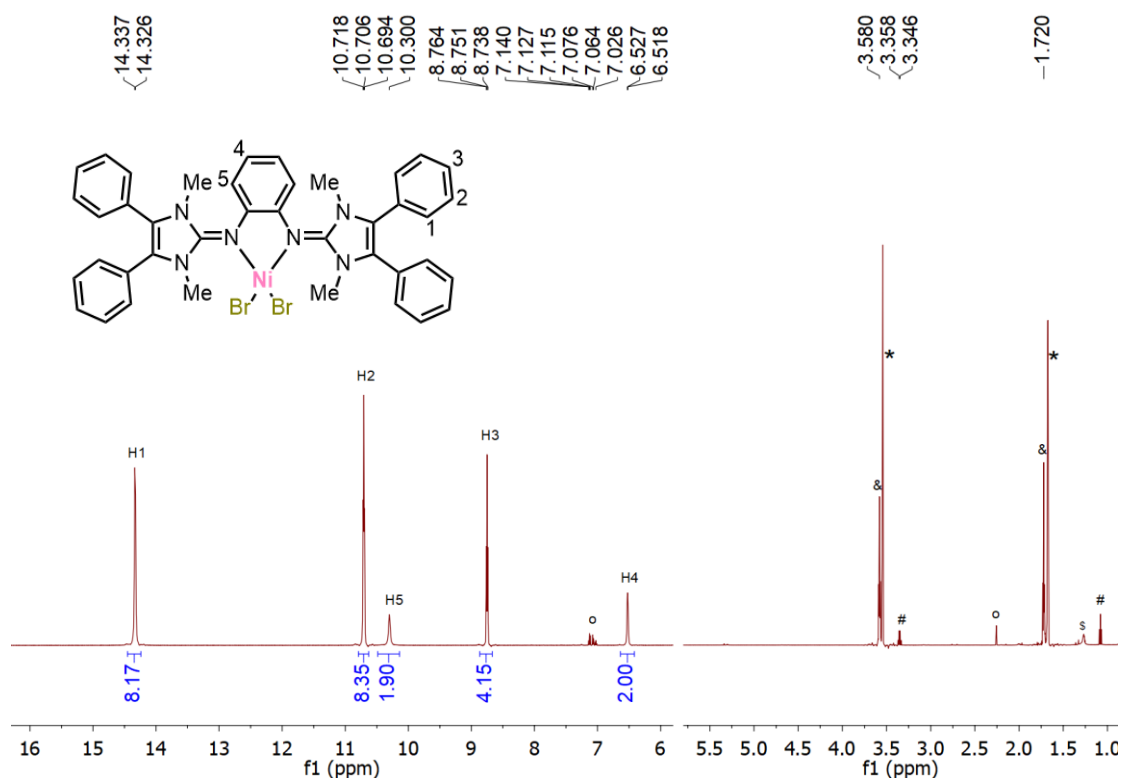


Figure 4.10. ^1H NMR spectrum of complex **4** recorded in THF- d_8 (600.3 MHz, 333 K). Signals of the THF- d_8 (*), residual toluene ($^\circ$), THF (&), Et $_2$ O (#) and unknown impurities (\$) have been marked.

The ^1H -NMR spectrum of complex **4** was measured in THF- d_8 at room temperature (Figure 4.10). Based on the analysis of ^1H NMR and by two-dimensional NMR spectra (Figure 9.2.17), the three resonances at $\delta = 14.33$ (d, $J_{\text{HH}} = 6.6$ Hz, 8H, 1-H), $\delta = 10.71$ (t, $J_{\text{HH}} = 7.2$ Hz, 8H, 2-H) and $\delta = 8.75$ (t, $J_{\text{HH}} = 7.8$ Hz, 4H, 3-H) can be attributed to the protons on the phenyl group directly bound to the imidazole ring. While the two broad singlets at $\delta = 10.30$ and 6.52 ppm can be assigned to the ^1H nuclei on the phenylene group directly bound to the N donor. The signal for N-Me could not be detected, which might be the result of enhanced paramagnetic relaxation because of close proximity to the Ni ion.

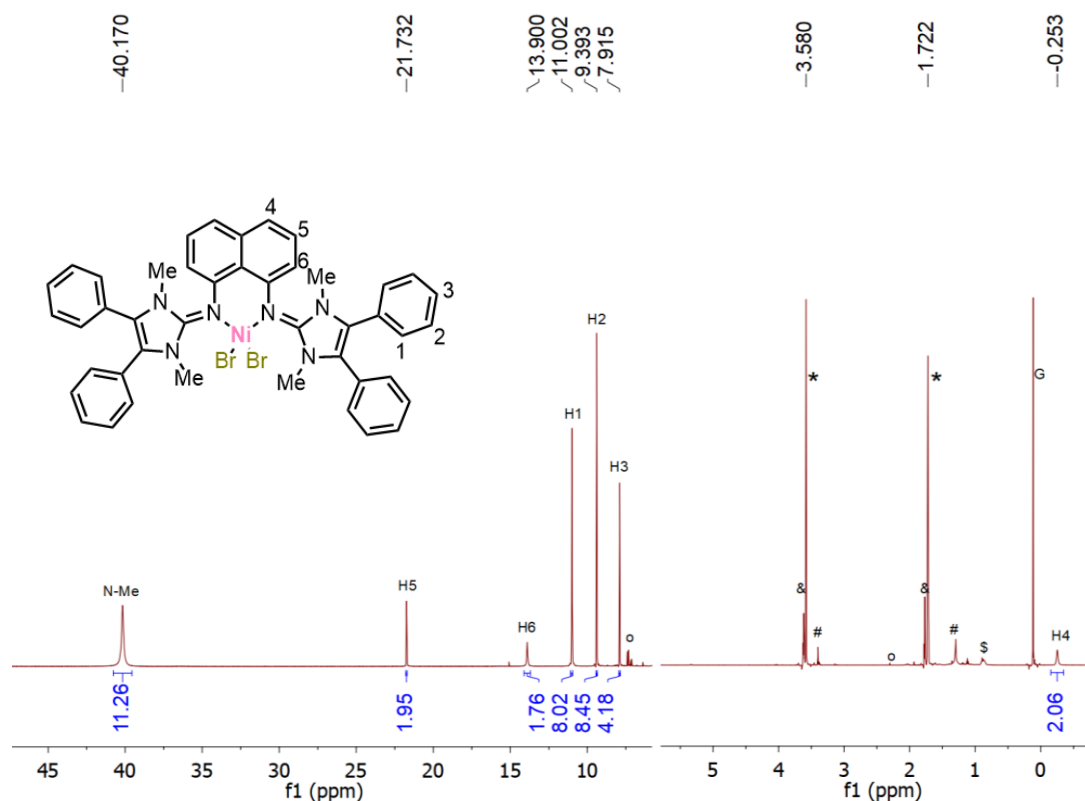


Figure 4.11. ^1H NMR spectrum of **5** recorded in THF-d_8 (600.3 MHz, 298 K). Signals of the THF-d_8 (*), residual toluene ($^\circ$), THF (&), diethyl ether (#), and silicone grease (G) and unknown impurities ($^\$$) have been marked.

The ^1H -NMR spectrum of complex **5** was also collected in THF-d_8 at room temperature (Figure 4.11). The broad singlet at $\delta = 40.17$ ppm can be assigned to the chemically equivalent methyl groups attached to the nitrogen atoms of the imidazole rings. According to ^1H NMR and two-dimensional NMR spectra of **5** (see chapter 9), three broad resonances at $\delta = 11.00$ (s_{br}), 9.39 (s_{br}) and 7.92 (s_{br}) ppm are assigned to the ^1H nuclei on the phenyl group directly bound to the imidazole rings. While the singlets at 21.73 ppm, 13.90 ppm and -0.25 ppm can be assigned to the naphthalene protons based on the two-dimensional NMR spectra. Complexes **4** and **5** show minor different ligand-derived resonances in their room-temperature NMR spectra. Their ^1H NMR resonances (like at 14.33 and 21.73 ppm for **4** and **5**, respectively) are shifted downfield from that of the free ligand (7.45 and 7.26 ppm for **L**⁵ and **L**⁶, respectively), reflecting both the expected downfield shift upon binding a Lewis acidic metal center and the population of paramagnetic states as is commonly observed in Ni(II) complexes.

UV-vis spectroscopy of complex **3** (Figure 4.12) was measured in THF solution under N_2 atmosphere. The spectrum shows one absorbance in the high-energy range at $\lambda_{\text{max}} = 323$ nm, which is attributed to LMCT coupled with ligand to ligand charge transfer (LLCT) according to TD-DFT calculations (chapter 9). The DFT calculation reveals that the optimized structure of **3** is in good agreement with the experimental one (Figure 9.2.12).

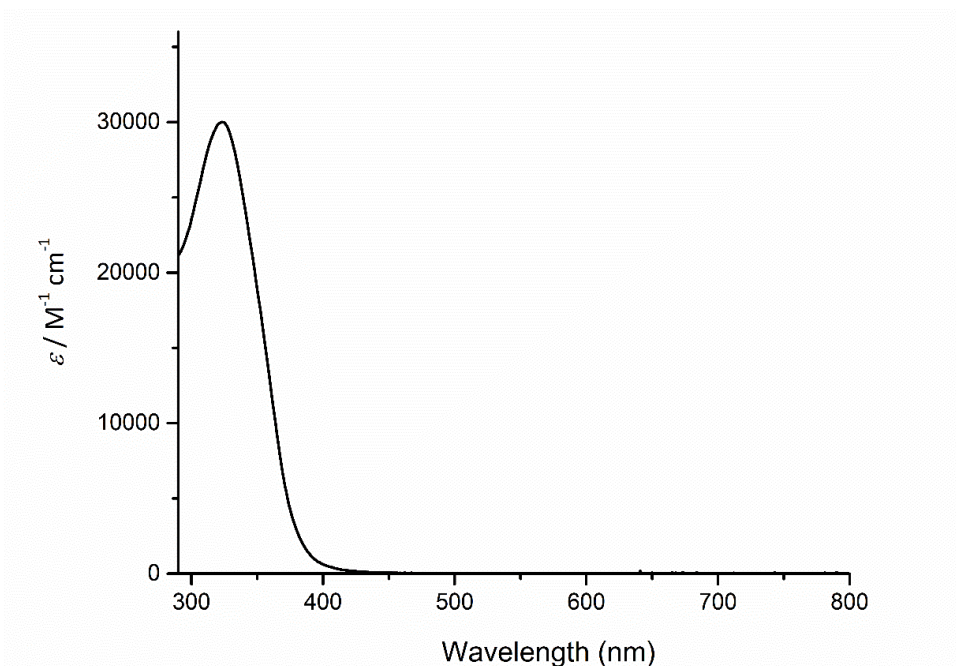


Figure 4.12. UV-vis absorption spectrum of **3** in THF solution at rt.

UV-vis spectroscopy of complex **4** (Figure 4.13) was measured in THF solution under N₂ atmosphere at rt. The intense band in the high-energy range at $\lambda_{\text{max}} = 324$ nm of complex **4** is quite similar to the high-energy band (323 nm) of complex **3** in THF solution measured at rt, and is signed to LLCT transitions according to TD-DFT calculations. The peak at 483 nm is attributed to LMCT and the absorbance features at $\lambda_{\text{max}} = 543$ nm, 607 nm, and 750 nm are assigned to LMCT transitions according to the TD-DFT calculation. The DFT calculations reveal that the optimized structure of **4** is in good agreement with the experimental one (Figure 9.2.16).

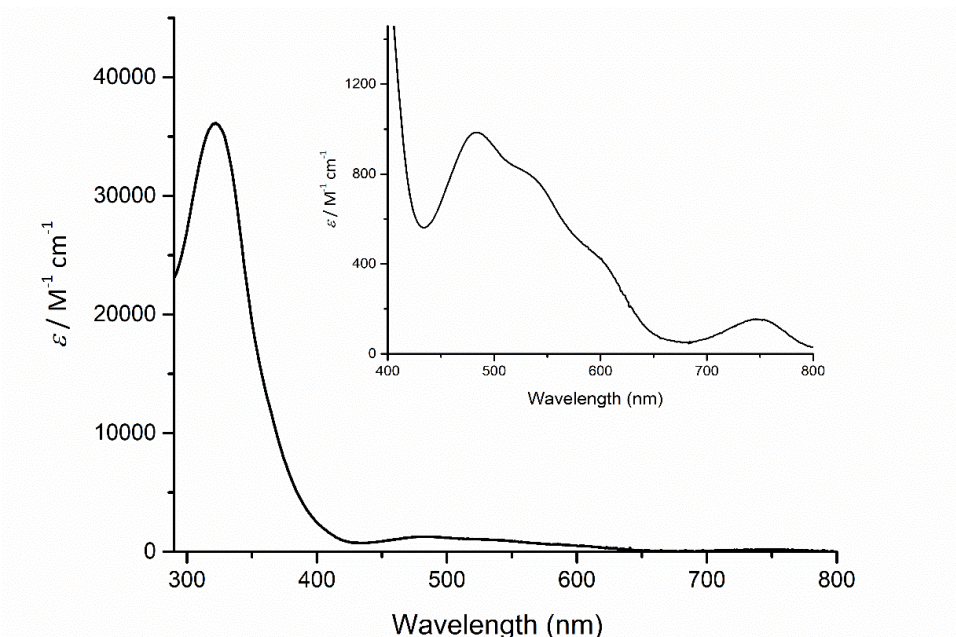


Figure 4.13. UV-vis absorption spectrum of **4** in THF solution at rt.

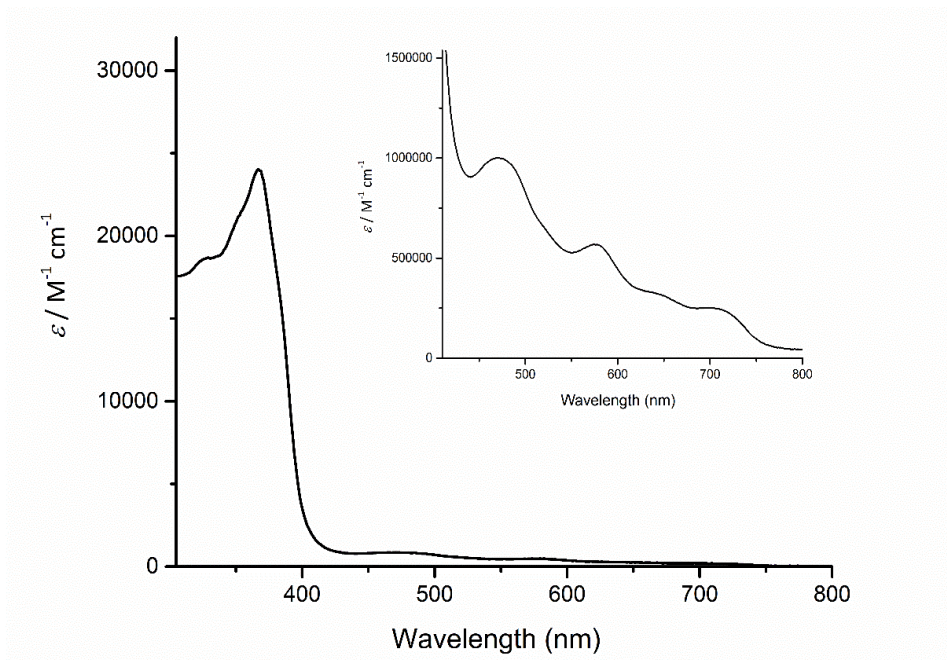


Figure 4.14. UV-vis absorption spectrum of **5** in THF solution at rt.

The UV-vis spectrum of the complex **5** (Figure 4.14) was measured in THF solution under N₂ atmosphere at room temperature. Similar to complexes **3** (323 nm) and **4** (324 nm), complex **5** also has a band in the high-energy range at 328 nm, which may also be signed to LLCT, but the absorbance of this band (328 nm, 18620 M⁻¹ cm⁻¹), is lower compared to complexes **3** (323 nm, 30000 M⁻¹ cm⁻¹), and **4** (324 nm, 36000 M⁻¹ cm⁻¹). The intense band at 367 nm is attributed to MLCT according to a TD-DFT calculation. And the bands at $\lambda_{\text{max}} = 472$ nm, 576 nm, 644 nm, 712 nm are assigned to ligand (including Br) to metal charge transfer transition (LMCT) according to the TD-DFT calculation. The DFT calculation reveals that the optimized structure of **5** is in good agreement with the experimental one (Figure 9.2.18).

4.5 Characterization in the Solid State

The zero-field ⁵⁷Fe Mössbauer spectrum in solid state of complex **3** was recorded at 80 K and is shown in Figure 4.15. The Mössbauer spectrum of **3** shows a single quadrupole doublet with isomer shift $\delta = 0.90$ mm s⁻¹ and quadrupole splitting $\Delta E_Q = 3.10$, which is typical for high-spin ferrous ions.^[111]

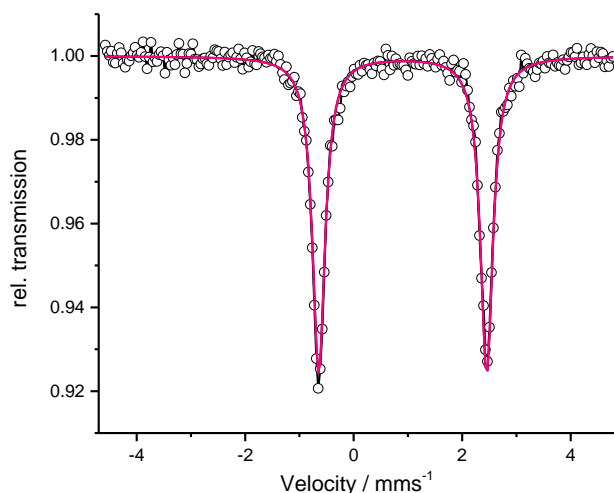


Figure 4.15. Zero-field ^{57}Fe Mössbauer spectrum of solid **3** recorded at 80 K. Simulation of the data gave the following parameters: $\delta = 0.90 \text{ mm s}^{-1}$ and $\Delta E_{\text{Q}} = 3.10 \text{ mm s}^{-1}$.

The direct current (dc) magnetic measurements for the mononuclear Fe(II) complex **3** and Ni(II) complexes **4** and **5** were carried out in the range of 2–210 K (Figure 4.16) under 0.5 T applied field. The samples were covered with low viscosity perfluoropolyether-based inert oil Fomblin Y45 to prevent any torquing and packed in a polycarbonate capsule. At 210 K, the room temperature $\chi_{\text{M}}T$ value of $3.47 \text{ cm}^3 \text{ K mol}^{-1}$ for **3** is slightly higher than the calculated spin-only value ($3.0 \text{ cm}^3 \text{ K mol}^{-1}$) of one isolated high-spin Fe(II) ion ($S = 2.0$, $g = 2.0$) indicating a small orbital contribution to the magnetic moment (Figure 4.16). The $\chi_{\text{M}}T$ value remains almost constant until 20 K before sharply falling to $1.68 \text{ cm}^3 \text{ K mol}^{-1}$. The experimental data was modelled using the *julX* program. The best fit parameters are $g = 2.16$ and $D = 5.7 \text{ cm}^{-1}$, with a Weiss temperature $\theta = -0.58 \text{ K}$ and $TIP = 13 \cdot 10^{-6} \text{ cm}^3 \text{ mol}^{-1}$ (subtracted).

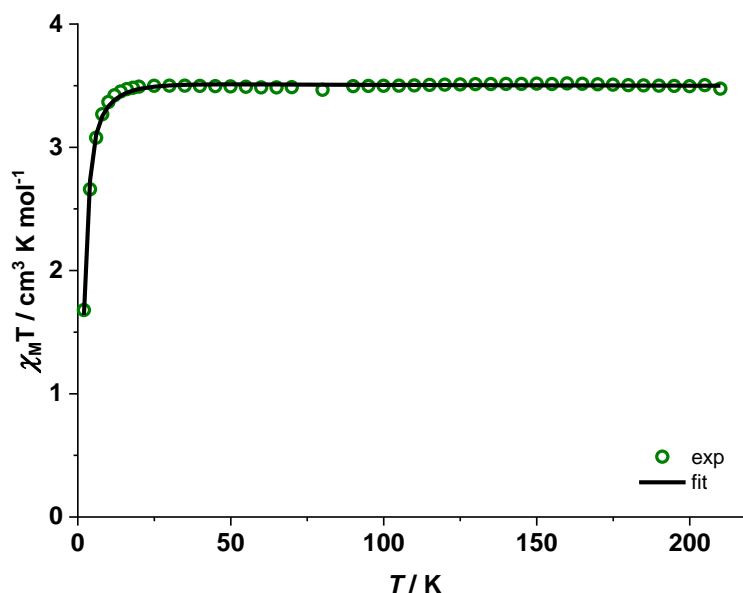


Figure 4.16. Temperature dependence of $\chi_{\text{M}}T$ for complex **3** at a applied field of 0.5 T. The solid black line represents a spin-Hamiltonian simulation. Best fit parameters for **3**: $g = 2.16$, $D = 5.7 \text{ cm}^{-1}$, Weiss temperature $\theta = -0.58 \text{ K}$ and $TIP = 13 \cdot 10^{-6} \text{ cm}^3 \text{ mol}^{-1}$ (subtracted).

The $\chi_{\text{M}}T$ value of $1.69 \text{ cm}^3 \text{ K mol}^{-1}$ for **4** at 210 K is much higher than the expected value (1.0

$\text{cm}^3 \text{K mol}^{-1}$) for an isolated non-interacting Ni(II) ion ($S = 1$ and $g = 2.0$). The $\chi_{\text{M}}T$ value only slightly decreases on cooling until 100 K before showing a gradual and then sharp fall to $0.135 \text{ cm}^3 \text{K mol}^{-1}$ at 2 K (Figure 4.17 left). The magnetization for **4** at 2.0 K increases linearly until 7.0 T reaching a value of $0.71 \mu_{\text{B}}$ without any saturation (Figure 4.17 left inset). This is well below the expected M_{sat} value of $2.0 \mu_{\text{B}}$. The magnetic susceptibility data were fitted along with the variable-field variable-temperature (VTVH) magnetization data (Figure 4.17 right) to the spin Hamiltonian

$$\hat{H} = D \left(\hat{S}_z^2 - \frac{S(S+1)}{3} \right) + E \left(\hat{S}_x^2 - \hat{S}_y^2 \right) + \mu_{\text{B}} \vec{B} g \vec{S}$$

with the *julX* program that yields $D = -91 \text{ cm}^{-1}$, $g_x = g_y = 2.41$, $g_z = 2.89$ and $TIP = 110 \cdot 10^{-6} \text{ cm}^3 \text{mol}^{-1}$ (subtracted).

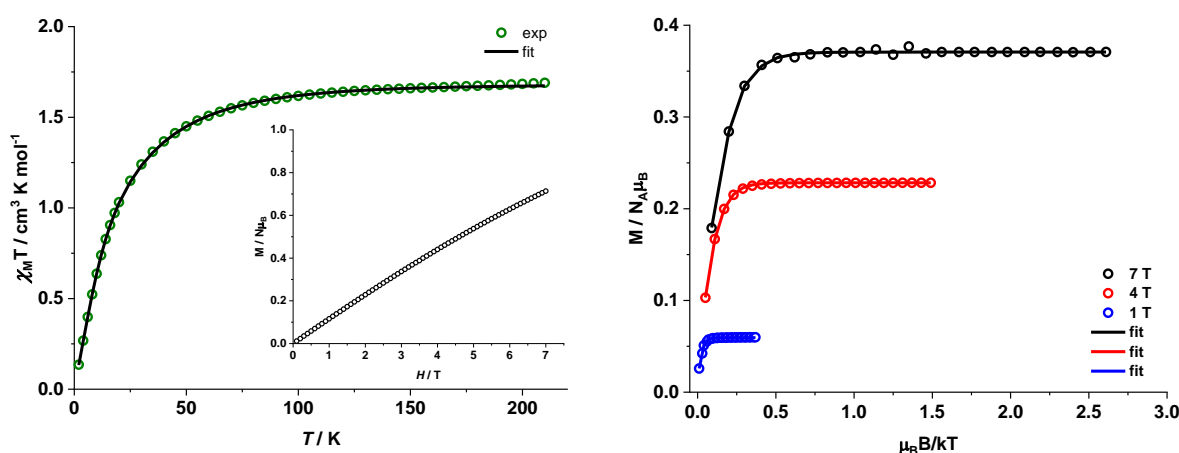


Figure 4.17. (Left) Temperature dependence of $\chi_{\text{M}}T$ value for complex **4** at an applied dc field of 0.5 T. Inset: Variable field magnetization at 2.0 K for **4**. (Right) Variable-temperature variable-field magnetization for complex **4**. The solid lines are the best fit with $D = -91 \text{ cm}^{-1}$, $g_x = g_y = 2.4$, $g_z = 2.89$ and $TIP = 110 \cdot 10^{-6} \text{ cm}^3 \text{mol}^{-1}$ (subtracted).

Complex **5** displays comparable magnetic behavior with the structurally similar complex **4**. The $\chi_{\text{M}}T$ value for **5** is $1.54 \text{ cm}^3 \text{K mol}^{-1}$ at 210 K indicating a significant orbital contribution to the magnetic moment. The $\chi_{\text{M}}T$ value falls to $0.21 \text{ cm}^3 \text{K mol}^{-1}$ at 2 K (Figure 4.18 left). The magnetization for **5** at 2.0 K also increases linearly until 7.0 T reaching a value of $0.92 \mu_{\text{B}}$ without any saturation (Figure 4.18 left inset). The magnetic susceptibility data were simultaneously fitted with the variable-field variable-temperature (VTVH) magnetization data (Figure 4.17 right) with the *julX-2S* program that yields $D = -95 \text{ cm}^{-1}$ and $g_x = g_y = 2.02$ and $g_z = 3.05$. Such large negative ZFS as observed in complexes **4** and **5** has been reported previously for four-coordinate Ni(II) systems.^{[112], [113], [114]}

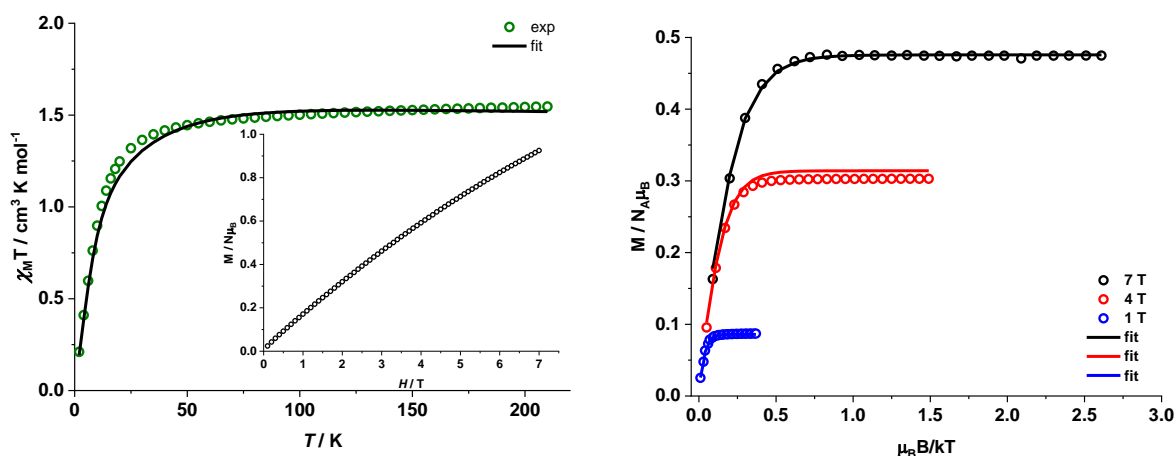
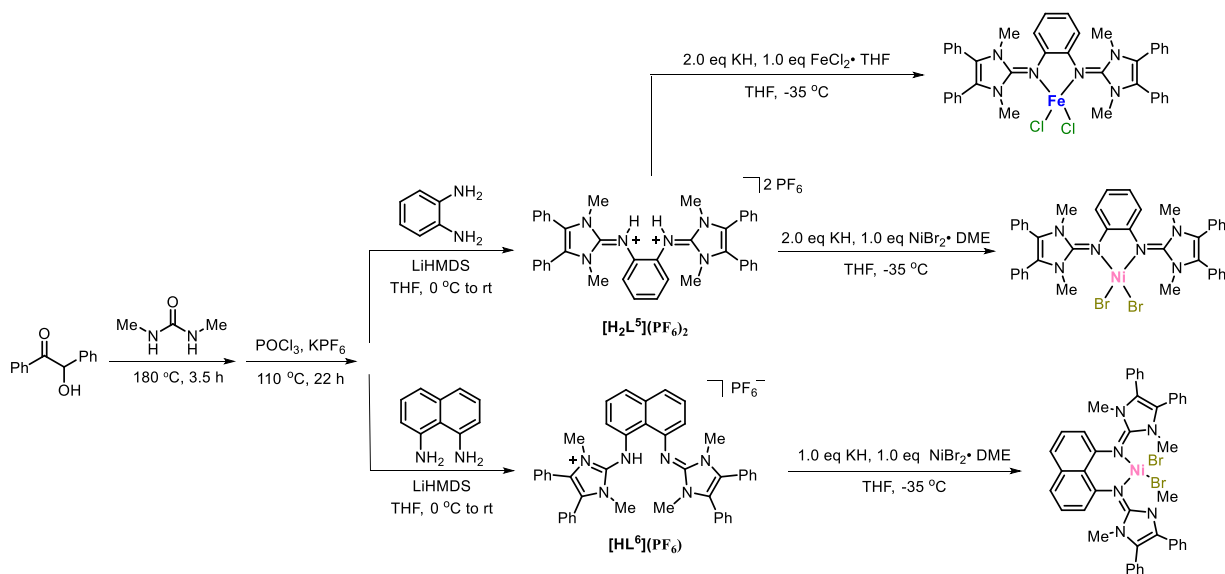


Figure 4.18. (Left) Temperature dependence of $\chi_M T$ value for complex **5** at an applied dc field of 0.5 T. Inset: Variable field magnetization at 2.0 K for **5**. (Right) Variable-temperature variable-field magnetization for complex **5**. The solid lines are the best fit with $D = -95 \text{ cm}^{-1}$, $g_x = g_y = 2.02$, $g_z = 3.05$ and $TIP = 23 \cdot 10^{-6} \text{ cm}^3 \text{ mol}^{-1}$ (subtracted).

4.6 Conclusions



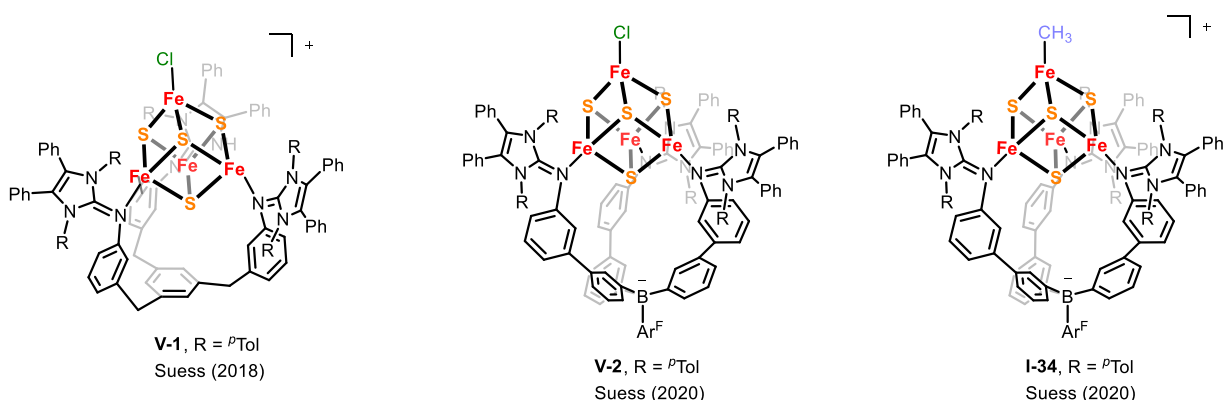
In summary, two new neutral imidazolin-2-imine ligands $[\text{H}_2\text{L}^5](\text{PF}_6)_2$ and $[\text{HL}^6](\text{PF}_6)$ have been successfully synthesized and isolated in the form of their PF_6^- salts. Apart from that, three anhydrous complexes, FeL^5Cl_2 (**3**), NiL^5Br_2 (**4**), and NiL^6Br_2 (**5**) have been prepared by reaction of metal(II) halide salts ($\text{FeCl}_2 \cdot \text{THF}$, NiBr_2) with the corresponding imidazolin-2-imine ligands (L^5 or L^6), and these new complexes (**3**, **4**, **5**) were fully characterized. The successful syntheses of **3**, **4**, and **5** evidence that imidazolin-2-imine ligands L^5 and L^6 have strong nucleophilicity to chelate metals, indicating these two ligands might be used to synthesize neutral [2Fe-2S] clusters.

Chapter 5. Well-Defined [2:2] Site-Differentiated $[\text{Fe}_4\text{S}_4\text{L}^5_2\text{Cl}_2]^{0/1+}$ Complexes Ligated by a Bidentated Imidazolin-2-imine

5.1 Introduction

Two imidazolin-2-imine ligands, $[\text{H}_2\text{L}^5](\text{PF}_6)_2$ and $[\text{HL}^6](\text{PF}_6)$ have been synthesized and their metalation has been investigated in the last chapter. The successful syntheses of the complexes FeL^5Cl_2 (**3**), NiL^5Br_2 (**4**), and NiL^6Br_2 (**5**) by the reaction of metal(II) halide salts ($\text{FeCl}_2 \cdot \text{THF}$, $\text{NiBr}_2 \cdot \text{DME}$) with the corresponding imidazolin-2-imine ligands (L^5 or L^6) prove that the imidazolin-2-imine ligands L^5 and L^6 have a strong tendency to chelate metals. As mentioned in chapter 4, these imidazolin-2-imine ligands were planned for the design of new iron sulfur clusters. As is evident from a literature research, imidazolin-2-imine ligands have started to find their application in Fe_4S_4 complexes in recent years.^[115] The Suess group reported several [4Fe-4S] complexes bearing imidazolin-2-imine ligands (Scheme 5.1),^{[60], [62]} and they showed this kind of ligands could stabilize alkyl-coordinated $[4\text{Fe-4S}]^{3+}$ clusters which are analogues of the short-lived intermediates in a multitude of Fe/S enzymatic reactions.

Scheme 5.1. Known [4Fe-4S] complexes bearing neutral tripodal imidazolin-2-imine ligands.



However, imidazolin-2-imine ligands have not been used in [2Fe-2S] complexes yet. In this chapter we tried synthesizing [2Fe-2S] complexes bearing imidazolin-2-imine by the template reaction of L^5 with the [2Fe-2S] precursor $(\text{Et}_4\text{N})_2[\text{Fe}_2\text{S}_2\text{Cl}_4]$. Surprisingly, instead of a [2Fe-2S] complex, a rare [2:2] site-differentiated $[4\text{Fe-4S}]^{3+}$ complex (**6**(PF_6)) has been obtained. Most of the reported [4Fe-4S] clusters are focused on homoleptic or [3:1] site-differentiated [4Fe-4S] clusters.^[115] In contrast, examples of the synthesis and characterization of [2:2] site-differentiated [4Fe-4S] clusters are very limited.^{[116], [68], [66]} It aroused our interest in understanding the structural as well as electronic characteristics of [2:2] site-differentiated [4Fe-4S] complexes, especially for the new $[4\text{Fe-4S}]^{3+}$ complex (**6**(PF_6)). Complex **6**(PF_6) was fully characterized, and its redox property was investigated. In addition, its one-electron reduced species, the $[4\text{Fe-4S}]^{2+}$ complex **6**, was also fully characterized and investigated in this chapter. Complex **6**(PF_6) has been proved to be a good precursor to synthesize other [4Fe-4S] derivatives because its two chlorides could be replaced by other groups, which will be discussed in the next chapter.

5.2 Synthesis and Structural Characterization

Complex $[\text{Fe}_4\text{S}_4\text{L}^5_2\text{Cl}_2](\text{PF}_6)$ (**6**(PF_6)) was obtained by metalation of $(\text{Et}_4\text{N})_2[\text{Fe}_2\text{S}_2\text{Cl}_4]$ with one equivalent of deprotonated ligand L^5 in THF solution (Scheme 5.2) at low temperature. The ESI-(+) mass spectrum shows a peak at $m/z = 1624.3$ characteristic of the cation $[\text{M}-\text{PF}_6]^+$ (Figure 5.1) indicating a successful complex synthesis (**6**(PF_6)).

Scheme 5.2. Synthesis of clusters $[\text{Fe}_4\text{S}_4\text{L}^5_2\text{Cl}_2]^{0/1+}$.

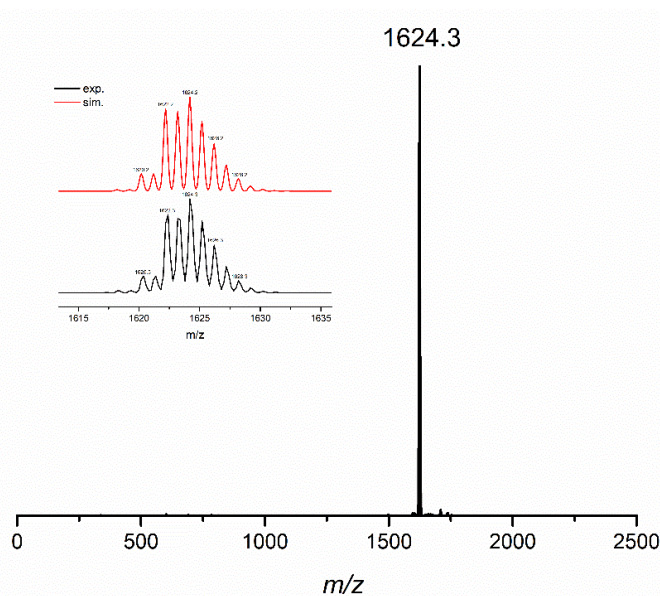
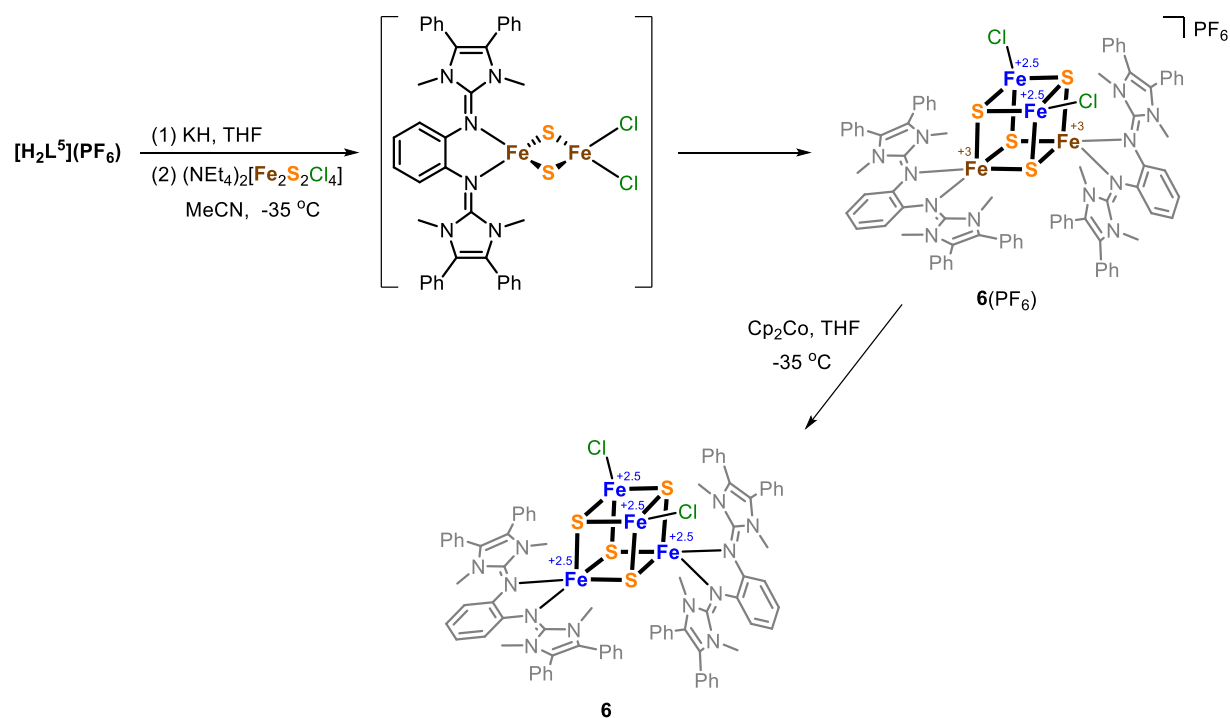


Figure 5.1. Positive ion ESI-MS of **6**(PF_6) in MeCN solution. The insets show the experimental and simulated isotopic distribution pattern of $[\text{M}-\text{PF}_6]^+$.

Diffusion of diethyl ether into a solution of **6**(PF₆) in MeCN afforded dark blue crystals. The molecular structure of **6**(PF₆) as determined by single-crystal X-ray diffraction (XRD) shows the first [2:2] site-differentiated [4Fe-4S]³⁺ cluster (Figure 5.2, left). **6**(PF₆) was exclusively isolated from the reaction mixture by crystallization from a mixture of MeCN or THF and Et₂O. The reaction is a reduction process, one Fe³⁺ was reduced to Fe²⁺, in which a sulfide (S²⁻) of the [2Fe-2S]²⁺ precursor or excess KH probably act as the reductant. The one-electron reduced species **6** was obtained by addition of an excess of cobaltocene (CoCp₂) to a solution of **6**(PF₆) in THF at -35 °C (Scheme 5.2). Crystals of **6** grew upon diffusion of Et₂O into a THF solution of **6** at room temperature (Figure 5.2, right).

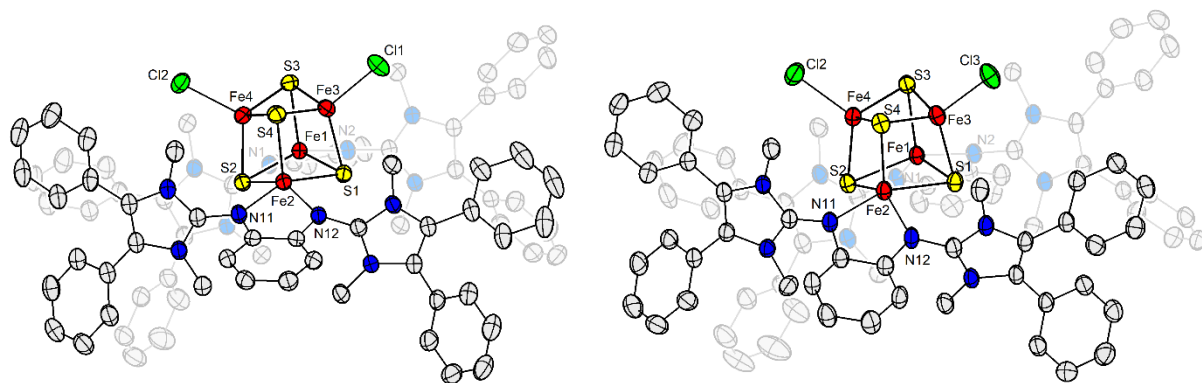


Figure 5.2. Thermal ellipsoid plots (50%) of the cations of **6**(PF₆) (left) and **6** (right). Red, yellow, blue, pinkish, lightsteelblue, green and grey ellipsoids represent Fe, S, N, P, F, Cl and C, respectively. Hydrogen atoms and solvent molecules are omitted for clarity.

While the [2Fe-2S]²⁺ ↔ [4Fe-4S]²⁺ interconversion is well-documented in biological systems and synthetic iron-sulfur chemistry,^{[117], [118]} the direct conversion [2Fe-2S]²⁺ → [4Fe-4S]³⁺ has never been reported, probably due to lacking suitable ligands. The reported [4Fe-4S]³⁺ clusters were mainly synthesized by oxidation reactions from [4Fe-4S]²⁺. Our work demonstrates that this inherent challenge can be overcome by modulating the steric effect of the ligand, in this case using the steric bulk of the L⁵ ligand to facilitate the formation of a [4Fe-4S]³⁺ cluster. While [2:2] site-differentiated clusters [Fe₄S₄Cl₂(Et₂Dtc)₂]²⁻ (Et₂Dtc = diethyldithiocarbamate) and Fe₄S₄Cl₂(depe)₂ (depe = bis(1,2-diethylphosphino)ethane) have been reported previously by using bidentate phosphine and thiolate ligands on two of the four iron atoms,^{[68], [119]} no nitrogen-based bidentate ligated [2:2] site-differentiated cluster could be synthesized to date. Hence, this work reports the synthesis as well as spectroscopic and crystallographic characterization of the first bidentate nitrogen ligated [2:2] site-differentiated [4Fe-4S] clusters.

Complexes **6**(PF₆) and **6** both crystallize in the monoclinic space group *P*2₁/*c* with four molecules in the unit cell. Structures of **6**(PF₆) and **6** determined by single crystal X-ray diffraction establish that both clusters have two different types of terminal groups, chloride and L⁵ (Figure 5.2). Two bidentate L⁵ ligands are bound to two Fe sites of the [4Fe-4S]³⁺ cluster core, thereby imparting the desired [2:2] site-differentiation, and the remaining two Fe sites are bound to a chloride each. As in other structures^[120] in this class of Fe/S clusters, the [4Fe-4S]₄ cores have a distorted cubic geometry that can be defined as two interpenetrating tetrahedra (Fe₄ and S₄). In the crystal structures of **6**(PF₆) and **6**, the [Fe₄S₄L⁵₂Cl₂]^{0/1+} are located on a crystallographic twofold axis of symmetry that coincides with the twofold molecular axis in idealized point group symmetry C₂. A close comparison of the subtle structural changes upon reduction (**6**(PF₆) versus **6**) is

interesting (in Figure 5.3 and Table 5.1) because it reveals that changes mainly occur around the [N]-coordinated iron atoms.

It is also in line with expected trends between reported $[\text{4Fe-4S}]^{3+}$ and $[\text{4Fe-4S}]^{2+}$ clusters,^{[121], [62]} the cluster bond lengths generally elongate upon reduction of **6**(PF₆): bonds between Fe and Cl elongate by 0.028 Å upon reaction; the Fe-S bonds show negligible elongation (<002 Å); however, the bond distances between Fe_N and the N change mostly, prolonging 0.069 Å upon reduction, indicating that reduction happened at N-coordinated Fe sites. In accordance with these considerations, reduction of **6**(PF₆) leads to a more pronounced lengthening of the bonds between Fe_N and the [N] capping ligand (0.069 Å) than for the bonds between Fe_{Cl} and the Cl (0.028 Å). Whereas, not like the prolongation of the mean Fe···Fe distance between $[\text{Fe}_4\text{S}_4(\text{SDpp})_4]^-$ (2.732 Å), $[\text{Fe}_4\text{S}_4(\text{SDpp})_4]^{2-}$ (2.759 Å) and $[\text{Fe}_4\text{S}_4(\text{SPh})_4]^{2-}$ (2.736 Å), $[\text{Fe}_4\text{S}_4(\text{SPh})_4]^{3-}$ (2.744 Å),^{[122], [123]} the Fe···Fe distance contracts from 2.935 to 2.903 Å upon the reduction of **6**(PF₆), which is consistent with the findings for $[\text{Fe}_4\text{S}_4(\text{DmpS})_4]^-$ (2.778 Å), $[\text{Fe}_4\text{S}_4(\text{DmpS})_4]^{2-}$ (2.742 Å)^[55], and the Fe···Fe distance in both of the cluster cores (**6**(PF₆) and **6**) are larger than that in normal [4Fe-4S] clusters.

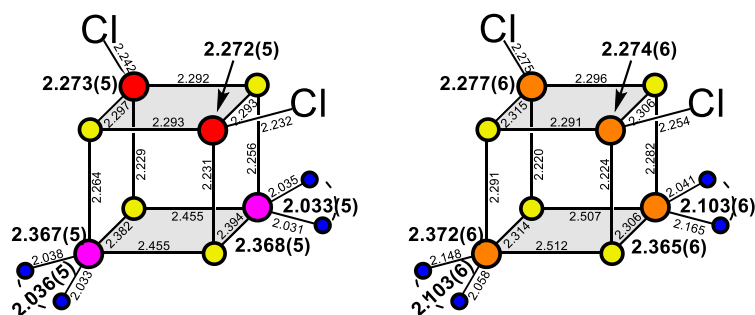


Figure 5.3. Schematics of the Fe_4S_4 cores showing Fe-S distances for **6**(PF₆) (left) and **6** (right) as determined by XRD. Large spheres = Fe, small yellow spheres = S, small blue spheres = N. The average Fe-N bond lengths (Å) and Fe-S bond lengths (Å) for each site of the cubane are shown in bold. Fe sites are colored according to their assigned solid-state valences: $\text{Fe}^{2.5+}$ = orange, $\text{Fe}^{2.75+}$ = pink, Fe^{3+} = red.

Table 5.1. Averaged bond lengths (Å) of clusters **6**(PF₆) and **6**.

	6 (PF ₆) (Å)	6 (Å)	Δ (Bond Length)
oxidation state	$[\text{4Fe-4S}]^{3+}$	$[\text{4Fe-4S}]^{2+}$	-
avg Fe _{Cl} -Cl	2.2368(8)	2.2646(9)	0.0278
avg Fe _N -N	2.0345(18)	2.1023(21)	0.0678
avg Fe _N -S	2.3679(8)	2.3687(7)	0.0008
avg Fe _{Cl} -S	2.2729(7)	2.2755(8)	0.0026
avg Fe-S	2.3204(8)	2.3221(8)	0.0017

5.3 Characterization in Solution

The ^1H -NMR spectrum of complex **6**(PF₆) was recorded in MeCN-*d*₃ at room temperature and is depicted in Figure 5.4. The broad peaks reveal the paramagnetic nature of complex **6**(PF₆). At rt, complex **6** exhibits C_{2v} symmetry on the NMR time scale in CD₂Cl₂ solution with resonances between +8 and +2 ppm in ^1H NMR spectrum (Figure 5.5). Integrals from aromatic resonances and signals from the methyl groups were found in 2:1 ratio. The modest shifting and the pronounced broadening of the ^1H resonances suggests that **6**, similar to nearly all other $[\text{4Fe-4S}]^{2+}$ complexes,^{[124], [125]} features an $S = 0$ ground state with some thermal population of paramagnetic excited states. In addition to the ^1H -NMR spectrum, it was tried to collect a 2D NMR spectrum, unfortunately, no discernable peaks were observed.

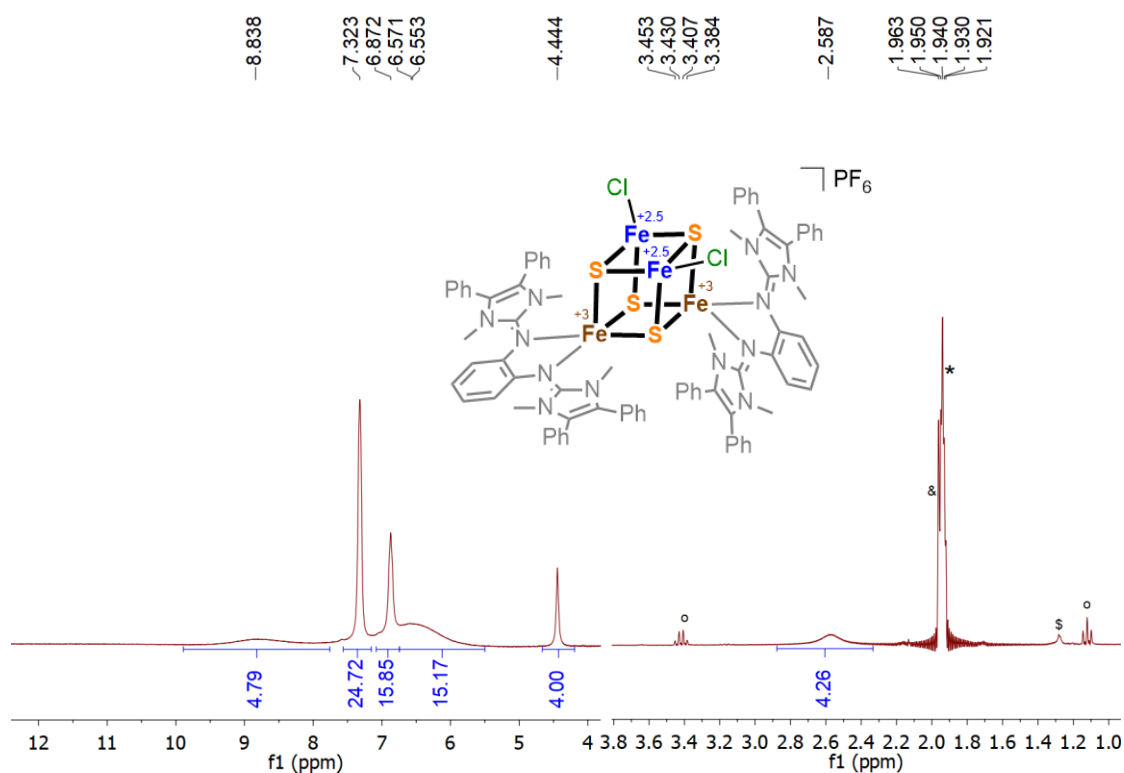


Figure 5.4. ^1H NMR spectrum of **6**(PF₆) recorded in MeCN-*d*₃ (300.1 MHz, 298 K). Signals of the MeCN-*d*₃ (*), and residual Et₂O (°), MeCN (&), unknown impurities (\$) have been labeled.

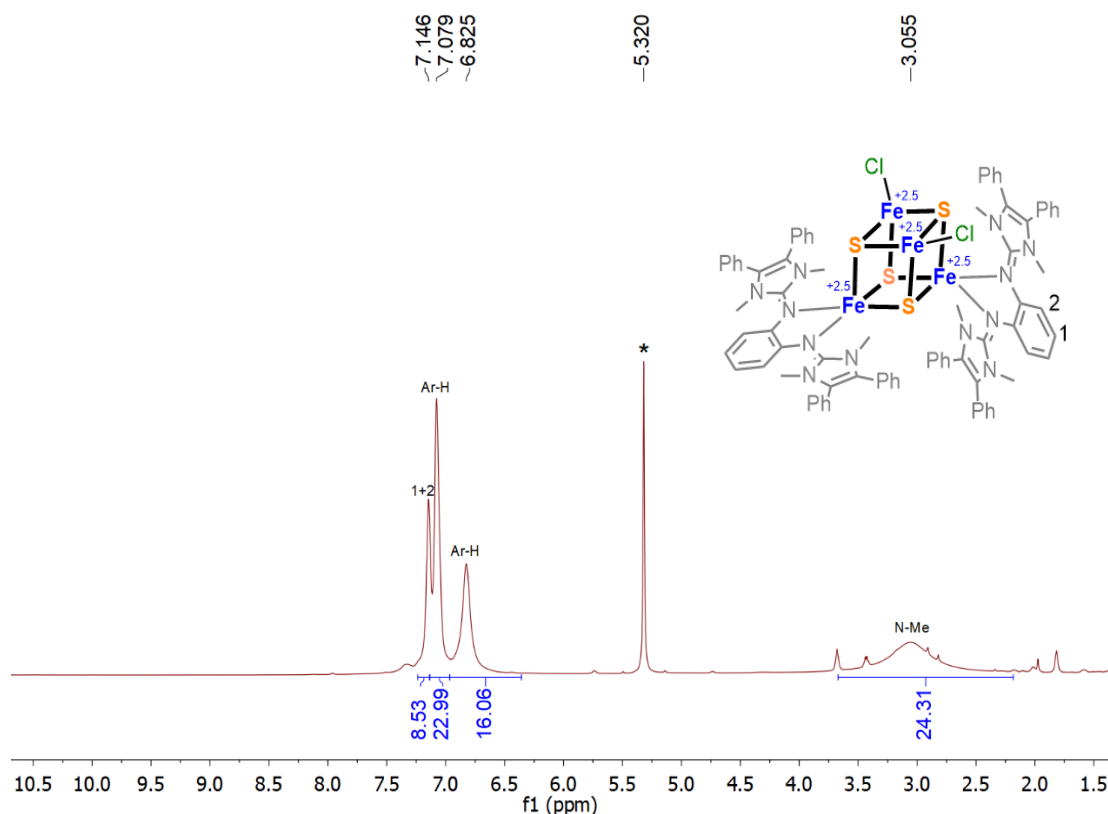


Figure 5.5. ^1H NMR spectrum of **6** recorded in CD_2Cl_2 (500.3 MHz, 298 K). Signals of the CD_2Cl_2 (*) has been labeled.

The UV-vis absorption spectra (Figure 5.6) of the [2:2] side differentiate complexes **6**(PF_6) and **6** (in THF) show broad bands with $\lambda_{\text{max}} = 480$ and 625 nm for **6**(PF_6) and 531 nm for **6**. The spectrum of **6** resembles that of the $[\text{Fe}_4\text{S}_4(\text{SC}_6\text{H}_4\text{-}p\text{-NMe}_2)_4]^{2-}$,^[126] only with smaller molar absorptivity. Both **6**(PF_6) and **6** the redox series show spectra dominated by intense features, which are almost certainly assigned to LMCT.^[23]

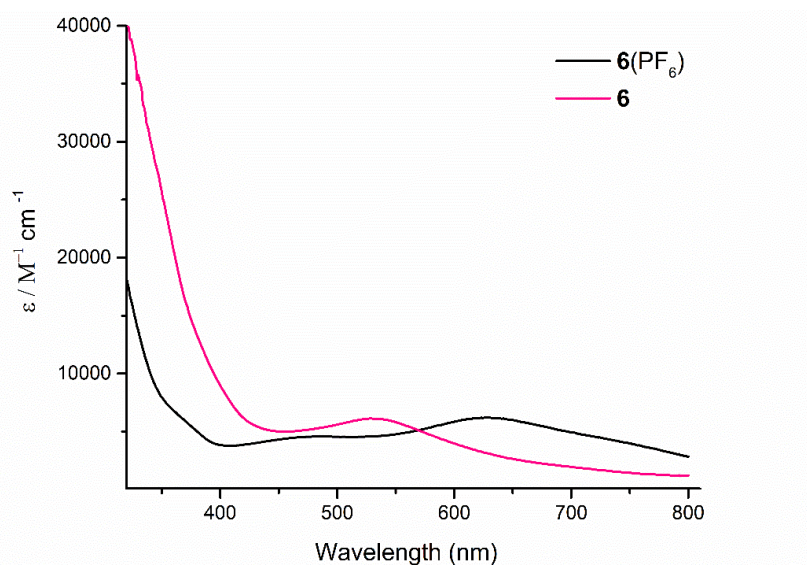


Figure 5.6. UV-vis absorption spectra of **6**(PF_6) (black trace) and **6** (red trace) in THF solution at 25 °C.

The overall appearances of the two spectra are kind of different with the change in electron count, with a high-energy shift evident upon reduction, particularly for the lowest energy transition in the visible range. The reductive hypsochromic shift causes a recognizable color change for the deeply colored solutions, from blue for $\mathbf{6}(\text{PF}_6)$ to purple-black for $\mathbf{6}$. The similar reductive blue shifts also exist in amide-ligated and thiolate-ligated cubane systems.^{[121], [23]} No new bands appeared, and the intensities of all the bands for two complexes remained stable at 298 K after 14 hours (Figure 8.2.25), indicating that complexes $\mathbf{6}(\text{PF}_6)$ and $\mathbf{6}$ are very stable.

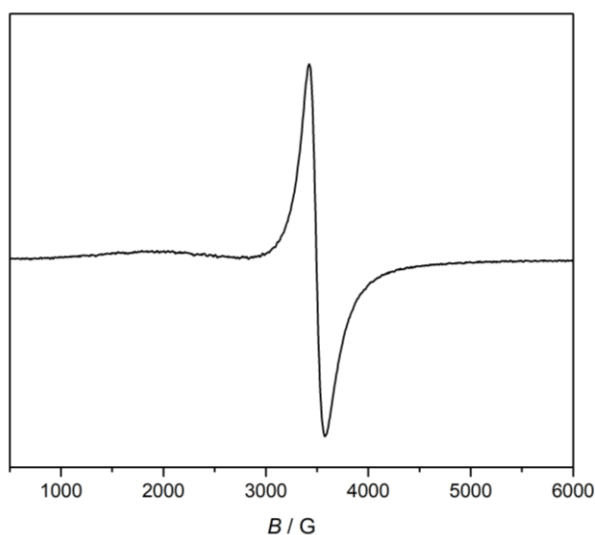


Figure 5.7. EPR spectrum of $\mathbf{6}(\text{PF}_6)$ in *o*-difluoro benzene measured as frozen glass at 141 K.

To gain more insight into the electronic structure of complex $\mathbf{6}(\text{PF}_6)$, an EPR measurement has been performed at 141 K in *o*-difluoro benzene solution (Figure 5.7). It shows a narrow isotropic signal with $g = 1.930$ with no discernable hyperfine interactions, which is smaller than that of most synthesized $[\text{Fe}_4\text{S}_4]^{3+}$ clusters ($g_{\text{av}} \geq 2.0$) as well as those $[\text{Fe}_4\text{S}_4]^{3+}$ clusters in oxidized high-potential iron proteins ($g_{\text{av}} \approx 2.06$). A measurement at lower temperature may help improve the resolution.

5.4 Redox Properties

Redox properties of $\mathbf{6}(\text{PF}_6)$ were studied by cyclic voltammetry (CV) in MeCN solution containing 0.1 M NBu_4PF_6 at different scan rates and at rt (Figure 5.8). $\mathbf{6}(\text{PF}_6)$ shows two cathodic redox events with the first reduction at $E_1 = -0.64$ V vs. the Fc^+/Fc couple, leading to the $[\text{4Fe-4S}]^{2+}$ cluster, and a second electrochemically quasi-reversible reduction at $E_2 = -1.64$ V, presumably leading to the $[\text{4Fe-4S}]^+$ cluster.^[116] The first process is reversible according to the currents for the first reduction process of $\mathbf{6}(\text{PF}_6)$ varying linearly with the square root of scan rate and $\Delta E_p = 72$ mV for the separation of anodic and cathodic peak potentials. The wide separation ($\Delta E = 1.0$ V) of the two sequential one-electron reductions is in line with the observation that preparative isolation of $\mathbf{6}$ is possible. The cyclic voltammogram of $\mathbf{6}(\text{PF}_6)$ is similar to the [2:2] site-differentiated cluster $[\text{Fe}_4\text{S}_4\text{Cl}_2(t\text{-BuNC})_6]$ ($E_1 = -0.23$ V and $E_2 = -1.35$ V vs. the Fc^+/Fc couple)^{[116], [127]} which also contains chloride and neutral ligands (*t*-BuNC). The ~100–200 mV cathodic shift of these processes for $\mathbf{6}(\text{PF}_6)$ as compared to $[\text{Fe}_4\text{S}_4\text{Cl}_2(t\text{-BuNC})_6]$ reflects the increased donicity of L^5 as compared to *t*-BuNC.

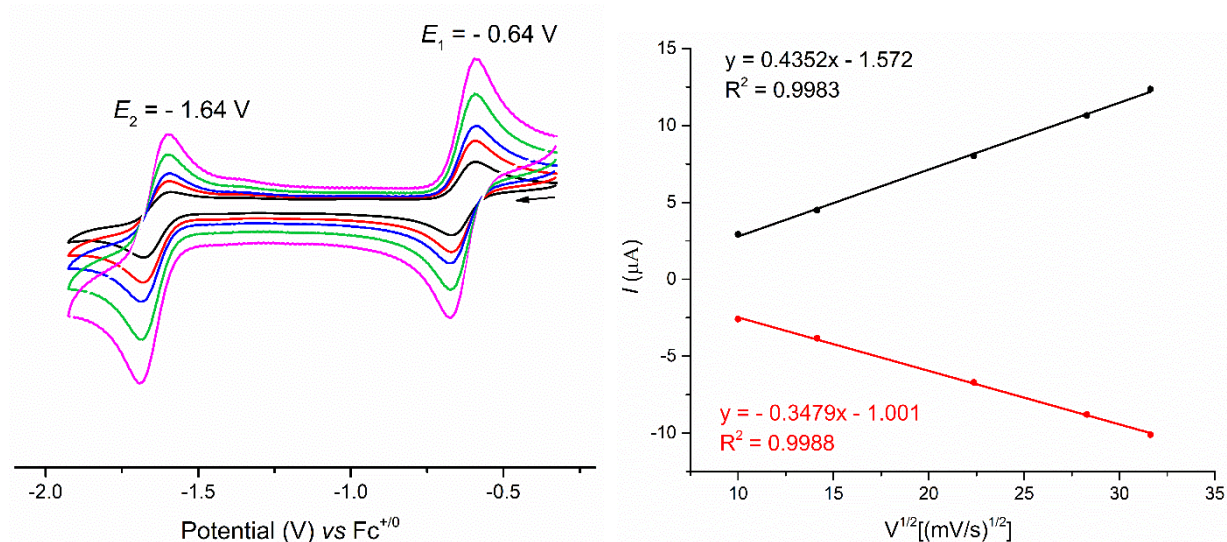


Figure 5.8. (Left) Cyclic voltammogram of **6**(PF₆) recorded at rt in MeCN/0.1 M NBu₄PF₆ vs. Fc⁺/Fc. $E_1 = -0.64$ V and $E_2 = -1.64$ V at various scan rates ($\nu = 100, 300, 500, 800, 1000$ mV s⁻¹). (Right) Linear dependence of current on square root of scan rate of the first redox event of **6**(PF₆); the forward peak (black) and backward peak (red) of $[\text{4Fe-4S}]^{3/2+}$ redox couple.

5.5 Characterization in the Solid State

The zero-field ⁵⁷Fe Mössbauer spectrum of solid **6**(PF₆) (Figure 5.9, left) shows a “simple” quadrupole doublet. The widths of resonance absorptions suggest that charge delocalization around the $[\text{4Fe-4S}]$ core is extensive. This spectrum could be best described by two quadrupole doublets in theoretically expected 1:1 ratio with similar isomer shift ($\delta_1 = 0.47$ mm s⁻¹, $\delta_2 = 0.49$ mm s⁻¹) but slightly different quadrupole splitting ($\Delta E_{Q1} = 0.82$ mm s⁻¹, $\Delta E_{Q2} = 1.10$ mm s⁻¹), reflecting the charge delocalization over iron sites and distinct coordination environment of the iron ions. The assignment of this “nested” configuration was based on comparison with other [2:2] site-differentiated $[\text{4Fe-4S}]$ complexes.^{[128], [118]}

The other alternative fit, “crossed” configuration, of this Mössbauer spectrum can lead to relatively similar quadrupole splitting ($\Delta E_{Q1} = 0.94$ mm s⁻¹, $\Delta E_{Q2} = 0.96$ mm s⁻¹), but differ isomer shift ($\delta_1 = 0.40$ mm s⁻¹, $\delta_2 = 0.54$ mm s⁻¹), corresponding to enhanced charge localization, which is opposite to the charge delocalization. Besides, an enhancement of charge localization can predict different quadrupole splitting, which is also in contrast to the results of similar ΔE_Q values. Thus, the spectrum of **6**(PF₆) probably best fit as two doublets with similar isomer shift, different quadrupole splitting.

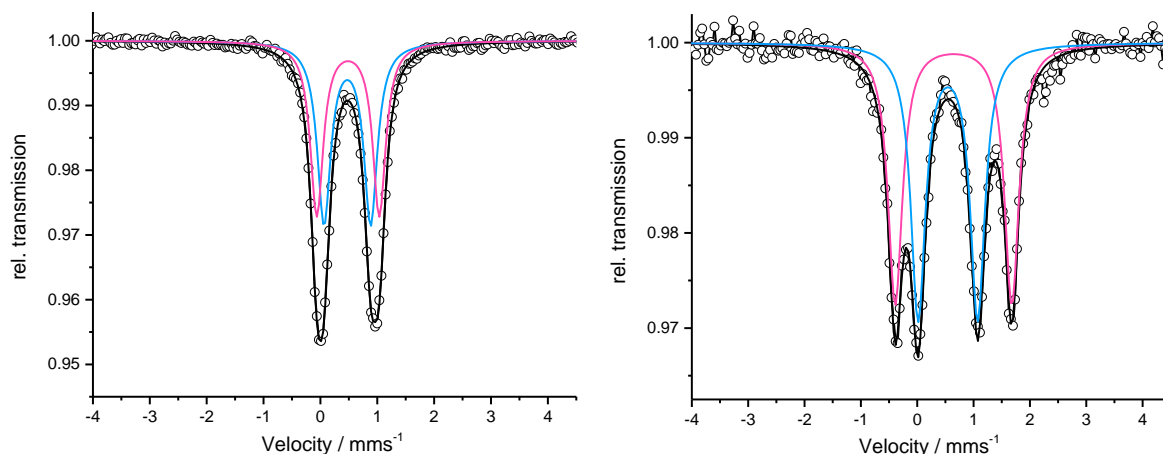


Figure 5.9. Zero-field ^{57}Fe Mössbauer spectra of solid **6**(PF₆) (left) and **6** (right) at 80 K. Simulation of the data gave the following parameters: (left) $\delta_1 = 0.47 \text{ mm s}^{-1}$, $\Delta E_{Q1} = 0.82 \text{ mm s}^{-1}$ (blue), $\delta_2 = 0.49 \text{ mm s}^{-1}$, $\Delta E_{Q2} = 1.10 \text{ mm s}^{-1}$ (red); (right) $\delta_1 = 0.54 \text{ mm s}^{-1}$, $\Delta E_{Q1} = 1.06 \text{ mm s}^{-1}$ (blue), $\delta_2 = 0.64 \text{ mm s}^{-1}$, $\Delta E_{Q2} = 2.07 \text{ mm s}^{-1}$ (red).

In contrast, the zero-field ^{57}Fe Mössbauer spectrum of cluster **6** shows two distinct doublets (Figure 5.9, right) in the expected 1:1 ratio, with $\delta_1 = 0.54 \text{ mm s}^{-1}$, $\Delta E_{Q1} = 1.06 \text{ mm s}^{-1}$ and $\delta_2 = 0.64 \text{ mm s}^{-1}$, $\Delta E_{Q2} = 2.07$ (“nested” configuration). Overall, the Mössbauer data of **6** show good agreement with parameters found for $(\text{Ph}_4\text{P})_2[\text{Fe}_4\text{S}_4(\text{Cl})_2(\text{Et}_2\text{Dtc})_2]$, $(\text{Ph}_4\text{P})_2[\text{Fe}_4\text{S}_4(\text{Cl})_3(\text{Et}_2\text{Dtc})]$ and $(\text{Ph}_4\text{P})_2[\text{Fe}_4\text{S}_4(\text{SPh})_2(\text{Et}_2\text{Dtc})_2]$ (see Table 5.2).^[68] The first set of doublet data of **6** ($\delta_1 = 0.54 \text{ mm s}^{-1}$, $\Delta E_{Q1} = 1.06 \text{ mm s}^{-1}$) are more close to the value of the single resonance in $(\text{Ph}_4\text{P})_2[\text{Fe}_4\text{S}_4\text{Cl}_4]$ ($\delta = 0.49 \text{ mm s}^{-1}$, $\Delta E_Q = 0.67 \text{ mm s}^{-1}$), corresponding to chloride ligated iron site. The second set of parameters ($\delta_2 = 0.64 \text{ mm s}^{-1}$, $\Delta E_{Q2} = 2.07$) is likely related with the iron atoms ligated by the bidentate L^5 ligands, which is consistent with the findings for $(\text{Ph}_4\text{P})_2[\text{Fe}_4\text{S}_4(\text{Cl})_2(\text{Et}_2\text{Dtc})_2]$ and $(\text{Ph}_4\text{P})_2[\text{Fe}_4\text{S}_4(\text{SPh})_2(\text{Et}_2\text{Dtc})_2]$.^{[67], [118], [68]} The isomer shift attributed to the five-coordinate iron sites is larger compared to the value of the four-coordinate iron sites. It also means, δ_2 should be attributed to L^5 ligated iron sites (five-coordinate iron sites); δ_1 should be assigned to chloride coordinated iron sites (four-coordinate iron sites). Comparing to oxidized species (**6**(PF₆)), the doublet 2 (δ_2 , ΔE_{Q2}) of the reduced species (**6**) changed much more than doublet 1 (δ_1 , ΔE_{Q1}), which certifies reduction happened at N-coordinated iron sites.

Table 5.2. Solid state ^{57}Fe Mössbauer parameters [mm s^{-1}] for cluster **6** and selected $[\text{4Fe-4S}]^{2+}$ complexes.

$[\text{4Fe-4S}]^{2+}$ complexes	T, K	δ_1	ΔE_{Q1}	δ_2	ΔE_{Q2}
$[\text{Fe}_4\text{S}_4\text{L}^5_2\text{Cl}_2]$ 6	80	0.54	1.06	0.64	2.07
$(\text{Ph}_4\text{P})_2[\text{Fe}_4\text{S}_4\text{Cl}_4]$	77	0.49	0.67	-	-
$(\text{Ph}_4\text{P})_2[\text{Fe}_4\text{S}_4(\text{Cl})_3(\text{Et}_2\text{Dtc})]$	77	0.51	1.07	0.64	2.13
$(\text{Ph}_4\text{P})_2[\text{Fe}_4\text{S}_4(\text{Cl})_2(\text{Et}_2\text{Dtc})_2]$	77	0.53	1.06	0.62	1.85
$(\text{Ph}_4\text{P})_2[\text{Fe}_4\text{S}_4(\text{SPh})_2(\text{Et}_2\text{Dtc})_2]$	77	0.47	1.06	0.64	1.84
$(\text{Ph}_4\text{P})_2[\text{Fe}_4\text{S}_4(\text{SPh})_4]$	77	0.43	0.93	-	-

The direct current (dc) temperature-dependent magnetic susceptibility measurements for both complexes **6** and **6**(PF₆) were carried out on powder polycrystalline samples on a Quantum

Design MPMS3 SQUID magnetometer under 0.5 T applied field in the range of 2–300 K for **6** and 2–295 K **6**(PF₆). The $\chi_{\text{M}}T$ value for **6** at 300 K is 0.70 cm³ mol⁻¹ K, which linearly decreases on cooling due to thermal depopulation of the excited states indicating a diamagnetic ground spin-state ($S_{\text{T}} = 0$) predominantly observed in $[\text{4Fe-4S}]^{2+}$ clusters (Figure 5.10 right).^{[87], [120], [129], [130]} The shape of the plot represents a dominant strong intramolecular antiferromagnetic coupling. A small residual magnetic susceptibility at lower temperatures is probably due to the presence of unidentified paramagnetic impurities. The $[\text{4Fe-4S}]^{2+}$ core in **6** formally contains two high-spin Fe³⁺ (d^5 , $S = 5/2$) and two high-spin Fe²⁺ (d^6 , $S = 2$) ions, however, the isomer shifts for the two doublets observed in the ⁵⁷Fe Mössbauer spectrum of **6** at 80 K are much lower than that of a typical tetrahedral Fe²⁺ ion and higher than those observed for tetrahedral Fe³⁺ ions (as in **6**²⁻). This indicates that the $[\text{4Fe-4S}]^{2+}$ cluster in **6** contains two delocalised mixed-valence Fe^{2.5+}Fe^{2.5+} dimers also called “rhombs” with $S = 9/2$.^{[61], [131], [48]} To model the experimental data, a few assumptions were made based on previous theoretical and spectroscopic studies.^{[132], [133], [134]} The double-exchange phenomenon among the delocalized mixed-valence $[\text{Fe}^{2.5+}\text{Fe}^{2.5+}]$ pair leads to a ferromagnetic coupling with $S = 9/2$. Further based on previous spectroscopic studies, the double-exchange interactions within the $[\text{Fe}^{2.5+}\text{Fe}^{2.5+}]$ pair are considered very strong so that they are treated as a single spin ($S = 9/2$). The antiferromagnetic exchange interaction between the two $S = 9/2$ “rhombs” leads to a diamagnetic ground spin-state ($S_{\text{T}} = 0$). The experimental data was modelled using the *julX* program by using the Heisenberg-Dirac-van-Vleck (HDvV) spin Hamiltonian (eq. 5.1),

$$\hat{H} = -2J\hat{S}_1\hat{S}_2 + g\mu_B\vec{B}(\vec{S}_1 + \vec{S}_2) \quad (5.1)$$

where J_{cubane} represents the magnetic exchange coupling constant between the two S_{A} and S_{B} “rhombs” formally with $S = 9/2$ (Figure 5.10 left). Since the exchange interaction between S_{A} and S_{B} is quite strong and only $S_{\text{T}} = 0, 1, 2$ states are occupied even at high temperatures, any $S_{\text{A}} = S_{\text{B}} \geq 1$ values would lead to the same results. Therefore, $S_{\text{A}} = S_{\text{B}} = 5/2$ were used for the simulation with the *julX*. The temperature-independent paramagnetism (*TIP*) and paramagnetic impurities (*PI*) were included as in the previous cases according to $\chi_{\text{calc}} = (1 - \text{PI}) \cdot \chi + \text{PI} \cdot \chi_{\text{mono}} + \text{TIP}$. The best fit to the experimental data leads to $J_{\text{cubane}} = -128 \text{ cm}^{-1}$, $\text{PI} = 1.7\%$ and $\text{TIP} = 10 \cdot 10^{-6} \text{ cm}^3 \text{ mol}^{-1}$ with $g = 2.0$ (fixed).

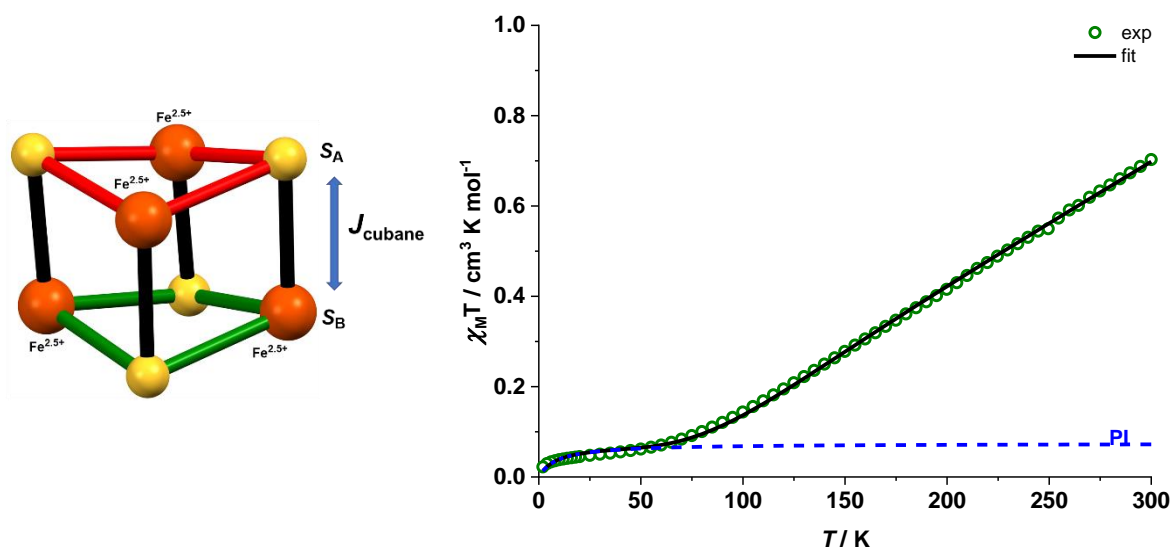


Figure 5.10. (Left) The magnetic exchange interaction between the delocalized mixed-valence $[\text{Fe}^{2+}\text{Fe}^{3+}]$ Fe “rhombs” within the cubane. J_{cubane} is the exchange coupling constant between two

S_A and S_B “rhombs” with $S = 9/2$. (Right) Temperature dependence of $\chi_M T$ for **6** at an applied dc field of 0.5 T. The solid black line represents the calculated curve fit with the parameters $J_{\text{cubane}} = -128 \text{ cm}^{-1}$, $PI = 1.7\%$ and $TIP = 10 \cdot 10^{-6} \text{ cm}^3 \text{ mol}^{-1}$ with $g = 2.0$ (fixed).

The $\chi_M T$ value for **6**(PF₆) is $1.04 \text{ cm}^3 \text{ mol}^{-1} \text{ K}$ at 295 K that linearly decreases on cooling due to thermal depopulation of the excited states before reaching a plateau indicating a paramagnetic ground spin-state ($S_T = 1/2$) (Figure 5.11), as also observed in other oxidized $[\text{4Fe-4S}]^{3+}$ clusters exhibiting dominant intramolecular antiferromagnetic interactions.^{[23], [135]} The parameters of the 1:1 doublet in the ^{57}Fe Mössbauer spectrum of **6**(PF₆) indicates that the high-spin iron ions (3Fe^{3+} , d^5 , $S = 5/2$ and 1Fe^{2+} , d^6 , $S = 2$) in oxidized $[\text{4Fe-4S}]^{3+}$ cluster exists in pairs, the delocalized $[\text{Fe}^{2.5+}\text{Fe}^{2.5+}]$ ($S = 9/2$) pair and localized $[\text{Fe}^{3+}\text{Fe}^{3+}]$ pair. The antiferromagnetic coupling between the mixed-valence $[\text{Fe}^{2.5+}\text{Fe}^{2.5+}]$ ($S = 9/2$) “rhomb” and the spin-aligned $[\text{Fe}^{3+}\text{Fe}^{3+}]$ “rhomb” formally ($S = 5$) in the ground state results in the net spin of $S = 1/2$ as observed in $[\text{4Fe-4S}]^{3+}$ clusters.^{[23], [135], [136]} The temperature-dependent experimental data was modelled using the Heisenberg-Dirac-van-Vleck (HDvV) spin Hamiltonian, as shown above in equation 5.1, where J_{cubane} represents the magnetic exchange coupling constant between the two S_A ($S = 9/2$) and S_B ($S = 5$) “rhombs”. The best fit to the experimental data leads to $J_{\text{cubane}} = -93 \text{ cm}^{-1}$, $\theta = -2.2 \text{ K}$, $PI = 0\%$ and $TIP = 430 \cdot 10^{-6} \text{ cm}^3 \text{ mol}^{-1}$ with $g = 2.0$ (fixed). These simulations were based on several assumptions (including those mentioned above), simulations considering Fe^{3+} sites as individual spin leads to many solutions with large deviations.

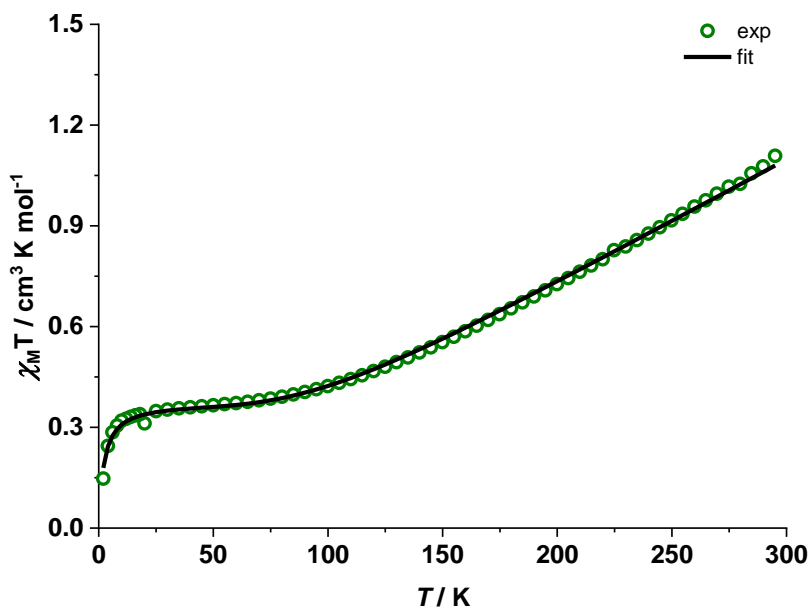
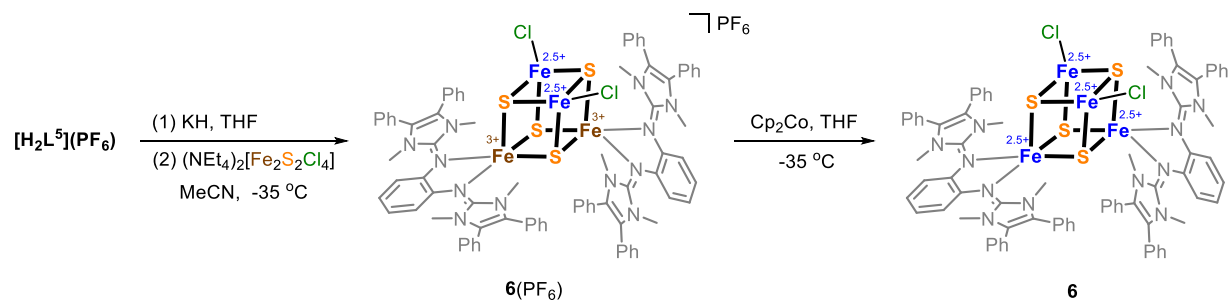


Figure 5.11. Temperature dependence of $\chi_M T$ for **6**(PF₆) at an applied dc field of 0.5 T. The solid black line represents the calculated curve fit with the parameters $J_{\text{cubane}} = -93 \text{ cm}^{-1}$, $\theta = -2.2 \text{ K}$, $PI = 0\%$ and $TIP = 430 \cdot 10^{-6} \text{ cm}^3 \text{ mol}^{-1}$ with $g = 2.0$ (fixed).

5.6 Conclusions



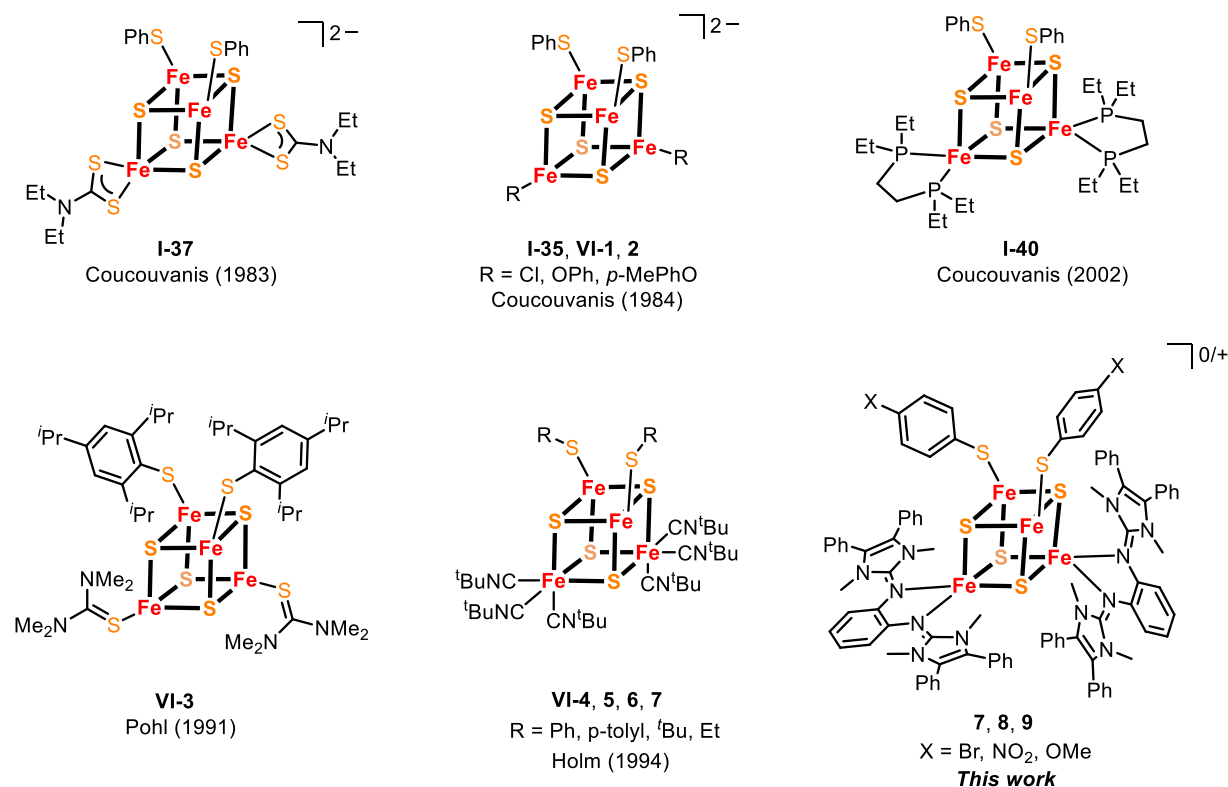
In summary, we herein describe the preparation and full characterization of the rare [2:2] site-differentiated $[\text{4Fe-4S}]^{3+}$ complex $\mathbf{6}(\text{PF}_6)_2$ bearing two bidentate imidazolin-2-imines ligands L^5 . $\mathbf{6}(\text{PF}_6)_2$ is special also because of its bidentate nitrogen ligands, which are rare in $[\text{4Fe-4S}]$ complexes. Besides, in the $\mathbf{6}(\text{PF}_6)_2$ synthesis, the direct conversion $[\text{2Fe-2S}]^{2+} \rightarrow [\text{4Fe-4S}]^{3+}$ is uncommon in $[\text{4Fe-4S}]^{3+}$ complex synthesis. Complex $\mathbf{6}(\text{PF}_6)_2$ and the one-electron reduced species $\mathbf{6}$ were studied by single-crystal X-ray diffraction. The variations of the bond lengths from $\mathbf{6}(\text{PF}_6)_2$ to $\mathbf{6}$, especially the elongate of the Fe-N bonds, reflect that the reduction happened at the N-coordinated Fe sites, which was also certified by Mössbauer studies.

Chapter 6. Well-Defined [2:2] Site-Differentiated $[\text{Fe}_4\text{S}_4\text{L}^5_2(\text{SR})_2]^{0/1+}$ Complexes: Syntheses and Characterization

6.1. Introduction

Iron-sulfur (Fe/S) clusters coordinated by cysteine residues are ubiquitous in biological systems.^[137] Among them, cuboidal $[\text{4Fe-4S}]$ clusters ligated by cysteine residues are the most represented structures and have a multitude of functional roles. They can serve as a source of sulfur, as O_2 or NO sensors of cellular environment,^[138] as relays of long-range electron transfer.^[139] To gain insight into cysteine residues coordinating $[\text{4Fe-4S}]$ complexes, many $[\text{4Fe-4S}]$ complexes bound to thiolate ligands which mimic cysteine residues $[\text{Fe}_4\text{S}_4(\text{SR})_n\text{L}_{4-n}]$ ($n = 1-4$) have been synthesized and investigated, especially homoleptic ($n = 4$) and [3:1] site-differentiated $[\text{4Fe-4S}]$ complexes ($n = 3$) ligated by thiolate. While only a few [2:2] site-differentiated $[\text{Fe}_4\text{S}_4(\text{SR})_2\text{L}_2]$ complexes ($n = 2$) were reported by the Coucouvanis^{[67], [118], [119]} Pohl^[140] and Holm^[116] groups (Scheme 6.1) up to now.

Scheme 6.1 [2:2] site-differentiated $[\text{4Fe-4S}]$ clusters with thiolate ligands.



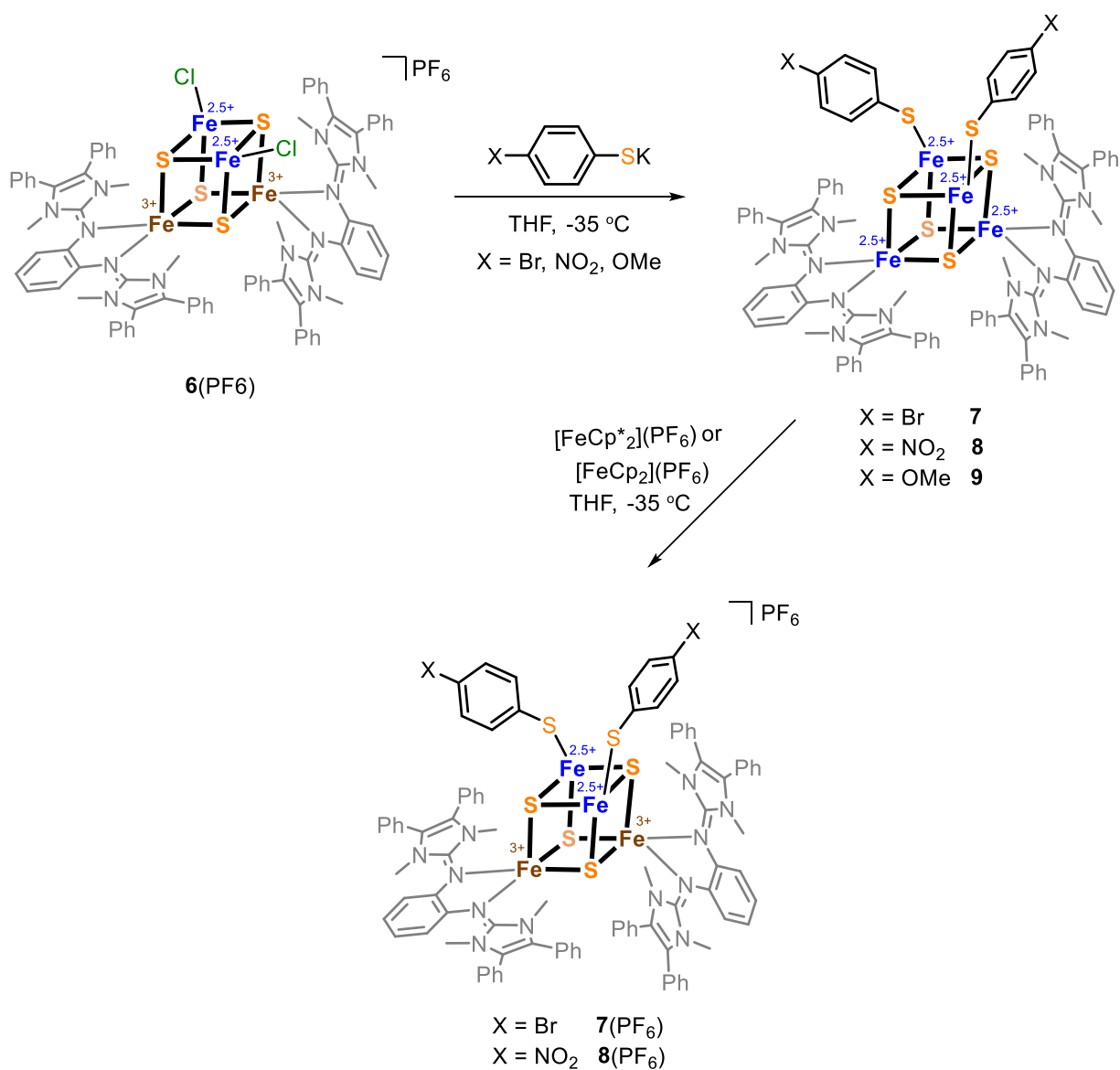
In chapter 5, we synthesized and fully characterized the chloride coordinated $[\text{4Fe-4S}]$ complex $[\text{Fe}_4\text{S}_4\text{L}^5_2\text{Cl}_2](\text{PF}_6)$ (**6**(PF_6)), which can be a good precursor to synthesize $[\text{4Fe-4S}]$ derivatives where chloride could be substituted by other groups. A series of [2:2] site-differentiated $[\text{4Fe-4S}]^{2/3+}$ complexes (**7**, **7**(PF_6), **8**, **8**(PF_6), **9**) were synthesized by using **6**(PF_6) together with various thiolates in this chapter. It is noteworthy that $[\text{4Fe-4S}]$ complexes coordinating both with thiolate and imidazolin-2-imine ligands have not been reported yet. Complexes **7**, **7**(PF_6), **8**,

8(PF₆), **9** have been fully characterized, and their redox properties were also investigated in this chapter.

6.2. Synthesis and Structural Characterization

The syntheses of the clusters **7**, **8**, and **9** are readily accomplished by stoichiometric reactions between **6**(PF₆) and 4-Br-C₆H₄SK, 4-NO₂-C₆H₄SK, and 4-OMe-C₆H₄SK, respectively (Scheme 6.2). 4-X-C₆H₄SH (X = Br, NO₂, OMe) were first deprotonated with KH in THF and then added to **6**(PF₆) at low temperature. The target complexes **7** and **8** were crystallized for X-ray diffraction by slow diffusion of Et₂O into THF solutions of the compounds (Figure 6.1).

Scheme 6.2. Synthesis of bidentate imidazolin-2-imine-ligated $[\text{Fe}_4\text{S}_4\text{L}^5_2(\text{SC}_6\text{H}_4\text{-4-X})_2]^{0/1+}$ (X = Br, NO₂, OMe) clusters.



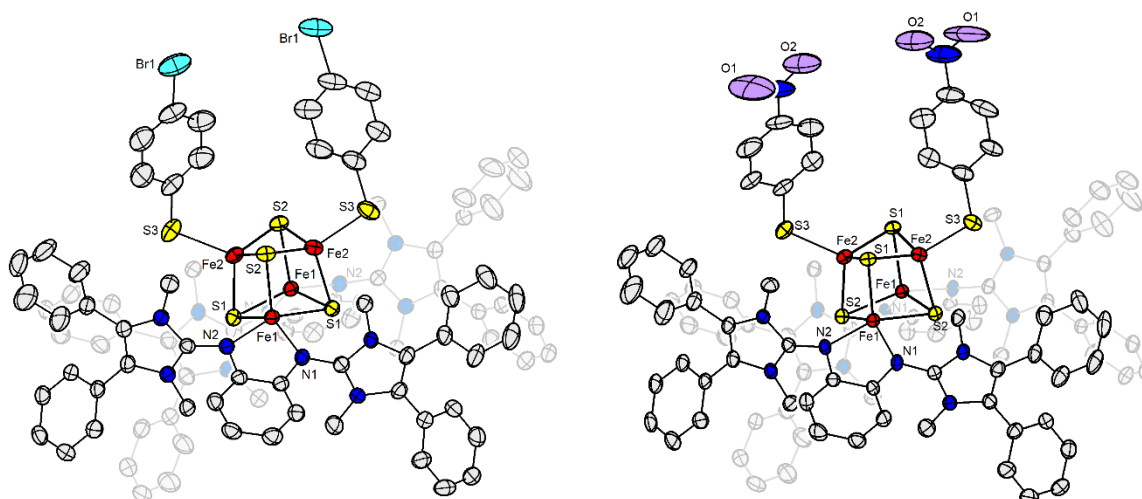
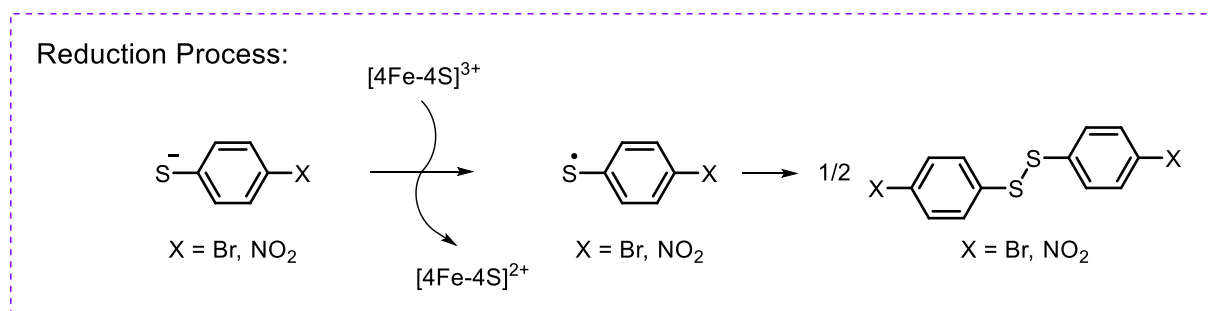


Figure 6.1. Thermal ellipsoid plots (50%) of the cations of **7** (left) and **8** (right). Red, yellow, blue, turquoise, magenta and grey ellipsoids represent Fe, S, N, Br, O and C, respectively. Hydrogen atoms and solvent molecules are omitted for clarity.

Single crystals of cluster **9** haven't been obtained in good quality yet, although several crystallizations attempts from THF / FeEt_2O , THF + MeCN / Et_2O , saturated THF solutions afforded some crystalline material. The crystalline material in one attempt gave a picture of the molecular structure of **9**, although refinement was impossible. It should be noticed that the $[\text{4Fe-4S}]^{3+}$ core of **6**(PF_6) has been reduced during the salt metathesis reaction. Mercaptides might act as both substitutional ligands and single electron reductants (Scheme 6.3). In fact, the corresponding disulfides were identified by ESI-MS in the reaction mixtures for **7** and **8** (Figure 6.2).

Scheme 6.3. Mercaptides can act as single-electron reductants.



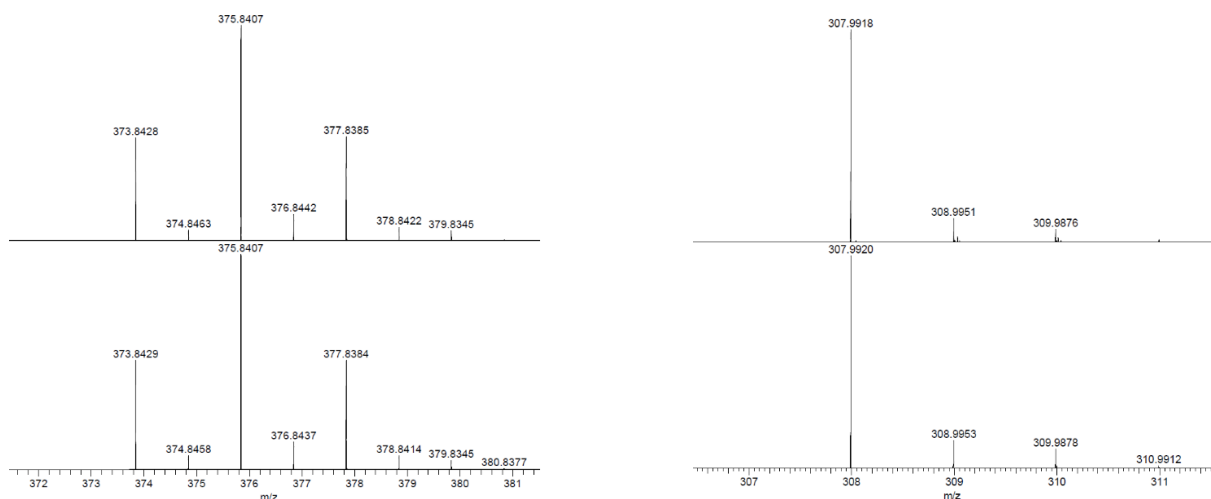


Figure 6.2. ESI spectrum of 1,2-bis(4-bromophenyl)disulfane in crude reaction mixture (left). Experimental spectrum (top) and simulated spectrum (bottom). ESI spectrum of 1,2-bis(4-nitrophenyl)disulfane in crude reaction mixture (right). Experimental spectrum (top) and simulated spectrum (bottom).

The oxidation of **7** and **8** by $[\text{FeCp}^*_2](\text{PF}_6)$ and $[\text{FeCp}_2](\text{PF}_6)$, respectively, lead to the formation of their one-electron oxidized species **7**(PF_6) and **8**(PF_6). And **7**(PF_6) could be crystallized by slow diffusion of diethyl ether into its MeCN solution (Figure 6.3). Single crystals of **8**(PF_6) have not been obtained in sufficient quality.

The molecular structures of **7**, **7**(PF_6), **8** (Figure 6.1 and 6.3) as determined by single-crystal diffraction show the anticipated [2:2] site differentiation with two iron atoms bound to ligand L^5 and the other two iron sites ligated by 4-Br/ NO_2 - $\text{C}_6\text{H}_4\text{S}^-$. Complexes **7** and **8** both crystallize in the hexagonal space group $P6_4$ with two MeCN molecules, whereas **7**(PF_6) crystallizes in space group $C2/c$ with one Et_2O molecules. **7**, **8** are located on a crystallographic twofold axis and contain a distorted central Fe_4S_4 core (Figure 6.1). A comparative analysis of the structure of **7** and **7**(PF_6) is shown in Figure 6.4 and table 6.1. Similar to **6** and **6**(PF_6), the [4Fe-4S] core of **7**(PF_6) shows negligible changes upon oxidation (**7**(PF_6) versus **7**), with Fe-S_C distance showing minor variations ($< 0.01 \text{ \AA}$). Structural changes upon oxidation (**7**(PF_6) versus **7**) mainly occur around the [N]-coordinated iron atoms: the bonds between Fe_N and N decreased by 0.0529 \AA upon oxidation, while bonds between Fe_S and thiolate decreased by 0.0356 \AA , which may indicate that L^5 ligated iron ions were oxidized.

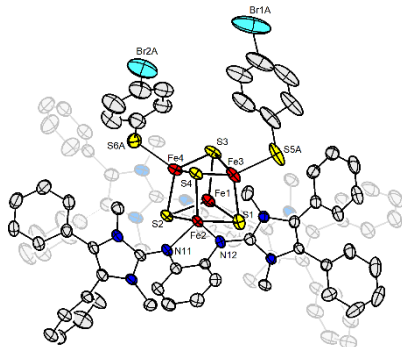


Figure 6.3. Thermal ellipsoid plots (50%) of the cation of **7**(PF_6). Red, yellow, blue, pinkish, lightsteelblue, turquoise and grey ellipsoids represent Fe, S, N, P, F, Br and C, respectively. Hydrogen atoms and solvent molecules are omitted for clarity.

The positive ion electrospray ionization mass spectrometry of complex **7**(PF₆) (Figure 9.2.29, left) shows a peak at $m/z = 1928.1$ corresponding to the ion **[7]**⁺. The positive ion ESI mass spectrometry of complex **8**(PF₆) (Figure 9.2.29, right) shows a peak at $m/z = 1860.1$ corresponding to the ion **[8]**⁺, indicating that ligands **L**⁵ and thiolate (SR⁻) in **7**(PF₆) and **8**(PF₆) are in the same ratio in solution as well as in solid states and do not scramble.

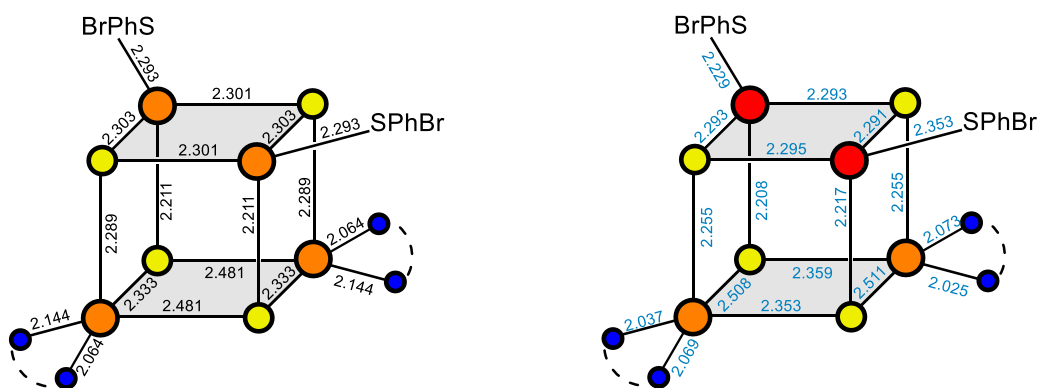


Figure 6.4. Schematics of the Fe_4S_4 cores showing Fe-S distances for **7** (black) and **7**(PF₆) (blue) as determined by XRD. Large spheres = Fe, small yellow spheres = S, small blue spheres = N. Fe sites are colored according to their assigned solid-state valences: $\text{Fe}^{2.5+/2+}$ = orange, Fe^{3+} = red. S_c is the S of the Fe/S core.

Table 6.1. Averaged bond lengths (Å) of clusters **7** and **7**(PF₆).

	7 (Å)	7 (PF ₆) (Å)	Δ (Bond Length)
oxidation state	$[\text{4Fe-4S}]^{2+}$	$[\text{4Fe-4S}]^{3+}$	-
avg $\text{Fe}_N\text{-N}$	2.1040(40)	2.0511(34)	0.0529
avg $\text{Fe}_S\text{-S}_T$	2.2930(19)	2.2574(19)	0.0356
avg $\text{Fe}_S\text{-S}_C$	2.2715(14)	2.2660(13)	0.0055
avg $\text{Fe}_N\text{-S}_C$	2.3675(14)	2.3736(12)	-0.0061
avg Fe-S_C	2.3195(14)	2.3198(13)	0.0003

$\text{S}_T = \text{S}(\text{thiolate}), \text{S}_C = \text{S}(\text{core})$

6.3 Characterization in Solution

The ¹H NMR spectra of $[\text{4Fe-4S}]^{2+}$ complexes **7**, **8** and **9** in THF-d₈, **6** in CD₂Cl₂ (Figure 6.5) exhibit similar distribution and intensity of all peaks between 0 ppm and 8 ppm, which could be attributed to the signals arising from ligand **L**⁵. Two singlets observed at lower field of the spectra of **7** and **8** were assigned to be the *H*-Ar of the thiolato groups.

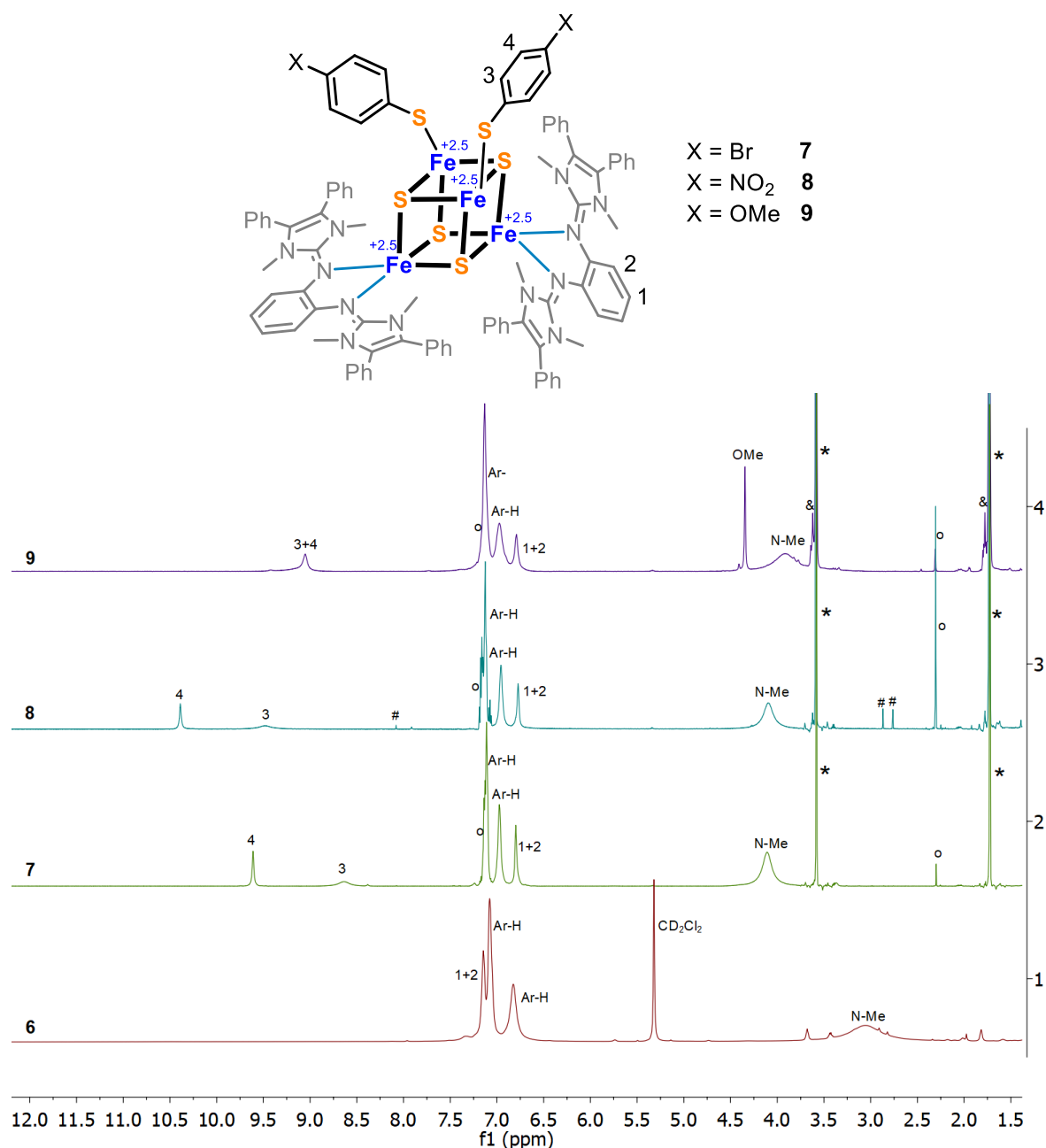


Figure 6.5. ^1H NMR spectra of $[\text{4Fe-4S}]^{2+}$ complexes (**6** recorded in CD_2Cl_2 (500.3 MHz, 298 K), **7** and **8** recorded in THF-d_8 (600.3 MHz, 333 K), **9** recorded in THF-d_8 (300.1 MHz, 298 K)). Signals of the THF-d_8 (*) and residual toluene (°), DMF (#) and THF (&) have been labeled.

Notably, the *H*-Ar of the thiolato groups on **9** shows only one broad peak at around $\delta = 9.2$ ppm, and the assignment was confirmed by its integral which is twice that of the corresponding singlets in **7** and **8**. The signal due to *para*-MeO group on the thiolate ligand of **9** was observed at $\delta = 4.3$ ppm as a singlet.

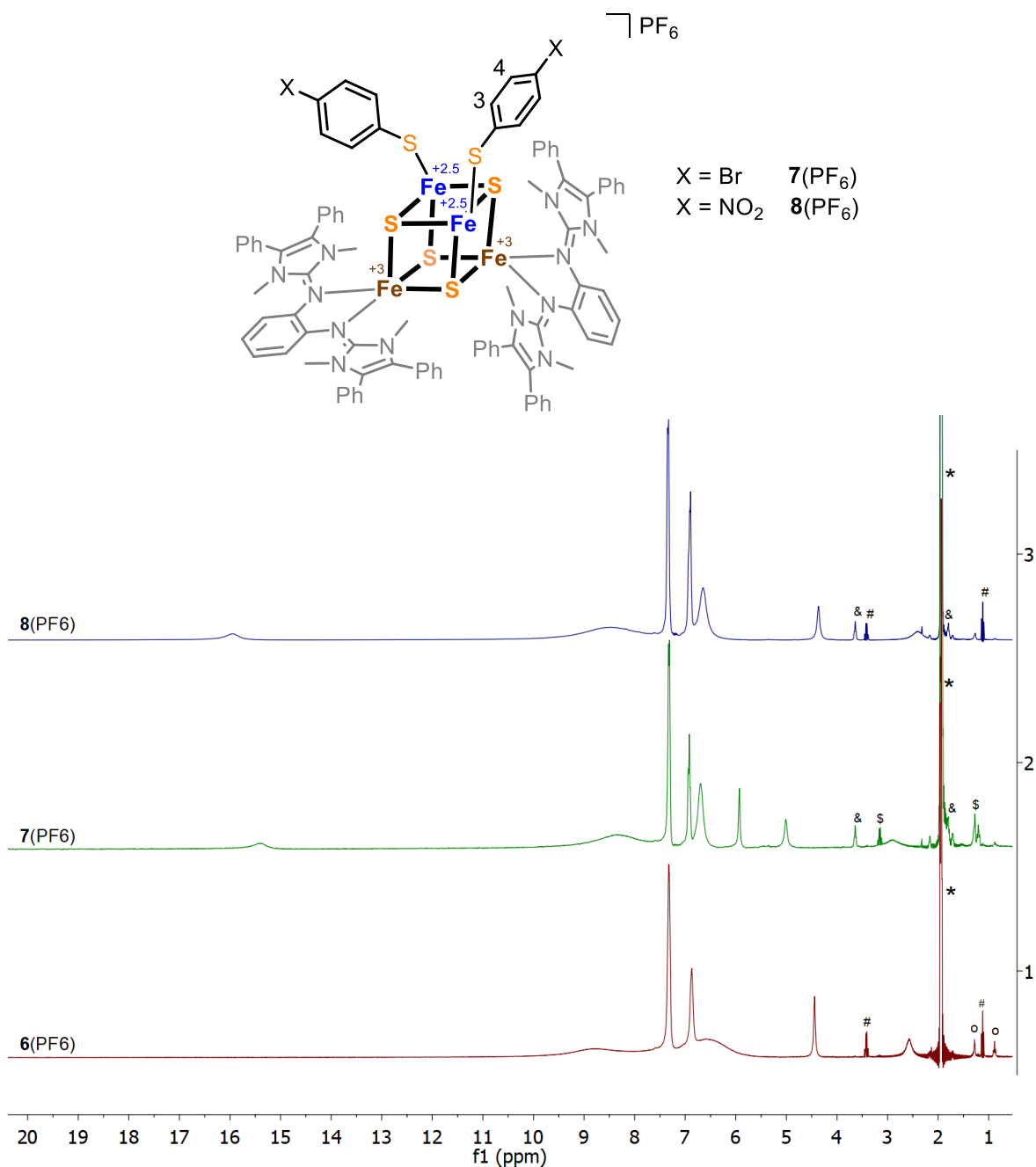


Figure 6.6. ^1H NMR spectra of $[\text{4Fe-4S}]^{3+}$ complexes (**6**(PF_6), **7**(PF_6), **8**(PF_6)) recorded in MeCN-d_3 (300.1 MHz, 298 K). Signals of the CD_3CN (*), residual n -pentane ($^\circ$), THF (&), Et_2O (#) and unknown impurities (§) have been labeled.

The ^1H NMR spectra of complexes **7**(PF_6) and **8**(PF_6) display similar peak patterns and chemical shifts (Figure 6.6) to complexes **6**(PF_6) between 0 ppm and 10 ppm, suggesting that these signals are from the N-donor ligand L^5 . However, due to the strong paramagnetic effect, these peaks are relatively broadened compared with their $[\text{4Fe-4S}]^{2+}$ counterparts. The singlets at around $\delta = 16$ ppm of complexes **7**(PF_6) and **8**(PF_6), which are attributed to be the signals from the respective thiolato groups, are dramatically down-field shifted compared with their $[\text{4Fe-4S}]^{2+}$ analogues. These results indicate that the chemical shift and peak pattern of the ^1H nuclei on the thiolato ligands are significantly influenced by the central metal. The electron-deficient metal center upon oxidation would lead to the flow of the electron density from ligand to metal which might

account for the largely down-field shifted ^1H signals of the thiolato ligands.

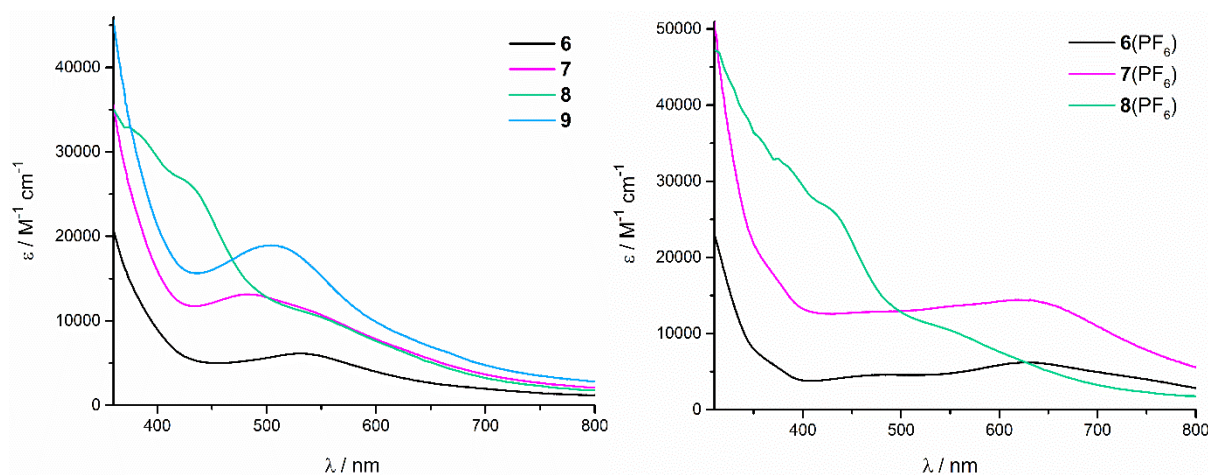


Figure 6.7. UV-vis absorption spectra of **6** (left, black), **7** (left, magenta), **8** (left, green), **9** (left, blue) in THF solution; **6**(PF₆) (right, black) in THF and **7**(PF₆) (right, magenta), **8**(PF₆) (right, green) in MeCN solution at 25 °C.

The UV-vis spectra of complexes **7**, **8** and **9** (Figure 6.7, left) show a broad band at 482 nm, 545 nm and 505 nm respectively. It is noteworthy that the spectrum of **8** is quite different from **6**, **7** and **9**. Except for the broad band (545 nm), **8** also has a broad band at around 360 and 430 nm. The obvious difference of **8** spectrum may be attributed to the special strong electron withdrawing group (NO₂) on its thiolate. Those bands of **7**, **8**, **9** in the visible region were assigned as ligand-to-metal charge transfer transition. The spectra of the thiolate analogues **7**, **8**, **9** have blue shifts in the visible region compared to halide-ligated cluster **6**. A similar blue shift also exists in $[\text{Fe}_4\text{S}_4\text{Cl}_2(\text{Et}_2\text{Dtc})_2]^{2-}$ / $[\text{Fe}_4\text{S}_4(\text{SPh})_2(\text{Et}_2\text{Dtc})_2]^{2-}$ and $[\text{Fe}_4\text{S}_4\text{Cl}_4]^{2-}$ / $[\text{Fe}_4\text{S}_4(\text{S}_4\text{-Pic})_4]^{2-}$.^{[68], [141]} After one-electron oxidation, similar to **6**(PF₆), the UV-vis spectrum of **7**(PF₆) (Figure 6.7, right) also has a significant red shift (630 nm) compared to **7** (482 nm). Yet the UV-vis spectrum of **8**(PF₆) does not change that much after one-electron oxidation (Figure 6.7, right). The monitoring UV-vis spectrum of complex **7** in THF solution at 298 K shows that the complex is very stable (Figure 9.2.27). Variable temperature UV-vis spectra of complex **7**(PF₆) were recorded in MeCN from 288 K to 315 K (Figure 9.2.28). And when the solution of **7**(PF₆) was heated up from 288 K to 315 K, the intensities of all bands decreased a bit, and bands were slightly shifted (Figure 9.2.28). The UV-vis spectra of **7**(PF₆) only decreased a bit after 28 hours in MeCN solution at 298 K, indicating complex **7**(PF₆) is stable in MeCN solution at 298 K.

To gain more insight into the electronic structures of complexes **7**(PF₆) and **8**(PF₆), EPR measurements was performed at 144 K and 133 K, respectively (Figure 6.8), in frozen 2-MeTHF solution. Both show a narrow and almost isotropic spectrum with $g = 1.968$ for complex **7**(PF₆) and 1.965 for complex **8**(PF₆) with no discernable hyperfine interaction indicating their $S = 1/2$ spin state. The g values of **7**(PF₆) and **8**(PF₆) (1.968 and 1.965) are larger than that of the **6**(PF₆) ($g = 1.930$), but smaller than that of most synthesized $[\text{Fe}_4\text{S}_4]^{3+}$ clusters ($g_{\text{av}} \geq 2.0$) as well as those $[\text{Fe}_4\text{S}_4]^{3+}$ clusters in oxidized high-potential iron proteins ($g_{\text{av}} \approx 2.06$). A measurement at lower temperature may provide more information.

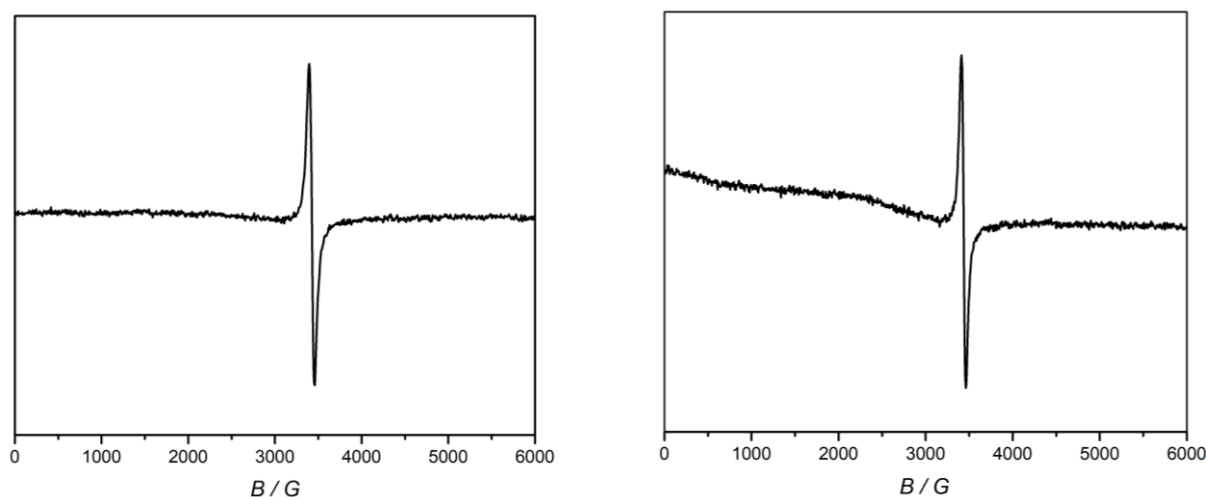


Figure 6.8. EPR spectra of **7**(PF₆) in Me THF measured as frozen glass at 144 K (left) and **8**(PF₆) in Me THF measured as frozen glass at 133 K (right).

6.4 Redox Properties

Redox properties of **7**, **8**, **9** were studied by cyclic voltammetry (CV) in THF solution containing 0.2 M NBu₄PF₆ at room temperature. Their voltammograms are shown in Figure 6.9, 6.11 and potentials are listed in Table 6.2. There are many redox events in the range -3 V to 1 V for complexes **7**, **8** and **9**, revealing their rich redox properties. Complex **7** undergoes two cathodic processes: a chemically reversible oxidation occurs at $E_{1/2} = -0.77$ V assigned to the $[\text{4Fe-4S}]^{2+/3+}$ couple. And beyond that, **7** shows a quasi-reversible peak with half-wave potential $E_{1/2} = -1.75$ V which might reflect the $[\text{4Fe-4S}]^{1+/2+}$ couple when scanning the range of -1.38 to -2.15 V. Both redox events of complex **7** shift cathodically around 100 mV as compared to **6** reflecting the increased electron-donor ability of BrPhS⁻ as compared to Cl⁻. Complexes **8** and **9** both show a reversible redox reaction, corresponding to the $[\text{4Fe-4S}]^{2+/3+}$ couples, with half-wave potentials of -0.68 V and -0.84 V (vs. Fc/Fc⁺), respectively. Yet the reduction further to the $[\text{4Fe-4S}]^{1+}$ of **8** and **9** are both irreversible. For complexes **7**, **8**, **9**, as electron donation ability of the substituents on their thiolate increases, their oxidation potentials decrease (Figure 6.11). The cathodic shift also exists in pyridinethiolate,^[141] benzylthiolate,^[141] phenylthiolate,^[141] (alkanethiolate) RS⁻,^[142] (phenolate) ArO⁻^[142] substitutions compared to their corresponding Cl⁻ ligated $[\text{4Fe-4S}]$ complexes. In addition, the reversibility of the oxidation of complexes **7**, **8**, **9** could be confirmed by a linear relationship of the current vs. the square root of the scan rate (Figure 6.10) and $\Delta E_p = 72\text{--}78$ mV for the separation of anodic and cathodic peak potentials.

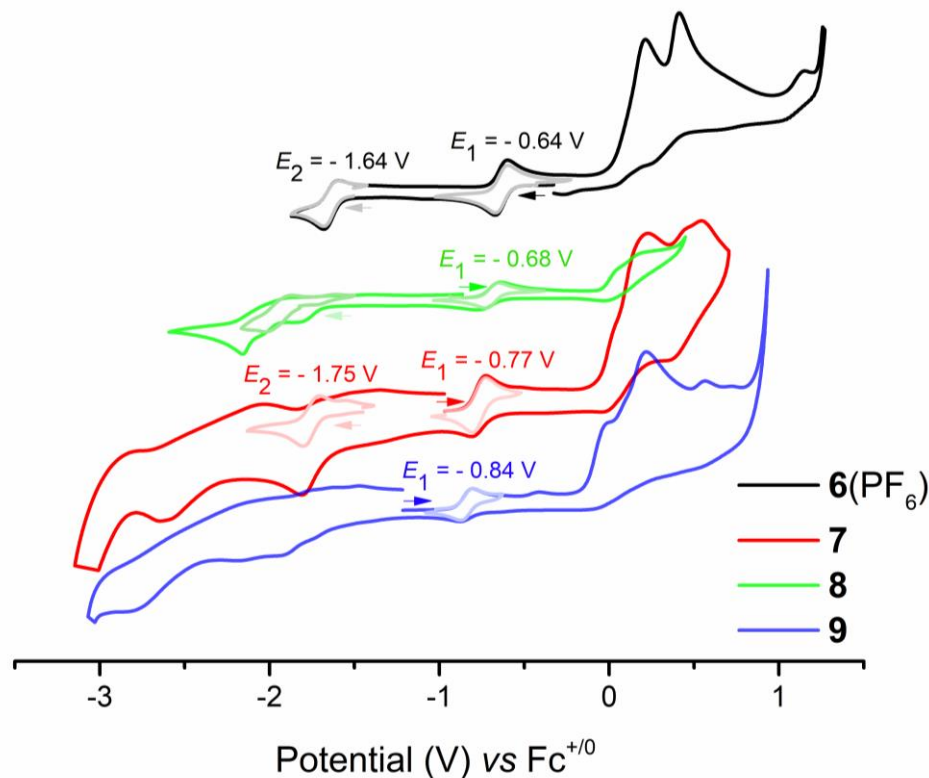


Figure 6.9. Cyclic voltammogram of **6**(PF₆) recorded at rt in MeCN/0.1 M NBu₄PF₆ vs. Fc/Fc⁺, **7**, **8**, **9** recorded at rt in THF/0.2 M NBu₄PF₆ vs. Fc/Fc⁺. Scan rate: 100 mV/s.

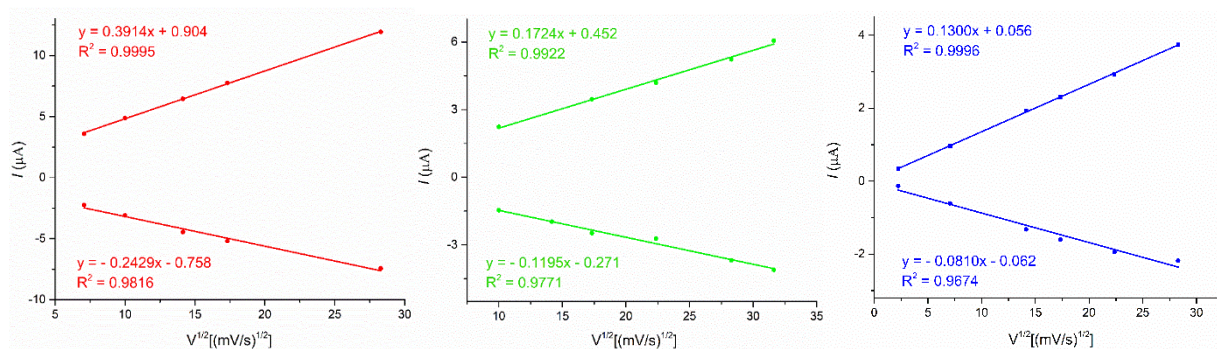


Figure 6.10. Linear dependence of current on square root of scan rate of the forward (top lines) and backward peaks (bottom lines). $[\text{4Fe-4S}]^{3/2+}$ redox couples of **7** (left), **8** (middle) and **9** (right).

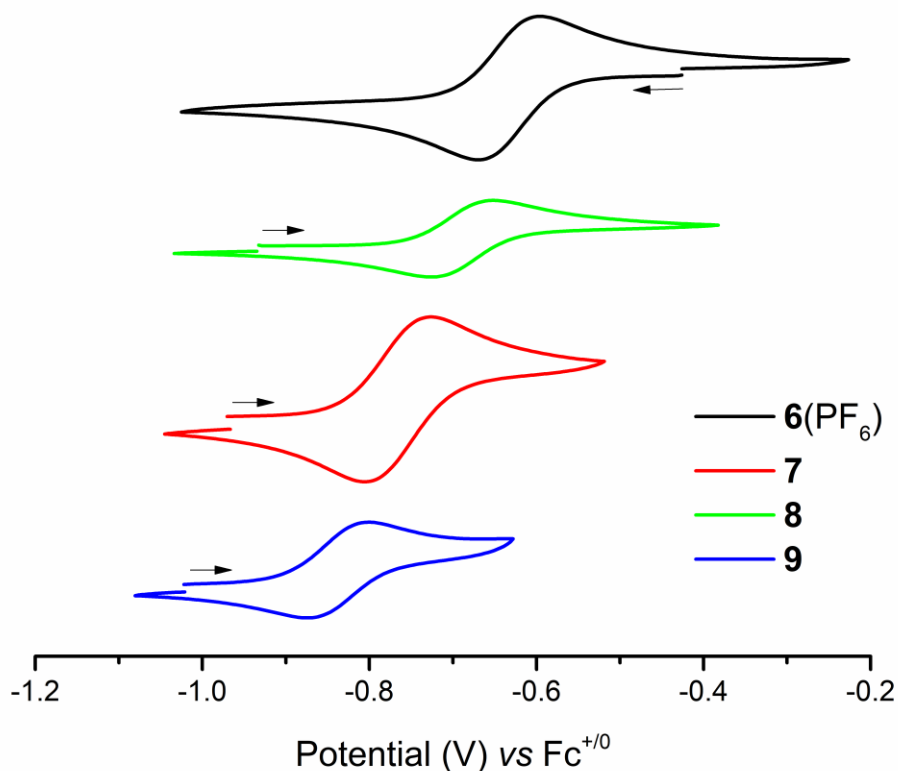


Figure 6.11. Cyclic voltammograms of **6**(PF₆) recorded at rt in MeCN/0.1 M NBu₄PF₆ vs. Fc/Fc⁺, **7**, **8**, **9** recorded at rt in THF/0.2 M NBu₄PF₆ vs. Fc/Fc⁺. Scan rate: 100 mV/s.

Table 6.2. Redox potentials [V] of the clusters **6–9**. All potentials have been converted to the Fc/Fc⁺ couple.

$[\text{4Fe-4S}]^{3/2+}$ complexes	E_1 V $[\text{4Fe-4S}]^{3/2+}$	ΔE_p	E_2 V $[\text{4Fe-4S}]^{2/1+}$	ΔE_p
6	-0.64	72	-1.64	88
7	-0.77	78	-1.75	99
8	-0.68	77	-	-
9	-0.84	72	-	-

In order to detect the electrochemically oxidized species of $[\text{4Fe-4S}]^{2+}$ complexes **7**, **8** and **9**, UV-vis titration experiments were performed by adding oxidants. Here we take the example of the titration of **8** with oxidant $[\text{FeCp}_2](\text{PF}_6)$. The UV-vis titration experiments of cluster **8** with $[\text{FeCp}_2](\text{PF}_6)$ were carried out in THF solution at 298 K (Figure 6.12). In the course of the oxidation, the band at 430 nm disappears, the band at 545 nm shifts a bit, and two shoulders at 360 nm and 440 nm appear. Furthermore, a broad band at about 635 nm develops. Clean conversion to **8**(PF₆) is indicated by two isosbestic points at 300 nm and 505 nm. No new bands appeared, and intensities of the bands were kept stable at rt even overnight indicating that the oxidized species **8**(PF₆) is very stable in THF at rt. Variable temperature UV-vis spectra of

complex **9** were recorded in THF from 298 K to 333 K (Figure 9.2.32). When the solution was heated up from 298 K to 333 K, the intensities of the bands decreased a bit but did not shift, reflecting that complex **9** is stable in THF solution from 288 K to 315 K.

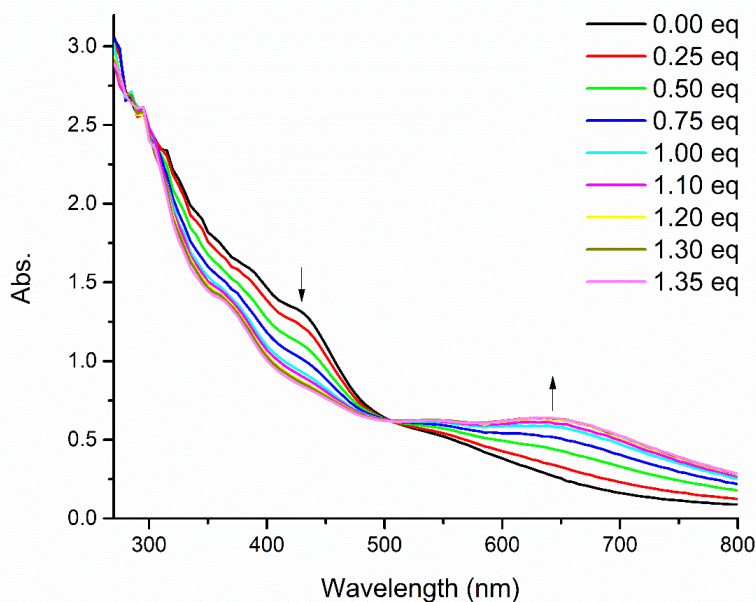


Figure 6.12. UV-vis titration spectra of complex **8** with $[\text{FeCp}_2]\text{PF}_6$ in THF solution at 298 K.

6.5. Characterization in the Solid State

The zero-field ^{57}Fe Mössbauer spectra of the clusters **7**, **8**, and **9** recorded at 80 K are shown in Figures 6.13, 6.14, and 6.15. All spectra were fitted satisfactorily as two doublets with almost 1:1 intensity ratio (Table 6), indicating that there are two different types of iron ions in these $[\text{4Fe-4S}]$ complexes, which is in accordance with their [2:2] site-differentiated configurations. Parameters obtained for clusters **7**, **8**, and **9**, using the same “nested” configuration as cluster **6** were reported in table 6.3. The parameters of clusters **7** ($\delta_1 = 0.47 \text{ mm s}^{-1}$, $\Delta E_{\text{Q1}} = 1.18 \text{ mm s}^{-1}$; $\delta_2 = 0.65 \text{ mm s}^{-1}$, $\Delta E_{\text{Q2}} = 2.00 \text{ mm s}^{-1}$), **8** ($\delta_1 = 0.46 \text{ mm s}^{-1}$, $\Delta E_{\text{Q1}} = 1.10 \text{ mm s}^{-1}$; $\delta_2 = 0.64 \text{ mm s}^{-1}$, $\Delta E_{\text{Q2}} = 1.97 \text{ mm s}^{-1}$) and **9** ($\delta_1 = 0.46 \text{ mm s}^{-1}$, $\Delta E_{\text{Q1}} = 1.20 \text{ mm s}^{-1}$; $\delta_2 = 0.67 \text{ mm s}^{-1}$, $\Delta E_{\text{Q2}} = 1.94 \text{ mm s}^{-1}$) are very similar with each other. And these parameters are comparable to **6** ($\delta_1 = 0.54 \text{ mm s}^{-1}$, $\Delta E_{\text{Q1}} = 1.06 \text{ mm s}^{-1}$; $\delta_2 = 0.64 \text{ mm s}^{-1}$, $\Delta E_{\text{Q2}} = 2.07 \text{ mm s}^{-1}$). The isomer shifts δ_1 of clusters **7**, **8** and **9**, in the range 0.46–0.47 mm s^{-1} , should be attributed to thiolate coordinated iron sites (four-coordinate iron sites) and assigned as $\text{Fe}^{2.5+}$,^[55] and the isomer shift δ_2 , in the range 0.64–0.67 mm s^{-1} , is assigned to ligand L^5 ligated iron sites (five-coordinate iron sites) also assigned as $\text{Fe}^{2.5+}$. The difference of iron coordination number (five-coordinate or four-coordinate) lead to the change of isomer shifts (δ_1 , δ_2). All these parameters correspond well to those found for $[\text{4Fe-4S}]^{2+}$ clusters: $(\text{Ph}_4\text{P})_2[\text{Fe}_4\text{S}_4(\text{Cl})_2(\text{Et}_2\text{Dtc})_2]$ ($\delta_1 = 0.53 \text{ mm s}^{-1}$, $\Delta E_{\text{Q1}} = 1.06 \text{ mm s}^{-1}$; $\delta_2 = 0.62 \text{ mm s}^{-1}$, $\Delta E_{\text{Q2}} = 1.85 \text{ mm s}^{-1}$), $(\text{Ph}_4\text{P})_2[\text{Fe}_4\text{S}_4(\text{Cl})_3(\text{Et}_2\text{Dtc})]$ ($\delta_1 = 0.51 \text{ mm s}^{-1}$, $\Delta E_{\text{Q1}} = 1.07 \text{ mm s}^{-1}$; $\delta_2 = 0.64 \text{ mm s}^{-1}$, $\Delta E_{\text{Q2}} = 2.13 \text{ mm s}^{-1}$), and $(\text{Ph}_4\text{P})_2[\text{Fe}_4\text{S}_4(\text{SPh})_2(\text{Et}_2\text{Dtc})_2]$ ($\delta_1 = 0.47 \text{ mm s}^{-1}$, $\Delta E_{\text{Q1}} = 1.06 \text{ mm s}^{-1}$; $\delta_2 = 0.64 \text{ mm s}^{-1}$, $\Delta E_{\text{Q2}} = 1.84 \text{ mm s}^{-1}$)^[68].

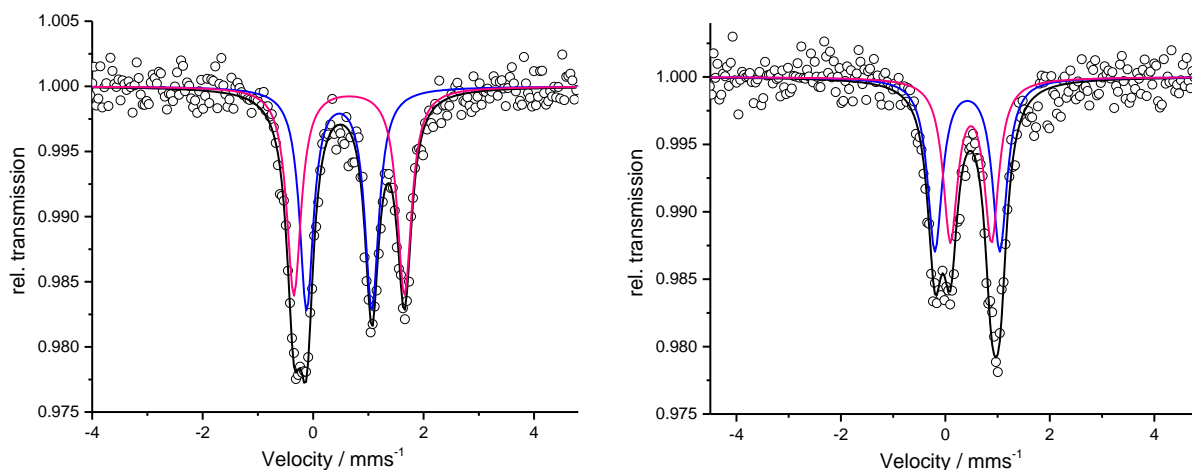


Figure 6.13. Zero-field ^{57}Fe Mössbauer spectra of solid **7** (left), **7**(PF_6) (right) at 80 K. Simulation of the data led to the following parameters: (left) $\delta_1 = 0.47 \text{ mm s}^{-1}$, $\Delta E_{Q1} = 1.18 \text{ mm s}^{-1}$ (blue) (51%), $\delta_2 = 0.65 \text{ mm s}^{-1}$, $\Delta E_{Q2} = 2.00 \text{ mm s}^{-1}$ (red) (49%); (right) $\delta_1 = 0.42 \text{ mm s}^{-1}$, $\Delta E_{Q1} = 1.24 \text{ mm s}^{-1}$ (blue) (52%), $\delta_2 = 0.49 \text{ mm s}^{-1}$, $\Delta E_{Q2} = 0.79 \text{ mm s}^{-1}$ (red) (48%).

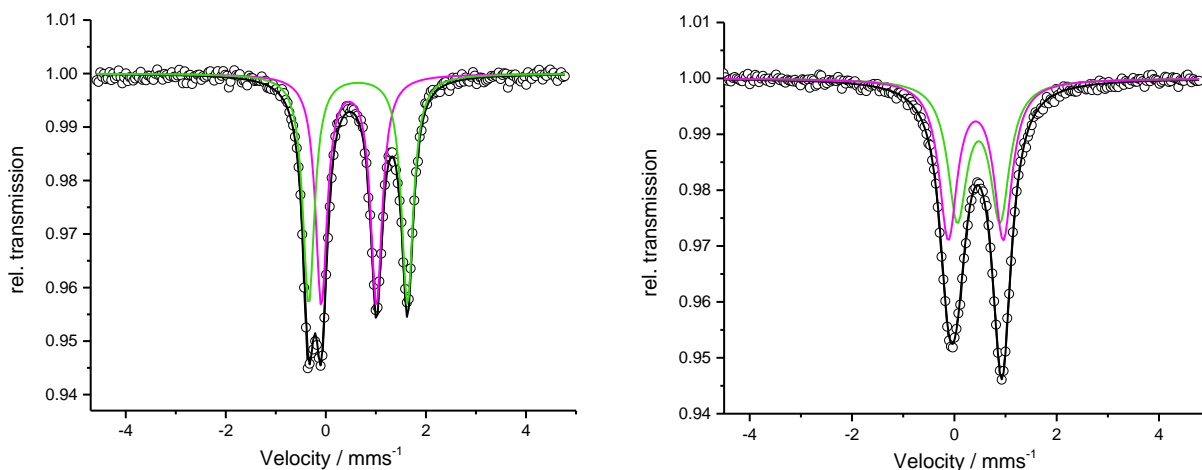


Figure 6.14. Zero-field ^{57}Fe Mössbauer spectra of solid **8** (left), **8**(PF_6) (right) at 80 K. Simulation of the data led to the following parameters: (left) $\delta_1 = 0.46 \text{ mm s}^{-1}$, $\Delta E_{Q1} = 1.10 \text{ mm s}^{-1}$ (magenta) (50%), $\delta_2 = 0.64 \text{ mm s}^{-1}$, $\Delta E_{Q2} = 1.97 \text{ mm s}^{-1}$ (greenish) (50%); (right) $\delta_1 = 0.42 \text{ mm s}^{-1}$, $\Delta E_{Q1} = 1.08 \text{ mm s}^{-1}$ (magenta) (52%), $\delta_2 = 0.47 \text{ mm s}^{-1}$, $\Delta E_{Q2} = 0.83 \text{ mm s}^{-1}$ (greenish) (48%).

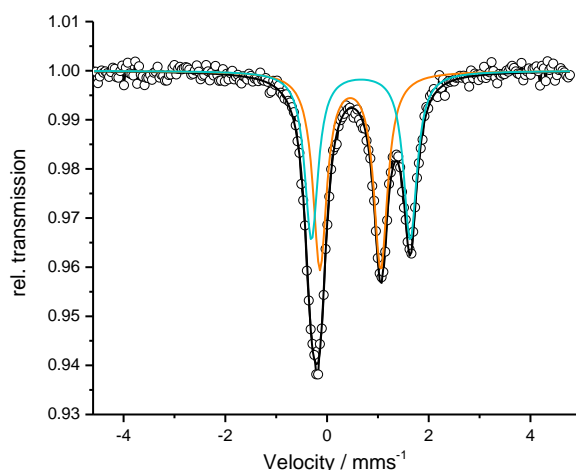


Figure 6.15. Zero-field ⁵⁷Fe Mössbauer spectra of solid **9** at 80 K. Simulation of the data led to the following parameters: $\delta_1 = 0.46 \text{ mm s}^{-1}$ and $\Delta E_{Q1} = 1.20 \text{ mm s}^{-1}$ (orange) (54%), $\delta_2 = 0.67 \text{ mm s}^{-1}$ and $\Delta E_{Q2} = 1.94 \text{ mm s}^{-1}$ (turquoise) (46%).

Table 6.3. Solid state ⁵⁷Fe Mössbauer parameters [mm s^{-1}] for [4Fe-4S]²⁺ complexes **6-9**, [Fe₄S₄X₂(Et₂Dtc)₂]²⁻ and [Fe₄S₄Cl₃(Et₂Dtc)]²⁻ at 80 K and 77 K (X = SPh, Cl).

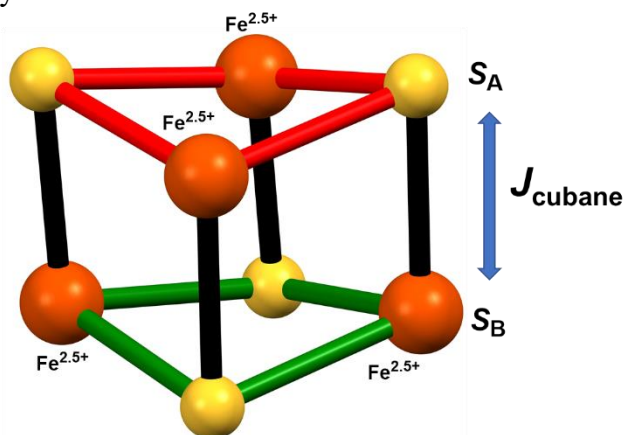
[4Fe-4S] ²⁺ complexes	T, K	δ_1	ΔE_{Q1}	δ_2	ΔE_{Q2}	Ratio 1:2
[Fe ₄ S ₄ L ⁵ ₂ (4-Br-C ₆ H ₄ S) ₂], 7	80	0.47	1.18	0.65	2.00	51:49
[Fe ₄ S ₄ L ⁵ ₂ (4-NO ₂ -C ₆ H ₄ S) ₂], 8	80	0.46	1.10	0.64	1.97	50:50
[Fe ₄ S ₄ L ⁵ ₂ (4-OMe-C ₆ H ₄ S) ₂], 9	80	0.46	1.20	0.67	1.94	54:46
[Fe ₄ S ₄ L ⁵ ₂ Cl ₂], 6	80	0.54	1.06	0.64	2.07	51:49
(Ph ₄ P) ₂ [Fe ₄ S ₄ (Cl) ₂ (Et ₂ Dtc) ₂]	77	0.53	1.06	0.62	1.85	-
(Ph ₄ P) ₂ [Fe ₄ S ₄ (SPh) ₂ (Et ₂ Dtc) ₂]	77	0.47	1.06	0.64	1.84	-
(Ph ₄ P) ₂ [Fe ₄ S ₄ (Cl) ₃ (Et ₂ Dtc)]	77	0.51	1.07	0.64	2.13	-

Parameters obtained for clusters **7**(PF₆) and **8**(PF₆), using the same “nested” configuration as cluster **6**(PF₆) were reported in table 6.4. The Mössbauer spectrum of cluster **7**(PF₆) (Figure 6.13, right) shows distinct two doublets with a ratio of almost 1:1 ($\delta_1 = 0.42 \text{ mm s}^{-1}$, $\Delta E_{Q1} = 1.24 \text{ mm s}^{-1}$; $\delta_2 = 0.49 \text{ mm s}^{-1}$, $\Delta E_{Q2} = 0.79 \text{ mm s}^{-1}$). In contrast, the Mössbauer spectrum of cluster **8**(PF₆) (Figure 6.14, right) shows “one” broad doublet which was simulated by two different iron centers with a ratio of almost 1:1 ($\delta_1 = 0.42 \text{ mm s}^{-1}$, $\Delta E_{Q1} = 1.08 \text{ mm s}^{-1}$; $\delta_2 = 0.47 \text{ mm s}^{-1}$, $\Delta E_{Q2} = 0.83 \text{ mm s}^{-1}$). For both clusters **7**(PF₆) and **8**(PF₆), the smaller isomer shift (δ_1) should be assigned to thiolate ligated iron ions (four-coordinate iron sites), and the larger isomer shifts (δ_2) should be attributed to ligand L⁵ coordinated iron ions (five-coordinate iron sites). Comparing to reduced species (**7**, **8**), the doublet 2 (δ_2 , ΔE_{Q2}) of the oxidized species (**7**(PF₆), **8**(PF₆)) changed much more than doublet 1 (δ_1 , ΔE_{Q1}), which demonstrates oxidation happened at N-coordinated iron sites.

Table 6.4. Solid state ⁵⁷Fe Mössbauer parameters [mm s⁻¹] for [4Fe-4S]³⁺ complexes **7**(PF₆), **8**(PF₆), **6**(PF₆) at 80 K.

[4Fe-4S] ³⁺ complexes	δ_1	ΔE_{Q1}	δ_2	ΔE_{Q2}	Ratio 1:2
[Fe ₄ S ₄ L ₅ (4-Br C ₆ H ₄ S) ₂](PF ₆), 7 (PF ₆)	0.42	1.24	0.49	0.79	52:48
[Fe ₄ S ₄ L ₅ (4-NO ₂ -C ₆ H ₄ S) ₂](PF ₆), 8 (PF ₆)	0.42	1.08	0.47	0.83	52:48
[Fe ₄ S ₄ L ₅ Cl ₂](PF ₆), 6 (PF ₆)	0.47	0.82	0.49	1.10	52:48

The temperature-dependent magnetic susceptibility measurements for the complexes **7**, [**7**]⁺, **8** and [**8**]⁺ were carried out under 0.5 T applied field in the range of 2–300 K for **7**, [**7**]⁺, **8** and 2–200 K for [**8**]⁺. The $\chi_M T$ value for the [4Fe-4S]²⁺ clusters **7** and **8** at 300 K is 0.64 and 0.55 cm³ mol⁻¹ K, respectively. The $\chi_M T$ value decreases linearly on cooling due to thermal depopulation of the excited states signifying strong intramolecular antiferromagnetic interactions with a diamagnetic spin ground state ($S_T = 0$) for the [4Fe-4S]²⁺ cluster (Figure 6.16 and 6.17).^{[87], [120], [129], [130]} A small residual moment at lower temperatures is probably due to the presence of unidentified paramagnetic impurities. The [4Fe-4S]²⁺ cluster in **7** and **8** contains two pairs of delocalised mixed-valence Fe^{2.5+}Fe^{2.5+} “rhombs” ($S = 9/2$) as indicated by the isomer shifts for the two doublets observed in the ⁵⁷Fe Mössbauer spectrum of **7** and **8** at 80 K.^{[61], [131], [48]} The experimental data was modelled with few assumptions were made built on previous theoretical and spectroscopic studies.^{[132], [133], [134]} The double-exchange phenomenon among the delocalised mixed-valence [Fe^{2.5+}Fe^{2.5+}] pair leads to a ferromagnetic coupling with $S = 9/2$ in the two “rhombs”. Based on previous spectroscopic studies, the double-exchange interaction within the [Fe^{2.5+}Fe^{2.5+}] pair is considered very strong and they are treated as a single spin ($S = 9/2$). The antiferromagnetic exchange coupling among the two $S = 9/2$ “rhombs” leads to a diamagnetic ground spin-state ($S_T = 0$). The experimental data was modelled using the *JulX* program by using the Heisenberg-Dirac-van-Vleck (HDvV) spin Hamiltonian, as shown in equation 5.1, where J_{cubane} represents the magnetic exchange coupling constant between the two S_A and S_B “rhombs” with $S = 9/2$ (Figure 6.16 top). The temperature-independent paramagnetism (*TIP*) and paramagnetic impurities (*PI*) were included according to $\chi_{\text{calc}} = (1 - PI) \cdot \chi + PI \cdot \chi_{\text{mono}} + TIP$. The best fit to the experimental data leads to $J_{\text{cubane}} = -146 \text{ cm}^{-1}$ and $J_{\text{cubane}} = -143 \text{ cm}^{-1}$ for **7** and **8**, respectively.



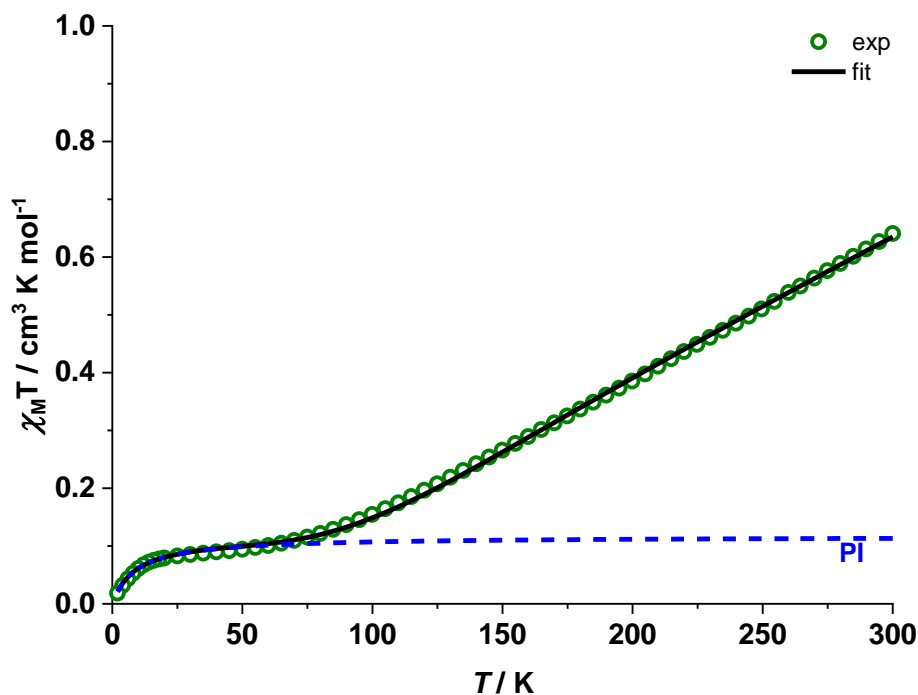


Figure 6.16. (Top) The magnetic exchange interaction between the delocalized mixed-valence $[\text{Fe}^{2+}\text{Fe}^{3+}] \text{Fe}$ “rhombs” within the cubane. J_{cubane} is the exchange energy between two S_A and S_B “rhombs” with $S = 9/2$. (Bottom) Temperature dependence of $\chi_M T$ for **7** at an applied dc field of 0.5 T. The solid black line represents the calculated curve fit with the parameters $J_{\text{cubane}} = -146 \text{ cm}^{-1}$, $PI = 2.7\%$ and $TIP = 450 \cdot 10^{-6} \text{ cm}^3 \text{mol}^{-1}$ with $g = 2.0$ (fixed).

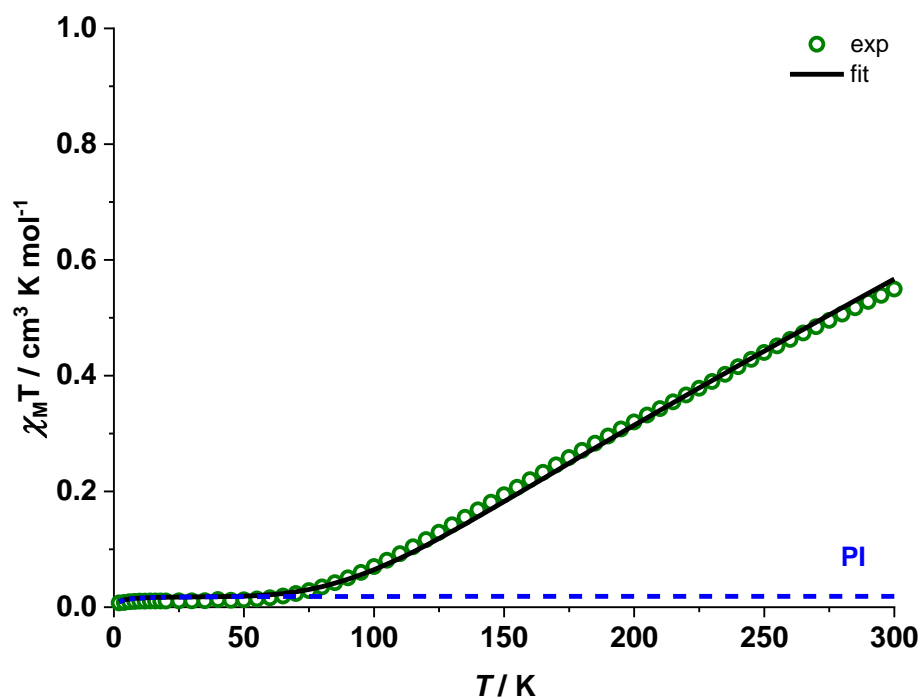


Figure 6.17. Temperature dependence of $\chi_M T$ for **8** at an applied dc field of 0.5 T. The solid black line represents the calculated curve fit with the parameters $J_{\text{cubane}} = -143 \text{ cm}^{-1}$, $PI = 0.4\%$ and $TIP = 100 \cdot 10^{-6} \text{ cm}^3 \text{mol}^{-1}$ with $g = 2.0$ (fixed).

The $\chi_{\text{M}}T$ value for $[\mathbf{7}]^+$ and $[\mathbf{8}]^+$ is $0.91 \text{ cm}^3 \text{ mol}^{-1} \text{ K}$ at 300 K and $0.97 \text{ cm}^3 \text{ mol}^{-1} \text{ K}$ at 200 K, respectively, and linearly decreases on cooling before reaching a plateau around 80 K indicating a paramagnetic ground spin-state ($S_{\text{T}} = 1/2$) (Figure 6.18 and 6.19). Similar magnetic behaviour has been observed in other oxidized $[\text{4Fe-4S}]^{3+}$ clusters exhibiting dominant intramolecular antiferromagnetic interactions.^{[23], [135]} The 1:1 doublet in the ^{57}Fe Mössbauer spectrum of $[\mathbf{7}]^+$ and $[\mathbf{8}]^+$ indicates that the high-spin iron sites in oxidized $[\text{4Fe-4S}]^{3+}$ cluster exists in pairs, the delocalized $[\text{Fe}^{2.5+}\text{Fe}^{2.5+}]$ ($S = 9/2$) pair and localized $[\text{Fe}^{3+}\text{Fe}^{3+}]$ pair. The resulting antiferromagnetic coupling between the mixed-valence $[\text{Fe}^{2.5+}\text{Fe}^{2.5+}]$ ($S = 9/2$) “rhomb” and the spin-aligned $[\text{Fe}^{3+}\text{Fe}^{3+}]$ “rhomb” ($S = 5$) results in the net spin of $S_{\text{T}} = 1/2$ in the ground state as observed in $[\text{4Fe-4S}]^{3+}$ cluster.^{[23], [135], [136]} The temperature dependent experimental data was modelled using the Heisenberg-Dirac-van-Vleck (HDvV) spin Hamiltonian, as shown in equation 5.1, where J_{cubane} represents the magnetic exchange coupling constant between the two S_{A} ($S = 9/2$) and S_{B} ($S = 5$) “rhombs”. The best fit to the experimental data leads to $J_{\text{cubane}} = -111 \text{ cm}^{-1}$ and $J_{\text{cubane}} = -97 \text{ cm}^{-1}$ for $[\mathbf{7}]^+$ and $[\mathbf{8}]^+$ respectively. The simulations were based on the assumptions mentioned above, while considering Fe^{3+} sites as individual spin leads to many solutions with large deviations.

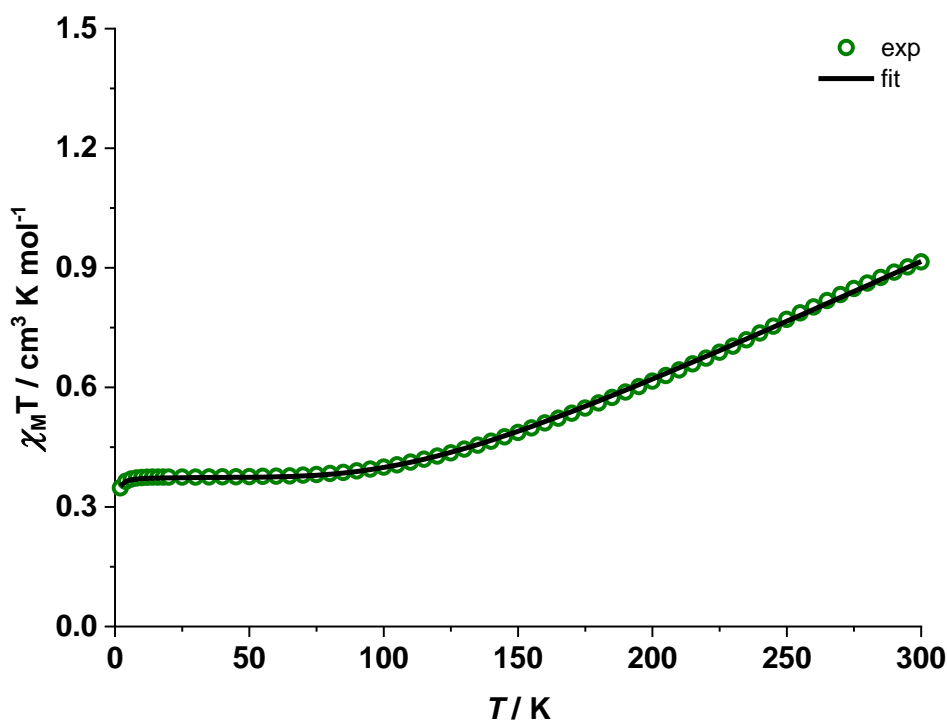


Figure 6.18. Temperature dependence of $\chi_{\text{M}}T$ for $\mathbf{7}(\text{PF}_6)$ at an applied dc field of 0.5 T. The solid black line represents the calculated curve fit with the parameters $J_{\text{cubane}} = -111 \text{ cm}^{-1}$, $\theta = -0.11 \text{ K}$, $PI = 0\%$ and $TIP = 930 \cdot 10^{-6} \text{ cm}^3 \text{ mol}^{-1}$ with $g = 2.0$ (fixed).

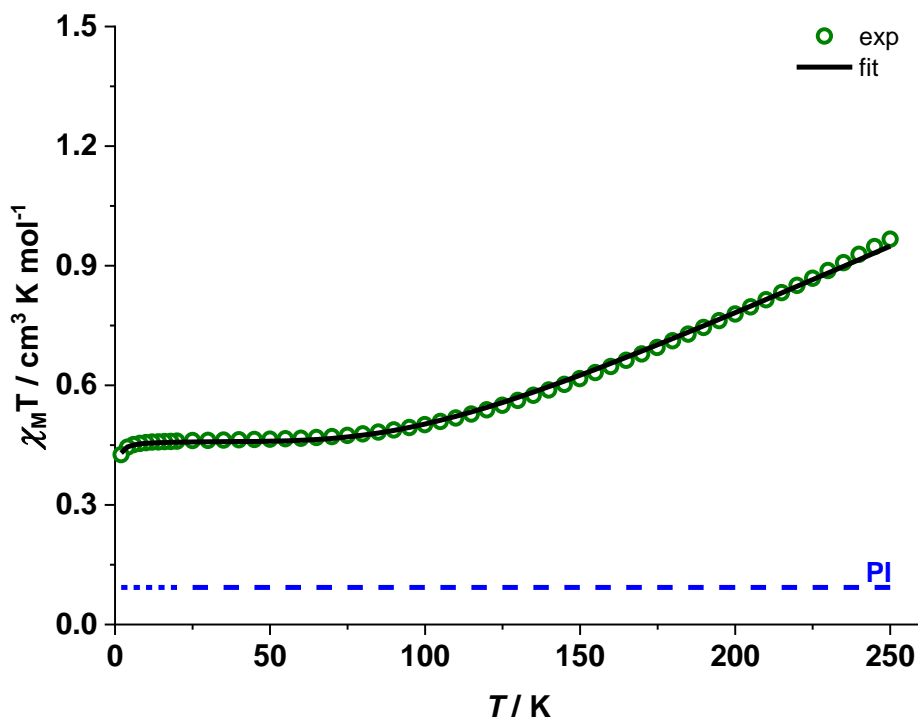
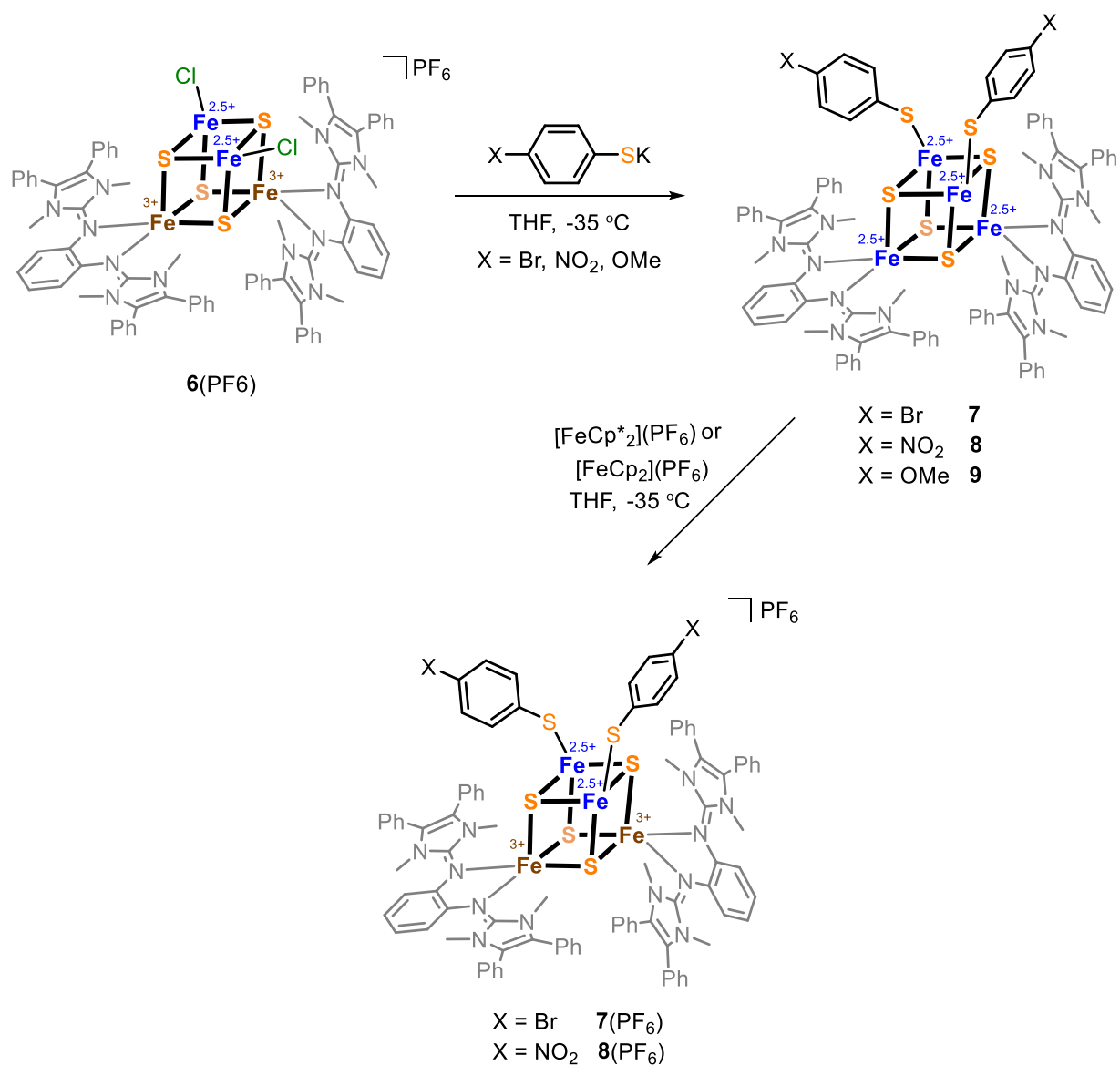


Figure 6.19. Temperature dependence of $\chi_M T$ for **8**(PF₆) at an applied dc field of 0.5 T. The solid black line represents the calculated curve fit with the parameters $J_{\text{cubane}} = -97 \text{ cm}^{-1}$, $\theta = -0.16 \text{ K}$, $PI = 2.1\%$ and $TIP = 910 \cdot 10^{-6} \text{ cm}^3 \text{ mol}^{-1}$ with $g = 2.0$ (fixed).

6.6 Conclusions

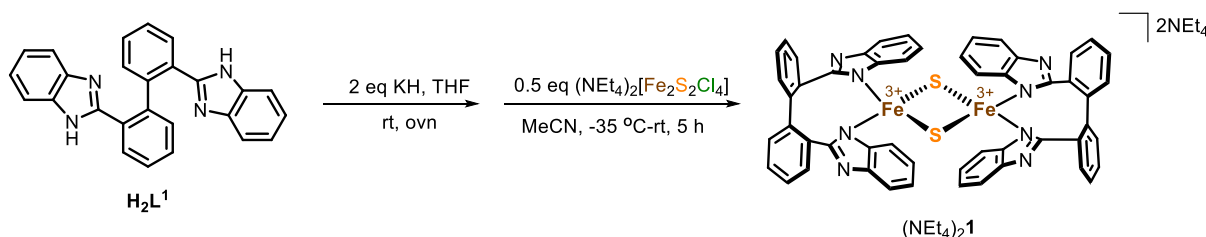
In summary, a series of [2:2] site-differentiated $[\text{4Fe-4S}]^{2+}$ complexes **7**, **8**, **9**, as well as their one-electron oxidized species **7**(PF₆) and **8**(PF₆) were synthesized, characterized and their redox properties were investigated. Structural data and Mössbauer analyses show that redox events predominantly happen on the imidazoline-2-imine ligated iron sites. CV studies of complexes **7**, **8** and **9** show that as the electron donation ability of the substituents on their thiolate increases, their $[\text{4Fe-4S}]^{2+/3+}$ redox potentials decrease. The detailed research of these complexes deepened our understanding of $[\text{4Fe-4S}]$ clusters.



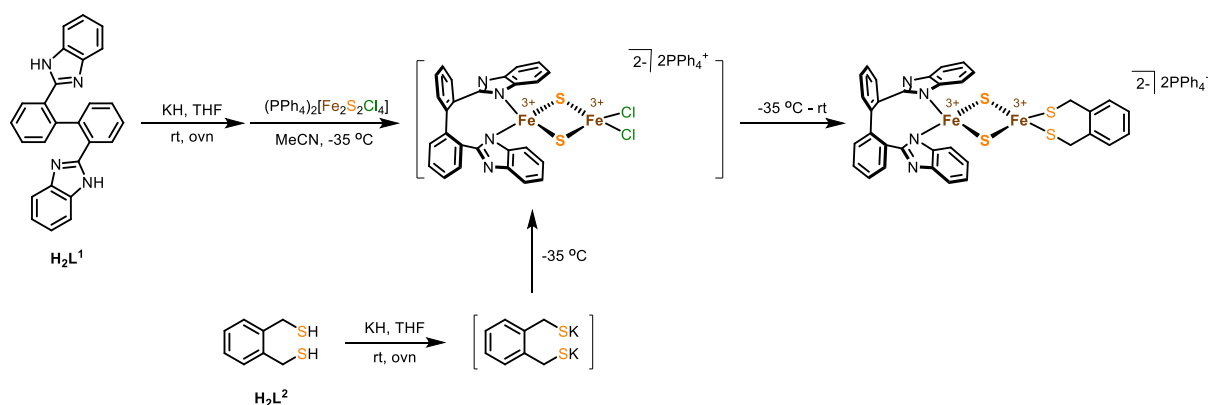
Chapter 7. Summary

The work described in this thesis mainly achieved the syntheses of symmetrically ligated cluster $(\text{NEt}_4)_2[\text{Fe}_2\text{S}_2\text{L}^1_2]$ ($(\text{NEt}_4)_2\mathbf{1}$) and asymmetrically ligated cluster $(\text{PPh}_4)_2[\text{Fe}_2\text{S}_2\text{L}^1\text{L}^2]$ ($(\text{PPh}_4)_2\mathbf{2}$) (Chapter 2 and 3), which are new models of Rieske-type [2Fe-2S] clusters. $(\text{NEt}_4)_2\mathbf{1}$ was fully characterized and its redox properties were also investigated. In order to obtain [2Fe-2S] clusters with high reduction potentials like their natural counterparts, neutral bidentate imidazoline-2-imine ligands (\mathbf{L}^5 and \mathbf{L}^6) were designed. The successful syntheses of the FeL^5Cl_2 ($\mathbf{3}$), NiL^5Br_2 ($\mathbf{4}$), and NiL^6Br_2 ($\mathbf{5}$) by the reaction of some halide salts ($\text{FeCl}_2\cdot\text{THF}$, $\text{NiBr}_2\cdot\text{DME}$) with the corresponding imidazoline-2-imine ligands (\mathbf{L}^5 or \mathbf{L}^6) (Chapter 4) demonstrated the ability of these neutral ligands to coordinate transition metal iron, especially iron ions. Therefore, these neutral ligands were used to synthesize Fe/S cluster. A series of 2:2 site-differentiated [4Fe-4S] clusters, $[\text{Fe}_4\text{S}_4\text{L}^5_2\text{Cl}_2](\text{PF}_6)$ ($\mathbf{6}(\text{PF}_6)$), $[\text{Fe}_4\text{S}_4\text{L}^5_2\text{Cl}_2]$ ($\mathbf{6}$), and their derivatives, $[\text{Fe}_4\text{S}_4\text{L}^5_2(4\text{-Br-C}_6\text{H}_4\text{S})_2]$ $\mathbf{7}$, $[\text{Fe}_4\text{S}_4\text{L}^5_2(4\text{-Br-C}_6\text{H}_4\text{S})_2](\text{PF}_6)$ $\mathbf{7}(\text{PF}_6)$, $[\text{Fe}_4\text{S}_4\text{L}^5_2(4\text{-NO}_2\text{-C}_6\text{H}_4\text{S})_2]$ $\mathbf{3}$, $[\text{Fe}_4\text{S}_4\text{L}^5_2(4\text{-Br-C}_6\text{H}_4\text{S})_2](\text{PF}_6)$ $\mathbf{3}(\text{PF}_6)$, $[\text{Fe}_4\text{S}_4\text{L}^5_2(4\text{-OMe-C}_6\text{H}_4\text{S})_2]$ $\mathbf{4}$), were isolated and comprehensively characterized, and their redox properties were also investigated (Chapter 5 and 6).

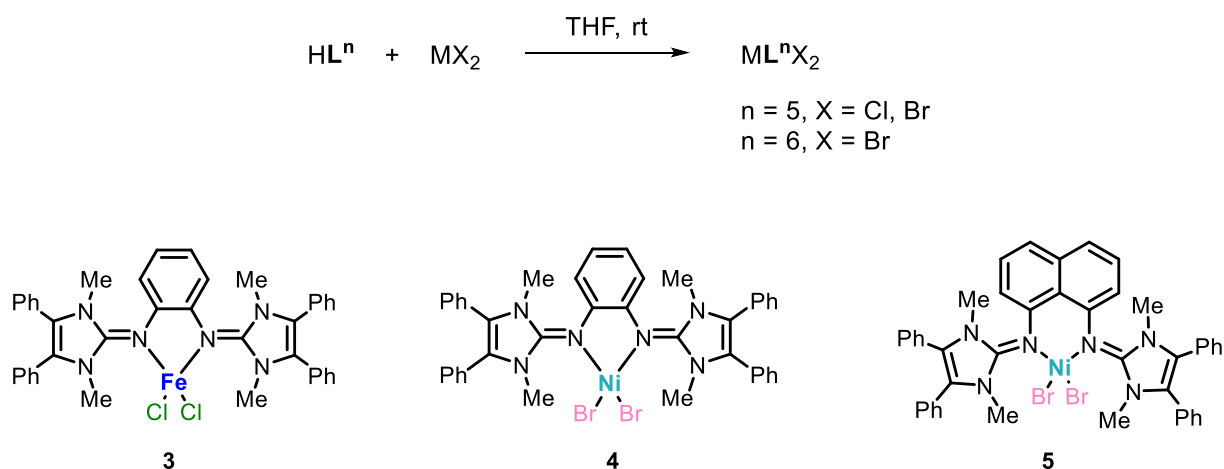
Scheme 7.1 Synthetic approaches for modified Rieske-type [2Fe-2S] cluster $(\text{NEt}_4)_2\mathbf{1}$.



Rieske-type [2Fe-2S] clusters are special biological transfer cofactors featuring two histidine and two cysteine ligands. In biological Rieske-type [2Fe-2S] clusters, the dihedral angles between the two imidazole rings of two histidine residues are near perpendicularity. However, in reported [2Fe-2S] clusters, the dihedral angles ($3^\circ\text{-}48^\circ$) are much smaller than 90° . In the present work it was tried to synthesize [2Fe-2S] clusters in which the dihedral angles are close to 90° in order to investigate the effect of such perpendicular arrangement on their properties. In order to imitate this coordination model ($\angle(\text{Im}/\text{Im}) \approx 90^\circ$), the ligand \mathbf{L}^1 with a large and rigid bridge linking two (benz-)imidazoles was used to synthesize a [2Fe-2S] cluster. A homoleptically coordinated [2Fe-2S] cluster ($(\text{NEt}_4)_2\mathbf{1}$) ligated by two ligands \mathbf{L}^1 was synthesized (Scheme 7.1) and investigated. The dihedral angle between the two imidazole rings in $(\text{NEt}_4)_2\mathbf{1}$ is 75° , which is much closer to 90° compared to the previously reported [2Fe-2S] models. The small quadrupole splitting of $(\text{NEt}_4)_2\mathbf{1}$ ($\Delta E_Q = 0.27 \text{ mm s}^{-1}$) reflects the decreased electric field gradient resulting from the higher symmetry of electronic charge distribution. Electrochemical studies show that diferric $(\text{NEt}_4)_2\mathbf{1}$ exhibits one reversible redox event for $\mathbf{1}^{2/3-}$. In addition, UV-vis titration experiments show that $(\text{NEt}_4)_2\mathbf{1}$ can be reduced and that the mixed-valent species is stable around one hour.

Scheme 7.2 Synthetic approach for Rieske-type [2Fe-2S] cluster (PPh₄)₂**2**.

Besides cluster (NEt₄)₂**1** with homoleptic ligand environment, heteroleptically coordinated Rieske-type cluster ((PPh₄)₂**2**) coordinated with ligand **L**¹ ([N]-ligand) and ligand **L**² ([S]-ligand) was synthesized by consecutive salt metathesis reaction (Scheme 7.2). The structure of (PPh₄)₂**2** was confirmed by X-ray crystallography. The purification of (PPh₄)₂**2** is very challenging because of the preferred formation of the homoleptic-coordinated byproducts. New synthesis methods for (PPh₄)₂**2** still need to be explored, and one possible way might be the stepwise ligands exchange strategy with isolation of the intermediate species.

Scheme 7.3 Synthetic approaches for mononuclear complexes **3**, **4**, **5**.**Figure 7.1.** Mononuclear complexes **3**, **4**, **5** with neutral imidazoline-2-imine ligand.

Most synthetic Fe/S clusters are coordinated by anionic ligands, and have much more negative reduction potentials than their natural counterparts. To obtain Fe/S clusters with a higher reduction potential, neutral imidazoline-2-imine ligands (**L**⁵ and **L**⁶) with strong nucleophilicity were synthesized and their metalation has been investigated. The imidazoline-2-imine ligands **L**⁵ and **L**⁶ show a strong tendency to chelate metals: complexes **FeL**⁵**Cl**₂ (**3**), **NiL**⁵**Br**₂ (**4**), and **NiL**⁶**Br**₂ (**5**) could be easily synthesized by the reaction of metal(II) halide salts (FeCl₂·THF, NiBr₂·DME) with the corresponding ligands (**L**⁵ or **L**⁶) (Scheme 7.3, Figure 7.1). The elongation of the C=N bonds after bonding to transition metal salts reflects that there is an effective charge delocalization within the guanidine CN₃ units, serving as an electron reservoir of the neutral ligands. Thus, these neutral ligands were further applied in the synthesis of [2Fe-2S] clusters.

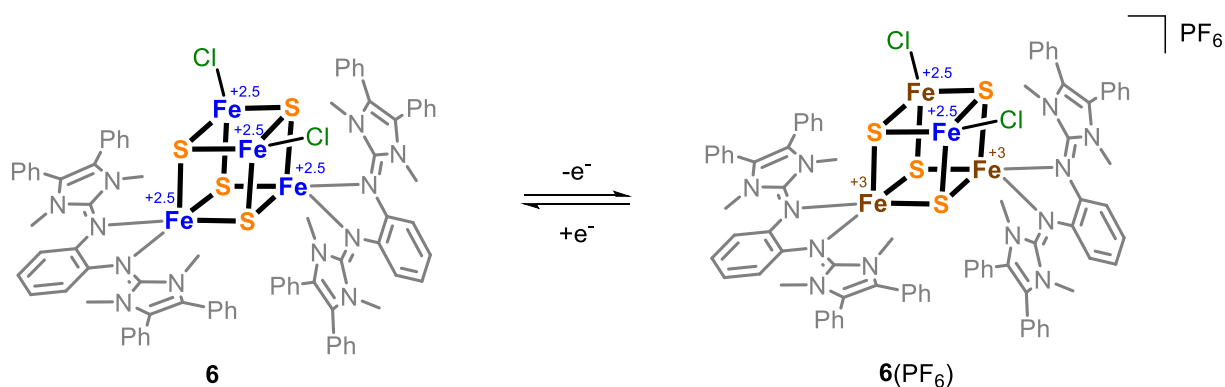


Figure 7.2. [2:2] site-differentiated $[4\text{Fe-4S}]^{2+}$ complexes **6**(PF₆) and **6** coordinated by neutral imidazoline-2-imine ligands and chlorides.

By treating $[2\text{Fe-2S}]$ precursor $(\text{NEt}_4)_2[\text{Fe}_2\text{S}_2\text{Cl}_4]$ with imidazoline-2-imine ligand **L**⁵, unexpectedly, instead of a $[2\text{Fe-2S}]$ complex, a rare $[2:2]$ site-differentiated $[4\text{Fe-4S}]^{3+}$ complex (**6**(PF₆)) was obtained (Figure 7.2 left). Notably, the direct conversion $[2\text{Fe-2S}]^{2+} \rightarrow [4\text{Fe-4S}]^{3+}$ is uncommon in $[4\text{Fe-4S}]^{3+}$ complex synthesis. Complex **6**(PF₆) could be reduced to **6** by using one equivalent of cobaltocene (Figure 7.2 right). The Mössbauer studies of **6**(PF₆) suggest that charge delocalization within the $[4\text{Fe-4S}]$ core is extensive. SQUID studies show that both clusters (**6**(PF₆) and **6**) exhibit dominant intramolecular antiferromagnetic interactions.

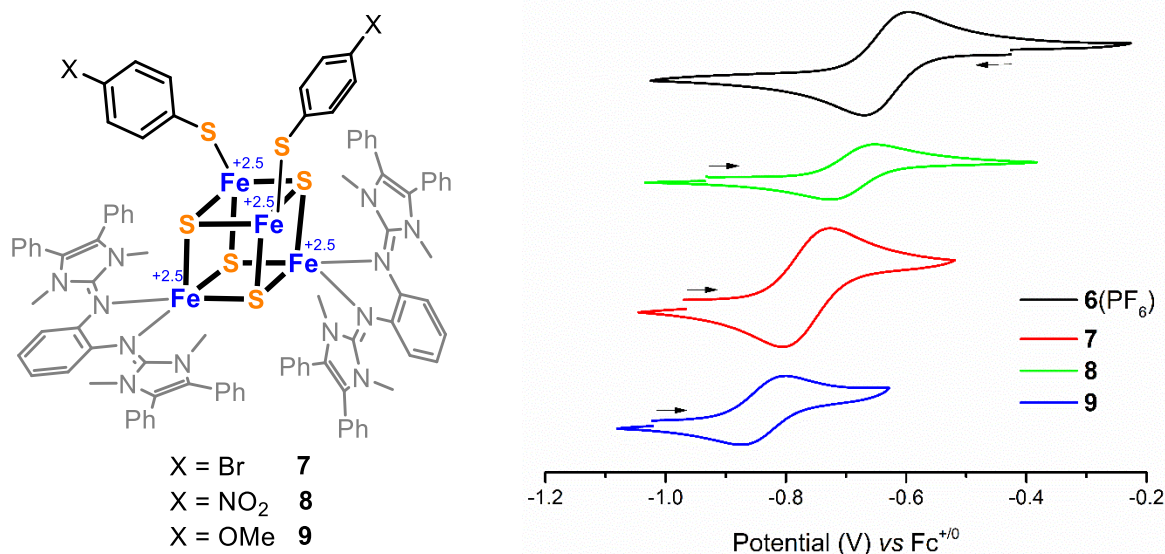


Figure 7.3. [2:2] site-differentiated $[4\text{Fe-4S}]^{2+}$ complexes (**7**, **8**, **9**) coordinated by neutral imidazoline-2-imine ligands and thiolates.

Most of the $[4\text{Fe-4S}]$ clusters ligated by cysteine residues in biological systems have shown various functional roles. **6**(PF₆) can act as precursor for $[4\text{Fe-4S}]$ clusters with different substitutions via salt metathesis reactions. To gain an insight into the electronic effect of cysteine residues coordinated to such $[4\text{Fe-4S}]$ clusters, the chlorides of the **6**(PF₆) were substituted by various thiolates to mimic cysteine coordination. Though the reaction of **6**(PF₆) and several thiolates, a series of complexes (**7**, **7**(PF₆), **8**, **8**(PF₆), **9**) were synthesized (Figure 7.3, left). Structural data and Mössbauer analyses show that redox events predominantly happen on the iron sites that are ligated by **L**⁵. CV studies of complexes **7**, **8** and **9** show that as the $[4\text{Fe-4S}]^{2+/3+}$

redox potentials decrease along with the increase of the electron donation ability of the substituents on their thiolate (Figure 7.3, right). SQUID studies show that all these clusters (**7**, **7**(PF₆), **8**, **8**(PF₆), **9**) feature dominant intramolecular antiferromagnetic interactions. The detailed research of these complexes deepened our understanding of site-differentiated [4Fe-4S] clusters.

Chapter 8. Experimental Section

8.1 General Considerations

All manipulations were carried out under an anhydrous and anaerobic atmosphere of dry argon or dinitrogen by using standard Schlenk techniques or in a glovebox ($O_2 < 0.1$ ppm, $H_2O < 0.1$ ppm), unless mentioned otherwise. Glassware was dried at 120 °C overnight. All solvents were dried by standard methods and distilled prior to use. MeCN, DMF, DMSO and EtCN were dried over CaH_2 ; Et_2O , Pentane and THF were dried over sodium in the presence of benzophenone. Deuterated solvents were dried and distilled according to the undeuterated analogues.

1H , ^{13}C , ^{31}P and ^{19}F NMR spectra were recorded on a Bruker 300 MHz, 400 MHz, 500 MHz or 600 MHz spectrometer. All chemical shifts are reported in ppm relative to residual proton or ^{13}C signals of MeCN- d_3 (1.94 ppm and 118.3 ppm), THF- d_8 at 3.58 ppm DMSO- d_6 at 2.50 ppm, DMF- d_7 at 8.02 ppm, $CDCl_3$ (7.26 ppm and 77.2 ppm).

UV-vis absorption spectra were recorded with a Cary5000 Bio Spectrophotometer, using Schlenk quartz cuvettes. UV-vis spectra at low temperature were measured with a quartz transmission probe (1 mm, Hellma analytics). Spectra were analyzed by Cary Win UV software.

ESI mass service is performed on a microOTOF ESI-TOF instrument (Bruker) and a maXis ESI-Q-TOF instrument (Bruker).

IR measurements of solid samples were performed inside a glovebox on a Cary 630 FTIR spectrometer equipped with Dial PathTechnology and analyzed by FTIR MicroLab software.

Elemental analyses were performed by the Analytical Laboratory of the Institute for Inorganic Chemistry at the University of Göttingen using an Elementar Vario EL III instrument.

EPR Spectra were recorded by using a Bruker ELEXSYS X-band spectrometer, equipped with a standard cavity (ER4102ST, 9.45 GHz). The temperature of the sample was maintained constant with an Oxford temperature controller (ITC-4) and an Oxford instrument nitrogen flow cryostat (ESP910). The magnetic field was calibrated with an NMR field probe (Bruker ER035M), and the microwave frequency was measured with a built-in frequency counter. EPR spectra were simulated using EasySpin.^{[143], [144]}

KH was purchased as dispersion in mineral oil, washed repetitively with hexanes and dried in vacuum. Cobaltocene was sublimed before usage according to reported methods. Decamethylcobaltocene was dissolved in pentane, filtered, and recrystallized from hexane prior to use according to reported methods.^[2] 1,3-Dimethyl-4,5-diphenylimidazol-2-one and 2-chloroimidazolium hexafluorophosphate were prepared according to Literatures.^{[145], [146]}

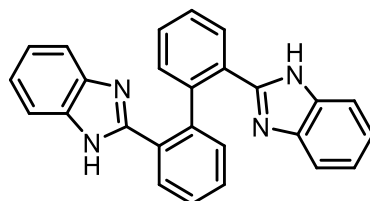
DFT calculations: the ORCA program package (version 4.2.1) was employed for all calculations. Geometry optimization of the cations were performed starting from the crystallographic data of $(NEt_4)_2\mathbf{1-5}$ (BP86 functional, def2-tzvp basis set,^[12] RI approximation using the auxiliary def2-tzvp/J basis set, D3 dispersion correction with Becke-Johnson damping,^[13] tight convergence and optimization criteria) at different spin states (spin restricted calculations in case of closed-shell molecules, otherwise spin unrestricted calculations, unless otherwise stated). The transition

state of $(\text{NEt}_4)_2\mathbf{1}$ to $\mathbf{5}$ were calculated using the OptTS feature of ORCA. TD-DFT calculations were carried out at the B3LYP/def2-tzvp level of theory as well as the Broken-Symmetry calculations. The COSMO package included in ORCA was employed to mimic MeCN or THF as solvent in form of an infinite dielectric field.

8.2 Ligand Synthesis

2,2'-bis[2-(1-hydrobenzimidazol-2-yl)]biphenyl H_2L^1

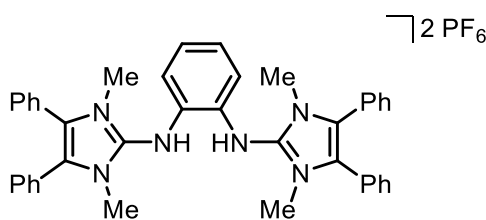
Ligand synthesis was partially adapted from literature. [76]



H_2L^1

To a 150 mL round-bottom flask were added 2.50 g (10.3 mmol) of biphenyl-2,2'-dicarboxylic acid, 2.23 g (20.6 mmol) of 1,2-phenylenediamine, and 7.5 g of polyphosphoric acid (PPA) sequentially to give a thick paste. The magnetically stirred mixture was heated at 180 °C for 4 h, cooled to 100 °C, and neutralized to pH 9 by the slow addition of a concentrated sodium hydroxide solution. The resulting solid was collected by filtration, washed repeatedly with water and ethyl acetate and dried in vacuo. Yield: 1.39 g, 35%. Spectral data were consistent with that reported.

di(2,2'-(*N,N*-dimethyl-4,5-diphenylimidazolin-2-imino))benzene [H_2L^5](PF_6)₂



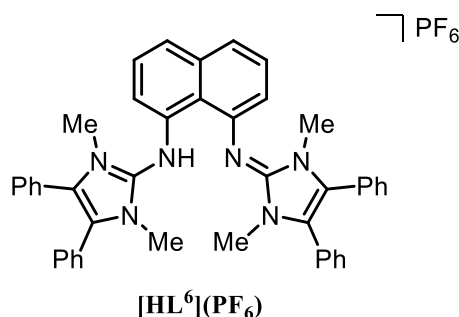
$[\text{H}_2\text{L}^5](\text{PF}_6)_2$

A solution of LiHMDS in THF (8.8 ml, 8.8 mmol) was added dropwise to a cold (0 °C) suspension of 2-chloroimidazolium hexafluorophosphate (1.715 g, 4.0 mmol) and *o*-phenylenediamine (0.216 g, 2.0 mmol) in THF (16 mL) with stirring. The mixture was allowed to come to RT and stirred for a further 20 h to give an orange solution. The following operations were performed in air. A saturated aqueous solution of KPF_6 (~30 mL) was slowly added to this reaction mixture. The aqueous layer was extracted with 30 ml ethyl acetate and the combined organic extracts were dried over Na_2SO_4 , filtered and concentrated. Flash chromatography (DCM/MeOH: 25/1) afforded the compound (0.57 g, 89%) as a pale-yellow powder.

$^1\text{H-NMR}$ (300.1 MHz, acetone- d_6 , 298 K): δ (ppm) 8.67 (s_{br}, 2H, 2 × NH), 7.57–7.41 (m, 22H, 22 × ArH), 7.40–7.313 (m, 2H, 2 × ArH), 3.64 (s, 12H, 12 × N-CH₃). $^{13}\text{C-NMR}$ (75.5 MHz,

acetone- d_6 , 298 K): δ (ppm) 142.79 (C=N), 131.97, 131.61, 130.83, 130.04, 129.91, 126.98, 126.88, 122.44 ($8 \times \text{ArC}$), 33.69 (N-CH $_3$). $^{31}\text{P-NMR}$ (121.5 MHz, acetone- d_6 , 298 K): δ (ppm) -132.62, 138.46, 144.29, 150.11, 155.94 (sept, $J_{\text{PF}} = 705$ Hz, $[\text{PF}_6]^-$). **ESI-MS** (+): m/z (%) 301.16 $[\text{M}]^+$. **ATR-IR** (powder, cm^{-1}): $\nu = 3359$ (m), 1618 (s), 1589 (s), 1558 (s), 1506 (w), 1448 (s), 1405 (m), 1387 (w), 1350 (w), 1303 (m), 1276 (w), 1200 (w), 1178 (w), 1114 (w), 1074 (w), 1055 (w), 1043 (w), 1023 (m), 825 (s), 766 (s), 735 (w), 708 (s), 699 (s), 690 (s), 665 (w), 653 (w).

di(1,8-(*N,N*-dimethyl-4,5-diphenylimidazolin-2-imino)naphthalene $[\text{HL}^6](\text{PF}_6)$



A solution of LiHMDS in THF (2.3 ml, 2.3 mmol) was added dropwise to a cold (0 °C) suspension of 2-chloroimidazolium hexafluorophosphate (0.857 g, 2.0 mmol) and 1,8-diaminonaphthalene (0.158 g, 1.0 mmol) in THF (8 mL) with stirring. The mixture was allowed to come to RT and stirred for a further 20 h to give a brown solution. The following operations were performed in air. A saturated aqueous solution of KPF_6 (~15 mL) was slowly added to this reaction mixture. The aqueous layer was extracted with 15 ml ethyl acetate and the combined organic extracts were dried over Na_2SO_4 , filtered and concentrated. Flash chromatography (ethyl acetate/hexane: 1/1) afforded the compound (0.42 g, 52%) as a pale powder.

$^1\text{H-NMR}$ (400.3 MHz, acetone- d_6 , 298 K): δ (ppm) 15.18 (s, 1H, NH), 7.40–7.32 (m, 20H, $20 \times \text{ArH}$), $\delta = 7.28$ (t, $J_{\text{H,H}} = 8.0$ Hz, 2H, naph-3,3'), 7.20 (d, $J_{\text{H,H}} = 8.4$ Hz, 2H, naph-4,4') and 6.40 (d, $J_{\text{H,H}} = 7.6$ Hz, 2H, naph-2,2') ppm 3.44 (s, 12H, $12 \times \text{N-CH}_3$). $^{13}\text{C-NMR}$ (100.7 MHz, acetone- d_6 , 298 K): δ (ppm) 146.66, 145.82, 138.44, 131.34, 130.08, 129.67, 128.29, 128.14, 127.29, 119.95, 110.50, 33.56 (N-CH $_3$). $^{31}\text{P-NMR}$ (162.0 MHz, acetone- d_6 , 298 K): δ (ppm) -135.54, -139.91, -144.28, -148.65, -153.02 (sept, $J_{\text{PF}} = 708$ Hz, $[\text{PF}_6]^-$). **ESI-MS** (+): m/z 651.32 $[\text{M}]^+$, 797.30 $[\text{M-HPF}_6]^+$: m/z 651.3231. **ATR-IR** (powder, cm^{-1}): $\nu = 3057$ (w), 2947 (w), 1737 (w), 1598 (w), 1558 (s), 1505 (s), 1460 (w), 1442 (w), 1424 (m), 1367 (m), 1335 (m), 1306 (m), 1277 (w), 1243 (w), 1161 (m), 1115 (w), 1094 (w), 1076 (w), 1057 (w), 1036 (m), 1018 (s), 923 (m), 874 (w), 831 (s), 778 (w), 766 (m), 754 (m), 739 (w), 720 (m), 696 (s), 673 (w).

8.3 Complex Synthesis

$(\text{NEt}_4)_2[\text{Fe}_4\text{S}_4\text{L}^1_2]$ $(\text{NEt}_4)_2\mathbf{1}$

To a suspension of L^1H_2 (386 mg, 1.0 mmol) in THF (20 mL) was added KH (80.2 mg, 2.0 mmol). The resulting solution was stirred 12 h at room temperature and added to a solution of $(\text{NEt}_4)_2[\text{Fe}_2\text{S}_2\text{Cl}_4]$ (289 mg, 0.5 mmol) in MeCN (25 mL) at -35 °C. The mixture was stirred for 5 h while warming up slowly to room temperature. After storage at -35 °C for 2 days, the precipitate was filtered off and Et_2O (10 mL) was added to the remaining solution. The crude

product could be filtered of after one week at -35°C . The remaining solid was rinsed with Et_2O and drying in vacuum. Slowly diffusion of Et_2O into a MeCN solution of $(\text{NEt}_4)_2\mathbf{1}$ afforded the black crystals of the product. (241 mg, 0.2 mmol, 40%).

$^1\text{H-NMR}$ (600.3 MHz, MeCN- d_6 , 298 K): [ppm] = 9.83–9.88 (m, 4H, 4-H), 7.98–7.81 (m, 4H, Ar-H), 7.20 (m, 4H, 3'-H), 6.8–6.87 (m, 8H, 4'-H and 6-H), 6.11 (s_{br}, 4H, Ar-H), 5.31–5.38 (m, 4H, 5-H) 3.10 (s_{br}, 16H, 8CH₂), 1.19 (s_{br}, 24H, 8CH₃). **UV-vis** (MeCN): λ_{max} (nm, ϵ [$\text{L mol}^{-1} \text{cm}^{-1}$]): 432 (8378), 475 (7575), 595 (2305). **Anal. calc** for $\text{C}_{72}\text{H}_{78}\text{Fe}_2\text{N}_{12}\text{S}_2$: C 67.18, H 6.11, N 13.06, S 4.98; Found: C 66.75, H 6.09, N 12.97, S 5.00.

$(\text{PPh}_4)_2[\text{Fe}_4\text{S}_4\text{L}^1\text{L}^2]$ $(\text{PPh}_4)_2\mathbf{2}$

H_2L^1 (30.90 mg, 0.08 mmol) in THF (8 mL) was deprotonated by addition of KH (6.40 mg, 0.16 mmol). The solution was stirred overnight (solution A). In the meantime, H_2L^2 (21.50 mg, 0.13 mmol) in THF (5 mL) was deprotonated with KH (10.10 g, 0.25 mmol) and the solution also stirred overnight (solution B). Solution A was added dropwise to a solution of $(\text{PPh}_4)_2[\text{Fe}_2\text{S}_2\text{Cl}_4]$ (111.58 mg, 0.11 mmol) in MeCN (3.5 mL) at -35°C , and the solution was stirred for 1.5 h at that temperature. Afterward, solution B was added, and the mixture was stirred for several minutes and then put in the fridge overnight, thereby warming slowly to rt. The precipitate was filtered off, and the filtrate was dried. The compound mixture was rinsed with THF and Et_2O , and then extracted with MeCN. Dark red crystals were obtained by diffusion of Et_2O into the MeCN solution at room temperature.

$\text{FeL}^5\text{Cl}_2\mathbf{3}$

To a stirred suspension of $[\text{H}_2\text{L}^5](\text{PF}_6)_2$ (89.3 mg, 0.10 mmol) in THF (6 ml), KH (4.0 mg, 0.1 mmol) was slowly added. After 0.5h stirring, this reaction mixture was added dropwise to a stirred solution of $\text{FeCl}_2\cdot\text{THF}$ (19.9 mg, 0.10 mmol) in THF (2 mL). The resulting solution was stirred for 22 h at room temperature. The yellowish-green reaction mixture was then filtered through a pad of Celite. The solvent was evaporated, and the residue was rinsed with 5 ml Et_2O . Yellowish-green crystals were obtained by diffusion of pentane into a THF solution at room temperature. Yield: 69 mg, 73%.

$^1\text{H-NMR}$ (600.3 MHz, THF- d_8 , 298 K): [ppm] = 17.53 (s_{br}, 2H, 5-H), 16.19 (s_{br}, 12H, N-Me), 8.66 (s_{br}, 2H, 4-H), 5.82 (s_{br}, 8H, 2-H), 4.85 (s_{br}, 4H, 3-H), 1.39 (s_{br}, 8H, 1-H). **UV-vis** (THF): λ_{max} (nm, ϵ [$\text{L mol}^{-1} \text{cm}^{-1}$]): 323 (30000). **ATR-IR** (powder, cm^{-1}): ν = 3053 (w), 2972 (w), 2853 (w), 2320 (w), 2117 (w), 2073 (w), 1995 (w), 1895 (w), 1820 (w), 1767 (w), 1601 (w), 1582 (w), 1522 (s), 1485 (s), 1467 (s), 1441 (m), 1423 (s), 1398 (s), 1345 (w), 1317 (w), 1288 (s), 1226 (m), 1197 (w), 1172 (w), 1150 (w), 1109 (s), 1074 (w), 1056 (w), 1043 (m), 1021 (s), 920 (m), 867 (w), 830 (m), 778 (m), 768 (s), 751 (s), 736 (s), 712 (s), 704 (s), 672 (w). **Anal. calc** for $\text{C}_{40}\text{H}_{36}\text{Cl}_2\text{FeN}_6$: C 65.93, H 5.78, N 10.48; Found : C 65.35, H 5.65, N 10.36.

$\text{NiL}^5\text{Br}_2\mathbf{4}$

To a stirred suspension of $[\text{H}_2\text{L}^5](\text{PF}_6)_2$ (89.3 mg, 0.10 mmol) in THF (6 ml), KH (4.0 mg, 0.1 mmol) was slowly added. After 0.5h stirring, this reaction mixture was added dropwise to a stirred solution of $\text{NiBr}_2\cdot\text{DMe}$ (30.8 mg, 0.10 mmol) in THF (2 mL). The resulting solution was stirred for 19 h at room temperature. The dark purple reaction mixture was then filtered through a pad of Celite. The solvent was evaporated and the residue was rinsed with 5 ml Et_2O . Dark purple crystals were obtained by diffusion of pentane into a THF solution at room temperature. Yield: 37 mg, 42%.

$^1\text{H-NMR}$ (600.3 MHz, THF- d_8 , 333 K): [ppm] = 14.33 (d, $J_{\text{HH}} = 6.6$ Hz, 8H, 1-H), $\delta = 10.71$ (t, $J_{\text{HH}} = 7.2$ Hz, 8H, 2-H), 10.30 (s_{br}, 2H, 5-H), $\delta = 8.75$ (t, $J_{\text{HH}} = 7.8$ Hz, 4H, 3-H), 6.52 (s_{br}, 2H, 4-H). **UV-vis** (THF): λ_{max} (nm, ϵ [$\text{L mol}^{-1} \text{cm}^{-1}$]): 324 (36000), 483 (991), 543 (754), 607 (389),

750 (156). **ATR-IR** (powder, cm^{-1}): $\nu = 3052$ (w), 2975 (w), 2948 (w), 2856 (w), 2326 (w), 2107 (w), 2077 (w), 1993 (w), 1895 (w), 1770 (w), 1660 (w), 1583 (w), 1528 (s), 1468 (s), 1443 (m), 1422 (s), 1401 (m), 1321 (w), 1300 (m), 1289 (m), 1172 (w), 1156 (w), 1111 (m), 1063 (w), 1055 (w), 1041 (w), 1020 (m), 998 (w), 924 (m), 900 (w), 869 (s), 834 (m), 769 (s), 748 (m), 736 (w), 727 (m), 700 (s), 671 (w). **Anal. calc** for $\text{C}_{40}\text{H}_{36}\text{Br}_2\text{N}_6\text{Ni}$: C 59.19, H 4.94, N 9.39; Found: C 59.29, H 4.98, N 9.43.

NiL⁶Br₂ 5

To a stirred suspension of $[\text{H}_2\text{L}^5](\text{PF}_6)_2$ (89.3 mg, 0.10 mmol) in THF (6 ml), KH (4.0 mg, 0.1 mmol) was slowly added. After 0.5 h stirring, this reaction mixture was added dropwise to a stirred solution of $\text{NiBr}_2 \cdot \text{DMe}$ (30.8 mg, 0.10 mmol) in THF (2 mL). The resulting solution was stirred for 25 h at room temperature. The dark gray reaction mixture was then filtered through a pad of Celite. The solvent was evaporated and the residue was rinsed with 5 ml Et_2O . Dark gray crystals were obtained by diffusion of Et_2O into a THF solution at room temperature. Yield: 46 mg, 53%.

¹H-NMR (600.3 MHz, THF- d_8 , 298 K): [ppm] = 40.17 (s_{br} , 12H, N-Me), 21.73 (s_{br} , 2H, 5-H), 13.90 (s_{br} , 2H, 6-H), 11.00 (s_{br} , 8H, 1-H), 9.39 (s_{br} , 8H, 2-H), 7.92 (s_{br} , 4H, 3-H), -0.25 (s_{br} , 2H, 4-H). **UV-vis** (THF): λ_{max} (nm, ϵ [$\text{L mol}^{-1} \text{cm}^{-1}$]): 328 (18620), 367 (24060), 472 (842), 576 (477), 644 (270), 712 (205). **ATR-IR** (powder, cm^{-1}): $\nu = 3056$ (w), 2974 (w), 2943 (w), 2848 (w), 2326 (w), 2102 (w), 1993 (w), 1601 (w), 1567 (w), 1527 (s), 1497 (s), 1474 (m), 1442 (m), 1418 (s), 1397 (w), 1379 (s), 1338 (w), 1320 (w), 1285 (s), 1258 (w), 1179 (w), 1165 (m), 1061 (m), 1037 (m), 1017 (s), 901 (m), 852 (m), 821 (s), 783 (m), 760 (s), 728 (m), 702 (s), 672 (w). **Anal. calc** for $\text{C}_{44}\text{H}_{38}\text{N}_6\text{NiBr}_2$: C 60.79, H 4.41, N 9.67; Found: C 59.89, H 4.79, N 8.76.

[Fe₄S₄L⁵₂Cl₂](PF₆) 6(PF₆)

To a stirred suspension of $[\text{H}_2\text{L}^5](\text{PF}_6)_2$ (71.4 mg, 0.08 mmol) in THF (6 ml), KH (7.4 mg, 0.184 mmol) was slowly added. The resulting solution was stirred for 1.5 h at room temperature. Then the orange reaction mixture was added to a solution of $(\text{NEt}_4)_2[\text{Fe}_2\text{S}_2\text{Cl}_4]$ (46.1 mg, 0.08 mmol) and KPF_6 (42.4 mg, 0.23 mmol) in MeCN (3.5 ml) at low temperature. Stirring was continued for 16 h. The dark blue reaction mixture was then filtered through a pad of Celite. The solvent was evaporated and the residue extracted with 5 ml THF and filtered. Dark blue crystals were obtained by diffusion of Et_2O into a MeCN or THF solution at room temperature. Yield: 54.1 mg, 76%.

¹H NMR (300.1 MHz, MeCN- d_3 , 298 K): [ppm] = 8.84 (s_{br}), 7.32 (s_{br}), 6.87 (s_{br}), 6.57 (s_{br}), 6.55 (s_{br}), 4.44 (s_{br}), 2.59 (s_{br}). **ESI(+)-MS** (CH_3CN , m/z): 1622.2 (100%), $[\text{C}_{80}\text{H}_{72}\text{Cl}_2\text{Fe}_4\text{N}_{12}\text{S}_4]^+$. **UV-vis** (THF): λ_{max} (nm, ϵ [$\text{L mol}^{-1} \text{cm}^{-1}$]): 480 (4584), 625 (6205). **ATR-IR** (powder, cm^{-1}): $\nu = 3052$ (w), 2945 (w), 2117 (w), 1590 (w), 1580 (w), 1520 (s), 1489 (m), 1477 (s), 1442 (s), 1417 (s), 1400 (m), 1359 (w), 1320 (w), 1286 (s), 1279 (s), 1228 (s), 1169 (m), 1158 (m), 1112 (w), 1074 (w), 1054 (w), 1041 (m), 1020 (m), 920 (m), 901 (w), 865 (w), 832 (s), 768 (s), 748 (w), 740 (m), 732 (m), 700 (s), 682 (w), 666 (w), 651 (w), 614 (w), 599 (w), 578 (w), 555 (s), 531 (w), 509 (m), 482 (w), 470 (w), 445 (w). **Anal. calc** for $\text{C}_{80}\text{H}_{72}\text{Cl}_2\text{F}_6\text{Fe}_4\text{N}_{12}\text{PS}_4$: C 54.32, H 4.10, N 9.50, S 7.25; Found: C 53.99, H 4.11, N 9.88, S 7.50.

[Fe₄S₄L⁵₂Cl₂] 6

A solution of **6**(PF₆) (17.7 mg, 0.01 mmol) in THF (4 ml) was cooled to -35°C and cobaltocene (2.3 mg, 0.012 mmol) was added. The reaction mixture was stirred for 20 minutes while warming up slowly to room temperature. Adding of Et_2O (5 ml) led to precipitation of the crude product. Rinsing with Et_2O and drying afforded the reduced cluster $[\text{Fe}_4\text{S}_4\text{L}^5_2\text{Cl}_2]$. Yield: 13.15 mg, 0.0081 mmol, 81%. Slow diffusion of Et_2O into a THF solution containing $[\text{Fe}_4\text{S}_4\text{L}^5_2\text{Cl}_2]$ afforded black crystals of the product.

¹H NMR (500.3 MHz, THF-d₈, 298 K): [ppm] = 7.15 (s_{br}, 8H, 1-H and 2-H), 7.08 (s_{br}, 24H, Ar-H), 6.83 (s_{br}, 16H, Ar-H), 3.06 (s_{br}, 24H, N-Me). **UV-vis** (THF): λ_{max} (nm, ε [L mol⁻¹ cm⁻¹]): 531 (6134). **ATR-IR** (powder, cm⁻¹): ν = 3046 (w), 2946 (w), 2333 (w), 2120 (m), 1816 (w), 1577 (m), 1515 (s), 1479 (s), 1470 (s), 1439 (m), 1416 (s), 1397 (m), 1362 (w), 1287 (s), 1229 (s), 1170 (m), 1157 (m), 1111 (w), 1075 (w), 1054 (w), 1041 (m), 1020 (m), 919 (m), 897 (m), 835 (s), 767 (s), 699 (s), 675 (w), 664 (w), 650 (w), 611 (m), 598 (w), 556 (s), 508 (m), 503 (m), 457 (w), 444 (w), 424 (w). **Anal. calc** for C₈₀H₇₂Cl₂Fe₄N₁₂S₄: C 60.29, H 5.48, N 8.79, S 6.71; Found: C 60.28, H 5.22, N 8.47, S 6.36.

[Fe₄S₄L⁵₂(4-Br-C₆H₄S)₂] 7

A solution of **6**(PF₆) (35.4 mg, 0.02 mmol) in THF (10 ml) was cooled to -35 °C and potassium 4-bromobenzenethiolate (18.5 mg, 0.08 mmol) was added. The reaction mixture was stirred for 5 h while warming up slowly to room temperature. Solvent was removed under reduced pressure and the crude solid was washed with hexane and Et₂O to afford the complex as dark-orange microcrystals (22.1 mg, 56%). Slow diffusion of Et₂O into a THF solution contain [C₉₂H₈₀Br₂Fe₄N₁₂S₆] led to growth of crystals suitable for X-ray diffraction.

¹H NMR (600.3 MHz, THF-d₈, 333 K): [ppm] = 9.61 (s_{br}, 4H, 4-H), 8.64 (s_{br}, 4H, 3-H), 7.10–7.14 (m, 24H, Ar-H), 6.97, (s_{br}, 16H, Ar-H), 6.80 (s_{br}, 8H, 1-H and 2-H), 4.11 (s_{br}, 24H, N-Me). **UV-vis** (THF): λ_{max} (nm, ε [L mol⁻¹ cm⁻¹]): 482 (13150), 543 (11087). **ATR-IR** (powder, cm⁻¹): ν = 3050 (w), 2921 (m), 2854 (w), 2115 (m), 1890 (w), 1680 (w), 1602 (w), 1576 (w), 1511 (s), 1484 (s), 1465 (s), 1441 (m), 1417 (s), 1399 (w), 1363 (w), 1287 (s), 1261 (w), 1231 (s), 1170 (m), 1157 (w), 1110 (w), 1082 (s), 1054 (w), 1042 (m), 1022 (m), 1006 (m), 975 (w), 921 (m), 897 (w), 863 (w), 841 (m), 808 (m), 766 (s), 727 (s), 699 (s), 674 (w), 651 (w), 614 (w), 561 (w), 508 (w), 496 (m), 481 (m), 464 (w), 444 (w), 441 (w). **Anal. calc** for C₁₀₀H₁₀₀Br₂Fe₄N₁₂O₂S₆: C 57.81, H 4.85, N 8.09, S 9.26; Found: C 57.54, H 4.44, N 8.03, S 8.89.

[Fe₄S₄L⁵₂(4-Br-C₆H₄S)₂](PF₆) 7(PF₆)

A solution of **7** (16.0 mg, 0.08 mmol) in THF (4 ml) was cooled to -35 °C and [FeCp*₂](PF₆) (3.9 mg, 0.08 mmol) was added. The reaction mixture was stirred for 12 h while warming up slowly to room temperature. Addition of hexane (10 ml) led to precipitation of the crude product. Rinsing with Et₂O and drying afforded the oxidized cluster [Fe₄S₄L⁵₂(4-Br-C₆H₄S)₂](PF₆). Yield: 11.2 mg, 65%. Slow diffusion of Et₂O into a THF solution afforded black crystals of the product. **¹H NMR** (300.1 MHz, MeCN-d₃, 298 K): [ppm] = 15.40 (s_{br}), 8.33 (s_{br}), 7.18–7.52 (m), 6.86–7.09 (m), 6.70 (s_{br}), 5.93 (s_{br}), 5.01 (s_{br}), 2.90 (s_{br}). **ESI(+)-MS** (CH₃CN, m/z): 1928.1 (100%), [C₉₂H₈₀Br₂Fe₄N₁₂PF₆S₆]⁺. **UV-vis** (CH₃CN): λ_{max} (nm, ε [L mol⁻¹ cm⁻¹]): 466 (12820), 630 (14422). **ATR-IR** (powder, cm⁻¹): ν = 3056 (w), 2944 (w), 2116 (m), 1891 (w), 1592 (w), 1578 (w), 1516 (s), 1477 (s), 1465 (s), 1443 (s), 1417 (s), 1402 (w), 1358 (w), 1320 (w), 1287 (s), 1230 (s), 1169 (m), 1113 (w), 1082 (m), 1054 (w), 1042 (m), 1021 (m), 1006 (m), 922 (m), 900 (w), 865 (w), 833 (s), 768 (s), 738 (m), 728 (m), 699 (s), 664 (w), 651 (w), 615 (w), 599 (w), 576 (w), 556 (s), 507 (m), 496 (m), 479 (m), 466 (w), 438 (w), 414 (w), 402 (w). **Anal. calc** for C₉₂H₈₀Br₂Fe₄N₁₂PF₆S₆: C 53.67, H 4.22, N 7.82, S 8.95; Found: C 53.06, H 4.67, N 7.48, S 9.00.

[Fe₄S₄L⁵₂(4-NO₂-C₆H₄S)₂] 8

To a stirred suspension of 4-nitrothiophenol (13.5 mg, 0.09 mmol) in THF (5 ml) KH (4.5 mg, 0.11 mmol) was added. The resulting solution was stirred for 4 h at room temperature. The orange reaction mixture was added to a solution of **6**(PF₆) (35.4 mg, 0.02 mmol) in THF (5 ml) at -35 °C. Stirring was continued for 16 h while warming up slowly to room temperature. Addition of hexane (10 ml) led to precipitation of the crude product. Rinsing with Et₂O and drying afforded the cluster [Fe₄S₄L⁵₂(4-NO₂-C₆H₄S)₂]. Yield: 31.9 mg, 78%. Slow diffusion of Et₂O into a THF solution afforded black crystals of the product.

¹H NMR (600.3 MHz, THF-d₈, 333 K): [ppm] = 10.40 (s_{br}, 4H, 4-H), 9.48 (s_{br}, 4H, 3-H), 7.09–7.15 (m, 24H, Ar-H), 6.96 (s_{br}, 16H, Ar-H), 6.77 (s_{br}, 8H, 1-H and 2-H), 4.10 (s_{br}, 24H, Ar-H). **UV-vis** (THF): λ_{max} (nm, ε [L mol⁻¹ cm⁻¹]): 430 (35088), 545 (14127). **ATR-IR** (powder, cm⁻¹): ν = 3048 (w), 2923 (w), 2851 (s), 2331 (w), 2115 (m), 1890 (w), 1808 (w), 1567 (s), 1512 (s), 1481 (s), 1468 (s), 1439 (m), 1416 (s), 1398 (w), 1351 (w), 1319 (s), 1285 (s), 1227 (s), 1170 (m), 1157 (m), 1111 (w), 1085 (s), 1069 (m), 1053 (w), 1041 (s), 1020 (s), 918 (m), 895 (m), 863 (w), 836 (s), 763 (s), 743 (m), 726 (m), 697 (s), 612 (m), 598 (w), 559 (m), 534 (m), 507 (m), 465 (m), 442 (m), 426 (w), 407 (w). **Anal. calc** for C₉₆H₉₀Fe₄N₁₄O₅S₆: C 59.57, H 4.69, N 10.13, S 9.94; Found: C 59.51, H 4.88, N 9.81, S 9.56.

[Fe₄S₄L⁵₂(4-NO₂-C₆H₄S)₂](PF₆) **8(PF₆)**

A solution of **8** (18.6 mg, 0.01 mmol) in THF (4 ml) was cooled to -35 °C and [FeCp₂]PF₆ (3.6 mg, 0.011 mmol) was added. The reaction mixture was stirred for 2 h while warming up slowly to room temperature. Addition of hexane (10 ml) led to precipitation of the crude product. Rinsing with THF, Et₂O and drying afforded the oxidized cluster [Fe₄S₄L⁵₂(4-Br-C₆H₄S)₂](PF₆). Yield: 11.2 mg, 65%. Slow diffusion of Et₂O into a MeCN solution afforded green-black crystals of the product.

¹H NMR (300.1 MHz, MeCN-d₃, 298 K): [ppm] = 15.93 (s_{br}), 8.46 (s_{br}), 7.15–7.53 (m), 5.89–7.05 (m), 4.37 (s_{br}), 2.40 (s_{br}). **ESI(+)-MS** (CH₃CN, m/z): 1860.1 (100%), [C₉₂H₈₀Fe₄N₁₄O₄S₆]⁺. **UV-vis** (CH₃CN): λ_{max} (nm, ε [L mol⁻¹ cm⁻¹]): 360 (32320), 440 (19380), 540 (14180), 635 (14580). **ATR-IR** (powder, cm⁻¹): ν = 3063 (w), 2944 (w), 2112 (m), 1993 (w), 1627 (w), 1593 (w), 1582 (w), 1568 (m), 1520 (s), 1494 (s), 1477 (s), 1443 (m), 1416 (m), 1357 (w), 1320 (s), 1288 (s), 1277 (s), 1230 (s), 1170 (m), 1158 (m), 1110 (w), 1085 (m), 1067 (w), 1053 (w), 1042 (m), 1019 (m), 920 (m), 901 (w), 866 (w), 832 (s), 766 (s), 741 (m), 732 (m), 701 (s), 681 (w). **Anal. calc** for C₉₂H₈₀Fe₄N₁₄O₄F₆PS₆: C 55.07, H 4.02, N 9.77, S 9.59; Found: C 54.81, H 4.15, N 9.44, S 9.35.

[Fe₄S₄L⁵₂(4-OMe-C₆H₄S)₂] **9**

A solution of **6**(PF₆) (35.4 mg, 0.02 mmol) in THF (5 ml) was cooled to -35 °C and potassium 4-methoxybenzenethiolate (14.2 mg, 0.08 mmol) was added. The reaction mixture was stirred for 12 h while warming up slowly to room temperature. Addition of hexane (10 ml) led to precipitation of the crude product. Rinsing with Et₂O and drying afforded the oxidized cluster [Fe₄S₄L⁵₂(4-OMe-C₆H₄S)₂]. Yield: 18.1 mg, 49%. Slow diffusion of Et₂O into a THF solution afforded black crystals of the product.

¹H NMR (300.1 MHz, THF-d₈, 298 K): [ppm] = 9.05 (s_{br}, 8H, 3-H and 4-H), 7.13 (s_{br}, 24H, Ar-H), 6.98 (s_{br}, 16H, Ar-H), 6.79 (s_{br}, 8H, 1-H and 2-H), 4.34 (s_{br}, 6H, O-Me), 3.91 (s_{br}, 24H, N-Me). **UV-vis** (CH₃CN): λ_{max} (nm, ε [L mol⁻¹ cm⁻¹]): 505 (12212). **ATR-IR** (powder, cm⁻¹): ν = 3046 (w), 2940 (w), 2826 (w), 2331 (w), 2118 (m), 1992 (w), 1867 (m), 1576 (m), 1511 (s), 1483 (s), 1439 (m), 1417 (s), 1398 (w), 1288 (w), 1271 (w), 1230 (s), 1171 (m), 1154 (w), 1110 (w), 1078 (w), 1086 (m), 1073 (w), 1053 (w), 1040 (m), 1022 (s), 998 (w), 982 (m), 920 (m), 986 (w), 862 (w), 838 (m), 817 (s), 765 (s), 748 (w), 728 (s), 698 (s), 671 (w).

8.4 Electrochemical Measurements

Cyclic voltammograms for all complexes were recorded at room temperature with an Interface 1000B potentiostat in a glovebox under an argon atmosphere. Glassy carbon was used as working electrode, Pt wire was used as auxiliary electrode, and Ag wire was used as reference electrode. Under the experimental conditions, all CVs were referenced internally to Fc/Fc⁺ (0 V) by addition of ferrocene to the solution of analytes. Tetrabutylammonium hexafluorophosphate (0.1 M in MeCN or 0.2 M in THF solution) was used as supporting electrolyte, which was prepared in the glovebox. The concentration of each sample was about 1.0 mM in 3.0 ml anhydrous THF or MeCN. The solvents were dried by standard methods, like distilled and degassed prior to use. Before recording the voltammograms, the sample was stirred for 2 min. For each sample two CV scans were performed, the first of which was discarded. As a final step, ferrocene was added to each sample for internal referencing at room temperature. Data were recorded and analyzed using the Gamry Framework software and BWSpec software.

Table 8.1. Redox potentials [V] of synthetic Fe/S clusters. All potentials have been referenced to the Fc/Fc⁺ ^{a)} couple.

	E_1	E_2	conditions
(NEt ₄) ₂ 1	-1.43	-	$c = 1.0$ mM in MeCN/0.1 M NBu ₄ PF ₆ at rt
6 (PF ₆)	-0.64	-1.64	$c = 1.0$ mM in MeCN/0.1 M NBu ₄ PF ₆ at rt
7	-0.77	-1.75	$c = 1.0$ mM in THF/0.2 M NBu ₄ PF ₆ at rt
8	-0.69	-	$c = 1.0$ mM in THF/0.2 M NBu ₄ PF ₆ at rt
9	-0.84	-	$c = 1.0$ mM in THF/0.2 M NBu ₄ PF ₆ at rt

a) Fc/Fc⁺ couple is a reversible redox couple, which shows a peak separation of $\Delta E = 0.076$ V (0.1 V/s) and also shows a slight dependence on scan rate.

8.5 Mössbauer Measurements

Zero-field ^{57}Fe Mössbauer spectra were recorded with a *Wissel* alternating constant-acceleration spectrometer operated in the transmission mode and equipped with a *Janis* closed-cycle helium cryostat using a ^{57}Co source in a Rh matrix at 80 K. The isomer shifts (δ) are given relative to α -iron metal at ambient temperature. All the experimental data were fitted with Lorentzian line shapes using the *Mfit* program: E. Bill, Max-Planck Institute for Chemical Energy Conversion, Mülheim/Ruhr, Germany.

Table 8.2. ^{57}Fe Mössbauer parameters [mm s^{-1}] of zero-field measurements for Solid samples of synthetic Fe/S clusters at 80 K.

	δ_1	ΔE_{Q1}	δ_2	ΔE_{Q2}	Ratio 1 : 2
(NEt ₄) ₂ 1	0.31	0.27	-	-	-
3	0.90	3.10	-	-	-
6 (PF ₆)	0.47	0.82	0.49	1.10	52:48
6	0.54	1.06	0.64	2.07	51:49
7	0.47	1.18	0.65	2.00	51:49
7 (PF ₆)	0.49	0.79	0.42	1.24	48:52
8	0.46	1.10	0.64	1.97	50:50
8 (PF ₆)	0.47	0.83	0.42	1.08	48:52
9	0.46	1.20	0.67	1.94	54:46

8.6 Magnetic Susceptibility

Temperature dependent susceptibility measurements of solid samples were carried out by using a Quantum Design MPMS 3 SQUID magnetometer equipped with a 7 Tesla magnet at a magnetic field of 0.5 T. The crystalline powdered samples were contained in polycarbonate capsules and fixed in non-magnetic sample holders. Every raw data file for the measured magnetic moment was corrected for the diamagnetic contribution of the non-magnetic sample holder and the polycarbonate capsule, according to $M^{\text{dia}} = \chi_g \times m \times H$, with experimentally obtained gram susceptibilities of the bucket. The molar susceptibility data of the Fe/S compounds were corrected for the diamagnetic contribution. Temperature-independent paramagnetism and a Curie-behaved paramagnetic impurity with spin $S = 5/2$ were included according to $\chi_{\text{calc}} = (1 - PI) \cdot \chi + PI \cdot \chi_{\text{mono}} + TIP$. The simulation of the experimental magnetic data with a full-matrix diagonalisation of exchange coupling and Zeeman splitting was performed with the *julX* or *julX-2S* program programmes (E. Bill: Max-Planck Institute for Chemical Energy Conversion, Mülheim/Ruhr, Germany).

Table 8.3. Best fit parameters for magnetic susceptibility measurements.

	g	$J [\text{cm}^{-1}]$	$PI [\%]$	$\chi (TIP)$ [$10^{-6} \text{ cm}^3 \text{ mol}^{-1}$]
(NEt ₄) ₂ 1	$g_1 = g_2 = 2.00$ (fixed)	-195	0.5	16
3	2.16	-	-	13
4	$g_x = g_y = 2.4, g_z = 2.89$	-	-	105
5	$g_x = g_y = 2.02, g_z = 3.05$	-	-	23
6	2.0 (fixed)	-128	1.7	10
6(PF₆)	2.0 (fixed)	-93	0.0	426
7	2.0 (fixed)	-146	2.7	449
7(PF₆)	2.0 (fixed)	-111	0.0	934
8	2.0 (fixed)	-143	0.4	100
8(PF₆)	2.0 (fixed)	-97	2.1	912

Chapter 9. Appendix

9.1 Crystallographic Details

Crystal data and details of the data collections are given in Tables 8.1.1–8.1.4. X-ray data were collected on a STOE IPDS II or a BRUKER D8-QUEST diffractometer (monochromated Mo-K α radiation, $\lambda = 0.71073 \text{ \AA}$) by use of ω or ω and ϕ scans at low temperature. The structures were solved with SHELXT and refined on F^2 using all reflections with SHELXL.^{[147], [148]} Most non-hydrogen atoms were refined anisotropically. Hydrogen atoms were placed in calculated positions and assigned to an isotropic displacement parameter of 1.5/1.2 $U_{\text{eq}}(\text{C})$. In some structures the unit cell contains highly disordered solvent molecules for which no satisfactory model for a disorder could be found. The solvent contribution to the structure factors was calculated with PLATON SQUEEZE^[149] and the resulting .fab file was processed with SHELXL using the ABIN instruction. The empirical formula and derived values are in accordance with the calculated cell content. Disordered parts, the treatment of disorder and the use of SQUEEZE are summarized in Table 9

.1.5. In case of **8**⁺ and **9** the overall structure could be established. The quality of the diffraction data, however, was not sufficient for anisotropic refinement or discussion of bonding parameters. Face-indexed absorption corrections were performed numerically with the program X-RED^[150] or by the multi-scan method with SADABS^[151].

Table 9.1.1. Crystal data and refinement details.

	(NEt ₄) 2	(PPh ₄) 2	3
Empirical formula	C ₇₂ H ₇₈ Fe ₂ N ₁₂ S ₂	C ₈₄ H ₆₇ Fe ₂ N ₅ P ₂ S ₄	C ₅₂ H ₆₀ Cl ₂ FeN ₆ O ₃
Formula weight	1287.28	1448.30	943.81
T [K]	120(2)	133(2)	133(2)
Crystal size	0.392 x 0.331 x 0.104	0.421 x 0.131 x 0.052	0.500 x 0.460 x 0.390
Crystal system	Monoclinic	Triclinic	Monoclinic
Space group	P2 ₁ /c	P-1	P2 ₁
a [Å]	13.6816(7)	12.9415(4)	9.9819(2)
b [Å]	18.8247(11)	13.2089(4)	13.6039(4)
c [Å]	25.4691(15)	22.4660(7)	18.0633(4)
α [°]	90	79.2850(10)	90

β [°]	96.837(2)	74.4300(10)	96.809(2)
γ [°]	90	72.3770(10)	90
V [Å ³]	6513.0(6)	3502.87(19)	2435.57(10)
Z	4	2	2
ρ [g/cm ³]	1.313	1.373	1.287
$F(000)$	2712	1504	996
μ [mm ⁻¹]	0.562	0.630	0.468
T_{\min}/T_{\max}	0.810 / 0.940	0.85 / 0.97	0.9717 / 0.9076
θ range [°]	2.066 to 27.939°	1.967 to 27.920°	1.879 to 26.819
hkl -range	18 / 24 / 33	-16 / 17, ± 17 / ± 29	± 12 / ± 17 / ± 22
Measured refl.	173536	64456	31044
Unique refl.	15583	16733	10327
Completeness to θ / %	99.9	99.9	100.0
Data	15583	16733	10327
Res. / Param.	0 / 803	0 / 875	31 / 634
Goodness-of-fit (F^2)	1.137	1.034	1.042
R_1, wR_2 ($I > 2$ (I))	0.0625, 0.1327	0.0557, 0.1109	0.0325, 0.0855
R_1, wR_2 (all data)	0.0829, 0.1419	0.0876, 0.1223	0.0357, 0.0874
Resid. el. dens. [e/Å ³]	0.887 / -1.162	0.707 / -0.512	0.549 / -0.342

Table 9.1.2. Crystal data and refinement details.

	4	5	6
Empirical formula	C ₄₄ H ₄₄ Br ₂ N ₆ Ni O	C ₅₂ H ₅₄ Br ₂ N ₆ Ni O ₂	C ₈₆ H ₈₁ Cl ₂ Fe ₄ N ₁₅ S ₄
Formula weight	891.38	1013.54	1747.19
T [K]	101(2)	100(2)	133(2)
Crystal size	0.346 x 0.235 x 0.219	0.469 x 0.326 x 0.234	0.430 x 0.300 x 0.280
Crystal system	Monoclinic	Orthorhombic	Monoclinic
Space group	P2 ₁ /c	P2 ₁ 2 ₁ 2	P2 ₁ /c
a [Å]	18.6018(8)	13.2815(6)	13.7649(2)
b [Å]	13.7081(6)	17.4573(10)	28.1298(5)
c [Å]	18.2697(8)	10.0672(5)	25.7276(4)
α [°]	90	90	90
β [°]	119.1930(10)	90	93.7520(10)

γ [°]	90	90	90
V [Å ³]	4066.9(3)	2334.2(2)	9940.5(3)
Z	4	2	4
ρ [g/cm ³]	1.456	1.442	1.167
$F(000)$	1824	1044	3616
μ [mm ⁻¹]	2.484	2.175	0.756
T_{\min}/T_{\max}	0.61 / 0.47	0.64 / 0.48	0.8949 / 0.7716
θ range [°]	1.944 to 27.903	1.927 to 28.719	1.448 to 25.783
hkl -range	-23, 24 / ±18 / ±24	-17, 16 / ±23 / ±13	-16, 15 / -33, 34 / ±31
Measured refl.	117915	25243	74499
Unique refl.	9715	6045	18737
Completeness to θ / %	99.9	99.9	100.0
Data	9715	6045	18737
Restraints	0	0	0
Parameters	491	288	1011
Goodness-of-fit (F^2)	1.061	1.041	1.040
R_1, wR_2 ($I > 2(I)$)	0.0336, 0.0798	0.0379, 0.0966	0.0383, 0.0881
R_1, wR_2 (all data)	0.0420, 0.0836	0.0399, 0.0978	0.0516, 0.0944
Resid. el. dens. [e/Å ³]	1.329 / -1.331	1.460, -0.990	0.510, -0.385

Table 9.1.3. Crystal data and refinement details.

	6(PF₆)	7	7(PF₆)
Empirical formula	C ₈₄ H ₇₈ Cl ₂ F ₆ Fe ₄ N ₁₄ P S ₄	C ₉₆ H ₈₆ Br ₂ Fe ₄ N ₁₄ S ₆	C ₉₆ H ₉₀ Br ₂ F ₆ Fe ₄ N ₁₂ O P S ₆
Formula weight	1851.11	2011.36	2148.34
T [K]	133(2)	133(2)	133(2)
Crystal size	0.500 x 0.490 x 0.480	0.460 x 0.450 x 0.360	0.287 x 0.105 x 0.098
Crystal system	Monoclinic	Hexagonal	Monoclinic
Space group	P2 ₁ /c	P6 ₄	C2/c
a [Å]	14.3427(2)	26.7258(4)	25.7779(8)
b [Å]	33.6887(6)	26.7258(4)	23.5587(7)
c [Å]	18.0264(2)	14.7015(2)	31.7004(9)
α [°]	90	90	90
β [°]	99.7260(10)	90	97.3040(10)

γ [°]	90	120	90
V [Å ³]	8584.9(2)	9094.0(3)	19095.2(10)
Z	4	3	8
ρ [g/cm ³]	1.432	1.102	1.495
$F(000)$	3804	3090	8776
μ [mm ⁻¹]	0.906	1.273	1.646
T_{\min}/T_{\max}	0.7154 / 0.5500	0.8453 / 0.6463	0.85 , 0.76
θ range [°]	1.209 to 25.716	1.524 to 25.805	2.160 to 27.885
hkl -range	$\pm 17 / \pm 40 / -21, 20$	$\pm 32 / \pm 32 / -16, 17$	$\pm 33 / \pm 30 / \pm 41$
Measured refl.	101754	75009	313850
Unique refl.	16195	11289	22756
Completeness to θ / %	100.0	100.0	99.9
Data	16195	11289	22756
Restraints	320	1	587
Parameters	1103	555	1281
Goodness-of-fit (F^2)	1.045	1.041	1.035
R_I, wR_2 ($I > 2(I)$)	0.0352, 0.0909	0.0393, 0.0988	0.0666, 0.1743
R_I, wR_2 (all data)	0.0423, 0.0961	0.0484, 0.1058	0.0996, 0.1987
Resid. el. dens. [e/Å ³]	0.679, -0.455	0.700, -0.483	1.056, -2.584

Table 9.1.4. Crystal data and refinement details.

	8	8(PF₆)	9
Empirical formula	C ₉₆ H ₈₆ Fe ₄ N ₁₆ O ₄ S ₆		
Formula weight	1943.56		
T [K]	133(2)		
Crystal size	0.366 x 0.334 x 0.187		
Crystal system	Hexagonal	monoclinic	monoclinic
Space group	P6 ₄	P2 ₁ /n	P2/c
a [Å]	26.7328(8)	35.7398(19)	18.4021(10)
b [Å]	26.7328(8)	14.1649(7)	14.8610(8)
c [Å]	14.7149(7)	40.810(2)	21.8428(12)
α [°]	90	90	90
β [°]	90	110.842(1)	104.082(2)

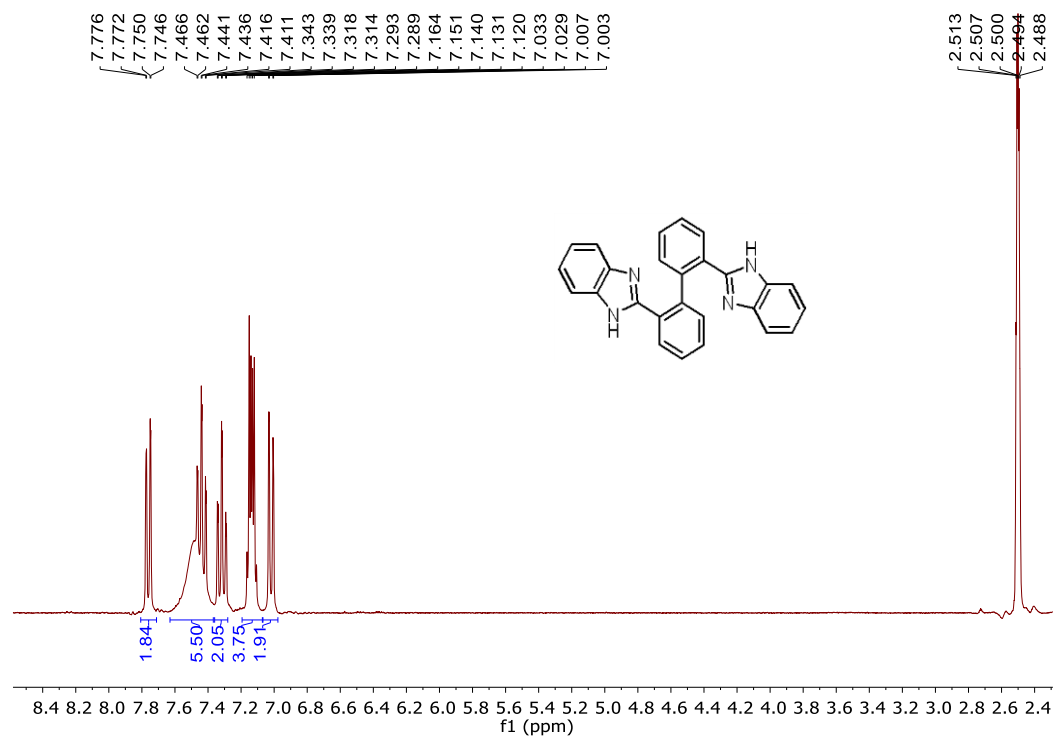
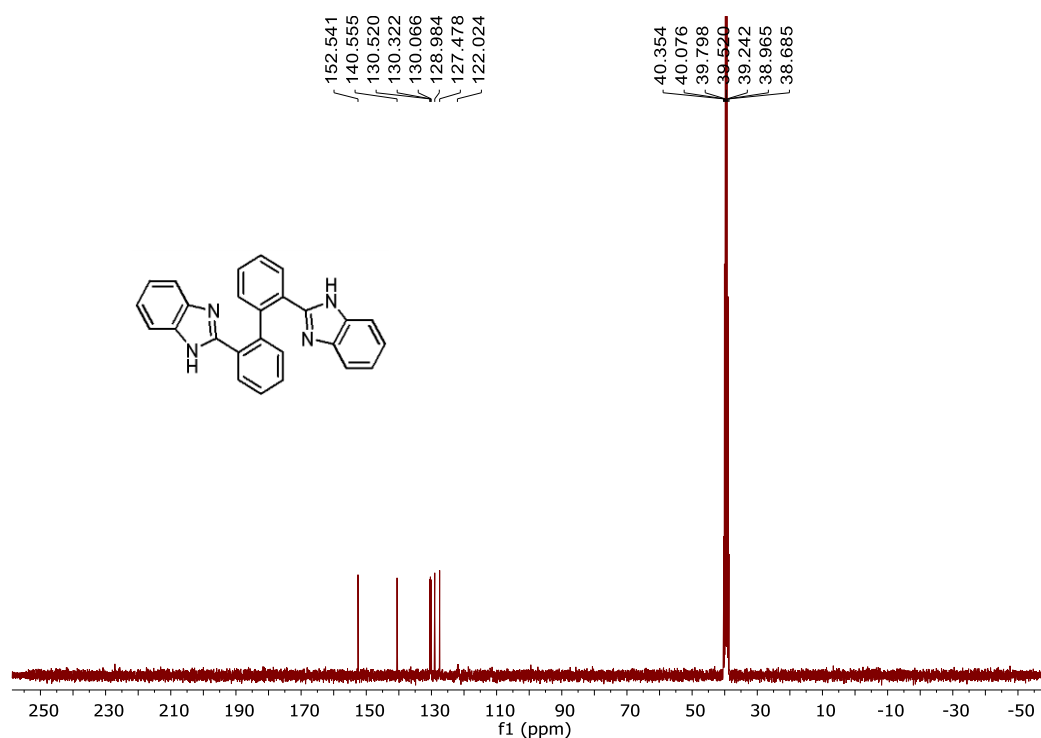
γ [°]	120	90	90
V [Å ³]	9107.0(7)	19308.1(17)	5793.9(5)
Z	3		
ρ [g/cm ³]	1.063		
$F(000)$	3018		
μ [mm ⁻¹]	0.618		
T_{\min}/T_{\max}	0.89 / 0.75		
θ range [°]	2.058 to 27.928		
hkl -range	-35, 26 / -33, 35 / -18, 19		
Measured refl.	105460		
Unique refl.	14477		
Completeness to θ / %	99.9		
Data	14477		
Restraints	1		
Parameters	574		
Goodness-of-fit (F^2)	1.085		
R_1, wR_2 ($I > 2$ (I))	0.0540, 0.1303		
R_1, wR_2 (all data)	0.0637, 0.1354		
Resid. el. dens. [e/Å ³]	1.661, -0.429		

Table 9.1.5. Summary of disorder, use of SQUEEZE or twinning.

Compound	disordered part	occupancy factors	restraints & constraints	remarks
3	THF (two atoms)	0.59(3) / 0.41(3)	SAME, EADP	
	THF (all atoms)	0.672(7) / 0.328(7)		
6⁺	PF ₆ ⁻	0.5 / 0.5	SADI (d(P-F), d(F...F)), RIGU, ISOR	disordered about a center of inversion
	PF ₆ ⁻	0.5 / 0.5	SADI (d(P-F), d(F...F)), RIGU, ISOR	disordered about a center of inversion
	MeCN	0.583(11) / 0.417(11)	DFIX (d(C-N) = 1.14 Å, d(C-C) = 1.47 Å, d(N...C) = 2.61 Å)	isotropic refinement

	MeCN	0.43(2) / 0.57(2)	DFIX (d(C-N) = 1.14 Å, d(C-C) = 1.47 Å, d(N...C) = 2.61 Å)	isotropic refinement
6				SQUEEZE
7				SQUEEZE
7+	Ph	0.655(7) / 0.345(7)	AFIX 66, RIGU, EADP	
	Ph	0.756(7) / 0.244(7)	AFIX 66, RIGU, EADP	
	S-C6H4-Br	0.9308(19) / 0.0692(19)	SAME, RIGU, EADP	
	S-C6H4-Br	0.897(2) / 0.103(2)	SAME, RIGU, EADP	
	PF ₆ ⁻	0.50(2) / 0.50(2)	SADI (d(P-F), d(F...F))	
	Et ₂ O	0.697(7) / 0.303(7)	DFIX (d(C-C) = 1.51 Å, d(C-O) = 1.43 Å), SAME, RIGU, EADP	
8				SQUEEZE

9.2. Supplementary Spectra and Information

Figure 9.2.1. 1H NMR spectrum of H_2L^1 recorded in $DMSO-d_6$ (300.1 MHz, 298 K).Figure 9.2.2. ^{13}C NMR spectrum of H_2L^1 recorded $DMSO-d_6$ (75.5 MHz, 300 K).

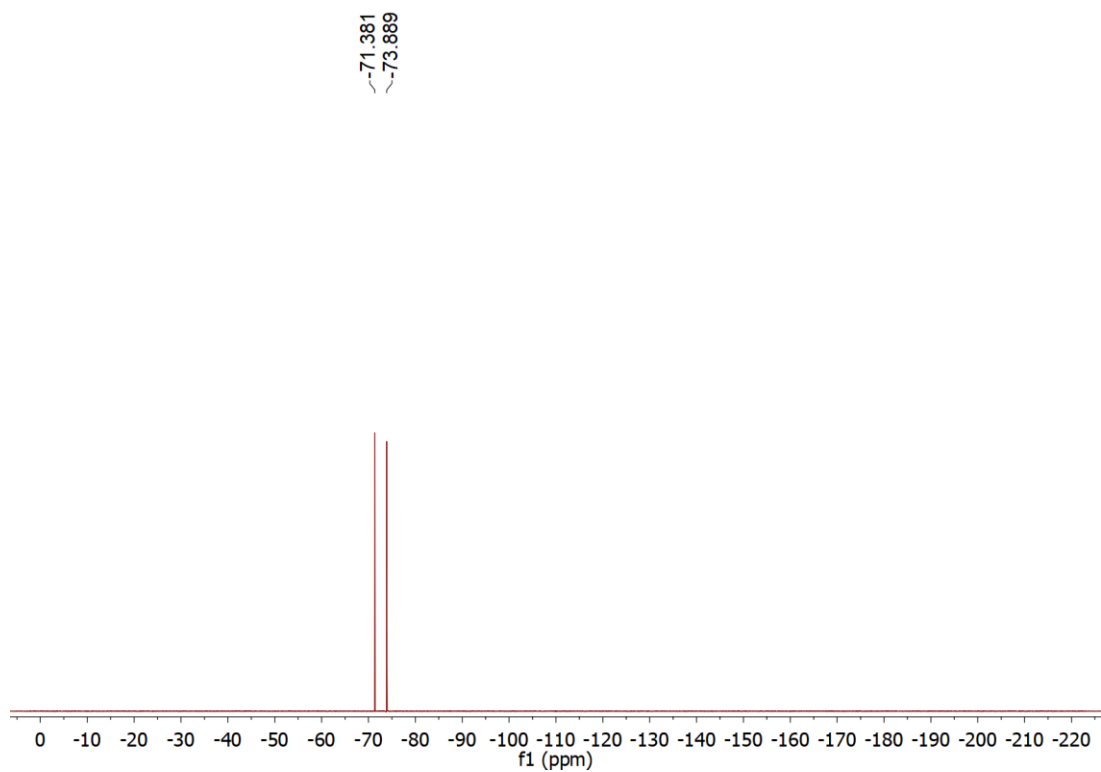


Figure 9.2.3. ^{19}F NMR spectrum of $[\text{H}_2\text{L}^5](\text{PF}_6)_2$ recorded in $(\text{CD}_3)_2\text{CO}$ (282.4 MHz, 298 K).

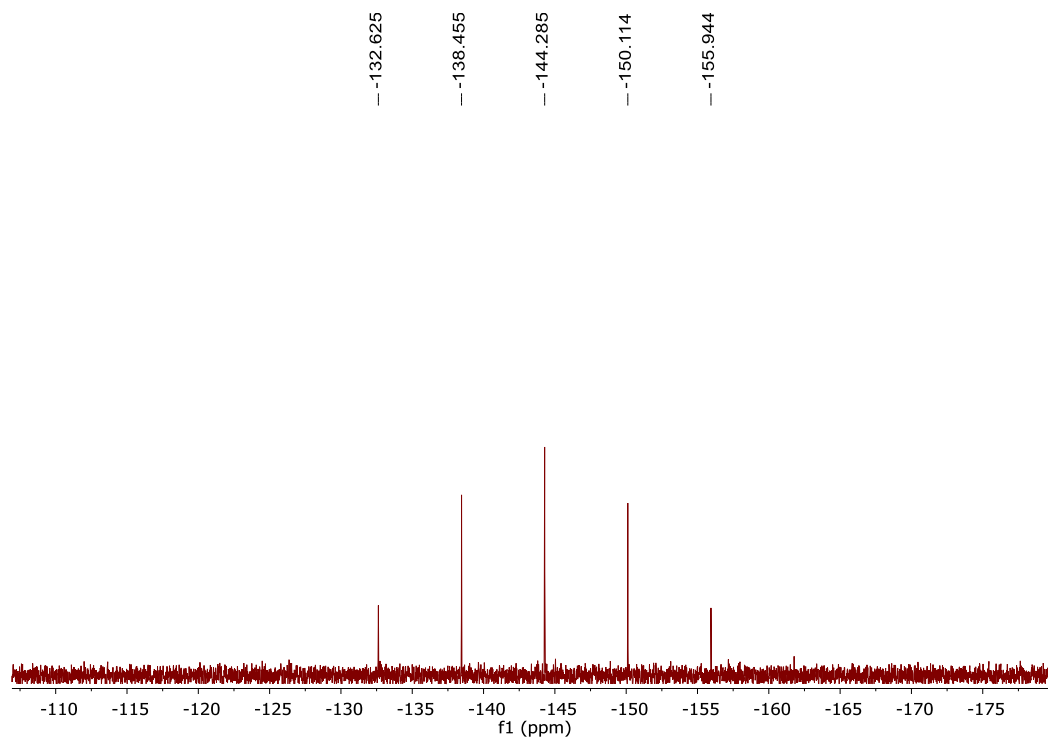


Figure 9.2.4. ^{31}P NMR spectrum of $[\text{H}_2\text{L}^5](\text{PF}_6)_2$ recorded in $(\text{CD}_3)_2\text{CO}$ (121.5 MHz, 298 K).

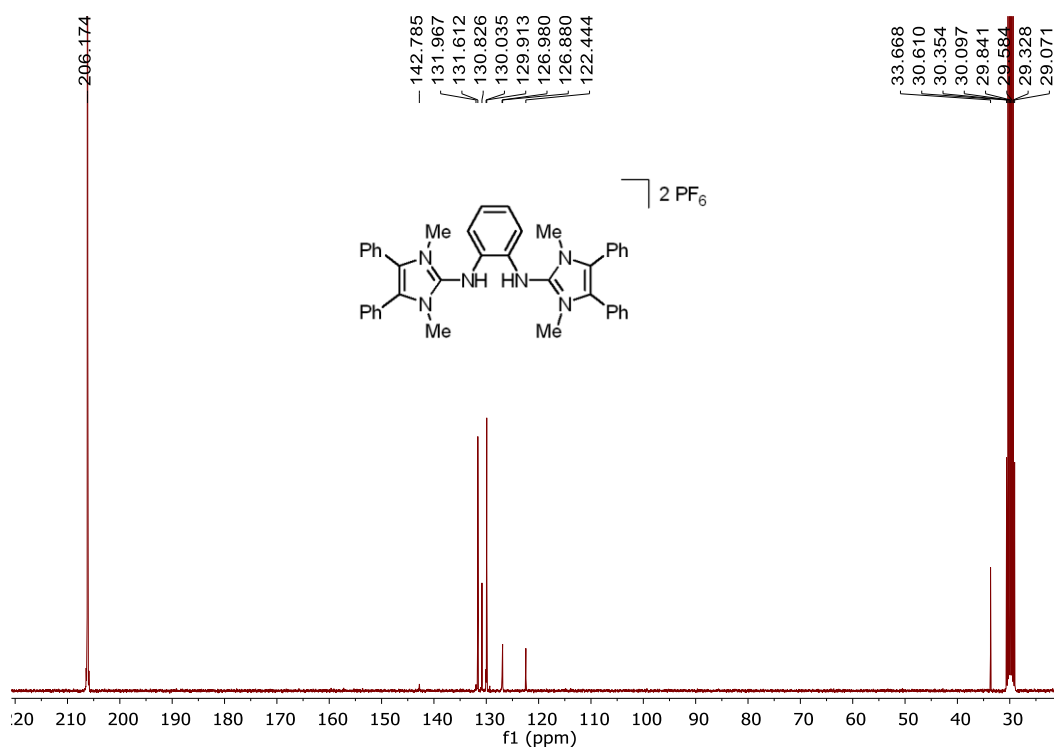


Figure 9.2.5. ^{13}C NMR spectrum of $[\text{H}_2\text{L}^5](\text{PF}_6)_2$ recorded in $(\text{CD}_3)_2\text{CO}$ at (75.5 MHz, 298 K).

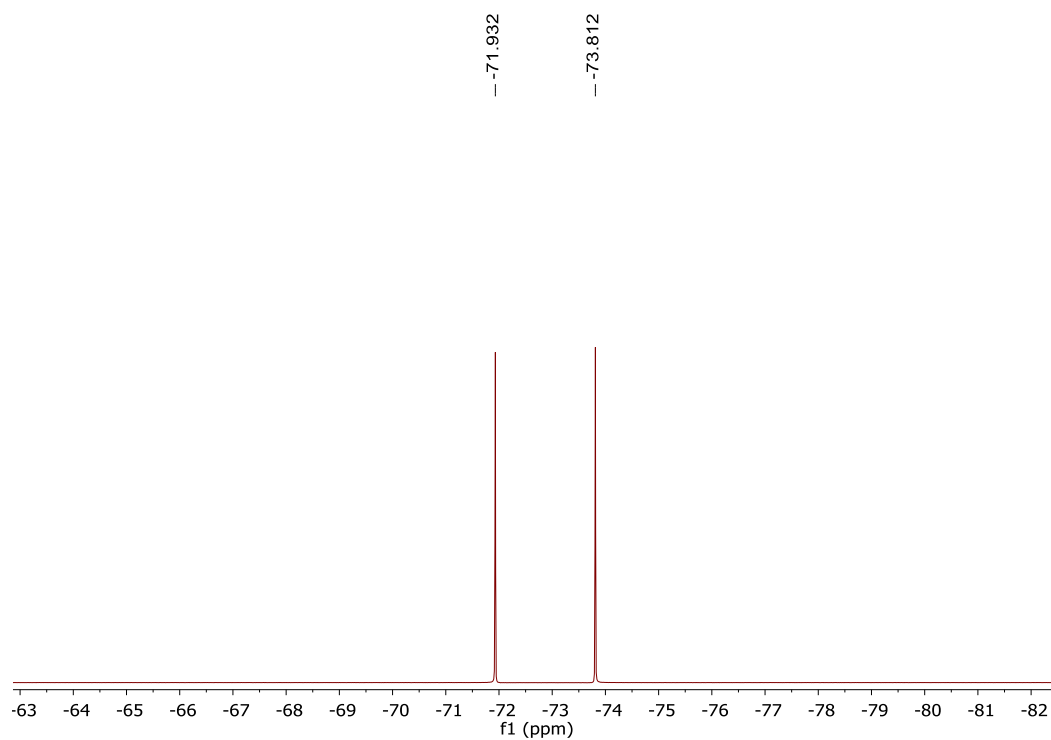


Figure 9.2.6. ^{19}F NMR spectrum of $[\text{HL}^6](\text{PF}_6)$ recorded in $(\text{CD}_3)_2\text{CO}$ (376.6 MHz, 298 K).

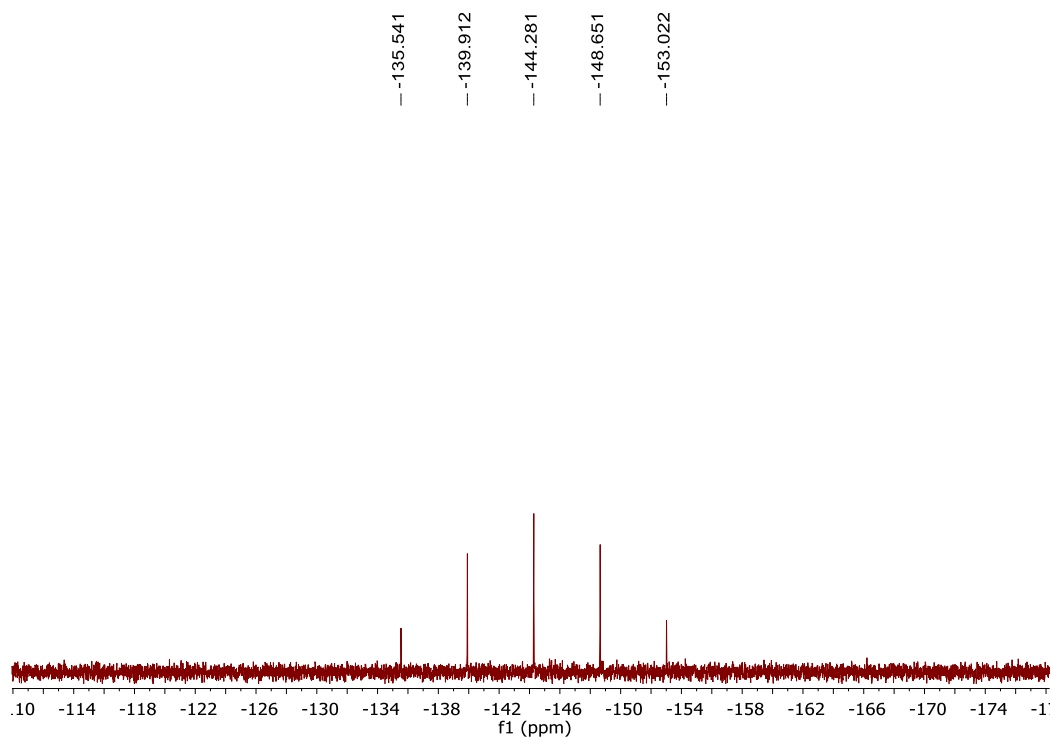


Figure 9.2.7. ^{31}P NMR spectrum of $[\text{HL}^6](\text{PF}_6)$ recorded in $(\text{CD}_3)_2\text{CO}$ (162.0 MHz, 298 K).

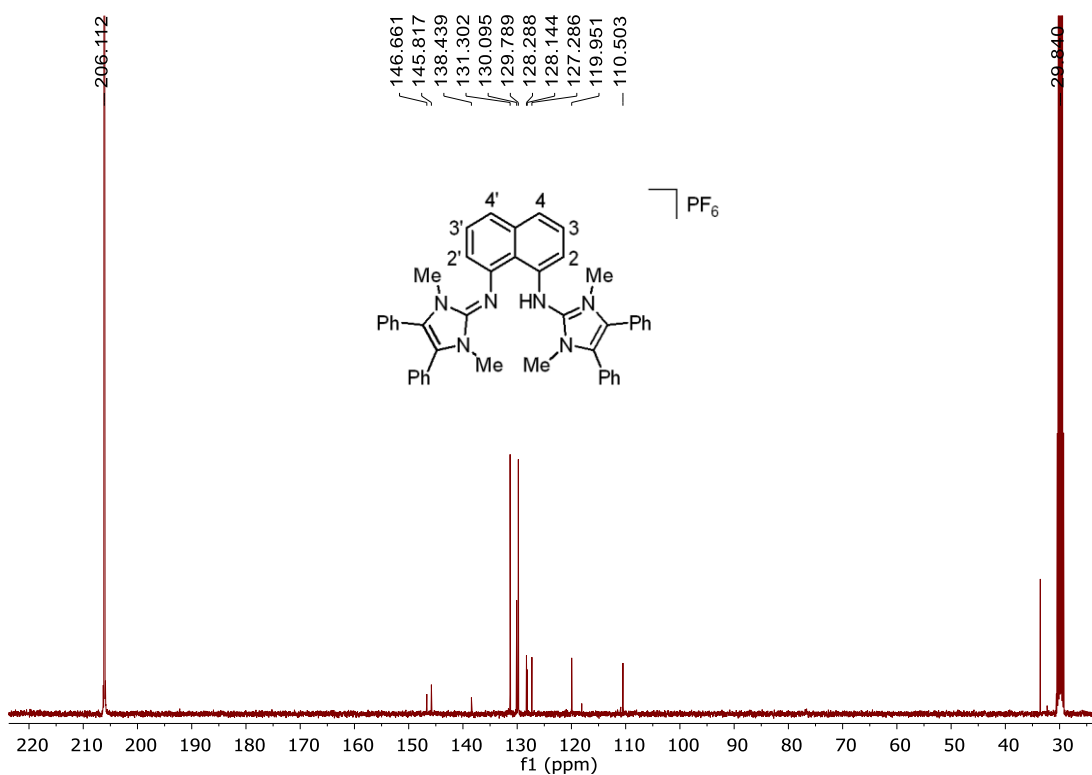


Figure 9.2.8. ^{13}C NMR spectrum of $[\text{HL}^6](\text{PF}_6)$ recorded in $(\text{CD}_3)_2\text{CO}$ (100.7 MHz, 298 K).

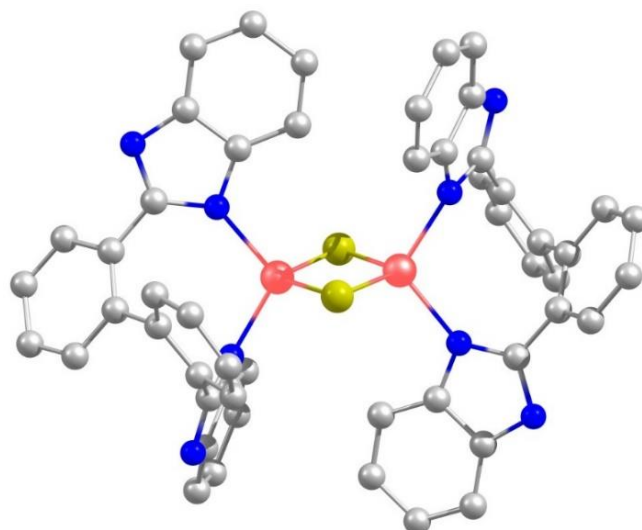


Figure 9.2.9. DFT optimized molecular structure of the anion of the complex $\mathbf{1}^{2-}$ (Fe = red, N = blue, S = yellow, C = gray). Spin restricted DFT calculations with ORCA 4.2.3, BP86 functional, def2-tzvp basis set, RI approximation using the auxiliary def2 /J basis set, D3 dispersion correction with Becke-Johnson damping, tight convergence and optimization criteria.

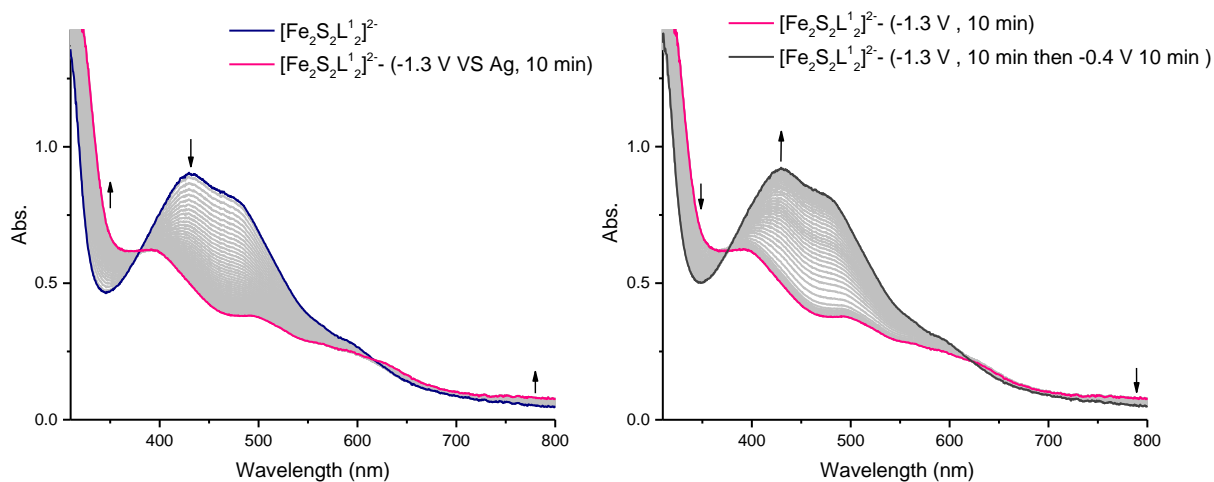


Figure 9.2.10. UV-vis (spectro)electrochemistry showing: (left) the reduction of $(\text{NEt}_4)_2\mathbf{1}$ to $(\text{NEt}_4)_3\mathbf{1}$ (at -1.3 V vs. Ag wire, $(\text{NEt}_4)_2\mathbf{1}$ (black), $(\text{NEt}_4)_3\mathbf{1}$ (red)); (right) from $(\text{NEt}_4)_3\mathbf{1}$ to $(\text{NEt}_4)_2\mathbf{1}$ (at -1.3 V vs. Ag wire; $(\text{NEt}_4)_3\mathbf{1}$ (red), $(\text{NEt}_4)_2\mathbf{1}$ (black)) in an MeCN solution containing 0.1M NBu_4PF_6 .

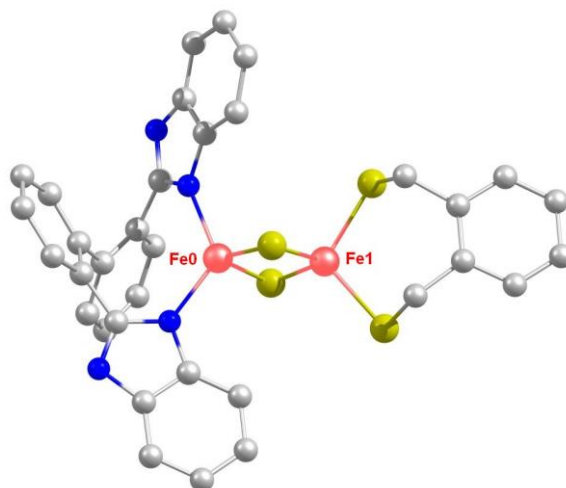


Figure 9.2.11. DFT optimized molecular structure of complex 2^{2-} (Fe = reddish, N = blue, S = yellow, C = gray). Spin restricted DFT calculations with ORCA 5.1.0, BP86 functional, def2-tzvp basis set, RI approximation using the auxiliary def2/J basis set, D3 dispersion correction with Becke-Johnson damping, tight convergence and optimization criteria. Mulliken Spin Population: Fe0 = 3.803932, Fe1 = 3.659288, S2 = 0.802513, S3 = 0.808966, S4 = 0.308090, S5 = 0.317934, N6 = 0.051349, N7 = 0.037365, N8 = 0.028793, N9 = 0.029347.

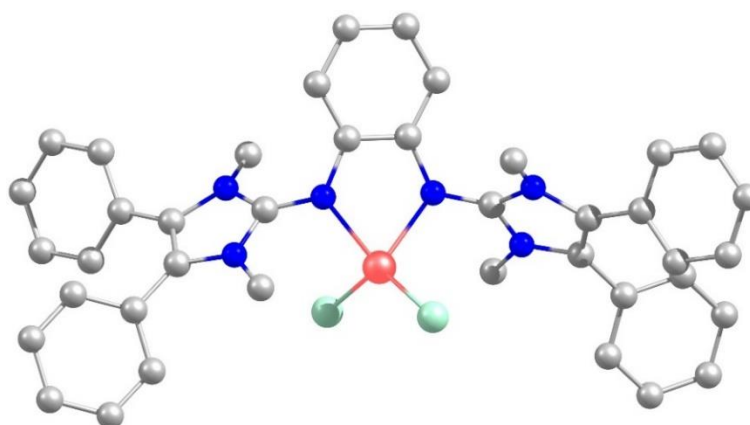


Figure 9.2.12. DFT optimized molecular structure of complex 3 (Fe = reddish, N = blue, Cl = greenish, C = gray). Spin restricted DFT calculations with ORCA 4.2.3, BP86 functional, def2-tzvp basis set, RI approximation using the auxiliary def2/J basis set, D3 dispersion correction with Becke-Johnson damping, tight convergence and optimization criteria. Mulliken Spin Population: Fe0 = 3.546130, Cl1 = 0.139900, Cl2 = 0.145009, N3 = 0.017383, N4 = 0.022439, N5 = 0.014717, N6 = 0.012877, N7 = 0.014631, N8 = 0.016974.

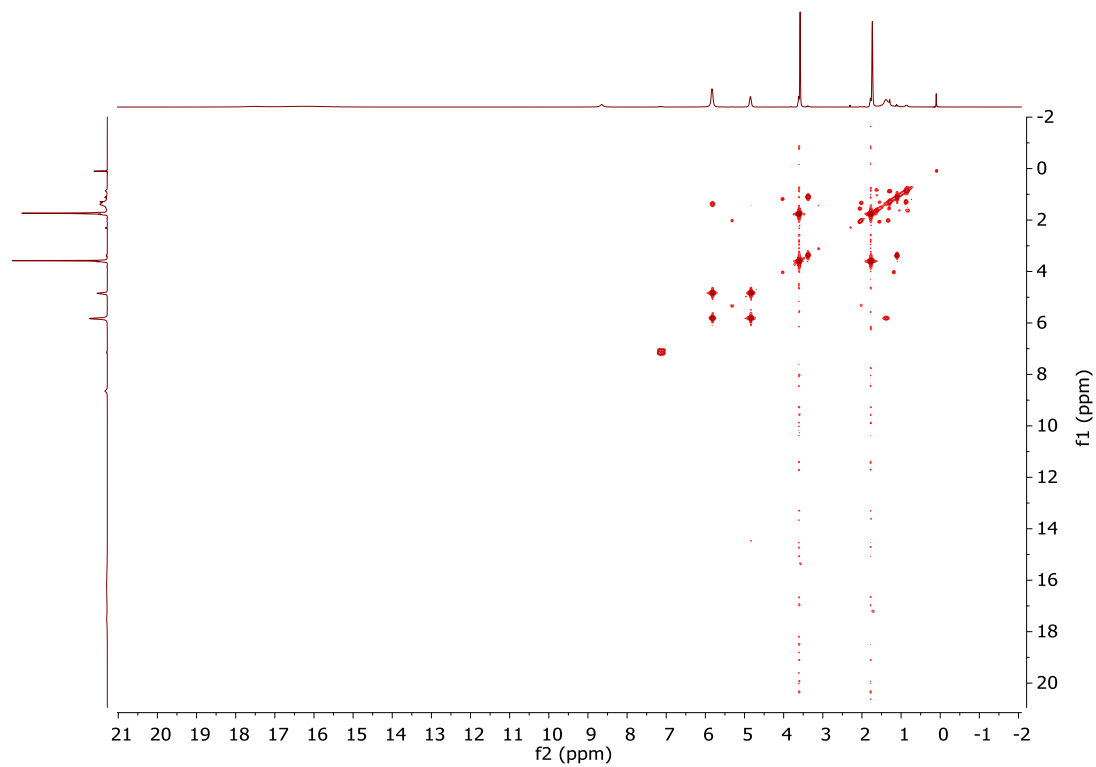


Figure 9.2.13. ^1H - ^1H COSY of complex **3** in THF- d_8 (600.3, 600.3 MHz, 298 K).

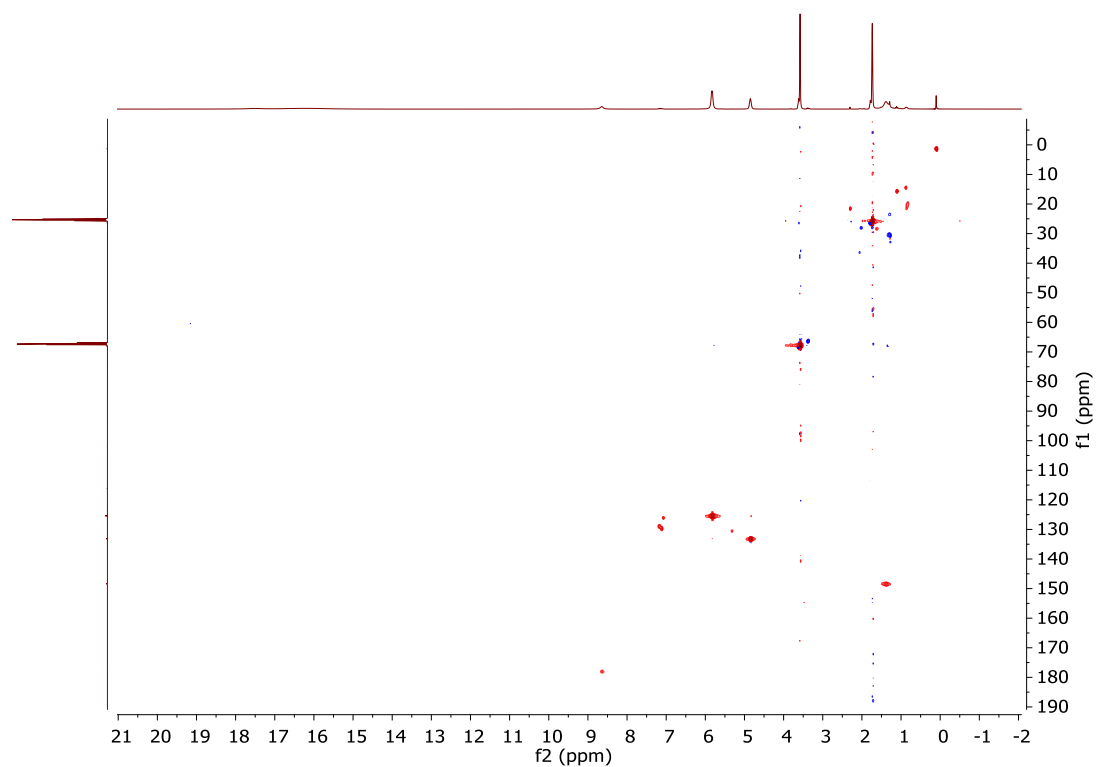


Figure 9.2.14. ^1H - ^{13}C HSQC of complex **3** in THF- d_8 (600.3, 151.0 MHz, 298 K).

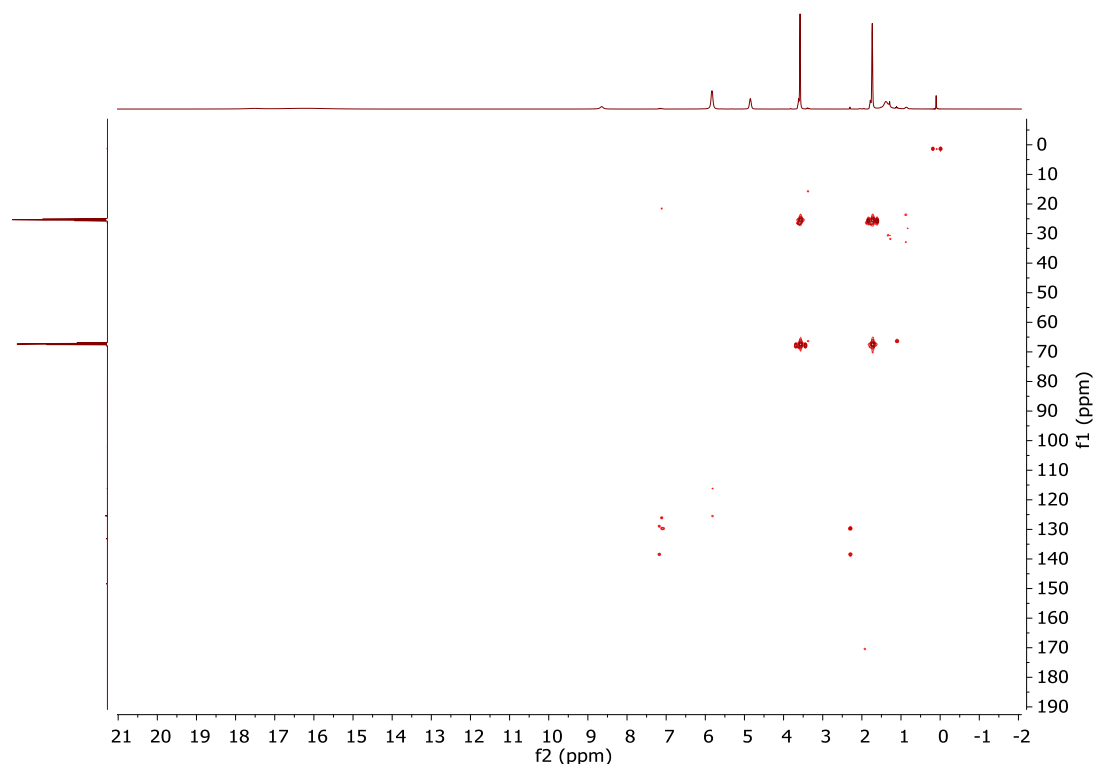


Figure 9.2.15. ^1H - ^{13}C HMBC of complex **3** in THF- d_8 (600.3, 151.0 MHz, 298 K).

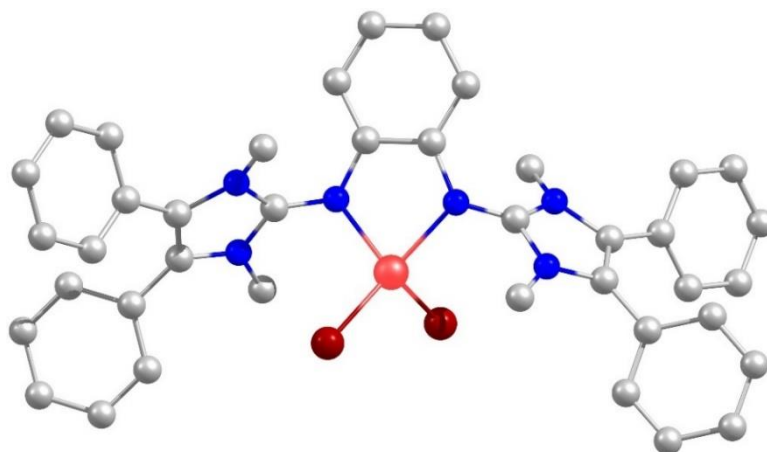


Figure 9.2.16. DFT optimized molecular structure of complex **4** (Ni = red, N = blue, Br = dark red, C = gray). Spin restricted DFT calculations with ORCA 4.2.3, BP86 functional, def2-tzvp basis set, RI approximation using the auxiliary def2/J basis set, D3 dispersion correction with Becke-Johnson damping, tight convergence and optimization criteria. Mulliken Spin Population: Ni0 = 1.374157, Br1 = 0.189436, Br2 = 0.127741, N3 = 0.063499, N4 = 0.101991, N5 = 0.020209, N6 = 0.020002, N7 = 0.016417, N8 = 0.017055.

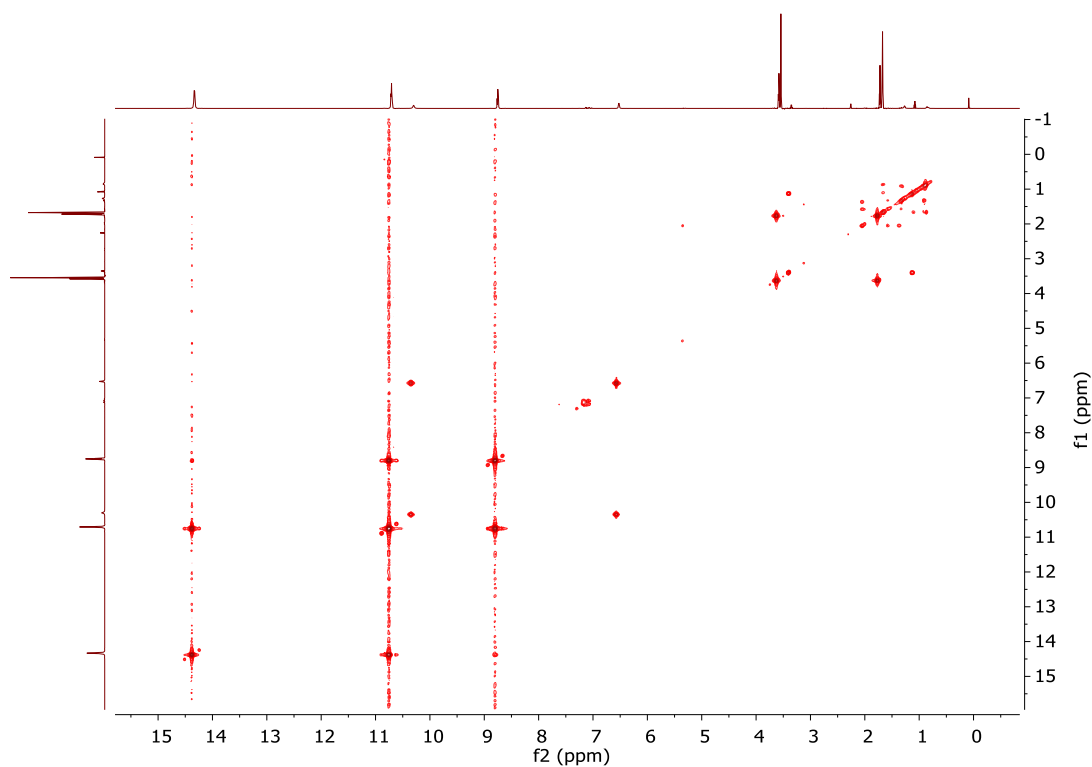


Figure 9.2.17. ^1H - ^1H COSY of complex **4** in THF- d_8 (600.3, 600.3 MHz, 333 K).

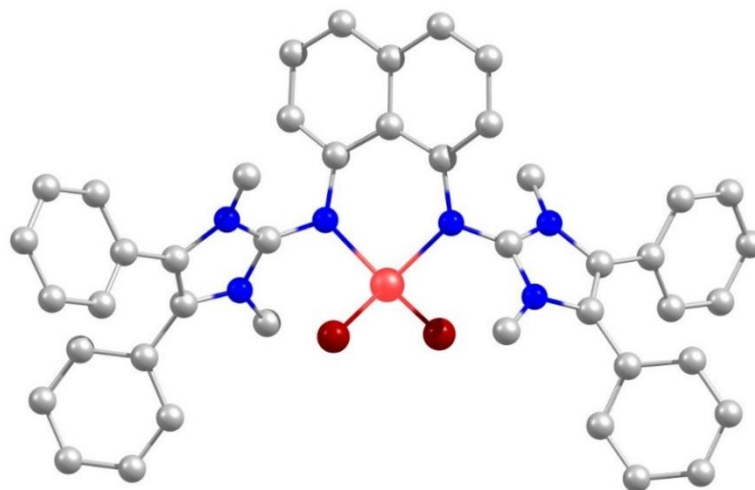


Figure 9.2.18. DFT optimized molecular structure of complex **5** (Ni = red, N = blue, Br = dark red, C = gray). Spin restricted DFT calculations with ORCA 5.1.0, BP86 functional, def2-tzvp basis set, RI approximation using the auxiliary def2/J basis set, D3 dispersion correction with Becke-Johnson damping, tight convergence and optimization criteria. Mulliken Spin Population: Ni0 = 1.420538, Br1 = 0.131845, Br2 = 0.131850, N3 = 0.086890, N4 = 0.086892, N5 = 0.017450, N6 = 0.017355, N7 = 0.017450, N8 = 0.017355.

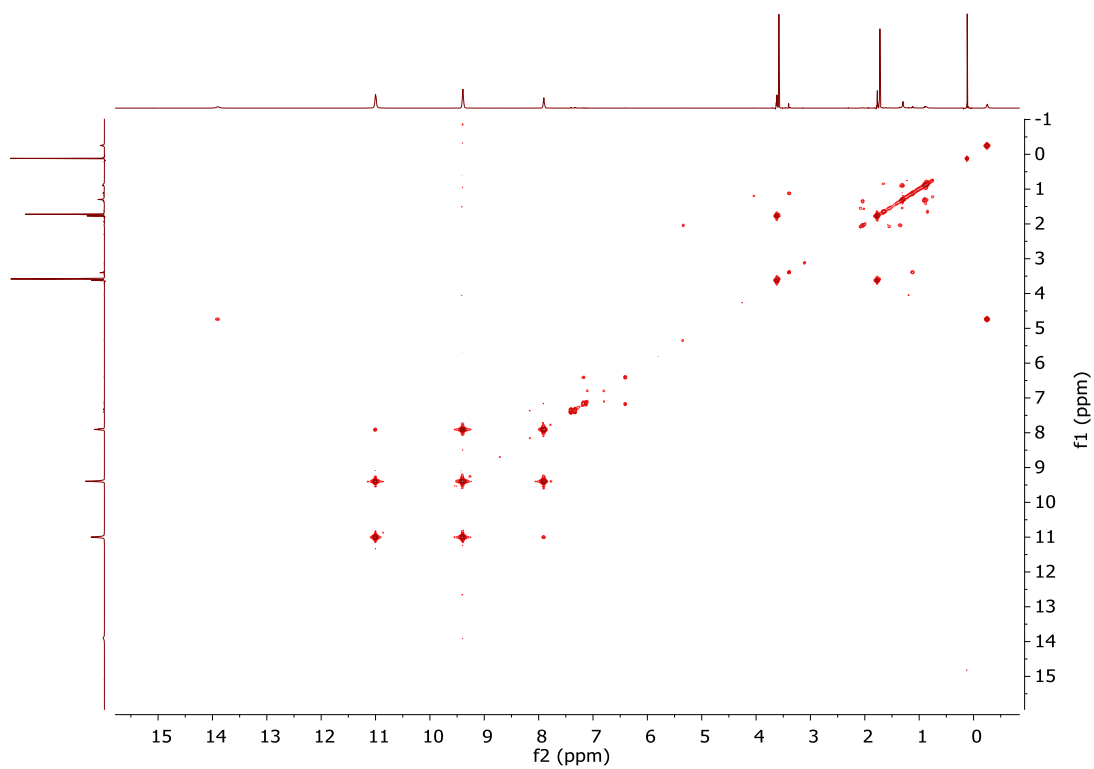


Figure 9.2.19. ^1H - ^1H COSY of complex **5** in THF- d_8 (600.3, 600.3 MHz, 298 K).

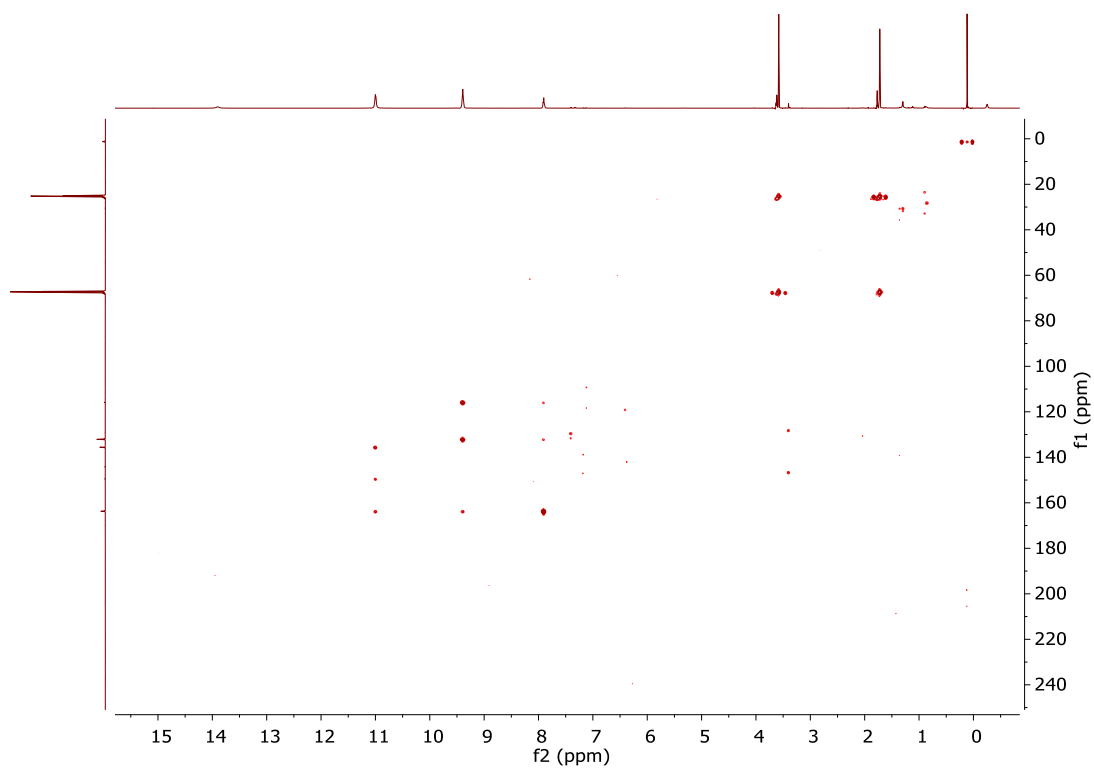


Figure 9.2.20. ^1H - ^{13}C HMBC of complex **5** in THF- d_8 (600.3, 151.0 MHz, 298 K).

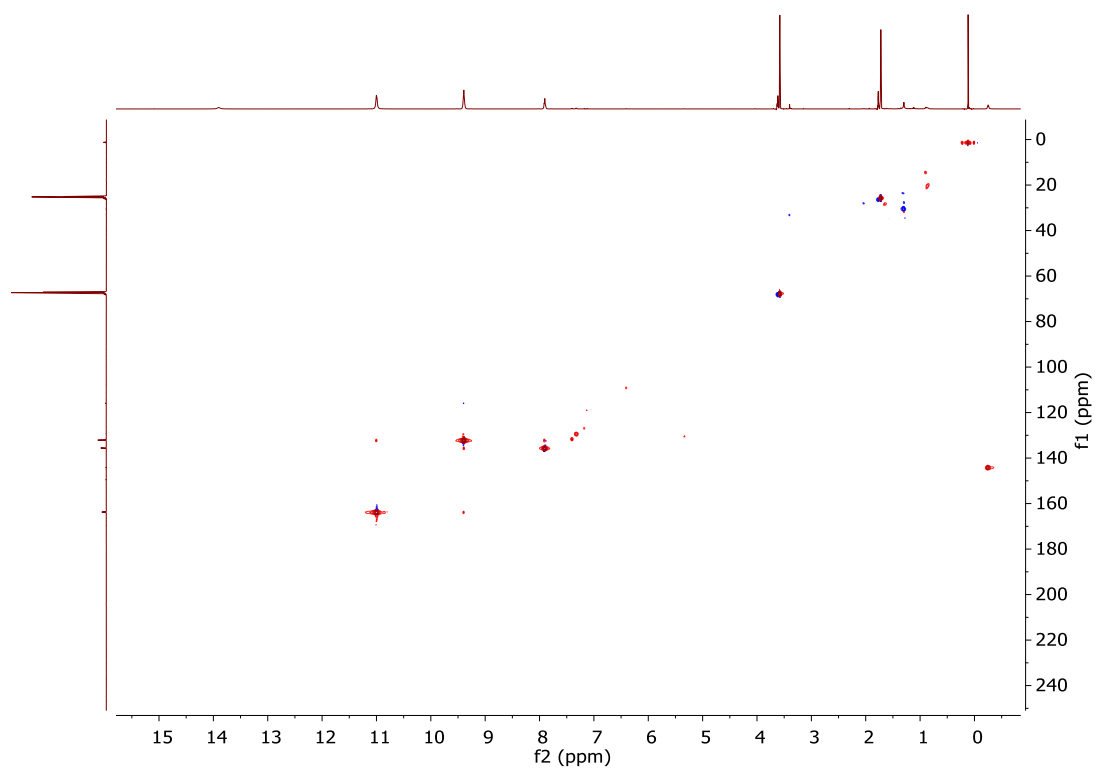


Figure 9.2.21. ^1H - ^{13}C HSQC of complex **5** in THF-d_8 (600.3, 151.0 MHz, 298 K).

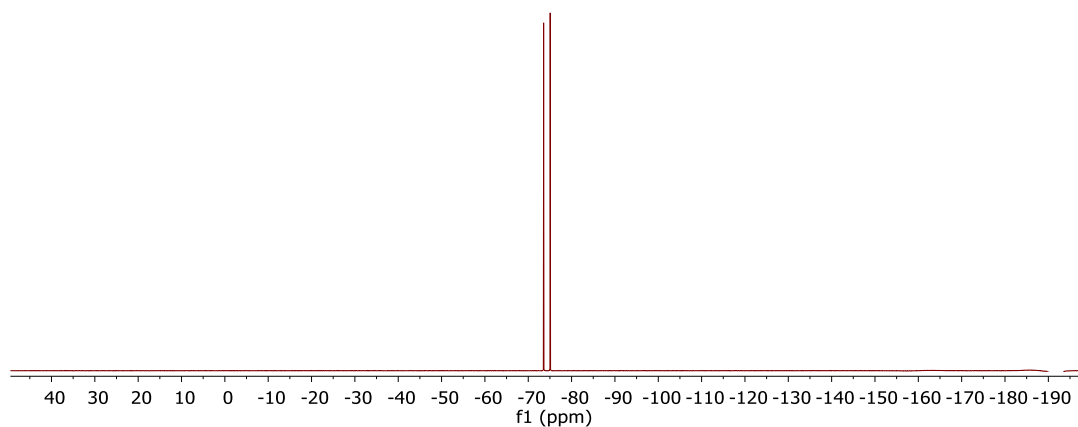


Figure 9.2.22. ^{19}F -NMR spectrum of complex **6**(PF_6) in MeCN-d_3 (470.7 MHz, 333 K).

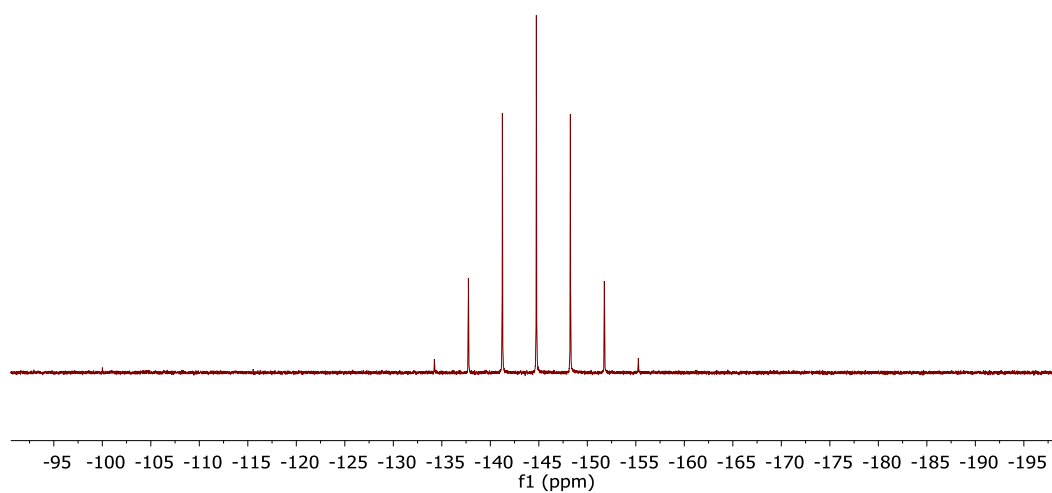


Figure 9.2.23. ^{31}P -NMR spectrum of complex **6**(PF₆) in MeCN-d₃ (202.5 MHz, 333 K).

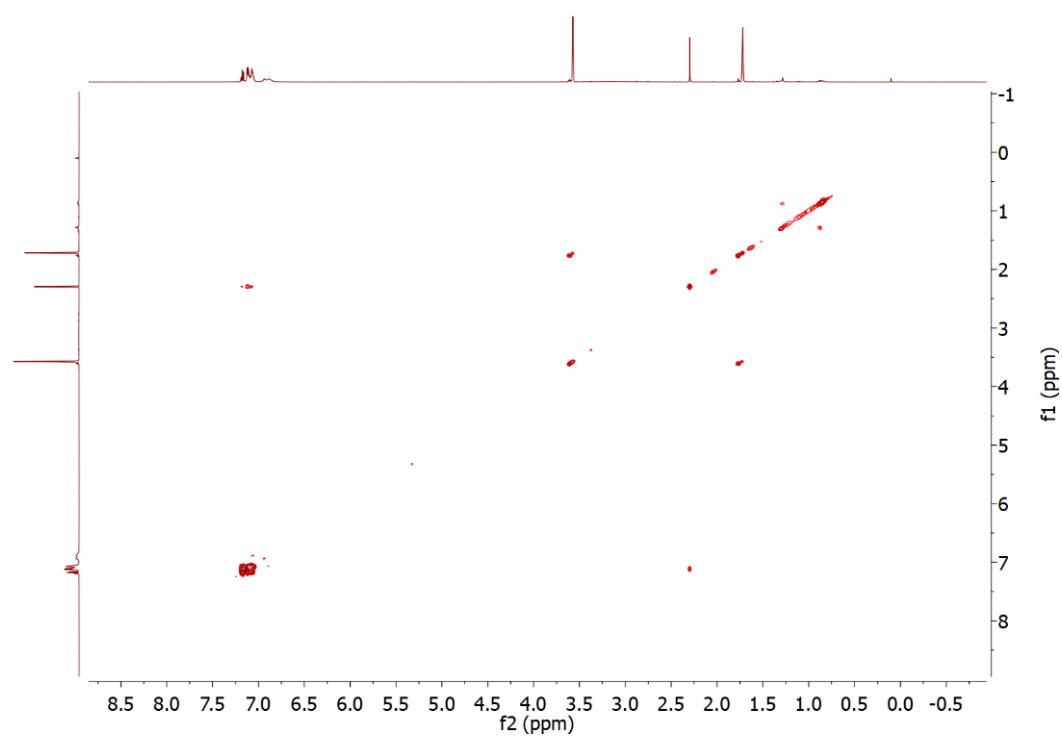


Figure 9.2.24. ^1H - ^1H COSY spectrum of complex **6** in CD₂Cl₂ (600.3, 600.3 MHz, 298 K).

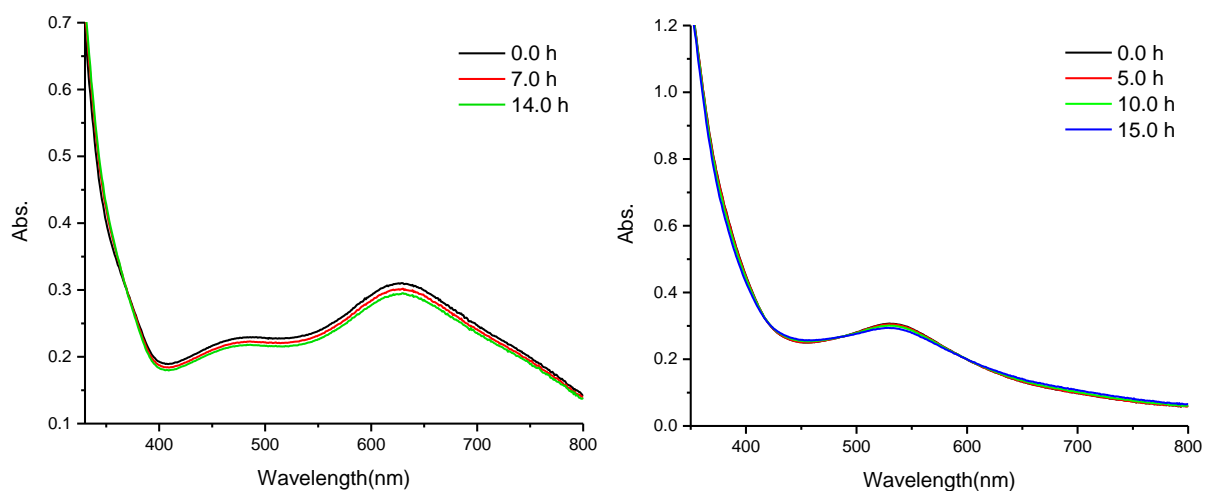


Figure 9.2.25. UV-vis absorption spectra of **6**(PF₆) (left) and **6** (right) in THF solution being kept at 298 K.

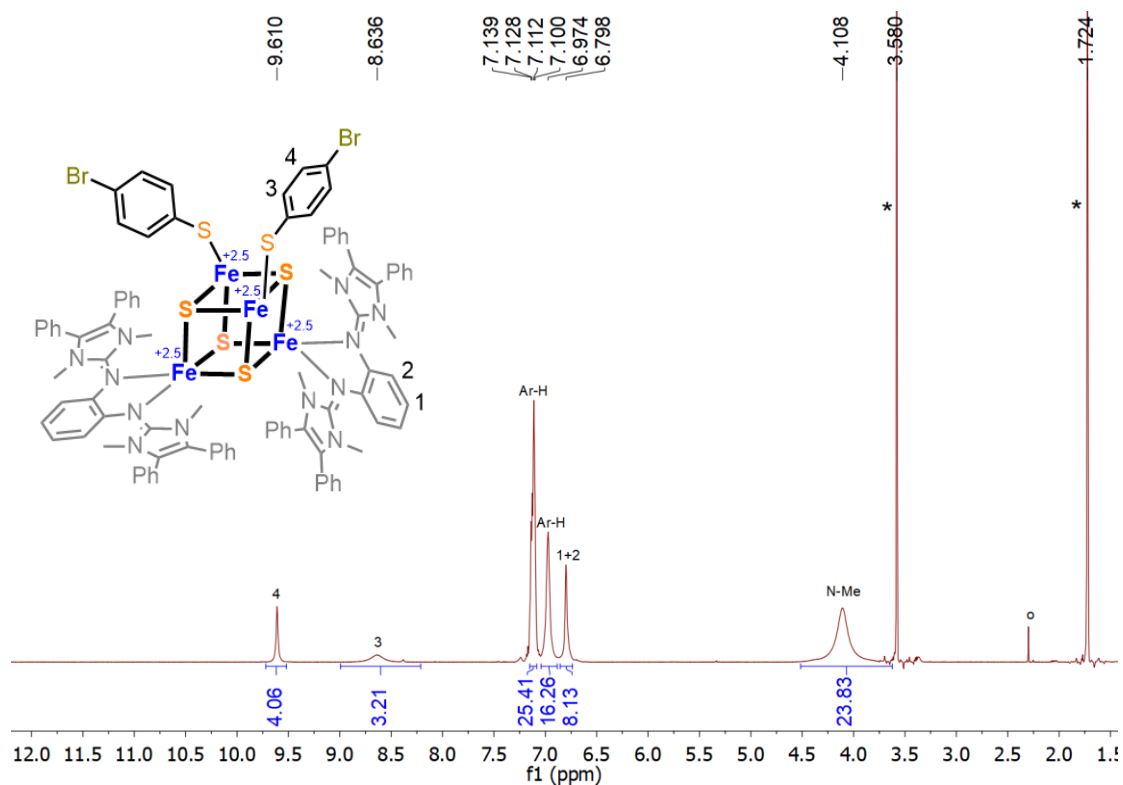


Figure 9.2.26. ¹H NMR spectrum of **7** recorded in THF-d₈ (600.3 Hz, 333 K). Signals of the THF-d₈ (*) and residual solvent (°) have been labeled.

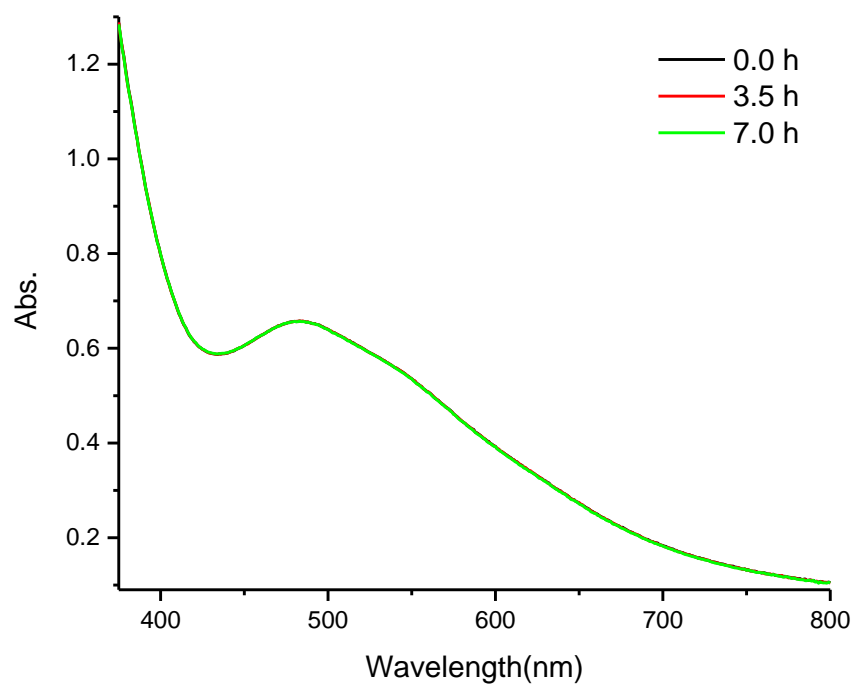


Figure 9.2.27. UV-vis absorption spectra of complex **7** in THF solution under the N₂ atmosphere being kept at 298 K.

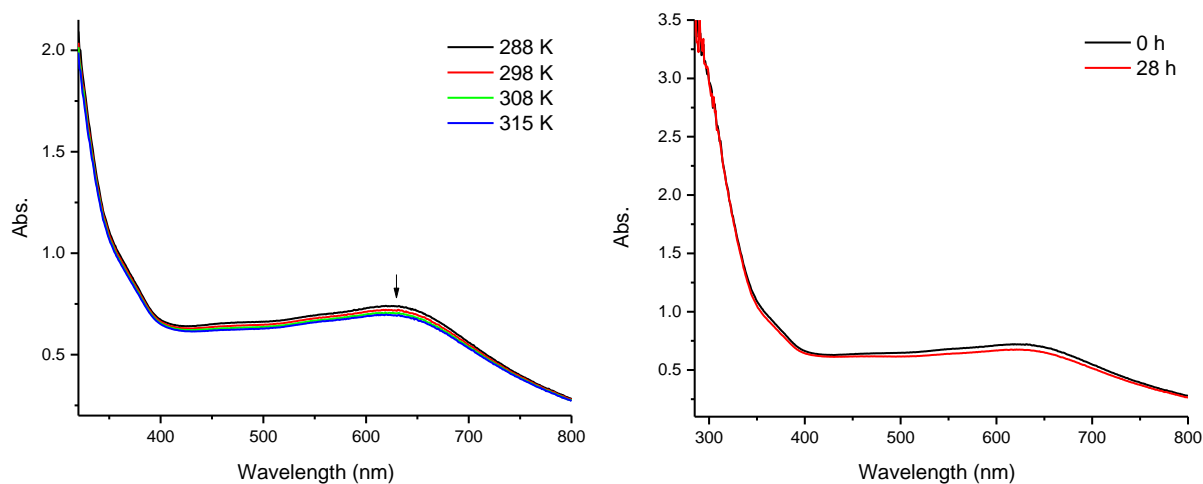


Figure 9.2.28. Variable temperature UV-vis absorption spectra of complex **7**(PF₆) in MeCN solution in the temperature range from 288 K to 315 K (left). UV-vis spectra of complex **7**(PF₆) in MeCN solution being kept at 298 K (right).

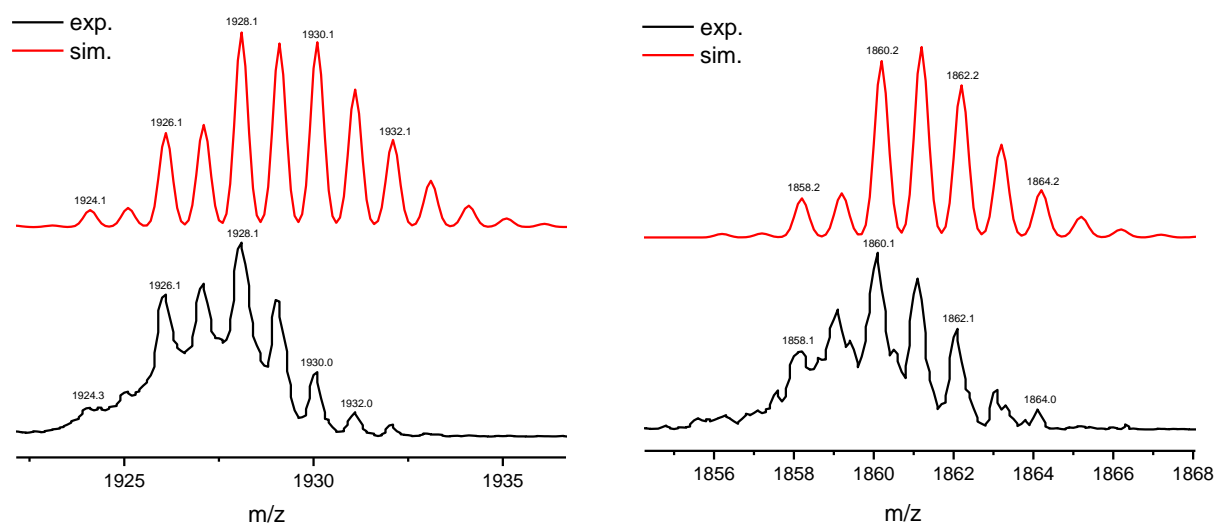


Figure 9.2.29. The experimental and simulated isotopic distribution pattern of $[M-PF_6]^+$ for $[7]^+$ in MeCN solution (left). The experimental and expected isotopic distribution pattern of $[M-PF_6]^+$ for $[8]^+$ in MeCN solution (right).

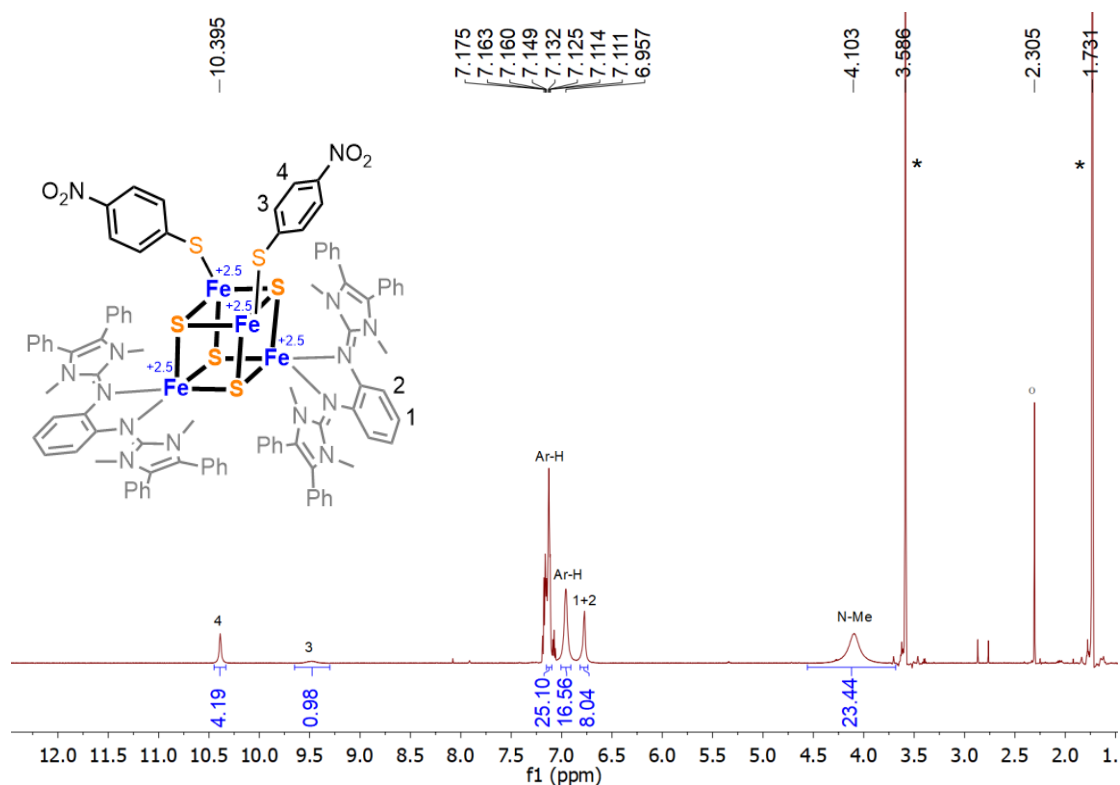


Figure 9.2.30. ¹H NMR spectrum of **8** recorded in THF-d₈ (600.3 Hz, 333 K). Signals of the THF-d₈ (*) and residual solvent (°) have been labeled.

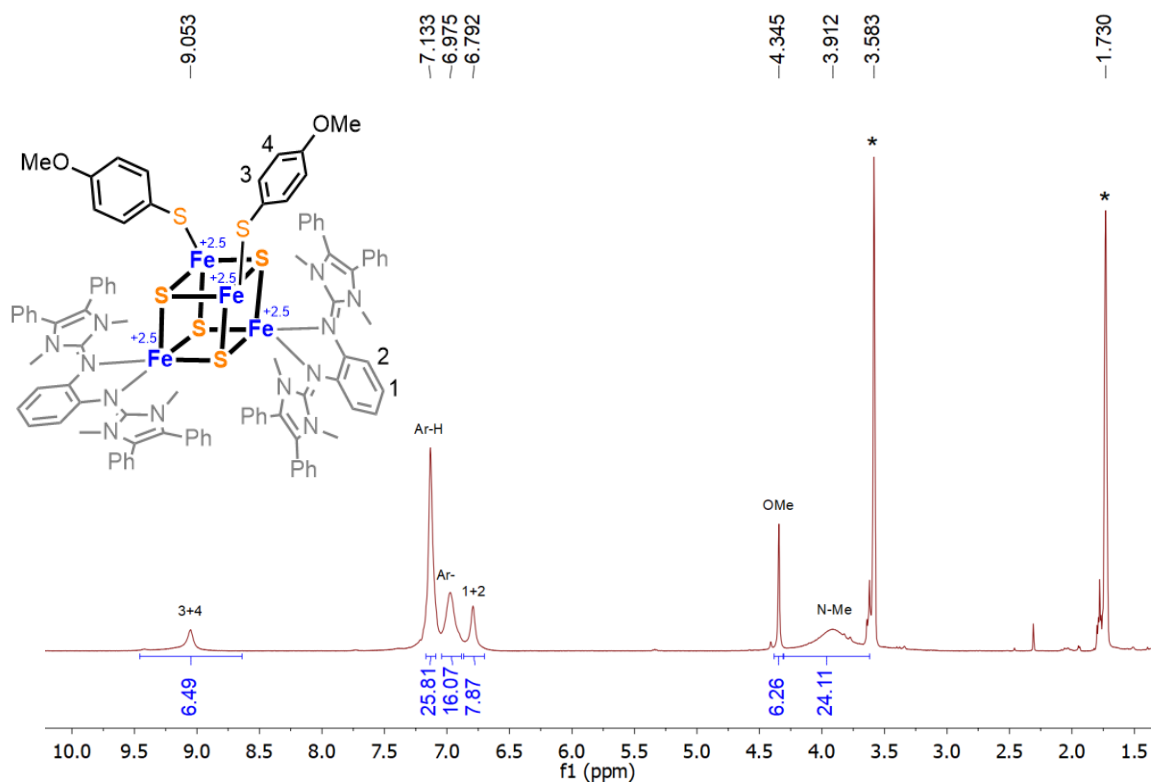


Figure 9.2.31. ^1H NMR spectrum of **9** recorded in THF-d_8 (300.1 MHz, 298 K). Signals of the THF-d_8 (*) has been labeled.

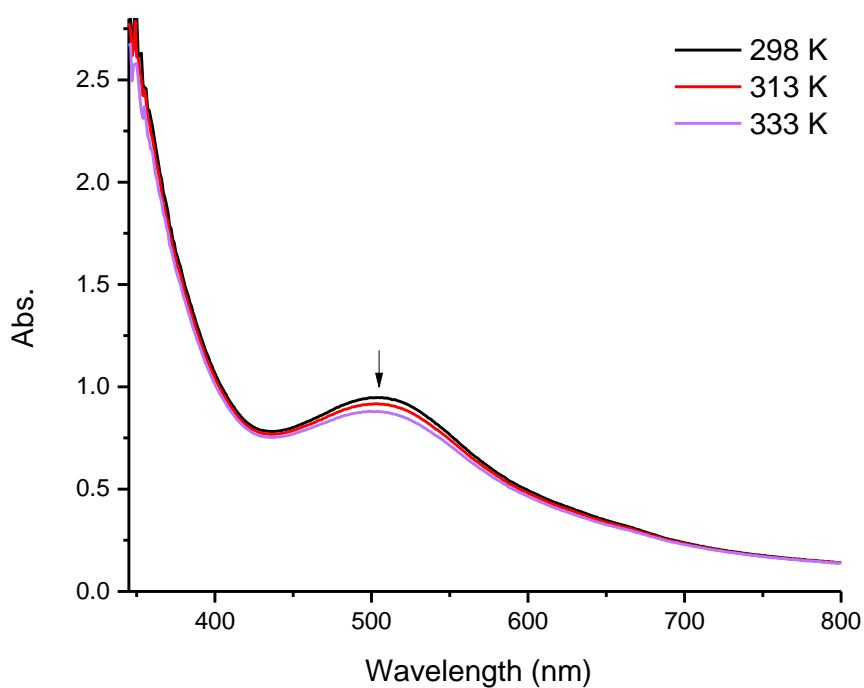
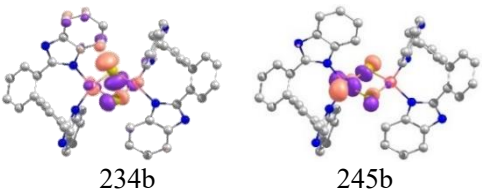
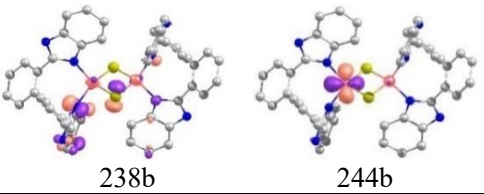
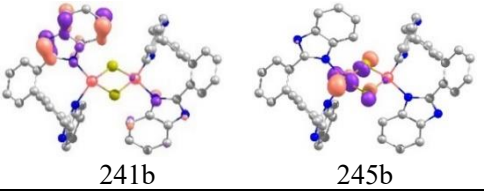
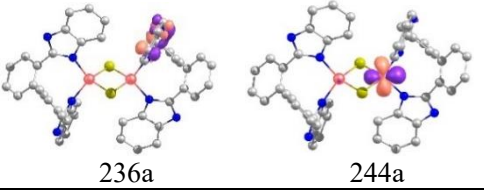
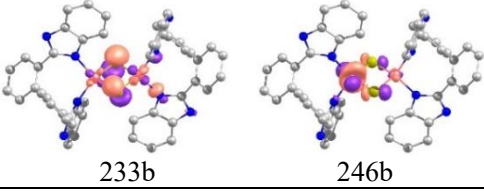
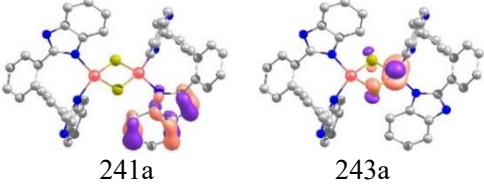
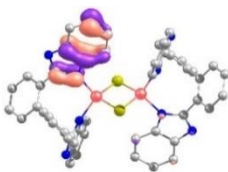
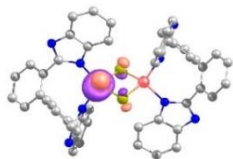
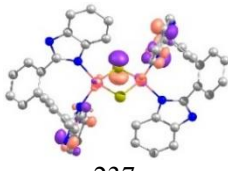
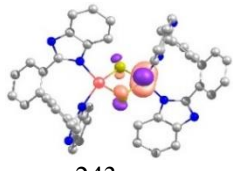
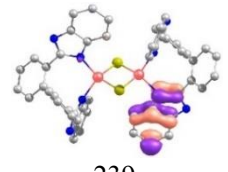

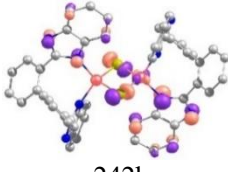
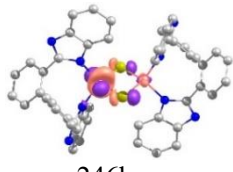
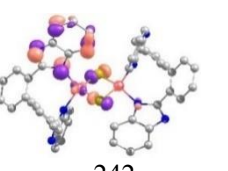
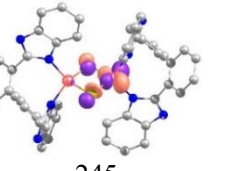
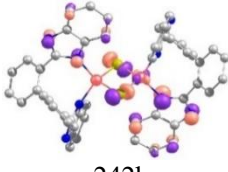
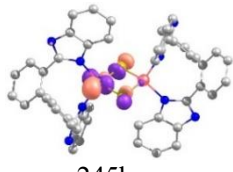

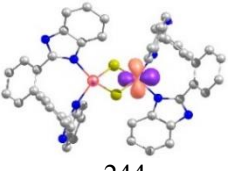
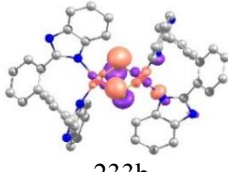
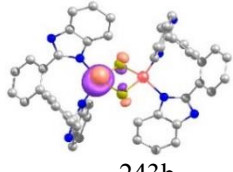


Figure 9.2.32. Variable temperature UV-vis absorption spectra of **9** in THF solution under the N_2 atmosphere in the temperature range from 193 K to 333 K.

9.3 Calculation

Table 9.3.1. Selected TD-DFT (BP86/def2-tzvp level) calculated energy, oscillator strengths, compositions of the major electronic transitions, and related natural transition orbitals of complex 1^{2-} .

Complexes	Wavelength (nm)	Fosc	Transition (%)	NTO surfaces
1^{2-}	426.3	0.010414266	234b → 245b (8.8%)	
			238b → 244b (9.3%)	
			241b → 245b (15.2%)	
	432	0.019296455	236a → 244a (8.6%)	
			233b → 246b (12.2%)	
	466.9	0.015176879	241a → 243a (18.3%)	

			239b -> 243b (23.8%)	 
				239b 243b
478.5	0.011027105	237a -> 243a (9.2%)	 	
		239a -> 243a (8.1%)	 	
		242b -> 246b (7.3%)	 	
		242a -> 245a (7.9%)	 	
495.4	0.019941532	242b -> 245b (7.2%)	 	
		234a -> 244a (7.1%)	 	
498.6	0.017121451	233b -> 243b (7.9%)	 	
			233b 243b	

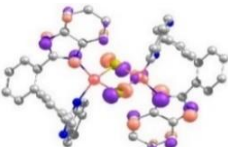
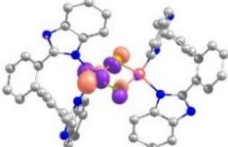

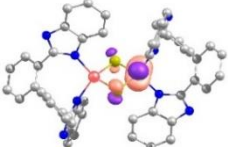
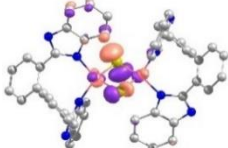
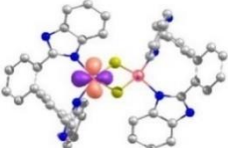
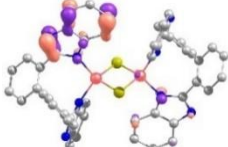
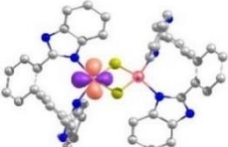
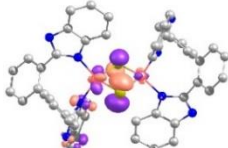
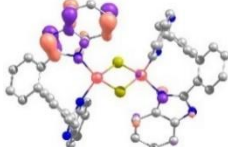
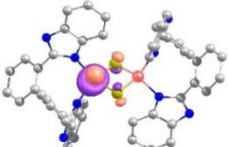
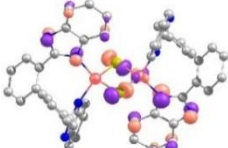
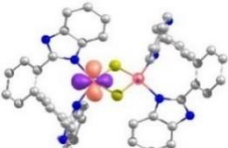
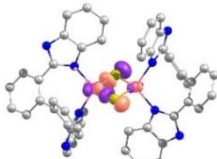
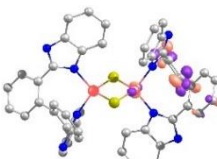
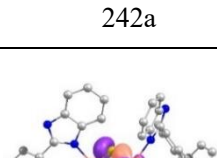
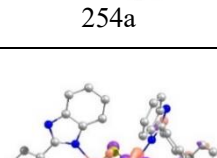
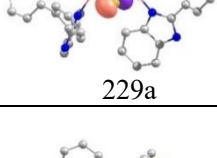
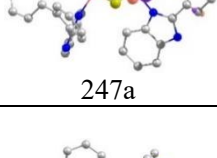
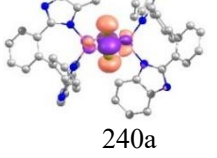
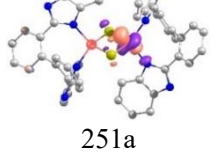
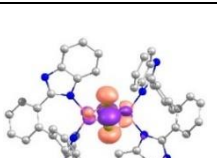
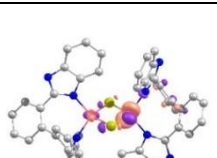
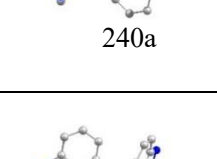
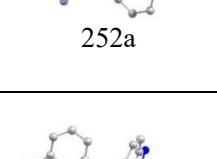
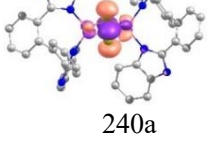

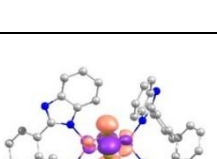
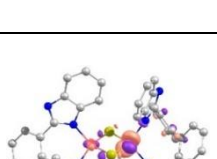
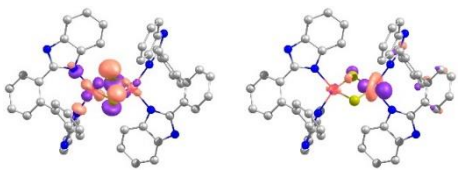
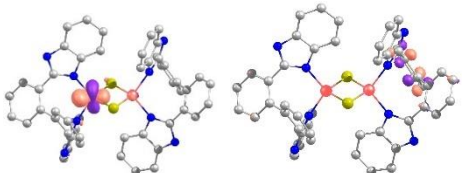
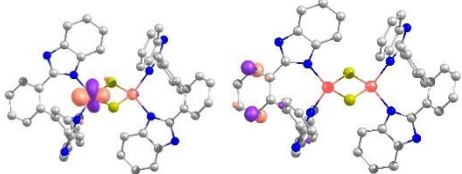
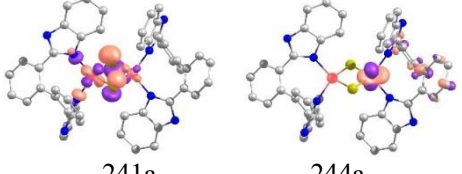
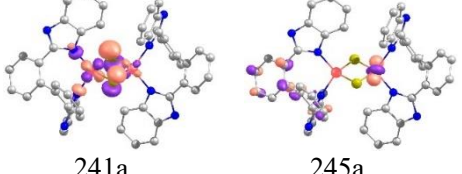
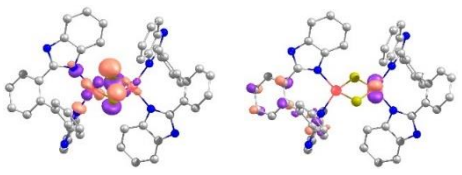
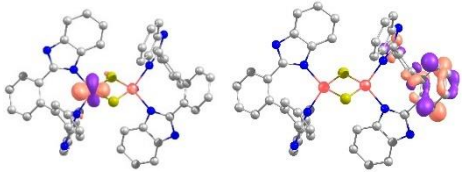
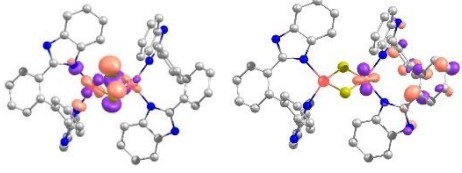
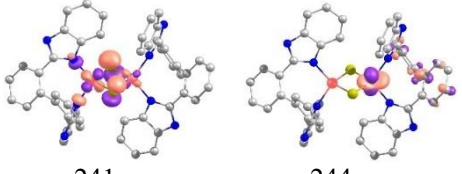
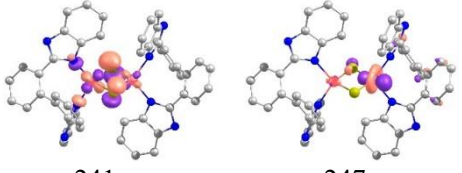
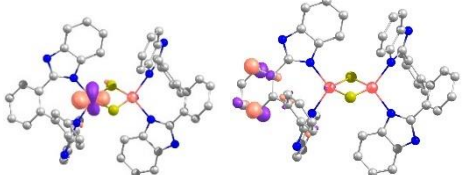
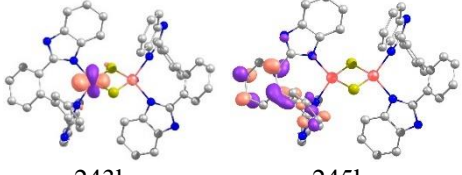
			242b -> 245b (14.1%)	 242b	 245b
545.0	0.005483270		237a -> 243a (9.4%)	 237a	 243a
			234b -> 244b (8.6%)	 234b	 244b
			241b -> 244b (8.1%)	 241b	 244b
			0.005038301	232b -> 243b (8.3%)	 232b
558.9			241b -> 243b (11.1%)	 241b	 243b
			242b -> 244b (17.1%)	 242b	 244b

Table 9.3.2. Selected TD-DFT (BP86/def2-tzvp level) calculated energy, oscillator strengths, compositions of the major electronic transitions, and related natural transition orbitals of complex **1**³⁻.

Complexes	Wavelength (nm)	Fosc	Transition (%)	NTO surfaces
$\mathbf{1}^{3-}$	369.1	0.012534028	242a -> 254a (24.3%)	 
	370.9	0.005473445	242a -> 254a (33.3%)	 
	381.7	0.005926252	229a -> 247a (7.7%)	 
	490.6	0.003175514	240a -> 251a (41.6%)	 
	492.7	0.001580570	240a -> 251a (15.8%)	 
			240a -> 252a (18.4%)	 
	494.4	0.002343171	240a -> 249a (14.8%)	 
			240a -> 252a (19.2%)	 

542.6	0.006989589	241a -> 247a (18.0%)	 241a 247a
594.6	0.003894593	243b -> 247b (22.1%)	 243b 247b
		243b -> 248b (67.6%)	 243b 248b
620	0.002387189	241a -> 244a (15.9%)	 241a 244a
		241a -> 245a (12.2%)	 241a 245a
		241a -> 246a (16.0%)	 241a 246a

			243b -> 246b (15.8%)	 243b 246b
659.6	0.001909123		241a -> 243a (31.4%)	 241a 243a
			241a -> 244a (37.6%)	 241a 244a
			241a -> 247a (10.9%)	 241a 247a
749.1	0.000423555		243b -> 244b (20.7%)	 243b 244b
			243b -> 245b (72.8%)	 243b 245b

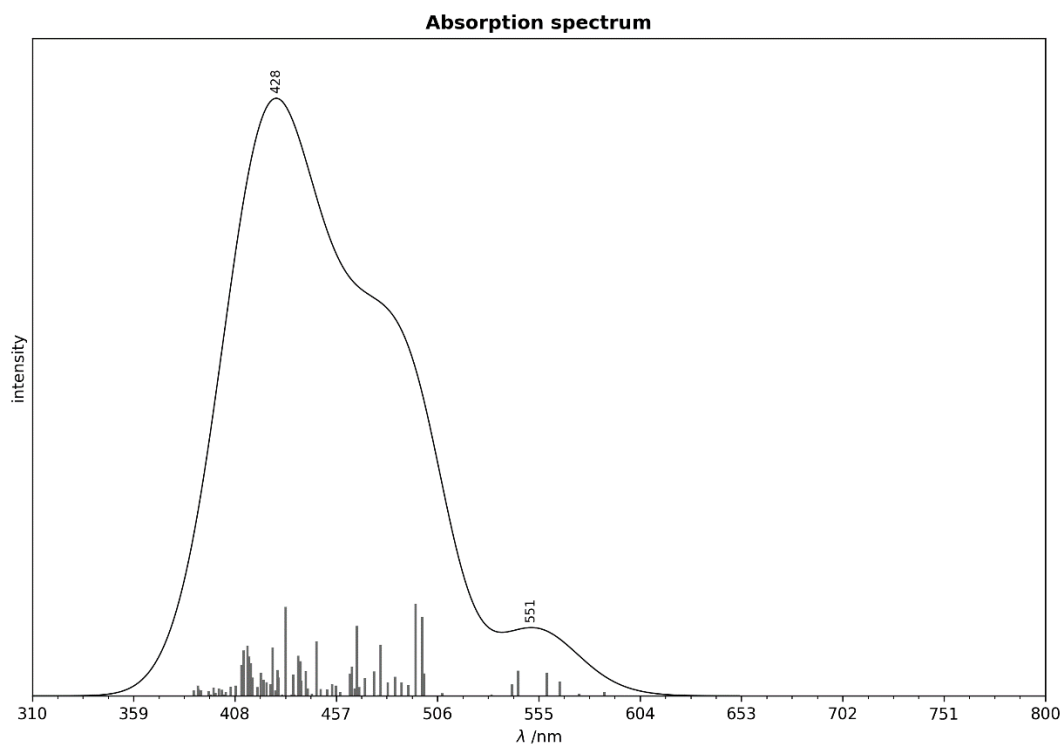


Figure 9.3.1. Calculated absorption spectra of the complex 1^{2-} . The spectrum was convoluted using a Gaussian line shape function with a half-width of 20 nm.

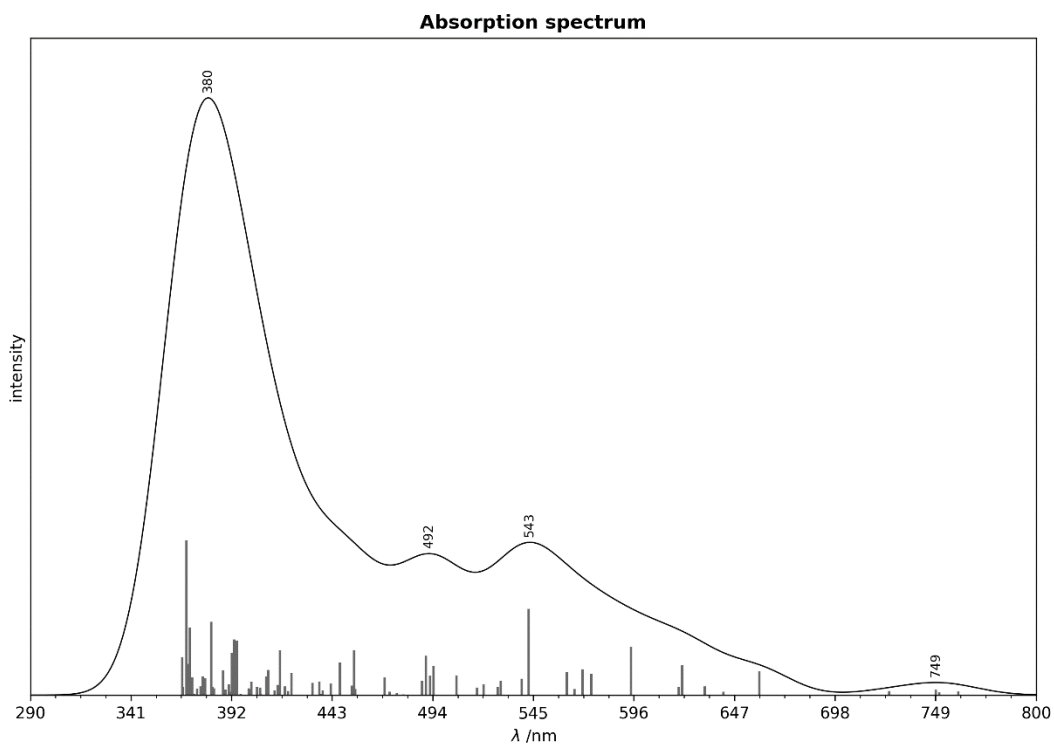


Figure 9.3.2. Calculated absorption spectra of the complex 1^{3-} . The spectrum was convoluted using a Gaussian line shape function with a half-width of 20 nm.

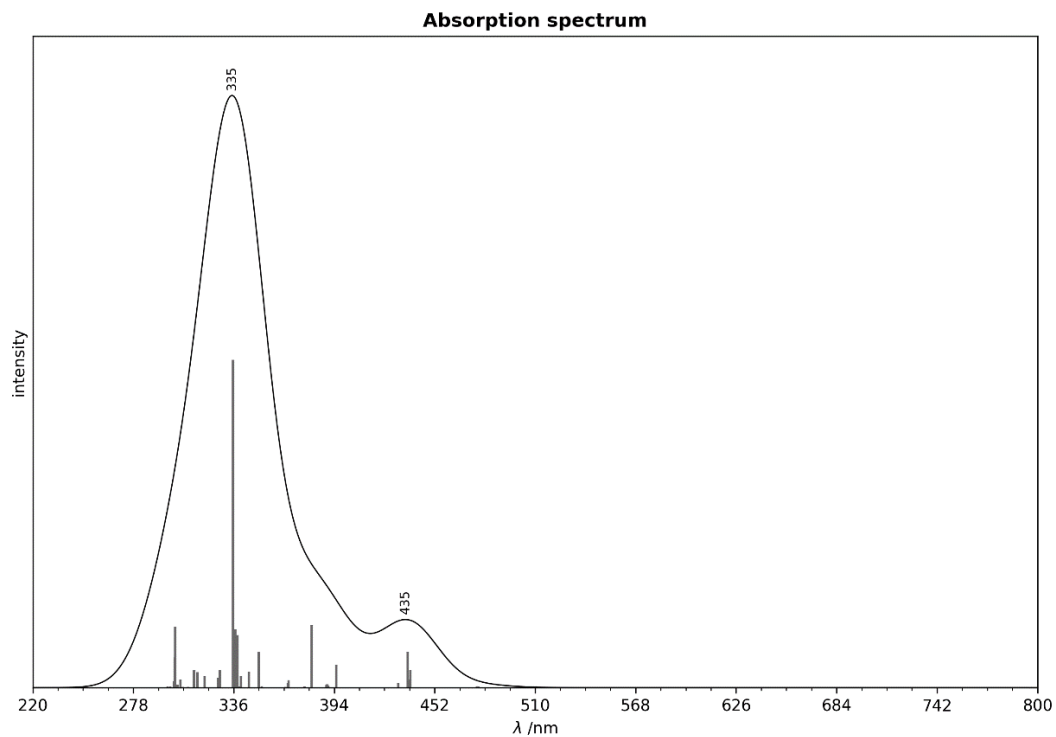


Figure 9.3.3. Calculated absorption spectra of the complex **3**. The spectrum was convoluted using a Gaussian line shape function with a half-width of 20 nm.

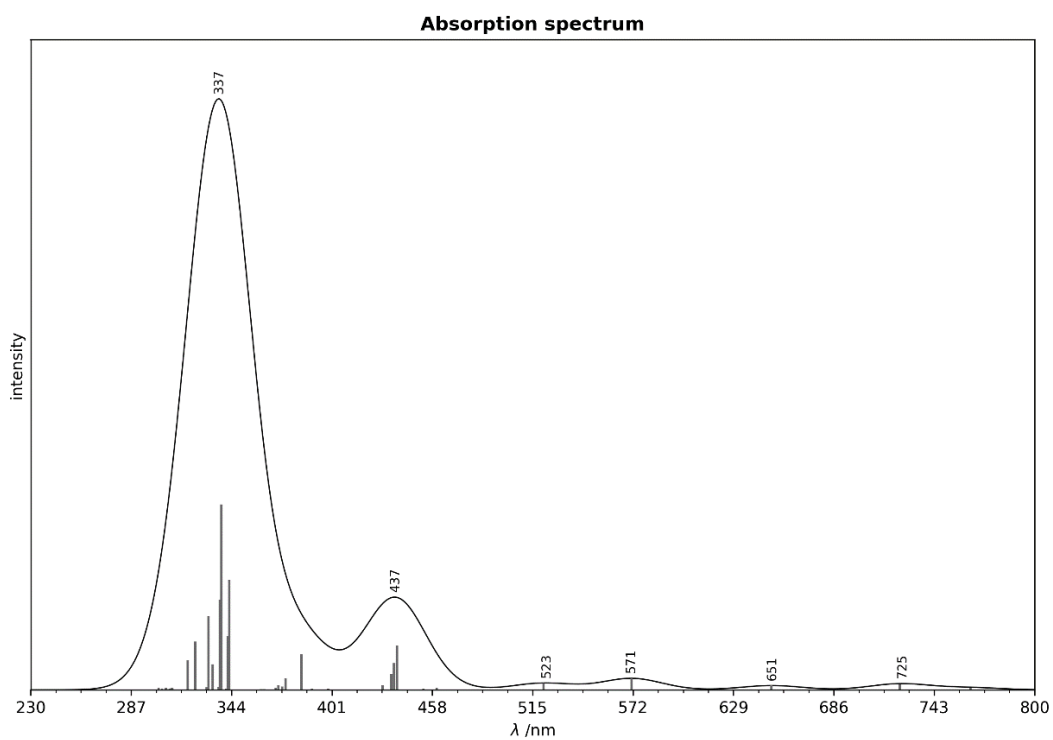


Figure 9.3.4. Calculated absorption spectra of the complex **4**. The spectrum was convoluted using a Gaussian line shape function with a half-width of 20 nm.

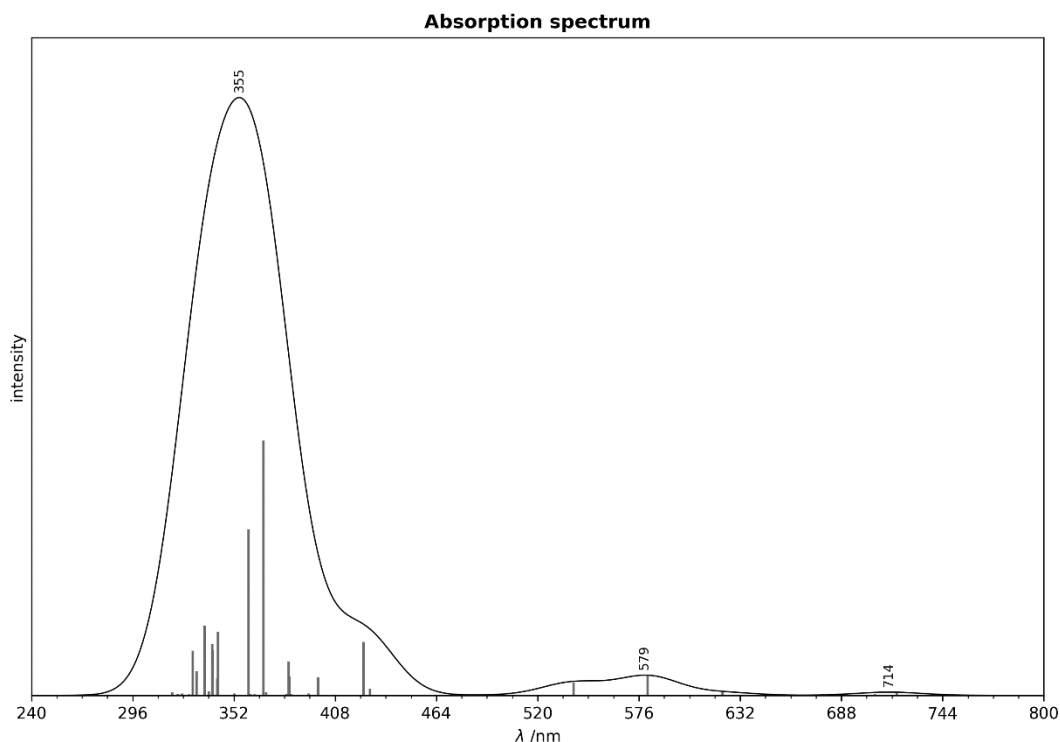


Figure 9.3.5. Calculated absorption spectra of the complex **5**. The spectrum was convoluted using a Gaussian line shape function with a half-width of 20 nm.

Table 9.3.3. Atomic coordinates for DFT optimization of complex **1**²⁻ ground state; theory level: BP86/ def2-tzvp.

Fe	1.326878	-0.15604	-0.11844
Fe	-1.31532	0.13333	0.312008
S	-0.20996	0.343183	-1.56009
S	0.2327	-0.3506	1.767376
N	2.174835	-1.91627	-0.63788
N	2.586614	1.412091	0.029369
N	-2.5878	-1.42943	0.180591
N	-2.2049	1.897746	0.737119
N	3.526006	-3.43216	-1.7198
N	3.985915	2.753374	1.269452
N	-3.81338	-2.9578	-1.02875
N	-3.72296	3.553204	1.233848
C	1.46811	-3.10439	-0.75756
C	3.394145	-2.19262	-1.22565
C	3.433126	1.549899	1.115217
C	2.616161	2.656694	-0.58249
C	-2.75713	-2.54972	0.97843
C	-3.25533	-1.7478	-0.9908
C	-3.52797	2.274819	0.877429
C	-1.49354	3.053547	1.035418
C	0.180821	-3.45982	-0.34505

C	2.316533	-4.03847	-1.42839
C	4.482939	-1.21059	-1.3079
C	3.750209	0.336956	1.888786
C	1.951814	3.159685	-1.70518
C	3.485333	3.483312	0.198568
C	-2.30804	-2.85021	2.268382
C	-3.516	-3.49504	0.215982
C	-3.40016	-0.68022	-1.99408
C	-4.66235	1.345442	0.768605
C	-2.44683	4.076676	1.327824
C	-0.11965	3.305105	1.099983
C	-0.24702	-4.76275	-0.59797
C	1.871201	-5.34518	-1.6786
C	5.108927	-0.99167	-2.54614
C	4.902655	-0.47482	-0.18099
C	4.357884	-0.72285	1.181567
C	3.35736	0.160219	3.218951
C	2.182314	4.492067	-2.04872
C	3.706101	4.818309	-0.16476
C	-2.64122	-4.09952	2.794489
C	-3.84243	-4.74262	0.763081
C	-2.81671	-0.74166	-3.26229
C	-4.03301	0.505884	-1.55995
C	-4.85635	0.474769	-0.32099
C	-5.57788	1.320085	1.8363
C	-2.01985	5.372354	1.656461
C	0.289165	4.597492	1.427571
C	0.585829	-5.6923	-1.25784
C	6.101981	-0.02565	-2.68609
C	5.896002	0.505891	-0.33827
C	4.492682	-1.97051	1.804035
C	3.521045	-1.07923	3.836448
C	3.047583	5.310267	-1.29311
C	-3.3985	-5.03208	2.055192
C	-2.79739	0.391748	-4.07599
C	-3.96983	1.648531	-2.36715
C	-5.92169	-0.44274	-0.27789
C	-6.63767	0.418547	1.858888
C	-0.64682	5.61799	1.699314
C	6.48624	0.738502	-1.57915
C	4.068046	-2.14938	3.120164
C	-3.34323	1.593599	-3.61331
C	-6.80025	-0.4824	0.801473
H	-0.46081	-2.74613	0.162946
H	1.257982	2.531632	-2.26568
H	-1.69803	-2.13548	2.822589
H	0.604563	2.520929	0.898414
H	-1.24503	-5.05918	-0.27398

H	2.521194	-6.06124	-2.18723
H	4.774891	-1.5855	-3.39735
H	2.866755	0.985317	3.735392
H	1.668895	4.915014	-2.91424
H	4.364689	5.450823	0.434779
H	-2.29948	-4.36391	3.79684
H	-4.41526	-5.46718	0.180228
H	-2.31861	-1.66162	-3.56864
H	-5.41349	2.017131	2.658545
H	-2.75066	6.154408	1.875474
H	1.356575	4.819239	1.458202
H	0.213658	-6.70347	-1.44002
H	6.55989	0.149306	-3.66183
H	6.188212	1.098299	0.529221
H	4.922542	-2.79978	1.240298
H	3.180798	-1.22471	4.863026
H	3.192025	6.351452	-1.59031
H	-3.63258	-6.00186	2.500188
H	-2.30544	0.352896	-5.04913
H	-4.41983	2.575343	-2.00882
H	-6.04269	-1.1382	-1.10952
H	-7.322	0.401121	2.710385
H	-0.28393	6.618303	1.948011
H	7.242739	1.519115	-1.68152
H	4.159197	-3.13132	3.588732
H	-3.2842	2.493623	-4.22851
H	-7.60901	-1.21595	0.815831

Item	value	Tolerance	Converged
Energy change	-0.0000003994	0.0000010000	YES
RMS gradient	0.0000102554	0.0000300000	YES
MAX gradient	0.0000866253	0.0001000000	YES
RMS step	0.0002319885	0.0006000000	YES

Zero Point Energy (Hartree)	0.6906000427
Inner Energy (Hartree)	-5764.0986109789
Enthalpy (Hartree)	-5764.0976667698
Electronic entropy	0.0000000000
Rotational entropy	0.0189241064
Vibrational entropy	0.0873906204
Translational entropy	0.0189241064
Entropy	0.1283664917
Gibbs Energy (Hartree)	-5764.2260332616

Table 9.3.4. Atomic coordinates for DFT optimization of complex 1^{3-} ground state; theory level: BP86/ def2-tzvp.

Fe	1.325521	-0.17137	-0.25235
Fe	-1.31206	0.109526	0.072262
S	-0.1621	0.233107	-1.80981
S	0.179508	-0.34929	1.610858
N	2.320237	-1.96384	-0.62341
N	2.643039	1.419312	-0.11264
N	-2.71123	-1.4321	-0.07597
N	-2.26802	1.902934	0.544467
N	3.838656	-3.61429	-1.16994
N	3.901973	2.923714	1.101826
N	-4.09859	-2.74779	-1.38027
N	-3.51898	3.400818	1.789559
C	1.614388	-3.12573	-0.89422
C	3.632827	-2.33012	-0.80631
C	3.325236	1.714552	1.045313
C	2.808149	2.54938	-0.89057
C	-2.73698	-2.69768	0.477126
C	-3.552	-1.53467	-1.15416
C	-3.42187	2.168814	1.239321
C	-1.5623	3.09123	0.630282
C	0.238561	-3.38579	-0.90758
C	2.566045	-4.14612	-1.21807
C	4.762733	-1.39478	-0.71866
C	3.477477	0.634208	2.036162
C	2.341699	2.869763	-2.17096
C	3.58964	3.480931	-0.12739
C	-2.08515	-3.23164	1.595744
C	-3.60173	-3.50815	-0.33967
C	-3.89324	-0.30137	-1.88103
C	-4.5074	1.190555	1.366001
C	-2.34397	4.013531	1.401243
C	-0.31469	3.455265	0.112969
C	-0.1746	-4.68151	-1.21257
C	2.131621	-5.44735	-1.52474
C	5.685336	-1.38557	-1.78165
C	4.948733	-0.49843	0.353785
C	4.135921	-0.53532	1.599117
C	2.877579	0.669206	3.297931
C	2.681262	4.120915	-2.6897
C	3.919455	4.731792	-0.66864
C	-2.31867	-4.57191	1.906409
C	-3.81957	-4.85552	-0.00759
C	-3.58098	-0.09239	-3.22936
C	-4.49197	0.73285	-1.13054
C	-4.9688	0.457814	0.251929

C	-5.10676	0.977027	2.620727
C	-1.86573	5.313675	1.638728
C	0.146206	4.748523	0.357633
C	0.758495	-5.69927	-1.51488
C	6.737229	-0.47488	-1.82184
C	6.000881	0.433263	0.289182
C	4.098558	-1.68357	2.4013
C	2.882989	-0.46698	4.10741
C	3.460782	5.039251	-1.95237
C	-3.17423	-5.37436	1.117846
C	-3.81467	1.149055	-3.8212
C	-4.70324	1.981653	-1.72763
C	-5.95456	-0.5247	0.437875
C	-6.09938	0.014683	2.789051
C	-0.62002	5.666124	1.112503
C	6.883472	0.457588	-0.78817
C	3.467585	-1.65095	3.645486
C	-4.35843	2.193056	-3.06411
C	-6.51269	-0.75651	1.695741
H	-0.48032	-2.60007	-0.68586
H	1.705515	2.165857	-2.71171
H	-1.39516	-2.61171	2.172319
H	0.266687	2.741431	-0.46641
H	-1.24161	-4.91029	-1.19676
H	2.857529	-6.22888	-1.76806
H	5.527732	-2.10395	-2.58719
H	2.34113	1.569082	3.598323
H	2.320569	4.402532	-3.68161
H	4.50512	5.448042	-0.086
H	-1.80771	-5.0187	2.762747
H	-4.47005	-5.47832	-0.62905
H	-3.09103	-0.89502	-3.78112
H	-4.7462	1.571887	3.460832
H	-2.45863	6.022094	2.225816
H	1.120117	5.045158	-0.03518
H	0.391231	-6.70403	-1.74463
H	7.423794	-0.46945	-2.67311
H	6.103469	1.155806	1.10043
H	4.560775	-2.60044	2.032092
H	2.368056	-0.44948	5.06974
H	3.693862	6.014465	-2.38916
H	-3.31852	-6.42525	1.385965
H	-3.52788	1.31876	-4.86167
H	-5.12453	2.789389	-1.12653
H	-6.26232	-1.12258	-0.4212
H	-6.53026	-0.15819	3.778947
H	-0.22497	6.671434	1.2887
H	7.678972	1.206088	-0.82182

H	3.42159	-2.55799	4.25266
H	-4.50447	3.178817	-3.51236
H	-7.26012	-1.54349	1.822447

Item	value	Tolerance	Converged
Energy change	-0.0000020156	0.0000010000	NO
RMS gradient	0.0000036547	0.0000300000	YES
MAX gradient	0.0000207131	0.0001000000	YES
RMS step	0.0001158279	0.0006000000	YES

Zero Point Energy (Hartree)	0.6861294518
Inner Energy (Hartree)	-5764.0023770341
Enthalpy (Hartree)	-5764.0014328250
Electronic entropy	0.0006544564
Rotational entropy	0.0189562670
Vibrational entropy	0.0894805350
Translational entropy	0.0189562670
Entropy	0.1311430233
Gibbs Energy (Hartree)	-5764.1325758483

Table 9.3.5. Atomic coordinates for DFT optimization of complex **3** ground state; theory level: BP86/ def2-tzvp.

Fe	-0.01847	-0.44918	0.210118
Cl	-1.23985	-1.65494	-1.22595
Cl	1.194412	-1.30563	1.879692
N	1.170094	1.076005	-0.51013
N	-1.20815	1.197481	0.578755
N	3.079998	-0.20601	-1.11374
N	3.407904	1.312424	0.446233
N	-3.38745	1.252192	-0.52537
N	-3.16225	0.054655	1.308688
C	0.653061	2.365445	-0.34364
C	2.467558	0.804261	-0.42106
C	-0.6692	2.424037	0.173358
C	-2.50271	0.917466	0.475
C	1.295887	3.551775	-0.72277
C	-1.30095	3.666631	0.312887
C	0.651346	4.785554	-0.58261
C	4.390443	-0.36893	-0.65803
C	2.405754	-0.95827	-2.15928
C	4.60451	0.588599	0.308236
C	3.026346	2.096871	1.615061
C	-0.64499	4.843534	-0.0636
C	-4.59315	0.557875	-0.32727
C	-2.92673	1.786629	-1.80324
C	-4.44346	-0.20083	0.811802

C	-2.55396	-0.49275	2.509959
C	5.305966	-1.38374	-1.18208
C	5.805048	0.860484	1.093536
C	-5.73777	0.667137	-1.22718
C	-5.39	-1.11407	1.452649
C	4.927112	-2.73818	-1.22237
C	6.595067	-1.02321	-1.61229
C	6.550518	-0.20267	1.636774
C	6.250895	2.178587	1.308164
C	-6.43929	-0.48662	-1.62344
C	-6.16848	1.919127	-1.7052
C	-5.00893	-2.43127	1.768906
C	-6.70724	-0.70245	1.721518
C	5.819287	-3.70522	-1.6853
C	7.486271	-1.99492	-2.06448
C	7.717671	0.04732	2.355165
C	7.412852	2.423851	2.039362
C	-7.54916	-0.38639	-2.45914
C	-7.27297	2.012831	-2.55126
C	-5.92542	-3.31102	2.344345
C	-7.62252	-1.58946	2.286256
C	7.101026	-3.33833	-2.10581
C	8.153824	1.360075	2.560806
C	-7.97046	0.861954	-2.92788
C	-7.23479	-2.89503	2.603105
H	2.296792	3.499953	-1.15634
H	-2.3041	3.705156	0.742055
H	1.162275	5.699921	-0.88605
H	3.151257	-1.32535	-2.87264
H	1.691468	-0.29191	-2.65558
H	1.839987	-1.80048	-1.7356
H	3.790804	1.963459	2.38663
H	2.065129	1.71914	1.986549
H	2.923402	3.161616	1.366652
H	-1.14667	5.804724	0.054692
H	-3.65872	1.521	-2.57168
H	-1.96167	1.322059	-2.04316
H	-2.80294	2.876681	-1.76067
H	-3.34044	-0.71821	3.238154
H	-1.85607	0.250403	2.912881
H	-1.97973	-1.40266	2.281394
H	3.942393	-3.03167	-0.85787
H	6.890478	0.025875	-1.58151
H	6.198932	-1.2243	1.495503
H	5.691745	3.011843	0.880319
H	-6.09804	-1.46086	-1.27479
H	-5.64306	2.822779	-1.3932
H	-4.0002	-2.77016	1.53101

H	-7.00585	0.317751	1.479977
H	5.515205	-4.75265	-1.70521
H	8.483565	-1.70081	-2.39345
H	8.284179	-0.78798	2.768217
H	7.747043	3.450882	2.192869
H	-8.08167	-1.29034	-2.75696
H	-7.5963	2.990611	-2.91016
H	-5.61811	-4.33056	2.579618
H	-8.6416	-1.25736	2.487846
H	7.797931	-4.09739	-2.46308
H	9.064798	1.553309	3.128179
H	-8.83647	0.937243	-3.58669
H	-7.95134	-3.58667	3.047966

Item	value	Tolerance	Converged
Energy change	0.0000005835	0.0000010000	YES
RMS gradient	0.0000097582	0.0000300000	YES
MAX gradient	0.0000458246	0.0001000000	YES
RMS step	0.0002033988	0.0006000000	YES

Table 9.3.6. Atomic coordinates for DFT optimization of complex **4** ground state; theory level: BP86/ def2-tzvp.

Ni	0.037361	0.231608	0.195231
Br	-1.31114	1.074536	-1.59249
Br	1.499537	1.878754	1.06752
N	-1.21793	-1.21989	0.833196
N	1.158605	-1.3327	-0.27177
N	-3.08219	0.133007	1.379797
N	-3.46773	-1.4277	-0.12368
N	3.081594	-0.23653	-1.14275
N	3.422565	-1.50086	0.623922
C	-0.71838	-2.50628	0.607837
C	-2.5094	-0.92088	0.721912
C	0.596187	-2.56366	0.068088
C	2.470084	-1.10439	-0.28452
C	-1.37167	-3.69834	0.950904
C	1.199558	-3.81099	-0.14949
C	-0.75171	-4.93439	0.743864
C	-4.38331	0.330765	0.917269
C	-2.36686	0.924696	2.367032
C	-4.63509	-0.65512	-0.01055
C	-3.11978	-2.24199	-1.285
C	0.529856	-4.99076	0.18757
C	4.400676	-0.02628	-0.74323
C	2.390471	0.3969	-2.25672
C	4.626761	-0.83492	0.349705

C	3.063276	-2.1061	1.900175
C	-5.25106	1.411518	1.388854
C	-5.84656	-0.90663	-0.78597
C	5.30085	0.917809	-1.40701
C	5.839729	-1.00517	1.145247
C	-4.81735	2.748506	1.330183
C	-6.54458	1.132066	1.861564
C	-6.3469	-2.21176	-0.95166
C	-6.54514	0.166297	-1.36984
C	4.912996	2.260387	-1.56961
C	6.57336	0.511368	-1.84201
C	6.597474	0.118625	1.523678
C	6.280659	-2.28321	1.536437
C	-5.66156	3.779526	1.742069
C	-7.38733	2.167301	2.26319
C	-7.51819	-2.43507	-1.67488
C	-7.72153	-0.0611	-2.08073
C	5.784151	3.172425	-2.16456
C	7.443228	1.430697	-2.42735
C	7.770056	-0.03636	2.259835
C	7.448507	-2.43156	2.284177
C	-6.94789	3.493346	2.208407
C	-8.21306	-1.36096	-2.23699
C	7.05017	2.762029	-2.59381
C	8.200008	-1.31012	2.6449
H	-2.36174	-3.64848	1.408537
H	2.190061	-3.84857	-0.60692
H	-1.27005	-5.85234	1.022212
H	-3.09017	1.385663	3.04779
H	-1.76328	1.704163	1.878105
H	-1.68978	0.261769	2.916759
H	-3.89448	-2.10252	-2.045
H	-3.0369	-3.30394	-1.02055
H	-2.15951	-1.88445	-1.67783
H	1.00955	-5.95395	0.010572
H	3.111829	0.594273	-3.05684
H	1.914958	1.330818	-1.92723
H	1.599634	-0.27823	-2.60079
H	3.846851	-1.8716	2.626896
H	2.945371	-3.19428	1.811029
H	2.111406	-1.67347	2.233353
H	-3.82882	2.975113	0.929013
H	-6.88285	0.096244	1.905257
H	-5.8217	-3.05099	-0.49364
H	-6.14921	1.176239	-1.26833
H	3.941568	2.585167	-1.19364
H	6.873729	-0.52864	-1.71204
H	6.250913	1.112138	1.241085

H	5.713052	-3.16453	1.234033
H	-5.31637	4.812741	1.685721
H	-8.38933	1.93703	2.626777
H	-7.89541	-3.45205	-1.79081
H	-8.25153	0.78114	-2.52673
H	5.476942	4.21243	-2.28129
H	8.42928	1.105163	-2.76044
H	8.345815	0.844706	2.545392
H	7.778684	-3.42895	2.576824
H	-7.60693	4.302021	2.526316
H	-9.13166	-1.53633	-2.79776
H	7.730731	3.479733	-3.05378
H	9.115411	-1.42799	3.22573

Item	value	Tolerance	Converged
Energychange	-0.0000005980	0.0000010000	YES
RMSgradient	0.0000125910	0.0000300000	YES
MAXgradient	0.0000820914	0.0001000000	YES
RMSstep	0.0004431424	0.0006000000	YES

Table 9.3.7. Atomic coordinates for DFT optimization of complex **5** ground state; theory level: BP86/ def2-tzvp.

Ni	-1.5E-05	-0.14464	-2.1E-05
Br	1.443786	-1.22657	-1.59058
Br	-1.44381	-1.22654	1.590576
N	-1.23694	1.215216	-0.7333
N	1.236902	1.215219	0.73327
N	-2.9615	-0.32787	-1.36594
N	-3.52886	1.217919	0.087383
N	2.961464	-0.32786	1.365921
N	3.52882	1.217922	-0.08741
C	-1.0226	2.596453	-0.77125
C	-2.50117	0.776324	-0.70761
C	1.022554	2.596455	0.771219
C	2.501128	0.776329	0.707583
C	-2.3E-05	3.258103	-1.5E-05
C	-1.87634	3.36103	-1.57624
C	1.876297	3.361034	1.576213
C	-2.5E-05	4.706752	-1.4E-05
C	-1.83829	4.762254	-1.58566
C	-4.25529	-0.62759	-0.93941
C	-2.17946	-1.04764	-2.35966
C	-4.61994	0.354522	-0.04195
C	-3.30806	2.166354	1.170618
C	1.838242	4.762258	1.585629
C	4.255254	-0.62758	0.939393

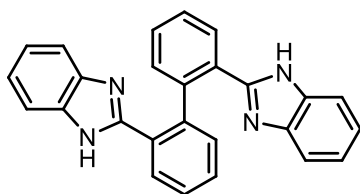
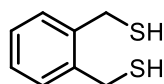
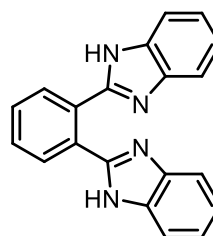
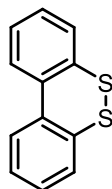
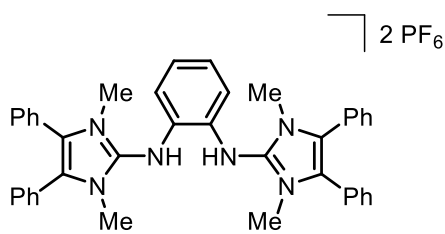
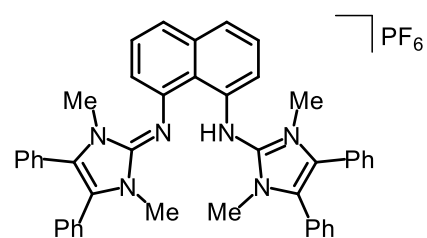
C	2.179416	-1.04763	2.359647
C	4.6199	0.354528	0.041937
C	3.308025	2.166352	-1.17065
C	-0.92968	5.428686	-0.79292
C	0.929633	5.428687	0.792894
C	-5.01071	-1.79102	-1.4025
C	-5.86759	0.509211	0.702758
C	5.010678	-1.79101	1.402499
C	5.867552	0.509215	-0.70277
C	-4.4429	-3.07665	-1.34152
C	-6.32832	-1.64659	-1.87073
C	-6.51512	1.75516	0.789332
C	-6.44722	-0.60442	1.336811
C	4.442868	-3.07663	1.341515
C	6.328281	-1.64658	1.870735
C	6.515085	1.755164	-0.78936
C	6.447183	-0.60442	-1.33682
C	-5.17803	-4.18924	-1.74884
C	-7.06205	-2.76368	-2.26632
C	-7.71448	1.881476	1.489865
C	-7.65096	-0.47506	2.026034
C	5.177996	-4.18923	1.748846
C	7.062015	-2.76366	2.266333
C	7.714443	1.881477	-1.48989
C	7.650931	-0.47506	-2.02604
C	-6.48865	-4.03753	-2.21112
C	-8.28863	0.766857	2.107001
C	6.488613	-4.03751	2.211131
C	8.288597	0.766855	-2.10702
H	-2.60198	2.833181	-2.19696
H	2.60193	2.833186	2.196929
H	-2.53371	5.315198	-2.21937
H	-2.8559	-1.45738	-3.11779
H	-1.60188	-1.85749	-1.89421
H	-1.46752	-0.34766	-2.80965
H	-4.10592	2.042568	1.908497
H	-3.29693	3.197582	0.794112
H	-2.34084	1.936939	1.636144
H	2.533654	5.315203	2.21934
H	2.855862	-1.45735	3.117785
H	1.601847	-1.85749	1.894199
H	1.467475	-0.34765	2.809623
H	4.105879	2.042563	-1.90852
H	3.296887	3.197582	-0.79414
H	2.3408	1.936935	-1.63617
H	-0.89789	6.518749	-0.76708
H	0.897841	6.51875	0.767053
H	-3.43618	-3.1986	-0.93989

H	-6.7703	-0.65099	-1.91765
H	-6.08336	2.622224	0.287154
H	-5.93639	-1.56583	1.291086
H	3.436146	-3.19859	0.939883
H	6.770264	-0.65097	1.917646
H	6.08332	2.62223	-0.28718
H	5.93636	-1.56583	-1.29109
H	-4.72904	-5.18163	-1.69166
H	-8.08391	-2.6387	-2.62688
H	-8.20735	2.852967	1.545781
H	-8.08772	-1.3469	2.514698
H	4.729013	-5.18162	1.691665
H	8.083866	-2.63868	2.626897
H	8.207311	2.852968	-1.54581
H	8.087689	-1.3469	-2.5147
H	-7.06239	-4.91019	-2.52556
H	-9.22764	0.866431	2.652691
H	7.062353	-4.91017	2.525579
H	9.227608	0.866427	-2.65271

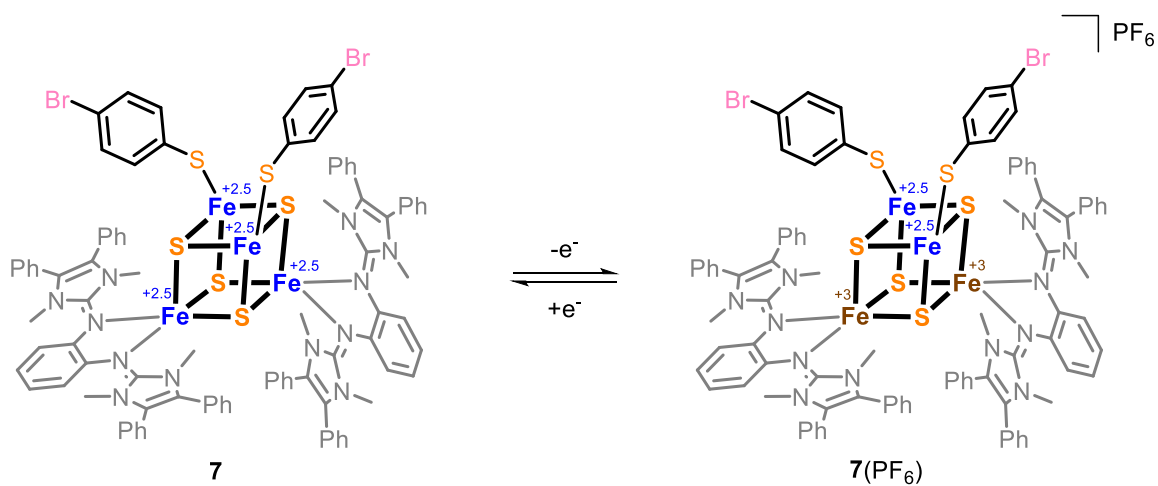
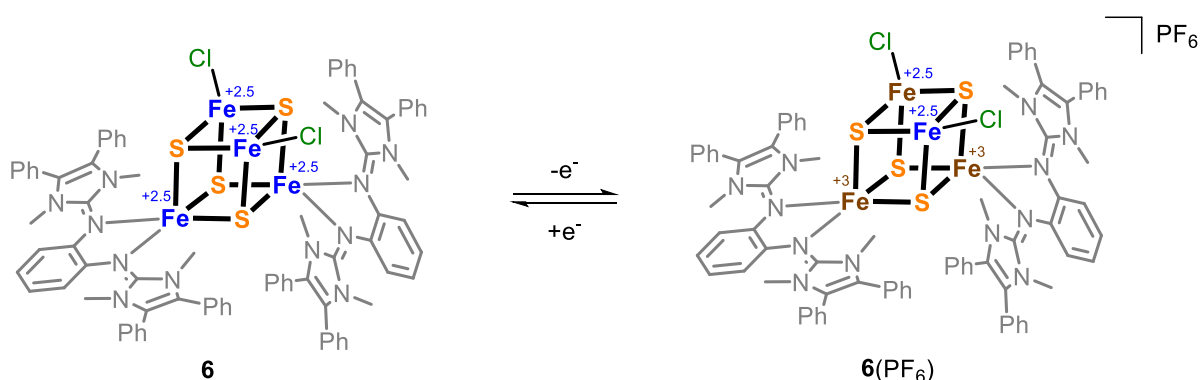
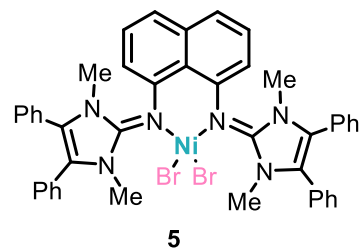
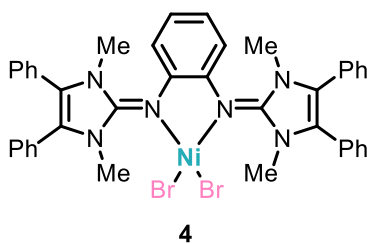
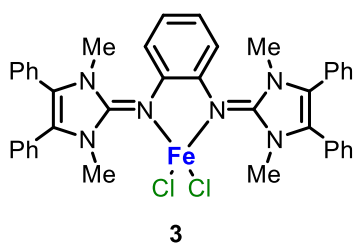
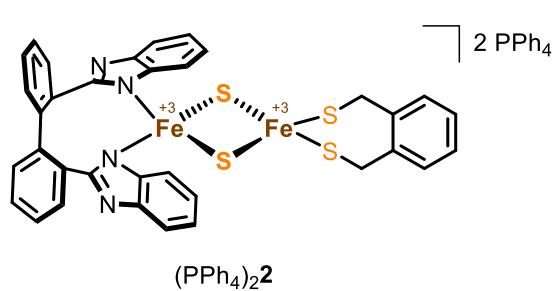
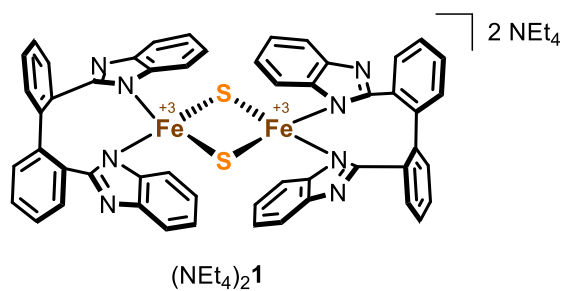
Item	value	Tolerance	Converged
Energychange	-0.0000009497	0.0000010000	YES
RMSgradient	0.0000084283	0.0000300000	YES
MAXgradient	0.0000514135	0.0001000000	YES
RMSstep	0.0002423127	0.0006000000	YES

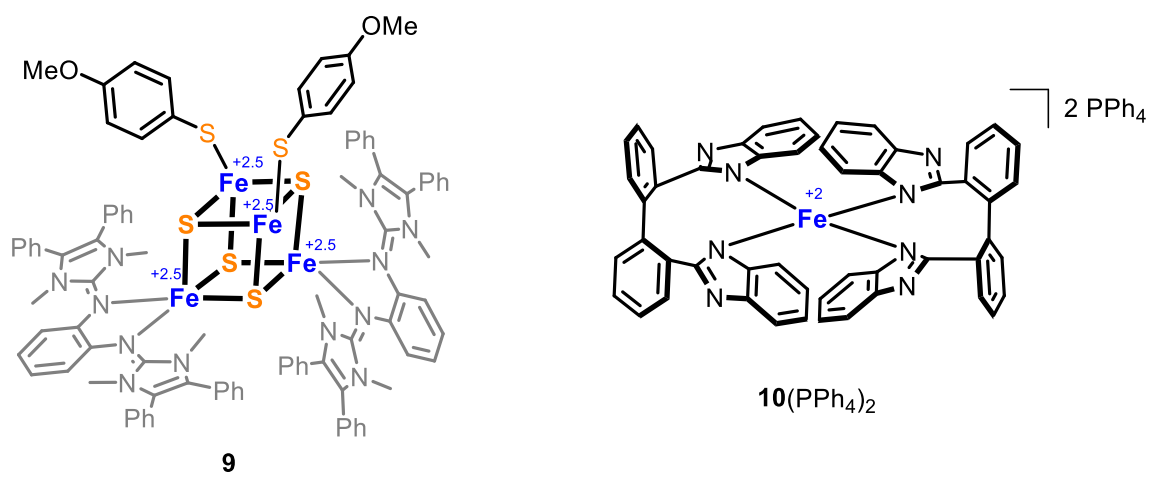
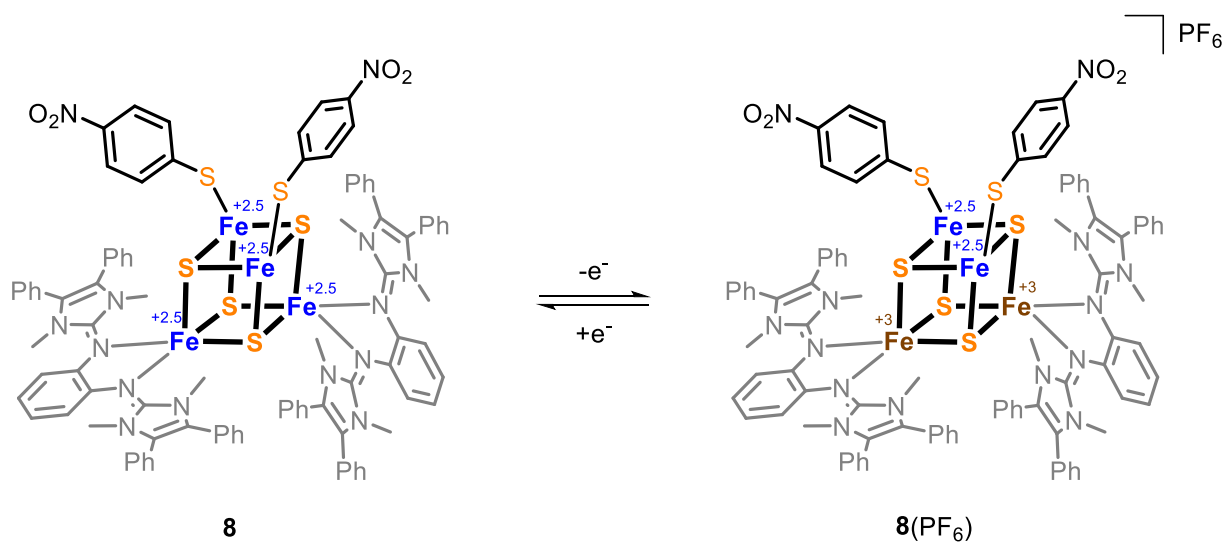
Formula Overview

Structures of Ligands

 H_2L^1  H_2L^2  H_2L^3  L^4  $[H_2L^5](PF_6)_2$  $[HL^6](PF_6)$

Structures of Complexes





References

- [1] H. Beinert, R. H. Sands, *Biochem. Biophys. Res. Commun.* **1960**, *3*, 41-46.
- [2] A. E. Boncella, E. T. Sabo, R. M. Santore, J. Carter, J. Whalen, J. D. Hudspeth, C. N. Morrison, *Coord. Chem. Rev.* **2022**, *453*, 214229.
- [3] H. Beinert, R. H. Holm, E. Munck, *Science* **1997**, *277*, 653-659.
- [4] D. C. Johnson, D. R. Dean, A. D. Smith, M. K. Johnson, *Annu. Rev. Biochem.* **2005**, *74*, 247-281.
- [5] J. Liu, S. Chakraborty, P. Hosseinzadeh, Y. Yu, S. Tian, I. Petrik, A. Bhagi, Y. Lu, *Chem. Rev.* **2014**, *114*, 4366-4469.
- [6] Z. Dauter, K. S. Wilson, L. C. Sieker, J. M. Moulis, J. Meyer, *Proc. Natl. Acad. Sci. U. S. A.* **1996**, *93*, 8836-8840.
- [7] J. Meyer, *J. Biol. Inorg. Chem.* **2008**, *13*, 157-170.
- [8] P. Zanello, *Coord. Chem. Rev.* **2013**, *257*, 1777-1805.
- [9] J. A. Zuris, Y. Harir, A. R. Conlan, M. Shvartsman, D. Michaeli, S. Tamir, M. L. Paddock, J. N. Onuchic, R. Mittler, Z. I. Cabantchik, P. A. Jennings, R. Nechushtai, *Proc. Natl. Acad. Sci. U.S.A.* **2011**, *108*, 13047-13052.
- [10] F. Camponeschi, S. Ciofi-Baffoni, L. Banci, *J. Am. Chem. Soc.* **2017**, *139*, 9479-9482.
- [11] D. W. Bak, S. J. Elliott, *Curr. Opin. Chem. Biol.* **2014**, *19*, 50-58.
- [12] A. Volbeda, M. T. P. Martinez, J. C. Crack, P. Amara, O. Gigarel, J. T. Munnoch, M. I. Hutchings, C. Darnault, N. E. Le Brun, J. C. Fontecilla-Camps, *J. Am. Chem. Soc.* **2019**, *141*, 2367-2375.
- [13] K. Kobayashi, *Acc. Chem. Res.* **2017**, *50*, 1672-1678.
- [14] J. T. Munnoch, M. T. Martinez, D. A. Svistunenko, J. C. Crack, N. E. Le Brun, M. I. Hutchings, *Sci. Rep.* **2016**, *6*, 1-14.
- [15] J. L. Busch, J. L. Breton, B. M. Bartlett, F. A. Armstrong, R. James, A. J. Thomson, *Biochem. J.* **1997**, *323*, 95-102.
- [16] J. J. Moura., I. Moura., K. T. A., J. D. Lipscomb., B. H. Huynh., J. LeGall., A. V. Xavier., E. Münck., *J. Biol. Chem.* **1982**, 6259-6267.
- [17] I. M. Ibrahim, H. Wu, R. Ezhov, G. E. Kayanja, S. D. Zakharov, Y. Du, W. A. Tao, Y. Pushkar, W. A. Cramer, S. Puthiyaveetil, *Commun. Biol.* **2020**, *3*, 13.
- [18] G. D. Watt, K. R. N. Reddy, *J. Inorg. Biochem.* **1994**, *53*, 281-294.
- [19] P. Strop, P. M. Takahara, H. Chiu, H. C. Angove, B. K. Burgess, D. C. Rees, *Biochemistry* **2001**, *40*, 651-656.
- [20] D. R. Breiter, T. E. Meyer, I. Rayment, H. M. Holden, *J. Biol. Chem.* **1991**, *266*, 18660-18667.
- [21] A. Hochkoeppler, S. Ciurli, G. Venturoli, D. Zannoni, *FEBS Lett.* **1995**, *357*, 70-74.
- [22] Y. Ohki, Y. Sunada, K. Tatsumi, *Chem. Lett.* **2005**, *34*, 172-173.
- [23] C. R. Sharp, J. S. Duncan, S. C. Lee, *Inorg. Chem.* **2010**, *49*, 6697-6705.
- [24] O. Einsle, F. A. Tezcan, S. L. Andrade, B. Schmid, M. Yoshida, J. B. Howard, D. C. Rees, *Science* **2002**, *297*, 1696-1700.
- [25] R. H. Holm, E. I. Solomon, *Chem. Rev.* **2004**, *104*, 347-348.
- [26] S. Ohta, Y. Ohki, *Coord. Chem. Rev.* **2017**, *338*, 207-225.
- [27] N. Ueyama, Y. Yamada, T. A. Okamura Ta, S. Kimura, A. Nakamura, *Inorg. Chem.* **1996**, *35*, 6473-6484.
- [28] J. J. Mayerle, R. B. Frankel, R. H. Holm, J. A. Ibers, W. D. Phillips, J. F. Weiher, *Proc. Natl. Acad. Sci. U S A* **1973**, *70*, 2429-2433.
- [29] S. C. Im, T. Kohzuma, W. McFarlane, J. Gaillard, A. G. Sykes, *Inorg. Chem.* **1997**, *36*, 1388-1396.
- [30] S. C. Lee, W. Lo, R. H. Holm, *Chem. Rev.* **2014**, *114*, 3579-3600.
- [31] P. K. Mascharak, G. C. Papaefthymiou, R. B. Frankel, R. H. Holm, *J. Am. Chem. Soc.* **1981**, *103*, 6110-6116.
- [32] P. Beardwood, J. F. Gibson, *J. Chem. Soc., Dalton Trans.* **1992**, 2457-2466.

- [33] A. Albers, S. Demeshko, S. Dechert, E. Bill, E. Bothe, F. Meyer, *Angew. Chem. Int. Ed.* **2011**, *50*, 9191-9194.
- [34] A. Albers, S. Demeshko, K. Propper, S. Dechert, E. Bill, F. Meyer, *J. Am. Chem. Soc.* **2013**, *135*, 1704-1707.
- [35] M. A. Bobrik, K. O. Hodgson, R. H. Holm, *Inorg. Chem.* **1977**, *16*, 1851-1858.
- [36] Y. Do, E. D. Simhon, R. H. Holm, *Inorg. Chem.* **1983**, *22*, 3809-3812.
- [37] J. Ballmann, X. Sun, S. Dechert, B. Schneider, F. Meyer, *Dalton Trans.* **2009**, 4908-4917.
- [38] M. G. Fuchs, S. Dechert, S. Demeshko, U. Ryde, F. Meyer, *Inorg. Chem.* **2010**, *49*, 5853-5858.
- [39] C. Schneider, S. J. Groß, S. Demeshko, S. Bontemps, F. Meyer, C. G. Werncke, *Chem. Commun.* **2021**, *57*, 10751-10754.
- [40] M. E. Reesbeck, M. M. Rodriguez, W. W. Brennessel, B. Q. Mercado, D. Vinyard, P. L. Holland, *J. Biol. Inorg. Chem.* **2015**, *20*, 875-883.
- [41] S. Yao, F. Meier, N. Lindenmaier, R. Rudolph, B. Blom, M. Adelhardt, J. Sutter, S. Mebs, M. Haumann, K. Meyer, M. Kaupp, M. Driess, *Angew. Chem. Int. Ed.* **2015**, *54*, 12506-12510.
- [42] L. Fohlmeister, K. R. Vignesh, F. Winter, B. Moubaraki, G. Rajaraman, R. Pottgen, K. S. Murray, C. Jones, *Dalton Trans.* **2015**, *44*, 1700-1708.
- [43] Q. Liang, J. C. DeMuth, A. Radovic, N. J. Wolford, M. L. Neidig, D. Song, *Inorg. Chem.* **2021**, *60*, 13811-13820.
- [44] J. Ballmann, A. Albers, S. Demeshko, S. Dechert, E. Bill, E. Bothe, U. Ryde, F. Meyer, *Angew. Chem. Int. Ed.* **2008**, *47*, 9537-9541.
- [45] J. S. Rieske, D. H. MacLennan, R. Coleman, *Biochem. Biophys. Res. Commun.* **1964**, *15*, 338-344.
- [46] J. A. Fee, K. L. Findling, T. Yoshida, R. Hille, G. E. Tarr, D. O. Hearshen, W. R. Dunham, E. P. Day, T. A. Kent, E. Münck, *J. Biol. Chem.* **1984**, *259*, 124-133.
- [47] A. Albers, S. Demeshko, S. Dechert, C. T. Saouma, J. M. Mayer, F. Meyer, *J. Am. Chem. Soc.* **2014**, *136*, 3946-3954.
- [48] P. V. Rao, R. H. Holm, *Chem. Rev.* **2004**, *104*, 527-559.
- [49] B. K. Burgess, D. J. Lowe, *Chem. Rev.* **1996**, *96*, 2983-3012.
- [50] H. L. Rutledge, F. A. Tezcan, *Chem. Rev.* **2020**, *120*, 5158-5193.
- [51] R. C. Job, T. C. Bruice, *Proc. Natl. Acad. Sci. U. S. A.* **1975**, *72*, 2478-2482.
- [52] H. L. Carrell, J. P. Glusker, R. Job, T. C. Bruice, *J. Am. Chem. Soc.* **1977**, *99*, 3683-3690.
- [53] T. A. Scott, C. P. Berlinguette, R. H. Holm, H. C. Zhou, *Proc. Natl. Acad. Sci. U. S. A.* **2005**, *102*, 9741-9744.
- [54] L. Deng, R. H. Holm, *J. Am. Chem. Soc.* **2008**, *130*, 9878-9886.
- [55] L. Grunwald, M. Clemancey, D. Klose, L. Dubois, S. Gambarelli, G. Jeschke, M. Worle, G. Blondin, V. Mougel, *Proc. Natl. Acad. Sci. U.S.A.* **2022**, *119*, e2122677119.
- [56] T. D. P. Stack, R. H. Holm, *J. Am. Chem. Soc.* **1987**, *109*, 2546-2547.
- [57] C. Walsdorff, W. Saak, D. Haase, S. Pohl, *Chem. Commun.* **1997**, 1931-1932.
- [58] C. Walsdorff, W. Saak, S. Pohl, *J. Chem. Soc. Dalton Trans.* **1997**, 1857-1862.
- [59] T. Terada, T. Wakimoto, T. Nakamura, K. Hirabayashi, K. Tanaka, J. Li, T. Matsumoto, K. Tatsumi, *Chem. Asian J.* **2012**, *7*, 920-929.
- [60] A. McSkimming, D. L. M. Suess, *Inorg. Chem.* **2018**, *57*, 14904-14912.
- [61] M. Ye, N. B. Thompson, A. C. Brown, D. L. M. Suess, *J. Am. Chem. Soc.* **2019**, *141*, 13330-13335.
- [62] A. McSkimming, A. Sridharan, N. B. Thompson, P. Muller, D. L. M. Suess, *J. Am. Chem. Soc.* **2020**, *142*, 14314-14323.
- [63] M. A. Whitener, G. Peng, R. H. Holm, *Inorg. Chem.* **1991**, *30*, 2411-2417.
- [64] G. P. F. van Strijdonck, J. A. E. H. van Haare, J. G. M. van der Linden, J. J. Steggerda, R. J. M. Nolte, *Inorg. Chem.* **1994**, *33*, 999-1000.
- [65] J. E. Barclay, D. J. Evans, G. Garcia, M. D. Santana, M. C. Torralba, J. M. Yago, *J. Chem. Soc., Dalton Trans.* **1995**, 1965-1971.
- [66] D. Coucouvanis, M. Kanatzidis, E. Simhon, N. C. Baenziger, *J. Am. Chem. Soc.* **1982**, *104*, 1874-1882.

- [67] M. Kanatzidis, M. Ryan, D. Coucouvanis, A. Simopoulos, A. Kostikas, *Inorg. Chem.* **1983**, *22*, 179-181.
- [68] M. G. Kanatzidis, D. Coucouvanis, A. Simopoulos, A. Kostikas, V. Papaefthymiou, *J. Am. Chem. Soc.* **1985**, *107*, 4925-4935.
- [69] U. B. S. Pohl, *Z. Naturforsch.* **1992**, *47b*, 1266-1270.
- [70] J. Han, D. Coucouvanis, *Inorg. Chem.* **2002**, *41*, 2738-2746.
- [71] P. M. Jordan, *Curr. Opin. Struct. Biol.* **1994**, *4*, 902-911.
- [72] R. L. Mössbauer, *Z. Physik* **1958**, *151*, 124-143.
- [73] P. Gütllich, H. Prange, *Chem. Ing. Tech.* **1971**, *43*, 1049-1061.
- [74] V. Schünemann, H. Winkler, *Rep. Prog. Phys.* **2000**, *63*, 263-353.
- [75] D. H. Flint, R. M. Allen, *Chem. Rev.* **1996**, *96*, 2315-2334.
- [76] R. T. Stibrany, M. V. Lobanov, H. J. Schugar, J. A. Potenza, *Inorg. Chem.* **2004**, *43*, 1472-1480.
- [77] A. Albers, *Dissertation thesis, Georg-August-Universität (Göttingen)* **2013**.
- [78] J. Ballmann, S. Dechert, S. Demeshko, F. Meyer, *Eur. J. Inorg. Chem.* **2009**, *2009*, 3219-3225.
- [79] D. Coucouvanis, A. Salifoglou, M. G. Kanatzidis, A. Simopoulos, V. Papaefthymiou, *J. Am. Chem. Soc.* **1984**, *106*, 6081-6082.
- [80] J. Ballmann, X. Sun, S. Dechert, E. Bill, F. Meyer, *J. Inorg. Biochem.* **2007**, *101*, 305-312.
- [81] J. Ballmann, *Dissertation thesis, Georg-August-Universität (Göttingen)*, **2008**.
- [82] M. Orio, J. M. Mouesca, *Inorg. Chem.* **2008**, *47*, 5394-5416.
- [83] J. T. Hoggins, H. Steinfink, *Inorg. Chem.* **1976**, *15*, 1682-1685.
- [84] G. Christou, P. K. Mascharak, W. H. Armstrong, G. C. Papaefthymiou, R. B. Frankel, R. H. Holm, *J. Am. Chem. Soc.* **1982**, *104*, 2820-2831.
- [85] A. Salifoglou, A. Simopoulos, A. Kostikas, R. W. Dunham, M. G. Kanatzidis, D. Coucouvanis, *Inorg. Chem.* **1998**, *27*, 3394-3406.
- [86] A. Albers, T. Bayer, S. Demeshko, S. Dechert, F. Meyer, *Chem. Eur. J.* **2013**, *19*, 10101-10106.
- [87] G. B. Wong, M. A. Bobrik, R. H. Holm, *Inorg. Chem.* **1978**, *17*, 578-584.
- [88] H. Bönisch, C. L. Schmidt, G. Schäfer, R. Ladenstein, *J. Mol. Biol.* **2002**, *319*, 791-805.
- [89] C. J. Carrell, H. M. Zhang, W. A. Cramer, J. L. Smith, *Structure* **1997**, *5*, 1613-1625.
- [90] S. Iwata, M. Saynovits, T. A. Link, H. Michel, *Structure* **1996**, *4*, 567-579.
- [91] A. G. Trambitas, T. K. Panda, M. Tamm, *Z. Anorg. Allg. Chem.* **2010**, *636*, 2156-2171.
- [92] T. Gloge, K. Jess, T. Bannenberg, P. G. Jones, N. Langenscheidt-Dabringhausen, A. Salzer, M. Tamm, *Dalton Trans.* **2015**, *44*, 11717-11724.
- [93] O. Bienemann, R. Haase, U. Flörke, A. Döring, D. Kuckling, S. Herres-Pawlis, *Z. Naturforsch.* **2010**, *65b*, 798-806.
- [94] N. Kuhn, R. Fawzi, M. Steimann, J. Wiethoff, D. Bläser, R. Boese, *Z. Naturforsch.* **1995**, *50b*, 1779-1784.
- [95] M. Tamm, D. Petrovic, S. Randoll, S. Beer, T. Bannenberg, P. G. Jones, J. Grunenberg, *Org. Biomol. Chem.* **2007**, *5*, 523-530.
- [96] D. Petrovic, C. G. Hrib, S. Randoll, P. G. Jones, M. Tamm, *Organometallics* **2008**, *27*, 778-783.
- [97] T. K. Panda, C. G. Hrib, P. G. Jones, J. Jenter, P. W. Roesky, M. Tamm, *Eur. J. Inorg. Chem.* **2008**, *2008*, 4270-4279.
- [98] T. Ochiai, D. Franz, S. Inoue, *Chem. Soc. Rev.* **2016**, *45*, 6327-6344.
- [99] D. Petrovic, T. Glöge, T. Bannenberg, C. G. Hrib, S. Randoll, P. G. Jones, M. Tamm, *Eur. J. Inorg. Chem.* **2007**, *2007*, 3472-3475.
- [100] D. Petrovic, L. M. Hill, P. G. Jones, W. B. Tolman, M. Tamm, *Dalton Trans.* **2008**, 887-894.
- [101] S. Herres-Pawlis, U. Flörke, G. Henkel, *Eur. J. Inorg. Chem.* **2005**, *2005*, 3815-3824.
- [102] N. Kuhn, M. Göhner, M. Grathwohl, J. Wiethoff, G. Frenking, Y. Chen, *Z. Anorg. Allg. Chem.* **2003**, *629*, 793-802.
- [103] T. Glöge, D. Petrovic, C. G. Hrib, P. G. Jones, M. Tamm, *Z. Naturforsch.* **2008**, *63b*, 1155-1159.
- [104] J. Volbeda, P. G. Jones, M. Tamm, *Inorganica Chim. Acta* **2014**, *422*, 158-166.
- [105] X. Wu, M. Tamm, *Coord. Chem. Rev.* **2014**, *260*, 116-138.

- [106] N. Kuhn, M. Grathwohl, M. Steimann, G. Henkel, *Z. Naturforsch.* **1998**, *53b*, 997-1003.
- [107] T. Glöge, D. Petrovic, Cristian G. Hrib, C. Daniliuc, E. Herdtweck, Peter G. Jones, M. Tamm, *Z. Anorg. Allg. Chem.* **2010**, *636*, 2303-2308.
- [108] T. Glöge, F. Aal, S.-A. Filimon, P. G. Jones, J. Michaelis de Vasconcellos, S. Herres-Pawlis, M. Tamm, *Z. Anorg. Allg. Chem.* **2015**, *641*, 2204-2214.
- [109] D. Franz, T. Szilvasi, A. Pothig, F. Deiser, S. Inoue, *Chemistry* **2018**, *24*, 4283-4288.
- [110] P. Roquette, A. Maronna, A. Peters, E. Kaifer, H. J. Himmel, C. Hauf, V. Herz, E. W. Scheidt, W. Scherer, *Chemistry* **2010**, *16*, 1336-1350.
- [111] G. Philipp, *Z. Anorg. Allg. Chem.* **2012**, *638*, 15-43.
- [112] S. D. Jiang, D. Maganas, N. Levesanos, E. Ferentinos, S. Haas, K. Thirunavukkuarasu, J. Krzystek, M. Dressel, L. Bogani, F. Neese, P. Kyritsis, *J. Am. Chem. Soc.* **2015**, *137*, 12923-12928.
- [113] D. Maganas, A. Grigoropoulos, S. S. Staniland, S. D. Chatziefthimiou, A. Harrison, N. Robertson, P. Kyritsis, F. Neese, *Inorg. Chem.* **2010**, *49*, 5079-5093.
- [114] A. T. Kowal, I. C. Zambrano, I. Moura, J. J. G. Moura, J. LeGall, M. K. Johnson, *Inorg. Chem.* **1988**, *27*, 1162-1166.
- [115] A. C. Brown, D. L. M. Suess, *Comprehensive Coordination Chemistry III* **2021**, 134-156.
- [116] C. Goh, J. A. Weigel, R. H. Holm, *Inorg. Chem.* **1994**, *33*, 4861-4868.
- [117] R. H. Holm, W. Lo, *Chem. Rev.* **2016**, *116*, 13685-13713.
- [118] M. G. Kanatzidis, N. C. Baenziger, D. Coucouvanis, A. Simopoulos, A. Kostikas, *J. Am. Chem. Soc.* **1984**, *106*, 4500-4511.
- [119] J. Han, D. Coucouvanis, *Inorg. Chem.* **2002**, *41*, 2738-2746.
- [120] T. Herskovitz, B. A. Averill, R. H. Holm, J. A. Ibers, W. D. Phillips, J. F. Weiher, *Proc. Nat. Acad. Sci. U. S. A.* **1972**, *69*, 2437-2441.
- [121] J. Cambray, R. W. Lane, A. G. Wedd, R. W. Johnson, R. H. Holm, *Inorg. Chem.* **1977**, *16*, 2565-2571.
- [122] K. Tanifuji, N. Yamada, T. Tajima, T. Sasamori, N. Tokitoh, T. Matsuo, K. Tamao, Y. Ohki, K. Tatsumi, *Inorg. Chem.* **2014**, *53*, 4000-4009.
- [123] J. G. Reynolds, E. J. Laskowski, R. H. Holm, *J. Am. Chem. Soc.* **1978**, *100*, 5315-5322.
- [124] L. Noodleman, C. Y. Peng, D. A. Case, J. M. Mouesca, *Coord. Chem. Rev.* **1995**, *144*, 199-244.
- [125] A. Sridharan, A. C. Brown, D. L. M. Suess, *Angew. Chem. Int. Ed.* **2021**, *60*, 12802-12806.
- [126] L. Que, Jr., M. A. Bobrik, J. A. Ibers, R. H. Holm, *J. Am. Chem. Soc.* **1974**, *96*, 4168-4178.
- [127] J. A. Weigel, K. K. P. Srivastava, E. P. Day, E. Munck, R. H. Holm, *J. Am. Chem. Soc.* **1990**, *112*, 8015-8023.
- [128] M. G. Kanatzidis, D. Coucouvanis, A. Simopoulos, A. Kostikas, V. Papaefthymiou, *J. Am. Chem. Soc.* **1985**, *107*, 4925-4935.
- [129] G. C. Papaefthymiou, E. J. Laskowski, S. Frota-Pessoa, R. B. Frankel, R. H. Holm, *Inorg. Chem.* **1982**, *21*, 1723-1728.
- [130] W. O. Gillum, R. B. Frankel, S. Foner, R. H. Holm, *Inorg. Chem.* **1976**, *15*, 1095-1100.
- [131] L. Noodleman, E. J. Baerends, *J. Am. Chem. Soc.* **1984**, *106*, 2316-2327.
- [132] V. Papaefthymiou, M. M. Millar, E. Muenck, *Inorg. Chem.* **1986**, *25*, 3010-3014.
- [133] A. T. Fiedler, T. C. Brunold, *Inorg. Chem.* **2005**, *44*, 9322-9334.
- [134] N. Elghobashi-Meinhardt, D. Tombolelli, M. A. Mroginski, *Catalysts* **2021**, *11*, 245.
- [135] J. Jordanov, E. K. H. Roth, P. H. Fries, L. Noodleman, *Inorg. Chem.* **1990**, *29*, 4288-4292.
- [136] P. Middleton, D. P. Dickson, C. E. Johnson, J. D. Rush, *Eur. J. Biochem.* **1980**, *104*, 289-296.
- [137] H. Beinert, R. H. Holm, E. Munck, *Science* **1997**, *277*, 653-659.
- [138] J. C. Crack, J. Green, A. J. Thomson, N. E. Le Brun, *Acc. Chem. Res.* **2014**, *47*, 3196-3205.
- [139] J. A. Cracknell, K. A. Vincent, F. A. Armstrong, *Chem. Rev.* **2008**, *108*, 2439-2461.
- [140] U. Bierbach, W. Saak, D. Haase, S. Pohl, *Z. Naturforsch.* **1991**, *46b*, 1629-1634.
- [141] Y.-J. Kim, J.-H. Han, *Bull. Korean Chem. Soc.* **2012**, *33*, 48-54.
- [142] C. Goh, J. A. Weigel, R. H. Holm, *Inorg. Chem.* **1994**, *33*, 4861-4868.
- [143] G. R. Hanson, K. E. Gates, C. J. Noble, M. Griffin, A. Mitchell, S. Benson, *J. Inorg. Biochem.* **2004**, *98*, 903-916.

- [144] S. Stoll, A. Schweiger, *J. Magn. Reson.* **2006**, *178*, 42-55.
- [145] Y. B. Kim, C. S. Kim, C. K. Lee, *J. Heterocycl. Chem.* **1994**, *31*, 1653-1656.
- [146] M. Noguchi, T. Fujieda, W. C. Huang, M. Ishihara, A. Kobayashi, S.-i. Shoda, *Helv. Chim. Acta.* **2012**, *95*, 1928-1936.
- [147] G. M. Sheldrick, *Acta Cryst.* **2015**, *A71*, 3-8.
- [148] G. M. Sheldrick, *Acta Cryst.* **2015**, *C71*, 3-8.
- [149] A. L. Spek, *Acta Cryst.* **2015**, *C71*, 9-18.
- [150] *X-RED*, STOE & CIE GmbH, Darmstadt, Germany, 2002.
- [151] *SADABS*, BRUKER AXS GmbH, Karlsruhe, Germany, 2016.

List of Abbreviations

Å	Angstrom (s) 10 ⁻¹⁰ m
CoCp* ₂	decamethylcobaltocene
CoCp	cobaltocene
[Cp ₂ Fe](PF ₆)	Ferrocenium hexafluorophosphate
[Cp* ₂ Fe](PF ₆)	Decamethylferrocenium hexafluorophosphate
d	Doublet (NMR)
DMSO	Dimethyl Sulfoxide
CV	cyclic voltammetry
EA	Elemental analysis
EPR	Electron Paramagnetic Resonance
eq.	equivalent(s)
ESI	Electrospray Ionization
<i>g</i>	landé <i>g</i> - factor
Cys	cysteine
His	histidine
d	day
DMF	N, N- dimethylformamide
ET	electron transfer
Et ₂ O	diethyl ether
HiPIP	High-potential iron sulfur protein
MLCT	Metal to ligand charge transfer
LMCT	Ligand to metal charge transfer
m	medium (IR), multiplet (NMR)
m/z	mass per charge (MS)
Me	Methyl
MeCN	acetonitrile
MS	Mass Spectrometry
Hz	Hertz
IR	infrared
NMR	Nuclear Magnetic resonance
M	molar
Ph	phenyl
<i>PI</i>	Paramagnetic impurity
ppm	parts per million
py	pyridine

r	molecular radius
rt	Room temperature (25°C)
s	singlet (NMR), Strong (IR)
br	broad
SQUID	Superconducting quantum interference device
^t Bu	Tert-buthyl
THF	Tetrahydrofuran
UV-vis	Ultraviolet-visible spectroscopy
<i>V</i>	volume
w	weak(IR)
DBD	dibenzo[<i>c,e</i>][1,2]dithiine
1,2-BIB	1,2-bis(1 <i>H</i> -benzo[<i>d</i>]imidazol-2-yl)benzene

Curriculum Vitae

Lanxia Hu

Date of Birth: 27.08.1989

Place of Birth: Shandong, China

Nationality: Chinese

Education

- | | | |
|----------------|---|---------------|
| PhD thesis | Georg-August University Göttingen, Germany.
Department of Inorganic Chemistry
“New Structural and Functional Synthetic Analogues for Fe/S Clusters”
Supervisor: Prof. Dr. Franc Meyer | 4/2018-9/2022 |
| M. Sc. Studies | Fuzhou University & Fujian Institute of Research on the Structure of Matter, CAS, China.
Department of Inorganic Chemistry
“Design, Synthesis and Properties of Copper Halogen Clusters”
Supervisor: Prof. Dr. Yao Kang & Prof. Dr. Jian Zhang | 9/2014-6/2017 |
| B. Sc. Studies | Taishan University, China.
Department of Inorganic Chemistry | 9/2010-6/2014 |

Academic Activities

- 7/2022 Poster presentation in 16th European Biological Inorganic Chemistry Conference (EuroBIC-16), Grenoble, France. Title: [2:2] Site-Differentiated [4Fe-4S] Clusters Ligated by Bidentate Imidazolin-2-imine Ligands: Syntheses and Characterizations.
- 6/2022 Talk and Poster presentation in 14th Göttinger Chemie-Forum, Göttingen, Germany. Title: [2:2] Site-Differentiated [4Fe-4S] Clusters Ligated by Bidentate Imidazolin-2-imine Ligands: Syntheses and Characterizations.
- 7/2021 Poster presentation in 13th Göttinger Chemie-Forum, Göttingen, Germany. Title: Synthesis of Well-Defined [2:2] Site-Differentiated [4Fe-4S] Clusters.
- 9/2019 Summer School on Spectroscopy and Electronic Structure of Transition Metal Complexes, Gelsenkirchen, Germany.
- 7/2015 The 9th National Conference on Inorganic Chemistry, NanChang, China.

Honors and Awards

2017-2021 Fellowship from the China Scholarship Council

2017 Outstanding Academic Scholarship

2012-2013 National Encouragement Scholarship

2012-2013 Outstanding Student Scholarship

2010-2011 Outstanding Student Scholarship

2010-2011 Second-class scholarship of Taishan University

Publications

Lanxia Hu, Sandeep Gupta, Yang Liu, Sebastian Dechert, Serhiy Demeshko, and Franc Meyer, [2:2] Site-Differentiated [4Fe-4S]³⁺ Clusters Stabilized by a Neutral Bidentate N-donor Ligand, Manuscript in preparation.

Lanxia Hu[#], Aiping Zheng[#], Yao Kang, Tian Wen, Jian Zhang, A Supersalt-type Copper(I)-Thiolate Cluster with Applications for Mechano/Thermochromism and Oxygen Evolution Reaction, *Chem. Commun.* **2020**, 56, 3967-3970.

Lan-Xia Hu, Mei-Yan Gao, Wen Tian, Yao Kang, Shumei Chen, Synthesis of Halide-modulated Cuprous (I) Coordination Polymers with Mechanochromic and Photocatalytic Properties, *Inorg. Chem.* **2017**, 56, 6507-6511.

Mei-Yan Gao, Shu-mei Chen, **Lan-Xia Hu**, Lei Zhang “Synthesis and photocatalytic H₂ evolution properties of four Titanium-oxo-Clusters based on cyclohex-3-ene-1-carboxylate ligand. *Dalton Trans.* **2017**, 46, 10630-10634.

Lan-Xia Hu, Fei Wang, Yao Kang, and Jian Zhang “Structural Design of Zeolitic Cluster Organic Frameworks from Hexamethylenetetramine and Copper-Halide Clusters”, *Cryst. Growth Des.* **2016**, 16, 7139–7144.

Acknowledgement

First of all, I would like to thank Prof. Dr. Franc Meyer, for offering me the opportunity to work in this group and for the supervision of this thesis. I am also truly grateful for his sympathetic guidance, for granting of scientific freedom, for providing an excellent working atmosphere, and also for his continuous support during the past years.

Furthermore, I would also like to thank Prof. Dr. Inke Siewert for the useful discussion about my questions and constructive comments and for co-supervising this thesis. I want to thank Dr. Lisa Vondung for co-supervising the final stage of my thesis. And I am also grateful to the other members of the thesis committee as well as the examination board for spending their precious time on this thesis project.

For correcting parts of my thesis, I thank Gan Xu, Xian Zhang, Yue Wang, Weiyang He, Shaoan Hua, Yang Liu.

There are many more people who have contributed to parts of this work to whom I want to address my thanks. For X-ray diffraction measurements and refinement of the obtained structure, I am grateful to Dr. Sebastian Dechert, Anna Kölpin, and Jana Löcken, especially to Dr. Sebastian Dechert for always patiently looking through hundreds of what looked like test tubes that actually did not contain any single crystals, for DFT calculations, and also for a lot of help in all kinds of computer problems. I want to thank Dr. Serhiy Demeshko for teaching me how to use Mössbauer spectrometer, for always patiently helping me solve problems, and also for SQUID measurements. Many thanks to Dr. Sandeep Gupta for many SQUID measurements, data fitting, and correcting the writing part of SQUID of my paper and thesis. I am grateful to Andreas Schwarz and Jörg Teichgräber for the distribution of chemicals and laboratory materials.

I am thankful to Dr. Michael John, the whole NMR service department, and especially Christiane Siebert for measuring my countless NMR spectra. I want to thank Dr. Claudia Stückl for the EPR measurements, thank all the staff in the MS facilities, and thank all the staff in the analytic laboratory.

I want to thank Britta Müller, Dr. Claudia Stückl, and all staff from the dean's office for taking care of all the administrative issues. I am grateful to all the staff, from the craft shops, to the cleaning staff, caretakers, and all others who contributed to their work.

I am grateful to everybody in AK Meyer, especially Dr. Yang Liu, for giving me a lot of good suggestions and always patiently helping me solve all kinds of problems for the past five years, so thank you for everything, Dr. Yang Liu! For the great working atmosphere and a lot of fun in the lab I want to thank Dr. Yang Liu, Dr. Jianfeng Wu, Dr. Ming Li, Dr. Shaoan Hua, Dr. Pengcheng Duan, Dr. Sandeep Gupta, Dr. Massimiliano Morganti, Dr. Anna Kölpin, Dr. Joanne Wong, Dr. Roland Alexander Schulz, Dr. Thomas Kothe, Dr. Xian Zhang, Dr. Weiyang He, Dr. Sheida Rajabi, Yue Wang, Yue Ma, Guillermo Duran-Solares, Giuseppe Lococciolo, Valeria Tagliavini, Juliane Kamlah, Manuel Oelschlegel, Disha Bhattacharya, Simindokht Gol Kar, Ting-Yi Chen, Isabelle Rüter, Moritz Joswig, Sara Ida Mozzi, Martin Dzemski, U-Hyun Kim, Kriti Gupta, Maximilian Seiss, Mareike Niemann, Jan Kruse, Leili Dadkhahan, Niclas Werthmann, Ajdin Velic.

I would like to thank my labmates, Dr. Christine Schiewer, Kevin Lüken, Valeria Tagliavini, Juliane Kamlah, Ajdin Velic and their students, for the great atmosphere in the lab, for sharing chemicals, and also help me translate German letters or emails. I would also thank our Fe/S glovebox caretakers, Dr. Thomas Kothe, Kevin Lüken, Dr. Sandeep Gupta, Valeria Tagliavini, and Juliane Kamlah, for spending a lot of time taking care of this high-maintenance and old Fe/S glovebox.

I am particularly thankful for the four-year financial support from the Chinese Scholarship Council (CSC). I would like to thank my friends in Germany, Yang Liu, Ming Li, Jiang Feng Wu, Yue Wang, Xian Zhang, Weiying He, Jing Li, Kui Zeng, Long Yang, Yu Zhang, Yue Ma, Sier Sang, Tao Chen, Huiping Li, Yihao Ren, Xiao Guo, Zheng Chen, Bangchang Zhu, Yujie Bai, Yajie Zhu, Xiaona Song, and so on. I want to thank my remote Chinese friends, Dan Wu, Fei Liu, Huilan Wu, Zaiyang Dong, Jianfang Wang, Yangyang Hu, Yujing Liu, Lei Zhang, Qingrong Ding, Tian Wen, Aiping Zheng, and other friends for a wonderful time during the past five years. I am deeply thankful to all my family for their unconditional support throughout my life. I am truly grateful to Dr. Xiangdong Li for his love and his great support!